Nanostructured Materials: an Experimental and Computational Study

by

Francesco Caddeo

Functional Materials Group
School of Physical Sciences
University of Kent

Supervisors:

Dr. Anna Corrias
Dr. Dean C. Sayle

A thesis submitted for the degree of
Doctor of Philosophy in Chemistry

Canterbury, September 2016

ABSTRACT

Nanostructured materials: an experimental and computational study.

School of Physical Sciences, University of Kent

Francesco Caddeo

In this thesis, experiment and atomistic simulations have been used in order to study the structure and properties of materials at the nanoscale focussing the attention, in particular, on metal oxide nanoparticles. Chapter 3 presents results on $CuFe_2O_4$-SiO_2 nanocomposites where copper ferrite nanoparticles are embedded within a silica aerogel and xerogel matrix. In this case, extended X-ray absorption fine structure (EXAFS) spectroscopy has been extremely valuable in order to elucidate the cation distribution of the spinel. CeO_2-SiO_2 nanocomposites in form of aerogel and xerogel have been also synthesised and characterised. The CeO_2 nanoparticles are either grown within the porous silica matrix (Chapter 4) or synthesised in advance by a hydrothermal method (Chapter 5). In order to enhance the reactivity, the attention has been focused on obtaining ceria cuboidal nanoparticles and on their dispersion in a silica aerogel matrix. An atomistic model of a CeO_2 cuboidal nanoparticle has been then obtained using Molecular Dynamics (MD) simulations (Chapter 6), by performing the crystallisation of the nanoparticle with a new technique, involving the use of a crystalline seed, which drives the crystallisation to the cubic shape. The atomistic model has been found to be in quantitative agreement with experiment. The mechanical properties of CeO_2 nanoparticles have been then calculated as a function of size, shape and microstructure, and are presented in Chapter 7. It has been found that the mechanical properties of CeO_2 nanoparticles are dominated by the presence of grain boundaries. Furthermore, the simulations predict that *Ostwald ripening* can be induced along a $\Sigma 11$ grain boundary by applying uniaxial force.

INDEX

CHAPTER 1.

Introduction to silica aerogels, xerogels and related nanocomposites

1.1. Silica aerogels

Following the last IUPAC recommendations[1], the aerogel can be defined as a '*gel comprised of a microporous solid in which the dispersed phase is a gas*'. These materials have a very high degree of porosity, an ultra-low apparent density, high specific surface area and exhibit a wide variety of extraordinary properties including low thermal conductivity, low dielectric constant and low refractive index. In Table 1.1, the typical properties of silica aerogels are shown.

Aerogels were synthesised for the first time by S. S. Kistler in the 1930's[2] as a proof that gels consist in a two-phase solid-liquid structure. In his work, Kistler synthesised silica aerogel together with a series of aerogels from other materials including alumina, tungsten oxide, ferric oxide, tin oxide and cellulose. The main idea was to replace the liquid phase of the gel with air preserving its solid microstructure; in order to do this and avoid any shrinkage of the gel, Kistler performed the extraction of the solvent in supercritical conditions. The material obtained was a solid with a very low apparent density.

However, Kistler's methods were expensive and time consuming. He synthesised silica aerogel using a mixture of waterglass and water as starting materials and hydrochloric acid as a catalyst. The gelation was very slow and a series of steps were

Table 1.1 Typical properties of a silica aerogel; ref.[3]

Property	**Value**
Apparent density	0.003 – 0.35 g/cm^3
Internal surface area	600 – 1000 m^2/g
% solid	0.13 – 15%
Mean pore diameter	~ 20 nm
Primary particle diameter	2 – 5 nm
Refractive index	1.0 – 1.08
Coefficient of thermal expansion	2.0 – 4.0 * 10^{-6}
Dielectric constant	~ 1.1
Sound velocity	100 m/s

required in order to remove the sodium chloride formed and to exchange the water with a more suitable solvent for the supercritical extraction, such as ethanol. Due to these reasons, there was not interest in the aerogel field until the 1970's, when the synthetic procedures have been reconsidered and simplified. Methods involving the use of organic silicates like tetraethylorthosilicate (TEOS)[4] as a silica precursor and ethanol as a solvent started to be developed and the interest in the study and commercial production of silica and other aerogel materials greatly increased.

Nowadays a huge amount of work has been published on the synthesis, properties and applications of aerogels. Silica aerogel is the most common and widely studied, finding application in the field of sensors,[5,6] adsorption of organic pollutants,[6-8] drug delivery,[9,10] integrated circuits,[11,12] thermal insulation technology,[13,14] and catalysis.[15,16]

The synthesis of silica aerogels is performed by means of the sol-gel process and it can be divided in 3 general steps:

- *Gel preparation:* A solution of a silica precursor is solubilised in a suitable solvent and treated with a catalyst that can be a mineral acid or a base. A series of hydrolysis and condensation reactions take place forming the silica network and the viscosity of the solution suddenly increases after a certain amount of time; at this moment, the transition from the solution to the gel takes place. The gel is generally called alcogel or hydrogel depending if the solvent used is respectively alcohol or water.
- *Aging of the gel:* The aging process is usually performed in order to strengthen the silica porous network. The gel can be aged in its mother solution or in a closed container in order to avoid the evaporation of the solvent.
- *Drying of the gel:* In order to obtain an aerogel the drying process is carried out in special conditions, to avoid the shrinkage of the gel. If the solvent is removed by evaporation the tension forces at the liquid vapour interphase causes the collapse of the porous microstructure and ultimately the shrinkage of the gel; the material obtained is more dense, mostly microporous and called xerogel. If the porous microstructure of the gel needs to be preserved the solvent is removed in supercritical conditions. This is usually performed in an

autoclave reaching the critical temperature and pressure of the solvent used during the synthesis.

In Figure 1.1, a schematic representation of the synthesis of an aerogel is shown.

1.1.1. Chemistry of the sol-gel process

The sol-gel process[17] is a widely used synthetic procedure to produce oxides starting from hydrolysable precursors, such as alkoxides. Through hydrolysis and condensation reaction the process give rises first to a sol, a colloidal suspension of particles in a solvent, and then to a gel, a semi-rigid solid which entraps the solvents within its pores.

From a chemical point of view, the precursors adopted in this kind of synthesis are usually metal alkoxides with general formula $M(OR)_n$ which are subjected, in solution, to a series of hydrolysis equilibria:

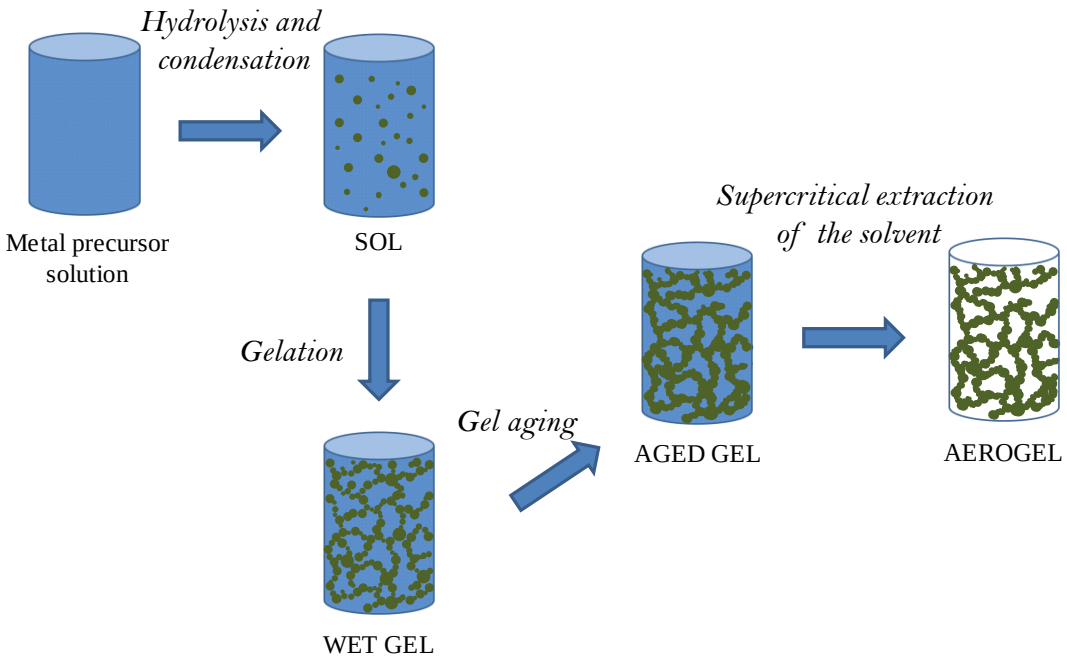

Figure 1.1 Schematic representation of the synthesis of aerogel

$$M(OR)_n + H_2O \rightleftharpoons M(OR)_{n-1}(OH) + ROH$$
$$M(OR)_{n-1}(OH) + H_2O \rightleftharpoons M(OR)_{n-2}(OH)_2 + ROH$$
$$\dots$$
$$M(OR)_{n-(n-1)}(OH)_{n-1} + H_2O \rightleftharpoons M(OH)_n + ROH$$

In the meantime, depending on parameters such as temperature, metal oxide precursor and use of catalysts, condensation reactions start taking place, with the consequent formation of M-O-M bonds. The condensation reactions may take place between two –OH groups or between a –OH and –OR group that has not been hydrolysed yet; in the following scheme two of the possible equilibria are reported:

$$M(OR)_{n-1}(OH) + M(OR)_n \rightleftharpoons (OR)_{n-1}M\text{-}O\text{-}M(OR)_{n-1} + ROH$$
$$2M(OR)_{n-1}(OH) \rightleftharpoons (OR)_{n-1}M\text{-}O\text{-}M(OR)_{n-1} + H_2O$$

The hydrolysis and condensation reactions lead to the formation of small particles, whose size is function of a multitude of factors like temperature, precursor used, solvent and catalyst. Depending on the growth process, the inorganic clusters formed can lead to a colloidal solution of particles or to the formation of branched chain polymers in solution. In both cases, if the relative amount of precursor and solvent is properly chosen, a 3D solid network is formed, enclosing the solvent medium within its porous structure. At this stage, the viscosity of the solution suddenly increases and gelation occurs. A gel can be then described as a material with a dual solid-liquid nature.[3]

The synthesis of materials with the sol-gel process requires at first a careful control of the relative amounts of starting materials. Most of the metal alkoxides are not soluble in water and a mutual solvent is needed; alcohols are the most used. The choice of the solvent is also crucial in order to plan the drying process: if a supercritical extraction of the solvent needs to be performed to obtain an aerogel, alcohols are more suitable than water as they have lower critical points[18]. However, it must be noted that alcohols

are present in the hydrolysis equilibrium as products and this leads to a decrease in the hydrolysis rate.

A catalyst is normally needed in order to enhance the reaction rate of both hydrolysis and condensation. Mineral acids like HCl, HNO_3, HF and H_2SO_4 can be used to catalyse the hydrolysis reactions[19]. Both hydrolysis and condensation reactions are also catalysed by basic conditions and diluted NH_3 or NaOH can be used as a basic catalyst[20]. Depending on the relative molar ratios $M(OR)_n/H_2O$/catalyst and nature of the catalyst, different products are obtained with different microstructural features.

It is accepted, as a general rule, that under basic catalysis the condensation reactions lead to particles that can grow to a sufficient size to form a colloidal solution. Under acidic conditions instead, the small particles start aggregating before their growth and a branched chain structure is formed[19]. In both cases, the aggregation of the particles leads to the formation of a 3D solid network of amorphous metal oxide, where the metal centres are connected with –oxo (M-O-M) and – hydroxo (M-OH-M) bridges.

1.1.2. Aging of the gel

Once the gel is formed, its structure can be considered in dynamic evolution. The solid phase of the gel may undergo structural changes after gelation during the gel aging. The result of the aging process is usually an increase in the connectivity between the particles that form the 3D solid network, strengthening the entire structure. Two main aging mechanisms have been identified and both of them happen by means of the solvent within the porous structure[21]. The first mechanism consists in the dissolution of some material from the surface of a particle and re-precipitation onto the necks between particles. This is due to the difference in solubility between two surfaces with different curvatures. The second mechanism is the dissolution of the small particles and re-precipitation into bigger ones. This ripening process is usually slower than the first mechanism and becomes important after long aging times, leading to a coarsening of the structure. Depending on the material and the microstructural features that one wants to obtain, different aging conditions can be chosen.

1.1.3. The drying process

Once the gel has been aged, a drying process is needed in order to remove the solvent from the pores. It must be taken into account that a capillary pressure (Δp) is present at the liquid-vapour interphase within the pores, Figure 1.2, which is inversely proportional to the pore radius, and it is described by the Laplace equation:

$$\Delta p = \frac{2\gamma cos\theta}{r} \qquad \text{eq. 1.1}$$

where γ is the surface tension of the liquid, θ the contact angle of the meniscus at the liquid-vapour interphase and r the radius of the pore. If the gel is dried by simple evaporation of the solvent, the capillary pressure leads to the collapse of the porous structure (black arrows, Figure 1.2). In this case, a denser and mainly microporous material is obtained, called xerogel.

In order to avoid the collapse of the porous structure, and to obtain an aerogel, the traditional way to dry the gel consists in extracting the solvent in supercritical conditions, avoiding the formation of the liquid-vapour interphase. This process is

carried out using a pressure-resisting vessel, filled with a certain amount of solvent, where the gels are placed, Figure 1.3(a). The system is equipped with a thermocouple, and inlet and outlet valves, through which N_2 gas is flushed. Once the atmosphere is completely inert, the valves are closed and the temperature is increased with a certain rate. The pressure also increases with the temperature, following the path represented in Figure 1.3(b). The quantity of solvent within the chamber is chosen so that the pressure increases with the temperature avoiding the transition to the vapour phase. Once the solvent reaches its supercritical state, the chamber can be slowly vented trying to keep the temperature constant.

The supercritical extraction of the solvent for the synthesis of aerogels was used for the first time by Kistler[18]. He firstly tried to synthesise aerogels by extracting the water used as solvent during the sol-gel process. However, this experiment failed, as when the water approaches the critical parameter, its solvent power induces the formation of a colloidal solution of silica in water. Kistler then performed the exchange of the water with solvents with lower critical points e.g. methanol, obtaining the aerogel after supercritical extraction. The critical points of some common solvents are reported in Table 1.2.

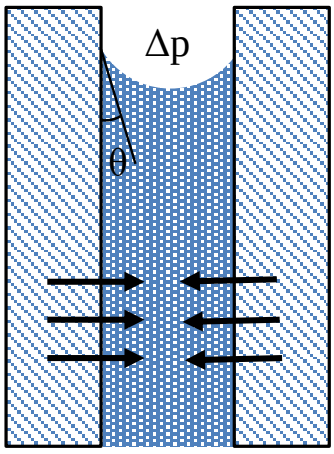

Figure 1.2 Representation of the capillary pressure, Δp, within a cylindrical pore, due to the formation of a meniscus with a contact angle θ.

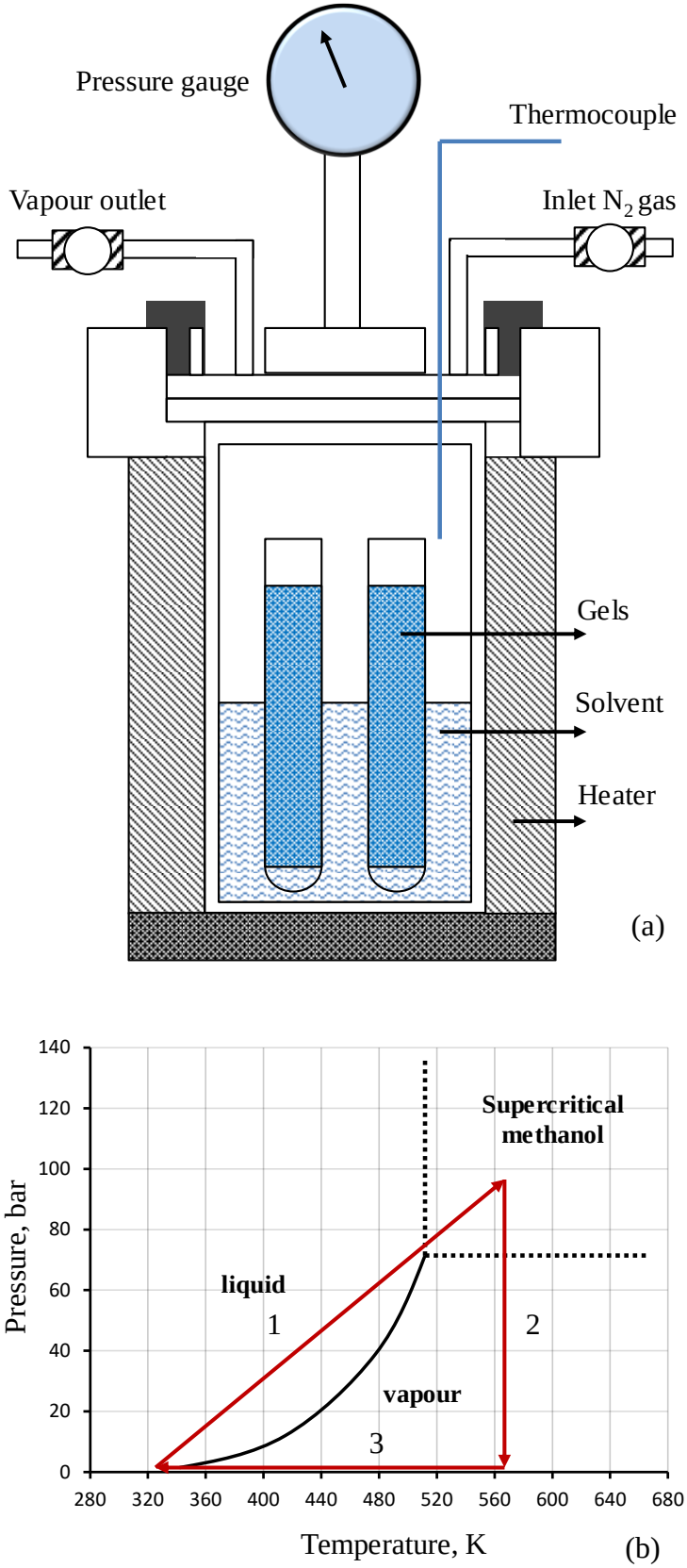

Figure 1.3 (a) representation of a autoclave for supercritical extraction of methanol; (b) schematic showing the path follwed during the supercritical drying. Figure (a) is reproduced with permission, ref.[3] [copyright © 2010, Jyoti L. Gurav et al.] Figure (b) is reproduced with permission, ref.[19] **[**copyright © 2008 Elsevier**]**

Peri[22] firstly and then Teichner and Nicolaon[23] introduced the process to obtain silica aerogels using alkoxysilanes, e.g. TEOS, as precursors, via supercritical extraction of the solvent. The aerogels obtained in this way are usually monolithic and hydrophobic. The hydrophobicity of the so obtained aerogels is due to the esterification of the silanol groups at its surface by the solvent, when alcohols like methanol or ethanol are used. The problems associated with this technique are related to the safety requirements and to its high cost, due to the high temperatures.

A *low temperature supercritical drying* method has been also suggested by Tewari[24] and then extensively used for the synthesis of aerogels. This method consists in using CO_2 as fluid for the solvent extraction, having a very low critical temperature. During this procedure, liquid CO_2 is introduced inside a pressure resistant vessel where the gel is placed, reaching around 100 bar. The outlet valve is then open while still introducing liquid CO_2 until the exchange of the solvent is completed. The temperature is then increased up to 40 ºC, with the pressure kept constant, in order to ensure that the CO_2 is in the supercritical state, avoiding the formation of a liquid-vapour interphase. The chamber is then vented, and the aerogels obtained are hydrophilic, with limited aging effects due to the low temperature of the procedure. However, the whole process is very long, because the solvent exchange within the porous structure of the aerogels is slow.

Alternative methods to supercritical drying have been then introduced, mainly with the aim of reducing the costs of the process. An *ambient pressure drying* method has been proposed by Brinker,[25] and later developed,[26] which consists in a solvent exchange/surface modification procedure. The gel is washed with a solution of an

Table 1.2 Critical parameters of common fluids. ref.[27]

Solvent	T_C (ºC)	P_C (Atm)
Water	374.1	218
Ethanol	243.0	63
Methanol	239.4	78
Acetone	235.0	46
Carbon dioxide	31.0	73

aprotic solvent and reacted at the same time with trimethylchlorosilane (TMCS). The reaction produces Si-O-R groups, and thus creates a surface which can be wetted by a solvent with very low surface tension, as heptane. The drying of the gel is then performed at low temperature and ambient pressure, with a very limited shrinkage of the silica porous structure. Also in this case, the procedure is very long due to the solvent exchange process.

Another method that avoids the liquid-vapour interphase and thus the capillary forces is known as *freeze drying*[28]. During this process, the liquid phase of the gel is exchanged using a solvent which must have a low expansion coefficient and high sublimation pressure. The gel is then frozen and sublimed under vacuum. The main disadvantages of this technique are related with the possibility of damaging (or destroying) the porous structure of the gel during the crystallisation of the solvent within the pores. Long aging times are thus needed, in order to strengthen the porous network.

1.2. Nanocomposites

1.2.1. Silica aerogel as a 'hosting matrix'

Within the wide range of applications that involve the use of silica aerogels, an interesting role is played by the opportunity to synthesise nanocomposites where a nanophase is dispersed within the porous network of the silica matrix[29]. The interest in the synthesis of this kind of nanocomposites originates from several reasons:

i) Materials consisting of particles with dimensions at the nanoscale are difficult to manipulate. For example, in the field of catalysis, one of the main problems of the use of nanoparticles is their tendency to coalesce, forming bigger particles, under thermal treatments[30]. This phenomenon leads to a dramatic decrease of the surface area of the particles, thus of their reactivity. The particle confinement within the aerogel matrix provides a way to avoid the nanocrystal aggregation and growth.

ii) The high specific surface area of the aerogel, combined with its open porous structure, makes possible the synthesis of nanocomposites with high loading of the dispersed nanophase and its accessibility by external species.

iii) If a co-gelation procedure is used to synthesise the nanocomposites, the crystal growth of the dispersed nanophase is influenced by the confinement imposed by the aerogel matrix. The size distribution of the nanoparticles may be tuned by changing synthetic parameters.

The sol-gel process has been therefore employed to synthesise functional nanocomposites where mainly metal and metal oxide nanoparticles are embedded within the porous matrix of the aerogel, with the main purpose of obtaining materials that synergistically exhibit the properties of both the hosting matrix and the dispersed nanophase.

Due to the number of variables associated with the sol-gel process, a direct rationalization of the relationship between synthetic parameters and microstructural features of these nanocomposites is still challenging. Synthetic parameters include solvent used, precursor of the silica phase, catalyst, temperature, drying process used and approach adopted to introduce the dispersed nanophase within the silica matrix. Microstructural features include specific surface area, size of the nanoparticles, their homogeneity and distribution within the host matrix. A very important role is played

by the strategy adopted to introduce the dispersed nanophase within the silica aerogel matrix.

One way consists in performing the co-gelation of the silica matrix together with the precursors of the nanophase[31] or in a solution of pre-formed nanoparticles[32]. This method allows a good control over the loading of the dispersed nanophase. However, the presence of the precursors of the metal phase, or of the pre-formed nanoparticles, may affect the formation of the silica matrix. A careful choice of the synthetic conditions must be made.

Another way consists in adding the nanophase to a pre-formed silica aerogel matrix, for example by impregnation of the gel with a solution of the nanophase, in form of pre-formed nanoparticles or solution of its precursors[33,34]. In this case, the disadvantages are related with the poor control of the loading and homogeneity of the dispersed nanophase within the nanocomposite, and with the possibility of damaging the pre-formed silica matrix.

For all the nanocomposites synthesised in this thesis, the first approach was adopted, using either the precursors of the metal oxide nanophase or the pre-formed nanoparticles.

1.2.2. The two-step catalysed sol-gel process and the use of urea

Silica aerogels have been synthesised using the sol-gel process following two main approaches in terms of the catalysts used: the one-step all acid[31] or all basic catalysis[35] and the two-step acid-basic catalysis[36]. In Figure 1.4, the dependence of the hydrolysis and condensation reaction rate on the pH is shown. The hydrolysis has a minimum centred at pH = 7 while the condensation reactions have a minimum rate at pH around 4.5. Both reactions are catalysed in strong acidic conditions or in basic conditions. At pH values higher than 7, the condensation kinetics are faster than hydrolysis.

It has been shown that the microstructural features of silica aerogels are strongly dependent on the pH of the sol. Aerogels with very high specific surface area (850 – 1100 m^2/g) and small pore volume are synthesised in acidic conditions. Basic conditions lead instead to lower values of specific surface area and bigger pore volumes[20].

A two-step acid-base catalysed approach has been shown by Sarawade et al[37]. The method consists in a first step catalysed by oxalic acid followed by a second step where ammonia is added. Aerogels with different features were obtained depending on the time interval between the two steps during gelation.

When dealing with the synthesis of silica aerogel nanocomposites incorporating metal and metal oxide nanophases within the matrix, a careful choice of the synthetic conditions has to be made, as a homogeneous sol must be obtained, containing both the precursor of the silica and the metal phase. Casula et al.[38] prepared nanocomposites containing a nanophase of nickel and nickel oxide in form of nanoparticles dispersed in the silica aerogel matrix. Co-gelation of the silica matrix with a solution of nickel nitrate was performed, under acidic conditions with pH values of 0.8. The authors showed the possibility to tune the porous structure of the aerogel matrix by choosing different supercritical drying conditions. The same strategy has been also adopted for the synthesis of iron oxide[39] and FeCo alloy nanoparticles within the silica aerogel matrix.[31]

In that work, a one-step acid catalysed reaction was performed, in order to obtain a homogeneous sol and avoid the precipitation of metal hydroxides, which occurs under

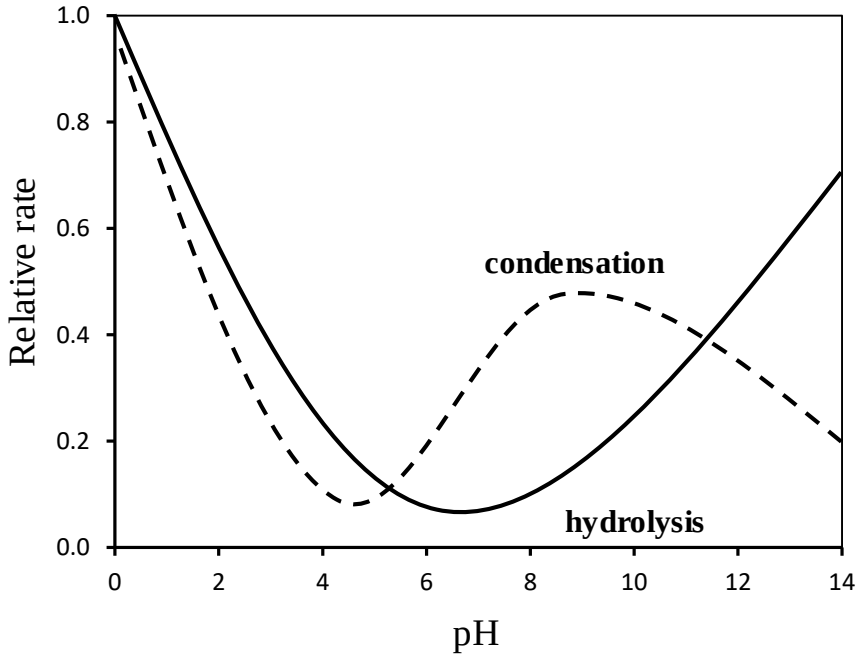

Figure 1.4 Dependence of the relative hydrolisys and condensation rates as a function of the pH of the solution. Reproduced with permission, ref.[19] **[**copyright © 2008 Elsevier]

basic conditions. However, this technique had some drawbacks: the silica aerogel matrix obtained in these conditions was mainly microporous, therefore with a limited accessibility to the dispersed nanophase. Furthermore, the synthesis required very long gelation times, up to 15 days.

A different approach has been then developed, which consists in a two-step acid-base catalysed synthesis involving urea as a gelation agent.[40] A first step under acidic conditions is performed, in order to promote the hydrolysis reactions. Subsequently, condensation reactions are promoted adding a solution of urea to the sol and performing the reaction at 85 ºC, in order to accelerate the sol-gel transition. These conditions have been found to be suitable for the preparation of silica aerogel nanocomposites using metal nitrates as precursors for the metal and metal oxide dispersed nanophase. At 85 ºC the urea undergoes a thermal decomposition that smoothly shifts the pH from acidic to basic, promoting the gelation. A series of different equilibria have been proposed in the literature for the decomposition of the urea, depending on the conditions.[41] It is known that, under thermal treatment, urea decomposes through the formation of isocyanic acid (HNCO), which in solution can be written as:

$$NH_2CONH_2 \rightleftharpoons NH_4^+ + CNO^-$$

The following equilibrium has been then proposed in acidic environment:[42]

$$CNO^- + 2H^+ + 2H_2O \rightleftharpoons NH_4^+ + H_2CO_3$$

The slow decomposition of urea leads therefore to a slow increase in the pH, thus the condensation reactions take place for the formation of the silica matrix, avoiding the precipitation of metal hydroxides.

1.2.3. Applications

This two-step catalysed sol-gel process has been then successfully used for the synthesis of several silica aerogel nanocomposites. Mn, Co and Ni ferrite nanoparticles within a silica aerogel matrix have been synthesised using this approach.[43] These nanocomposites have been recently tested as catalysts for the production of carbon nanotubes by catalytic chemical vapour deposition,[44] showing that the $NiFe_2O_4$-SiO_2 aerogel nanocomposite exhibits the highest catalytic performance.

FeCo-SiO_2 nanocomposites in form of aerogels have been also prepared with the same sol-gel process.[45] FeCo nanocrystals, with sizes ranging between 4 to 10 nm, were obtained homogeneously dispersed within the amorphous porous silica matrix of the aerogel. These nanocomposites have been recently tested as catalysts for the Fisher-Tropsch reaction,[46] showing excellent performances, if compared with other catalysts used for this process. One of the main advantages of these nanocomposites is their thermal stability, over very long reaction times.

Similar nanocomposites have been synthesised using different procedures. Yang et al.[47] reported the synthesis of a silica aerogel nanocomposite with metallic Co nanoparticles homogeneously dispersed within the matrix. The aerogel matrix was prepared following a procedure that involves the use of TEOS and a template, in methanol.[48] The nanocomposite has been then prepared by dispersion of the aerogel matrix in a Co^{2+} solution, using an ultrasonic processor, followed by a reduction step to reduce the Co^{2+}. A freeze-drying procedure has been then employed, to obtain the solid nanocomposite. This nanocomposite was then tested as a catalyst for the generation of hydrogen from NH_3BH_3,[49] as a less expensive alternative to precious metal catalysts such as Pt, Pd and Ru.

Han et al.[50] synthesised a silica aerogel nanocomposite with nickel nanoparticles embedded within the matrix. The method for the synthesis of the nanocomposite involves the use of a solution of pre-formed nanoparticles that are mixed with the sol containing the precursor for the amorphous silica. A one step procedure has been used, with a basic catalyst. The drying process has been performed at ambient pressure, after few solvent exchange steps. The nanocomposite has been then tested as catalyst for CO_2 mineralization, showing an enhanced catalytic activity if compared with the non-supported Ni nanoparticles.

Different nanostructures from metal oxide nanoparticles have been also embedded within the silica aerogel matrix in order to obtain nanocomposites with specific properties. Bargozin et al.[51] synthesised nanocomposites where multi-walled carbon nanotubes (MWCNT) are embedded within the silica aerogel matrix. These nanocomposites showed excellent performances in the absorption of organic pollutants from water, with a very low loading of dispersed nanophase. In this case, the dispersed MWCNT ensure an enhanced hydrophobicity, which coupled with the high porosity

of the aerogel, ensures absorption capacities for toxic pollutants like benzene or toluene up to 5 times the composite weight. Recently, Loche et al.[52] synthesised the first aerogel nanocomposite with graphene as dispersed nanophase, as novel oil sorbent from water. In this case, with very low loadings of dispersed nanophase within the silica matrix, these aerogel nanocomposites can absorb oil from water up to 7 times their weight and represent an excellent alternative as sorbents for water clean-up treatments.

1.3. References

[1] Alemán, J.V., Chadwick, A.V., He, J., Hess, M., Horie, K., Jones, R.G., Kratochvíl, P., Meisel, I., Mita, I., Moad, G. and Penczek, S., 2007. Definitions of terms relating to the structure and processing of sols, gels, networks, and inorganic-organic hybrid materials (IUPAC Recommendations 2007). *Pure and Applied Chemistry*, 79(10), pp.1801-1829.

[2] Kistler, S.S., 1932. Coherent expanded-aerogels. *The Journal of Physical Chemistry*, *36*(1), pp.52-64.

[3] Gurav, J.L., Jung, I.K., Park, H.H., Kang, E.S. and Nadargi, D.Y., 2010. Silica aerogel: synthesis and applications. *Journal of Nanomaterials*, 2010, 23, pp.1-11.

[4] Russo, R.E. and Hunt, A.J., 1986. Comparison of ethyl versus methyl sol-gels for silica aerogels using polar nephelometry. *Journal of Non-crystalline Solids*, *86*(1), pp.219-230.

[5] Wang, C.T. and Wu, C.L., 2006. Electrical sensing properties of silica aerogel thin films to humidity. *Thin Solid Films*, 496(2), pp.658-664.

[6] Sani, S., Muhid, M.N.M. and Hamdan, H., 2011. Design, synthesis and activity study of tyrosinase encapsulated silica aerogel (TESA) biosensor for phenol removal in aqueous solution. *Journal of Sol-gel Science and Technology*, 59(1), pp.7-18.

[7] Perdigoto, M.L.N., Martins, R.C., Rocha, N., Quina, M.J., Gando-Ferreira, L., Patrício, R. and Durães, L., 2012. Application of hydrophobic silica based aerogels and xerogels for removal of toxic organic compounds from aqueous solutions. *Journal of Colloid and Interface Science*, 380(1), pp.134-140.

[8] Dou, B., Li, J., Wang, Y., Wang, H., Ma, C. and Hao, Z., 2011. Adsorption and desorption performance of benzene over hierarchically structured carbon–silica aerogel composites. *Journal of Hazardous Materials*, 196(1), pp.194-200.

[9] Alnaief, M., Antonyuk, S., Hentzschel, C.M., Leopold, C.S., Heinrich, S. and Smirnova, I., 2012. A novel process for coating of silica aerogel microspheres for controlled drug release applications. *Microporous and Mesoporous Materials*, 160(1), pp.167-173.

[10] Caputo, G., Scognamiglio, M. and De Marco, I., 2012. Nimesulide adsorbed on silica aerogel using supercritical carbon dioxide. *Chemical Engineering Research and Design*, 90(8), pp.1082-1089.

[11] Jung, S.B., Park, S.W., Yang, J.K., Park, H.H. and Kim, H., 2004. Application of SiO_2 aerogel film for interlayer dielectric on GaAs with a barrier of Si_3N_4. *Thin Solid Films*, 447(1), pp.580-585.

[12] Park, S.W., Jung, S.B., Kang, M.G., Park, H.H. and Kim, H.C., 2003. Modification of GaAs and copper surface by the formation of SiO_2 aerogel film as an interlayer dielectric. *Applied Surface Science*, 216(1), pp.98-105.

[13] Saboktakin, A. and Saboktakin, M.R., 2015. Improvements of reinforced silica aerogel nanocomposites thermal properties for architecture applications. *International Journal of Biological Macromolecules*, 72, pp.230-234.

[14] Sing, K.S.W., 1982. Reporting physisorption data for gas/solid systems with special reference to the determination of surface area and porosity (Provisional). *Pure and Applied Chemistry*, 54(11), pp.2201-2218.

[15] Cao, S., Yeung, K.L. and Yue, P.L., 2006. Preparation of freestanding and crack-free titania–silica aerogels and their performance for gas phase, photocatalytic oxidation of VOCs. *Applied Catalysis B: Environmental*, 68(3), pp.99-108.

[16] Tai, Y., Murakami, J., Tajiri, K., Ohashi, F., Daté, M. and Tsubota, S., 2004. Oxidation of carbon monoxide on Au nanoparticles in titania and titania-coated silica aerogels. *Applied Catalysis A: General*, *268*(1), pp.183-187.

[17] Hench, L.L. and West, J.K., 1990. The sol-gel process. *Chemical Reviews*, 90(1), pp.33-72.

[18] Kistler, S.S., 1931. Coherent Expanded Aerogels and Jellies. *Nature*, 127(3211), pp.741.

[19] Dorcheh, A.S. and Abbasi, M.H., 2008. Silica aerogel; synthesis, properties and characterisation. *Journal of Materials Processing Technology*, 199(1), pp.10-26.

[20] Sinkó, K., 2010. Influence of chemical conditions on the nanoporous structure of silicate aerogels. *Materials*, 3(1), pp.704-740.

[21] Strøm, R.A., Masmoudi, Y., Rigacci, A., Petermann, G., Gullberg, L., Chevalier, B. and Einarsrud, M.A., 2007. Strengthening and aging of wet silica gels for up-scaling of aerogel preparation. *Journal of Sol-gel Science and Technology*, 41(3), pp.291-298.

[22] Peri, J.B., 1966. Infrared study of OH and NH_2 groups on the surface of a dry silica aerogel. *The Journal of Physical Chemistry*, 70(9), pp.2937-2945.

[23] Teichner, S.J., Nicolaon, G.A., Vicarini, M.A. and Gardes, G.E.E., 1976. Inorganic oxide aerogels. *Advances in Colloid and Interface Science*, 5(3), pp.245-273.

[24] Tewari, P.H., Hunt, A.J. and Lofftus, K.D., 1985. Ambient-temperature supercritical drying of transparent silica aerogels. *Materials Letters*, 3(9), pp.363-367.

[25] Prakash, S.S., Brinker, C.J. and Hurd, A.J., 1995. Silica aerogel films at ambient pressure. *Journal of Non-Crystalline Solids*, 190(3), pp.264-275.

[26] Shi, F., Wang, L. and Liu, J., 2006. Synthesis and characterisation of silica aerogels by a novel fast ambient pressure drying process. *Materials Letters*, 60(29), pp.3718-3722.

[27] Pierre, A.C. and Pajonk, G.M., 2002. Chemistry of aerogels and their applications. *Chemical Reviews*, 102(11), pp.4243-4266.

[28] Tamon, H., Ishizaka, H., Yamamoto, T. and Suzuki, T., 1999. Preparation of mesoporous carbon by freeze drying. *Carbon*, 37(12), pp.2049-2055.

[29] Aegerter, M.A., Leventis, N. and Koebel, M.M. eds., 2011. Aerogels Handbook. Springer: New York, NY, USA.

[30] Zhang, J., Kumagai, H., Yamamura, K., Ohara, S., Takami, S., Morikawa, A., Shinjoh, H., Kaneko, K., Adschiri, T. and Suda, A., 2011. Extra-low-temperature oxygen storage capacity of CeO_2 nanocrystals with cubic facets. *Nano Letters*, 11(2), pp.361-364.

[31] Casula, M.F., Corrias, A. and Paschina, G., 2002. FeCo–SiO_2 nanocomposite aerogels by high temperature supercritical drying. *Journal of Materials Chemistry*, 12(5), pp.1505-1510.

[32] Legrand-Buscema, C., Malibert, C. and Bach, S., 2002. Elaboration and characterisation of thin films of TiO_2 prepared by sol–gel process. *Thin Solid films*, 418(2), pp.79-84.

[33] Casas, L., Roig, A., Molins, E., Greneche, J.M., Asenjo, J. and Tejada, J., 2002. Iron oxide nanoparticles hosted in silica aerogels. *Applied Physics A*, 74(5), pp.591-597.

[34] Popovici, M., Gich, M., Roig, A., Casas, L., Molins, E., Savii, C., Becherescu, D., Sort, J., Surinach, S., Munoz, J.S. and Baró, M.D., 2004. Ultraporous single phase iron oxide-silica nanostructured aerogels from ferrous precursors. *Langmuir*, 20(4), pp.1425-1429.

[35] Dieudonné, P., Alaoui, A.H., Delord, P. and Phalippou, J., 2000. Transformation of nanostructure of silica gels during drying. *Journal of Non-Crystalline Solids*, 262(1), pp.155-161.

[36] Rao, A.V. and Bhagat, S.D., 2004. Synthesis and physical properties of TEOS-based silica aerogels prepared by two step (acid–base) sol–gel process. *Solid State Sciences*, 6(9), pp.945-952.

[37] Sarawade, P.B., Kim, J.K., Kim, H.K. and Kim, H.T., 2007. High specific surface area TEOS-based aerogels with large pore volume prepared at an ambient pressure. *Applied Surface Science*, 254(2), pp.574-579.

[38] Casula, M.F., Corrias, A. and Paschina, G., 2000. Nickel oxide–silica and nickel–silica aerogel and xerogel nanocomposite materials. *Journal of Materials Research*, 15(10), pp.2187-2194.

[39] Casula, M.F., Corrias, A. and Paschina, G., 2001. Iron oxide–silica aerogel and xerogel nanocomposite materials. *Journal of Non-Crystalline solids*, 293, pp.25-31.

[40] Casula, M.F., Loche, D., Marras, S., Paschina, G. and Corrias, A., 2007. Role of urea in the preparation of highly porous nanocomposite aerogels. *Langmuir*, 23(7), pp.3509-3512.

[41] Chen, J.P. and IsA, K., 1998. Thermal Decomposition of Urea and Urea Derivatives by Simultaneous TG/(DTA)/MS. *Journal of the Mass Spectrometry Society of Japan*, 46(4), pp.299-303.

[42] Loche, D., 2009. Ph.D. Thesis; Preparazione e caratterizzazione di nanocompositi aerogel per applicazioni catalitiche, University of Cagliari, IT.

[43] Loche, D., Casula, M.F., Falqui, A., Marras, S. and Corrias, A., 2010. Preparation of Mn, Ni, Co ferrite highly porous silica nanocomposite aerogels by an urea-assisted sol–gel procedure. *Journal of Nanoscience and Nanotechnology*, 10(2), pp.1008-1016.

[44] Loche, D., Casula, M.F., Corrias, A., Marras, C., Gozzi, D. and Latini, A., 2016. Catalytic chemical vapour deposition on MFe_2O_4–SiO_2 (M= Co, Mn, Ni) nanocomposite aerogel catalysts for the production of multi walled carbon nanotubes. *Journal of Nanoscience and Nanotechnology*, 16(7), pp.7750-7757.

[45] Carta, D., Mountjoy, G., Gass, M., Navarra, G., Casula, M.F. and Corrias, A., 2007. Structural characterisation study of FeCo alloy nanoparticles in a highly porous aerogel silica matrix. *The Journal of chemical physics*, 127(20), pp.204705-204705.

[46] Loche, D., Casula, M.F., Corrias, A., Marras, S. and Moggi, P., 2012. Bimetallic FeCo nanocrystals supported on highly porous silica aerogels as Fischer–Tropsch catalysts. *Catalysis Letters*, 142(9), pp.1061-1066.

[47] Yu, P.J., Lee, M.H., Hsu, H.M., Tsai, H.M. and Chen-Yang, Y.W., 2015. Silica aerogel-supported cobalt nanocomposites as efficient catalysts toward hydrogen generation from aqueous ammonia borane. *RSC Advances*, 5(18), pp.13985-13992.

[48] Tsai, C.H., Yang, F.L., Chang, C.H. and Chen-Yang, Y.W., 2012. Microwave-assisted synthesis of silica aerogel supported Pt nanoparticles for self-humidifying proton exchange membrane fuel cell. *International Journal of Hydrogen Energy*, 37(9), pp.7669-7676.

[49] Chandra, M. and Xu, Q., 2006. Dissociation and hydrolysis of ammonia-borane with solid acids and carbon dioxide: An efficient hydrogen generation system. *Journal of Power Sources*, 159(2), pp.855-860.

[50] Han, X., Williamson, F., Bhaduri, G.A., Harvey, A. and Šiller, L., 2015. Synthesis and characterisation of ambient pressure dried composites of silica aerogel matrix and embedded nickel nanoparticles. *The Journal of Supercritical Fluids*, 106, pp.140-144.

[51] Bargozin, H., Amirkhani, L., Moghaddas, J.S. and Ahadian, M.M., 2010. Synthesis and application of silica aerogel-MWCNT nanocomposites for adsorption of organic pollutants. *Scientia Iranica*, 17(2), pp.122-132.

[52] Loche, D., Malfatti, L., Carboni, D., Alzari, V., Mariani, A. and Casula, M.F., 2016. Incorporation of graphene into silica-based aerogels and application for water remediation. *RSC Advances*, 6(71), pp.66516-66523.

CHAPTER 2.

Synthesis, characterisation techniques and atomistic simulation

In this chapter, the experimental conditions used during the synthesis of the aerogel and xerogel nanocomposites are reported, together with a brief overview of the theoretical background regarding the characterisation techniques. This includes X-ray diffraction (XRD), N_2-physisorption, thermo-gravimetric analysis with simultaneous differential scanning calorimetry (TGA/DSC), transmission electron microscopy (TEM) and X-ray absorption spectroscopy (XAS). A brief overview on molecular dynamics simulations is also given, with particular attention on the potential model used in this thesis.

2.1. Synthetic conditions of the aerogel and xerogel nanocomposites

In this section, the synthetic conditions used to synthesise the aerogel and xerogel nanocomposites are presented, together with the drying processes and the thermal treatments required after the alcogel is obtained.

2.1.1. The sol-gel synthesis

The synthesis of the aerogel and xerogel nanocomposites presented in this thesis is based on a method previously developed by our group[1] and successfully used for the synthesis of silica aerogels nanocomposites containing Co, Ni and Mn ferrite nanoparticles[2] and FeCo alloy nanoparticles[3] with a loading of the dispersed nanophase up to 10% in weight. The procedure uses both the acidic and basic catalysis in a two-step approach (see Chapter 1), with the use of urea in the second step as a basic catalyst. Urea is used during the second step of the synthesis in order to have a smooth change of the pH of the solution, from acid to basic, avoiding the precipitation of the metal hydroxides. During the first step the TEOS is hydrolysed in acidic conditions and then a solution of urea is added. During the second step the solution is heated up to 85 ºC, in order to promote the gelation. Table 2.1 summarises the molar ratio of the reactants used.

Table 2.1 Molar ratios of the reactants used during the sol-gel process

STEP 1			
TEOS	H_2O	Ethanol	HNO_3
1	4.09	6.24	0.017
STEP 2			
Urea		Ethanol	H_2O
1.78		4.70	8.31

The synthetic procedure can be summarised as follows:

STEP 1

1) 200 ml of the hydrolysing acidic solution is prepared by mixing 80 ml of ethanol, 129.5 ml of H_2O and 2 ml of HNO_3
2) An ethanolic solution of TEOS is prepared by mixing 3 ml of ethanol and 7.90 ml of TEOS (0.035 mol) in a 100 ml conical flask
3) 3.965 ml of the hydrolysing solution is slowly added to the TEOS solution
4) The solution is heated up to 50 °C to promote the hydrolysis of the TEOS
5) A solution of the appropriate amount of the metal nitrates is prepared in 7.5 ml of ethanol
6) The ethanolic solution of the metal nitrates is added to the solution of TEOS at room temperature

STEP 2

7) A solution of urea is prepared by dissolving 3.513 g of urea (0.0579 mol) in 4.92 ml of distilled water and 9 ml of ethanol
8) The solution of urea is added to the TEOS solution containing the metal salts
9) After the solution has been stirred for 10 min at room temperature, this is transferred in an 85 °C bath at reflux until the change of its viscosity. The time at 85 °C is recorded as $T_{85\,°C}$.
10) The sol is transferred in a vial with a diameter of 1.7 mm, closed with Parafilm and put in an oven at 40 °C in order to complete its gelation.
11) The gelation time is also recorded

The aerogel and xerogel nanocomposites presented in Chapter 3 contain $CuFe_2O_4$ as the dispersed nanophase. In the first step of the synthesis, an ethanolic solution of $Fe(NO_3)_3$ and $Cu(NO_3)_2$ as the precursor for the nanophase is added to the solution of the pre-hydrolysed TEOS. Table 2.2 summarises the details of the synthesis.

In Chapter 4, the synthesis of new CeO_2-SiO_2 nanocomposites in form of aerogel and xerogel is presented. During the synthesis, a capping agent was added together with the cerium nitrate in order to control the size of the nanoparticles. Different nanocomposites have been prepared, changing the loading of CeO_2 and amount and

type of capping agent. Table 2.3 summarises the nanocomposites synthesised and details which capping agent has been used and in which molar ratio. In the case of the xerogel, the letter 'X' is used instead of 'A' in the name.

CeO_2-SiO_2 nanocomposites in form of aerogel have been also synthesised by embedding pre-formed CeO_2 nanoparticles previously synthesised by hydrothermal methods, and are presented in Chapter 5. In this case, the cerium salt is not used during the sol-gel synthesis but a solution of pre-formed nanoparticles in toluene (3 ml) is added during the step 1 (point 5). The pre-formed nanoparticles are synthesised in the presence of a capping agent; the use of a different capping agent leads to nanoparticles with different shapes. In Table 2.4, the details of the sol-gel synthesis are summarised. The details of the hydrothermal synthesis are outlined in Sections 5.2.1 and 5.2.2.

Table 2.2 Synthesis details of the nanocomposites presented in Chapter 3

Sample	% $CuFe_2O_4$	$Fe(NO_3)_3 \cdot 9H_2O$ (g)	$Cu(NO_3)_2 \cdot 2.5H_2O$ (g)	$T_{85\,°C}$ (min)	Name
AEROGEL	10	0.7825	0.2253	128	ACuFe
XEROGEL	10	0.7825	0.2253	128	XCuFe

Table 2.3 Synthesis details of the nanocomposites presented in Chapter 4. "Dod" stands for dodecanoic acid, "Hex" for hexanoic acid

Sample	% CeO_2	$Ce(NO_3)_3 \cdot 5H_2O$ (g)	Ce^{3+}: capp. agent	$T_{85\,°C}$ (min)	Name
AEROGEL	15	0.9235	Dod 1 : 4	65	A15CeO_2_dod1:4
XEROGEL	15	0.9235	Dod 1 : 4	65	X15CeO_2_dod1:4
AEROGEL	10	0.5868	Dod 1 : 4	62	A10CeO_2_dod1:4
AEROGEL	5	0.2785	Dod 1 : 4	61	A5CeO_2_dod1:4
AEROGEL	5	0.7825	Dod 1 : 1	60	A5CeO_2_dod1:1
AEROGEL	5	0.7825	Dod 1 : 8	60	A5CeO_2_dod1:8
AEROGEL	10	0.5868	Hex 1 : 4	60	A5CeO_2_hex1:8

Table 2.4 Synthesis details of the nanocomposites obtained in Chapter 5. All the nanocomposites are aerogels.

% CeO_2	CeO_2 (g)	Shape	Capping agent	$T_{85\,°C}$ (min)	Name
1.5	0.0167	Polyhedral	Dodecanoic acid	60	A1.5CeO_2_poly
1.5	0.0167	Cubic	Oleic acid	60	A1.5CeO_2_cubic

2.1.2. The drying processes

Depending on the desired product, the gel is subjected to a specific drying process. In the case of the xerogel, the ethanol was removed from the gel by slow evaporation performed at 40 °C by opening the vial containing the gel to the air. This drying process usually took place within 72 hours.

The aerogel samples have been obtained by extracting the ethanol from the gel in supercritical conditions. This was done using a stainless steel autoclave with a volume of 300 ml, Figure 2.1.

The pressure resistant container is equipped with a pressure gauge, a thermocouple and an inlet and outlet valves. The gel is placed within the sample chamber with 70 ml of ethanol. The sample chamber is then closed and pure N_2 is flushed within the chamber for a few minutes at room temperature, in order to ensure an inert atmosphere. The autoclave is then placed in a heating mantle connected to a temperature programmer, which is also connected to the thermocouple inserted inside the sample chamber. The following programmed ramp is performed, in two steps:

- From 25 °C the temperature is increased by 5 °C / min up to 250 °C
- From 250 °C up to 330 °C with a rate of 1 °C / min.

Once the temperature reaches 330 °C the pressure should reach a value around 70 atm; in these conditions the ethanol is in supercritical conditions

The chamber is then vented by slowly opening the outlet valve. The venting process must be done slowly trying to keep the temperature to a constant value of 330 °C. At the end of the process, N_2 is flushed for few a minutes, in order to eliminate any gaseous residues from the sample chamber.

The aerogel obtained is monolithic, with a mass loss of around 93% and a very limited volume contraction. The apparent density of these aerogels is usually around 0.07 g/cm^3.

2.1.3. Thermal treatments

After the drying process, the nanocomposites are submitted to thermal treatments. In the case of the nanocomposites synthesised by adding the metal salts to the solution of the silica precursor, this is needed in order to promote the formation of the nanoparticles. For all the nanocomposites, aerogels and xerogels, the first thermal treatment is performed under air at 450 ºC for 1 hour. This first thermal treatment is

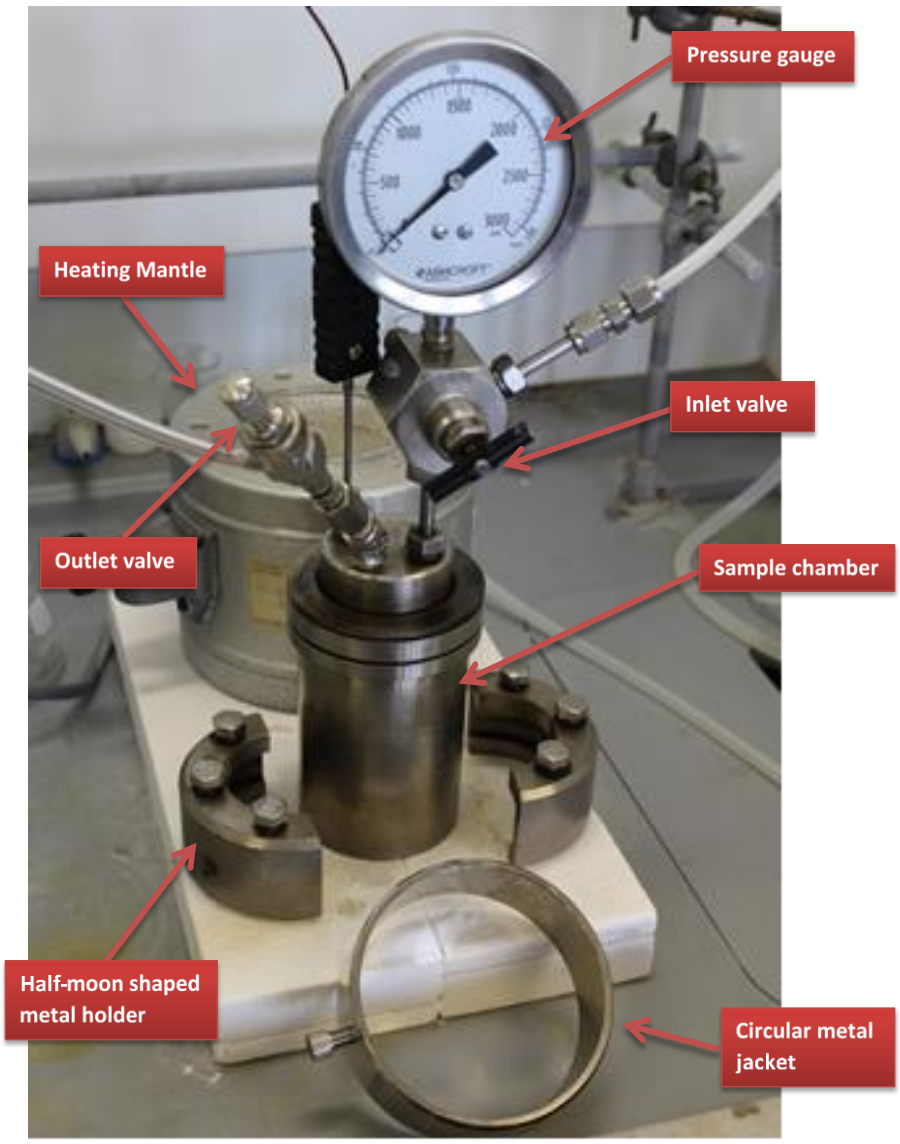

Figure 2.1 The autoclave used for the synthesis of all the aerogel composites presented in this thesis

needed in order to burn all the organics that are still present within the silica matrix. In the case of the xerogel, a consistent amount of urea is also still present. After this first thermal treatment, the nanocomposites are further thermally treated, generally at 750 ºC and 900 ºC for variable amounts of time, to achieve the crystallisation of the dispersed nanophase. For all the thermal treatment, the desired temperature is reached with a ramp of 10 ºC per minute.

All the names used to indicate the samples are completed using the numbers indicating the thermal treatment and the time. For example the aerogel nanocomposite containing copper ferrite and treated at 750 for 6 hours will be indicated as 'ACuFe_750_6h'.

2.1.4. Reagents used during the synthesis

- Tetraethyl orthosilicate ($Si(OCH_2CH_3)_4$), TEOS, Aldrich (98%)
- Urea (CH_4N_2O), Aldrich (99.0 – 100.5%)
- Ethanol absolute (C_2H_6O), Fisher Chemical
- Iron (III) nitrate nonahydrate ($Fe(NO_3)_3 \cdot 9H_2O$), Aldrich (98%)
- Copper (II) nitrate hemipentahydrate ($Cu(NO_3)_2 \cdot 2.5H_2O$), Aldrich (98%)
- Cerium (III) nitrate hexahydrate ($Ce(NO_3)_3 \cdot 6H_2O$), Aldrich (≥ 99%)
- Dodecanoic acid ($C_{12}H_{24}O_2$), Aldrich (98%)
- *tert*-butylamine ($C_4H_{11}N$), Aldrich (98%)
- Oleic acid ($C_{18}H_{34}O_2$), Fisher Chemical (97%)
- Hexanoic acid ($C_6H_{12}O_2$), Aldrich (≥98%)
- Nitric acid (HNO_3), Fisher Chemical (70%)
- Toluene (C_7H_8), Aldrich (99.9%)
- Distilled water

2.2. Characterisation techniques: theoretical principles

2.2.1. Thermal Analysis

Thermal analysis techniques investigate the evolution of certain physical and chemical properties of materials as a function of temperature, including phase transitions, thermal decompositions, solid-state reactions etc. The main thermal analysis techniques are *thermogravimetric analysis*, TGA[4], and *differential thermal analysis* (DTA)[4]. A variation of DTA is *differential scanning calorimetry* (DSC)[5].

2.2.1.1. TGA

With TGA, the change in mass of a sample is monitored as function of time and temperature. In a typical experiment, the temperature is linearly increased at a certain rate, as function of time, and results appear plotted as % of weight against time or temperature. This technique, based on a simple concept, is very useful because it can be used to quantitatively determine the mass loss from a sample as consequence of a specific phenomenon, like the thermal decompositions. Instruments are also equipped to run the experiment in different conditions, including vacuum, air or inert gases such as N_2 or Ar.

2.2.1.2. DTA and DSC

In DTA, the sample, together with a reference material, is heated with a controlled temperature rate and the difference between the temperature of the sample and the reference are recorded, as a function of the temperature of the sample chamber. The reference must be a material that does not manifest any phase change under the range of temperature investigated. During the experiment, the temperature of the sample and the reference should be the same, unless a physical or chemical transformation occurs in the sample. The temperature of the sample will be higher than the reference if an exothermic event occurs; conversely, will be lower in the case of an endothermic event. The difference in temperature between sample and reference is plotted against the temperature of the chamber.

DSC is very similar to DTA, with some differences in the design of the instrument. Specifically, in a DSC instrument, the sample and reference cells are maintained at the same temperature. If an exothermic or endothermic event occurs in the sample cell, the extra heat used to keep its temperature equal to the temperature of the reference

cell is recorded. The enthalpy change correspondent to the specific thermal event is directly measured. Compared with the DTA, DSC technique is more suitable for quantitative enthalpy measurements.

2.2.1.3. Equipment

All the thermal analyses presented in this thesis have been carried out on a NETZSCH model STA 409 PC, which allows the simultaneous acquisition of the TGA and DSC curves. Data were collected in the range 25-900 ºC with a heating rate of 10 ºC / min, under air flow.

2.2.2. X-ray diffraction

X-ray diffraction is a technique that permits the characterisation of crystalline materials by exploiting the interaction of X-rays with matter[6,7]. Two main phenomena are associated with such interaction: *scattering* and *absorption*.

The scattering is a consequence of the interaction between the X-rays and the electrons of each atom. During this process, the atoms can be considered as a secondary source of X-rays, which are scattered in all directions. If there is not a loss in energy, this process is called *coherent scattering* and the scattered and incident radiation have the same wavelength. Scattered X-rays may also lose some energy, in which case the phenomenon is called *incoherent scattering*, and the scattered radiation has a longer wavelength than the incident one.

During an X-ray diffraction experiment, only the coherent scattered radiation is important. The radiation that has been scattered by one atom in all directions interacts with the radiation produced by the other atoms, with constructive or destructive interference, depending on the optical path. In the case of ordered materials, such as crystals, a diffracted beam is produced just in specific directions, depending on the position of the atoms within the crystal structure.

2.2.2.1. Generation of X-rays

Concerning the generation of X-rays, a laboratory diffractometer is equipped with the so-called X-ray tube. Within the X-ray tube, an evacuated chamber is present, containing a tungsten filament and a target material, generally Cu or Mo, which acts as an anode. The tungsten filament is electrically heated with emission of electrons that are accelerated by a high potential difference (20-50 kV) and allowed to collide

with the target material. The collision leads to the ionization of the Cu atom and the formation of an electronic vacancy in the 1s orbital, Figure 2.2(a). X-rays are thus emitted as a consequence of the relaxation of one electron from the orbitals 2p or 3p to occupy the vacant 1s. The radiation emitted from the transition '2p to 1s' is called Kα, while the emission corresponding to the transition '3p to 1s' is called Kβ. The Kα emission is more frequent, therefore more intense hence the one used during a diffraction experiment. The Kα radiation is more specifically a doublet, $K\alpha_1$ and $K\alpha_2$, due to the two possible spin states of the 2p electrons.

Figure 2.2(b) represents a typical emission spectrum of Cu. We note that, together with the peaks related with the Kα and Kβ emission, a so-called 'white radiation' is also present. This is due to the fact that the electrons are slowed while approaching the surface of the Cu anode, and some of them lose their energy by emission of X-ray.

For the diffraction experiments, a monochromatic beam is required. In order to isolate the Kα contribution, in the case of Cu radiation, a sheet of Ni foil can be used as a filter, which is able to absorb the Kβ contribution but is transparent to the Kα. A representation of the absorption spectrum of Ni, superimposed to the emission spectra of Cu, is shown in Figure 2.2(b). A more selective monochromatisation can be achieved using a monocromator.

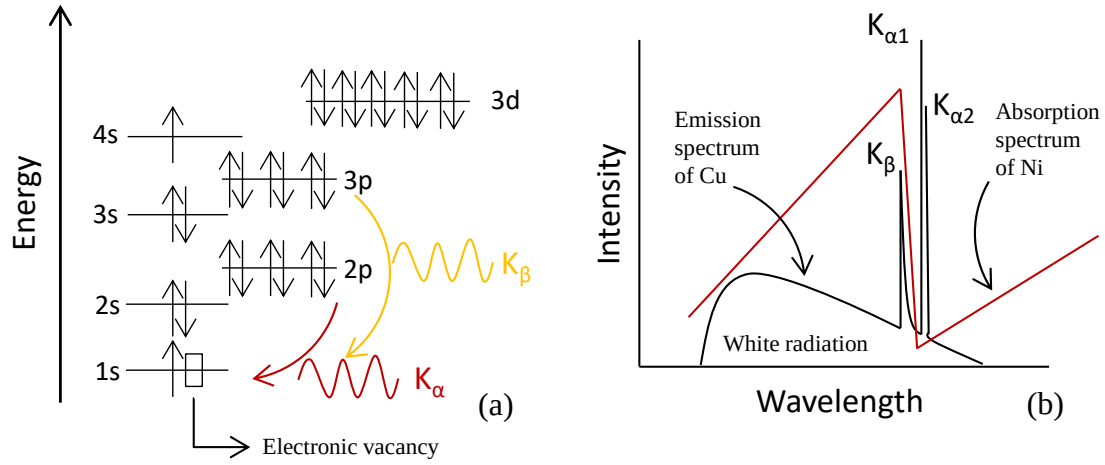

Figure 2.2 The emission of X-rays from a Cu target; (a) mechanism behind the emission of the K_α and K_β radiation; (b) emission spectrum of Cu target and superimposed absorption spectrum of Ni. Figure (b) is reproduced with permission from ref. [6]. [Copyright © John Wiley and Sons]

2.2.2.2. The Bragg's law

When X-rays interact with an ordered array of atoms, such as in crystals, a diffracted beam will be noted just in specific directions relatively to the crystal. This is due to the fact that the wavelength of the X-rays is of the same order of magnitude of the spacing between atoms. Therefore, there must be a relationship between the direction of the diffracted beam and structural parameters like the distance between atoms in a crystal.

The easiest and most used approach that explains this relationship is given by the Bragg's law[8]. In this regard, two arrays of atoms are considered, (A and B), Figure 2.3, and with 1 and 2 we identify two X-ray beams. The Bragg approach considers the array of atoms as a semi-transparent mirror; one of the X-ray beams (beam 1) is reflected by the first array of atoms (A) while the other traverses the first array of atoms and is reflected by the second one (B). The two arrays of atoms are separated by the interplanar distance d_{hkl}, where *h*, *k* and *l* are the Miller indices of that specific family of planes.

Being reflected by the second array of atoms, the beam 22' has to travel an extra distance, given by the segment *xyz*, compared to the path travelled by the beam 11'. Geometrically, we can write that:

$$xy = yz = d_{hkl}\, sin\theta$$

$$xyz = 2d_{hkl}\, sin\theta$$

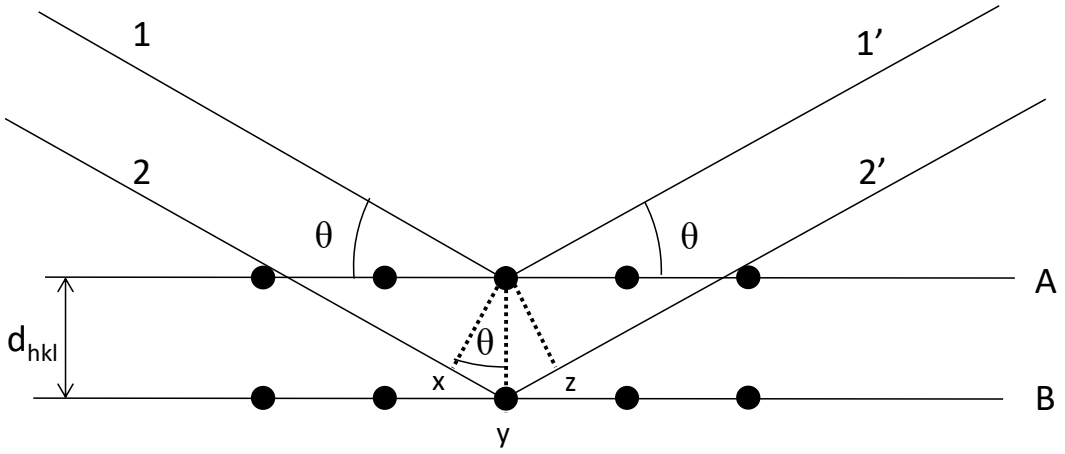

Figure 2.3 Schematic representation of the derivation of the Bragg's law. Reproduction with permission; ref. [6]; [Copyright © John Wiley and Sons]

The reflected beams are in phase if the extra path travelled by the beam 22' is equal to an integer number of wavelengths. We can therefore write the Bragg's law as:

$$n\lambda = 2d_{hkl}\, sin\theta \qquad \text{eq. 2.1}$$

The Bragg's law thus relates the distance between specific crystal planes (d_{hkl}) with the particular Bragg angle (θ) at which constructive interference is occurring. In this case, we can say that these particular crystal planes are in diffraction conditions.

2.2.2.3. The powder method

One of the most used ways of using X-ray diffraction for the characterisation of crystalline materials is the analysis of their powders. In a finely ground crystalline powder, a huge amounts of crystallites are present and randomly oriented. For some specific Bragg angles, part of the crystallites will be oriented in such a way that one specific family of crystalline planes will be in diffraction conditions. Furthermore, the crystallites can lie in all possible directions while maintaining the Bragg condition for a specific crystal plane; the consequence of this is that the diffracted beam lies on the surface of cones, as shown in the representation in Figure 2.4.

Powder diffraction analysis is done with automatic diffractometers equipped with a source of X-rays and a detector that records the angle and intensity of the diffracted beam. Two are the main geometrical configurations that are adopted in modern X-ray diffractometers: the so-called θ-θ and θ-2θ geometries. In a θ-θ diffractometer, the X-ray tube and the detector describe a synchronous circular movement of an angle θ with respect to the sample, which does not move. In the case of a diffractometer with a θ-

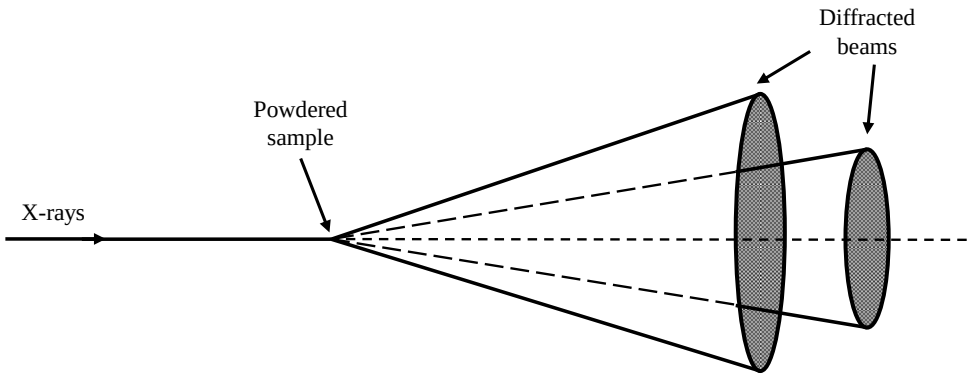

Figure 2.4 Cones produced by a powder diffraction experiment. Reproduced with permission; ref. [7] [Copyright © Taylor and Francis Group LLC Books]

2θ configuration, the X-ray tube is fixed and sample and detector move of an angle of θ and 2θ respectively. In Figure 2.5, a schematic representation of a θ-2θ diffractometer is shown.

The result of an XRD measurement is recorded in a *diffraction pattern* also called *diffractogram*, where the intensities of the peaks are plotted against the angle, 2θ. A huge number of powder diffraction patterns are stored in different databases, which are regularly updated, allowing the qualitative identification of a known crystalline phase by a *fingerprint method* that can be carried out with the help of specific software. This method allows also the identification of crystalline impurities possibly present in the sample.

Each peak in a diffraction pattern originates from a huge number of crystal planes that are in diffraction condition, therefore peaks are very sharp. However, if the size of the crystallites decreases, there are not enough crystalline planes in diffraction conditions to give a sudden destructive interference, therefore broadened peaks appear, especially for nano-crystallites.

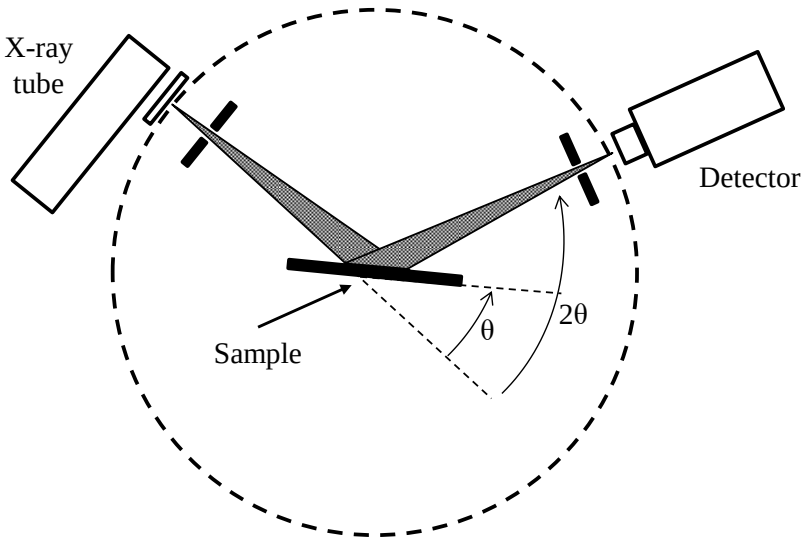

Figure 2.5 Schematic representation of a θ-2θ X-ray diffractometer. Reproduced with permission; ref. [7] [Copyright © Taylor and Francis Group LLC Books]

The thickness of a crystallite can be therefore calculated from the peak widths, using the Debye-Scherrer equation[9]:

$$T = \frac{C\,\lambda}{B\cos\theta} = \frac{C\,\lambda}{(B_M^2 - B_S^2)^{1/2}\cos\theta} \qquad \text{eq. 2.2}$$

where T is the thickness of the crystallite, λ the wavelength of the x-rays, B the full-width at half-maximum (FWHM) of the peak, C is a shape factor, usually a value near 1, and θ is the Bragg angle. The FWHM observed (B) is usually corrected by instrumental broadening (B_M and B_S are the FWHM of the sample and a standard respectively).

2.2.2.4. Equipment

The diffraction patterns shown in Chapter 3 were recorded with a PANalytical X-ray powder diffractometer, model Empyrean, with θ-θ geometry. The diffractometer is equipped with an X-ray tube with Cu as anode (Kᾱ, λ = 1.5418 Å), a graphite flat monocromator on the diffracted beam and a linear detector X-Celerator.

The diffraction patterns shown in Chapters 4 and 5 were recorded with a PANalytical, model Empyrean, with a θ-2θ geometry. The diffractometer is equipped with an X-ray tube with Cu as anode, a focusing germanium monocromator on the incident beam producing a pure $K\alpha_1$ Cu radiation (λ = 1.5406 Å) and a X-Celerator linear detector.

The diffraction patterns on the CeO_2 nanoparticles reported in Chapter 5 have been recorded on a Rigaku benchtop diffractometer, model MiniFlex600., equipped with a Cu anode tube, Ni filter and a linear detector.

In all cases data were collected by using a Silicon 0-background sample holder.

2.2.3. Electron Microscopy

Electron microscopy comprises a wide range of techniques that are widely used in the characterisation of solid materials, allowing to study their microstructural features such as crystallite size, morphology, porosity and presence of defects, and to determine the distribution of elements. Among these techniques we find *scanning electron microscopy* (SEM)[10], *transmission electron microscopy* (TEM)[11], *high resolution transmission electron microscopy* (HRTEM)[12], *energy dispersive analysis of X-rays*

(EDXA)[13], *scanning transmission electron microscopy* (STEM)[14], *high-angle annular dark-field imaging* (HAADF)[15] also called *Z-contrast imaging*, etc.

An electron microscope differs from an optical microscope because a beam of accelerated electrons is used rather than visible light. Considering the wave-particle dualism, electrons have a much lower wavelength than light, reaching, with these techniques, resolutions down to the nanoscale.

The electron beam is produced by heating a tungsten filament and accelerated through a voltage, V. The wavelength of the electron beam depends on the voltage trough the relation:

$$\lambda = 1.23(V)^{-1/2} \text{ nm} \qquad \text{eq. 2.3}$$

For an electron microscope operating at 100 kV, the wavelength of the electron beam is 0.0123 nm, which represent the resolution limit of the technique.

In the following sections, details on the electron microscopy techniques used in this thesis are given.

2.2.3.1. Transmission Electron Microscopy (TEM)

With TEM, a direct image of a solid with high magnification can be produced from the transmission of the electrons through the sample. The electron beam is focused by a condenser lens onto the sample and then collected on a fluorescent screen through an assembly of other electromagnetic lenses. As the electron beam passes through the sample, its maximum thickness must be around 0.1 μm. Some of the electrons are deflected through elastic or inelastic scattering and some are transmitted, forming a two-dimensional projection on the fluorescent screen. When the primary beam is collected, the image appears as dark feature on a bright background. The dark areas represent the sample, where more electrons have been absorbed. The quantity of the electrons absorbed depends on the atomic numbers of the elements that constitute the sample and on its thickness. In these conditions, the image has been collected in *bright field* mode. A *dark field* mode can be also used, which is particularly effective in the presence of crystalline materials. In this mode, the coherent back-scattered electrons are collected, ether by tilting the electron beam or the specimen. A particular Bragg reflection can be selected and an aperture is used to exclude the primary electron beam.

In these conditions, the regions of the sample contributing to the selected Bragg reflection appear bright on a dark background. This configuration is particularly effective, for example, to detect a crystalline phase dispersed within an amorphous matrix.

2.2.3.2. High resolution TEM (HRTEM)

In high resolution TEM instruments, a very large objective aperture is used in order to allow the transmitted beam and all the diffracted beams to contribute to the image. The diffracted beams, due to the difference in optical path caused by the interaction with the atoms, are phase shifted, interfering with the transmitted beam in their travel to the detector. A *phase contrast* image is obtained, allowing for resolutions of less than 0.1 nm: columns of atoms are distinguished. However, the interpretation of a phase contrast image is not straightforward: the image is the composition of all the possible wavefronts generated by the diffracted beams that interfere with each other and with the transmitted beam. The interpretation of the image is done with the help of computer simulations that predict what contrasts are given by a certain crystal structure. Therefore, a certain amount of information about the sample should be known in advance.

Because the interpretation of the phase contrast image is based on the phase shift of the electron beams due to the crystal structure, any other instrumental effect that can cause a phase shift can make this process more difficult. For this reason, a very low degree of spherical aberration, caused by the system of lenses, is required for these instruments.

The importance of the use of this technique comes from the fact that direct information upon the crystal structure is obtained, allowing the characterisation of microstructural features such as point defects, grain boundaries and dislocations.

2.2.3.3. Equipment

The TEM images in Chapter 3 and 4 were acquired in collaboration with the Functional Materials Group at University of Cagliari (Italy) using a Hitachi microscope, model 7000, equipped with a W filament as source of electrons, operating at 125 kV, corresponding to a wavelength of $3.28 \cdot 10^{-2}$ Å. The samples were deposited on a carbon-coated copper grid without being dispersed in a solvent.

The TEM characterisation of the samples presented in Chapter 5 was performed at the KAUST (Saudi Arabia) using a FEI Tecnai Spirit microscope, equipped with a lanthanum hexaboride thermionic electron source, a Twin objective lens, a Gatan Orius CCD camera and operating at an acceleration voltage of 120 kV.

HRTEM and imaging were performed at the KAUST (Saudi Arabia) using a FEI Titan microscope, equipped with an X-FEG Schottky electron source, a SuperTwin objective lens, a Gatan 2kx2k CCD camera, and operating at an acceleration voltage of 300 kV.

The CeO_2-SiO_2 aerogel nanocomposites presented in Chapter 5 were prepared for the HRTEM imaging at the KAUST (Saudi Arabia) by inclusion in an Epon-Spurr Epoxy Resin left to polymerise for 48h at 60 ºC. Samples have been then cut using a Leica EM UC7 ultra-microtome in ultra-thin sections with a width of 50 nm, with a diamond Diatome 45º blade and put in ultra-thin carbon-coated copper grid (3-4 nm width).

2.2.4. N_2-physisorption measurements

One of the most important methods that allows obtaining additional information about the surface area and porous structure of a solid involves the use of gas physisorption[16]. Porous materials are mainly classified according with their pore dimensions: pores with diameter less than 2 nm are called *micropores*; pores with diameter between 2 and 50 nm are called *mesoporous*; if the pores size is bigger than 50 nm then we can refer to *macropores*.

The adsorption of a gas on the surface of a solid can mainly follow two paths: *chemisorption* or *physisorption*. These two phenomena can be distinguished for many reasons:

- Physisorption is not site specific while chemisorption depends on the chemical functionalities of the surface
- Chemisorption is usually confined to a mono-layer, while more layers are allowed when physisorption occurs.
- The energy involved during chemisorption is usually related with the formation and rupture of chemical bonds. Physisorption is always exothermic, due to van der Waals interactions between the gas molecule and the atoms that constitute the surface of the solid
- The chemisorption process always depends on activation energy; therefore, it might not happen at low temperatures.

If the physisorption of a gas on a surface is used to study its features, chemisorption must be avoided.

From an energetic point of view, the physisorption of a gas molecule on the surface of a solid can be described considering the Lennard-Jones potential[17], which takes into account the interactions between neutral pair of atoms (or molecules) considering an attractive contribution in the van der Waals form and a short range repulsive term:

$$\varepsilon(r) = \frac{B}{r^{12}} - \frac{C}{r^{6}} \qquad \text{eq. 2.4}$$

The first and second term on the right hand side of the equation are the repulsive and attractive interaction respectively.

Once a gas molecule approaches the surface of a solid, the interaction between the molecule and all the atoms of the surface must be taken into account:

$$\Phi_i(z) = \sum_j \varepsilon_{ij}(r_{ij}) \qquad \text{eq. 2.5}$$

Φ_i (z) is the potential energy of the molecule *i* that have a distance *z* from the surface and a distance r_{ij} with the atom j of the surface. Eq. 2.5 is graphically represented in Figure 2.6: the potential energy has a minimum corresponding to the equilibrium distance between the adsorbed molecule and the surface of the solid.

2.2.4.1. Adsorption-desorption isotherms

In a typical N_2-physisorption experiment, the surface of the solid is firstly vacated from any gas adsorbed by a process called *degassing*. This is done under vacuum while the sample is submitted to a thermal treatment, with a temperature program that depends on the porous structure of the material. After degassing, the physisorption measurement starts by bringing the sample to the liquid nitrogen temperature. The instruments are designed to perform known injections of N_2 gas and measure the equilibrium pressure. The gas injected reaches the surface of the solid and is physically

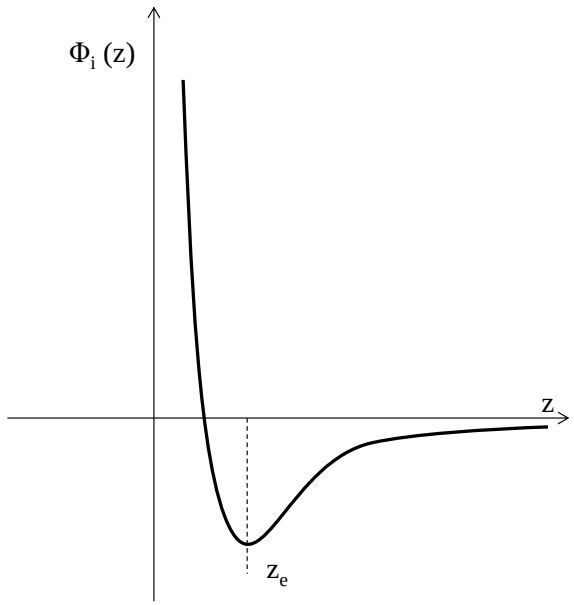

Figure 2.6 The Lennard-Jones potential; dependence of the potential energy of a molecule on the distance 'z' from the surface of the solid.

adsorbed. The amount of gas adsorbed is plotted against the equilibrium pressure and the *adsorption-desorption isotherm* is obtained.

Adsorption-desorption isotherms represent the macroscopic evidence of the physisorption phenomenon and their shape is indicative of the texture of the sample. Figure 2.7 represents the extended classification of the isotherms released in the last IUPAC technical report in 2015[18].

The type I(a) and I(b) isotherms show a very high amount of adsorbed gas at very low relative partial pressure, with a concave shape. This is typical of a microporous material, where the very low pores diameter enhances the solid-gas interactions, leading to the pores filling and reaching the saturation pressure at very low relative pressure values. The type I(b) isotherm is generated by micropores with bigger size, compared with the I(a).

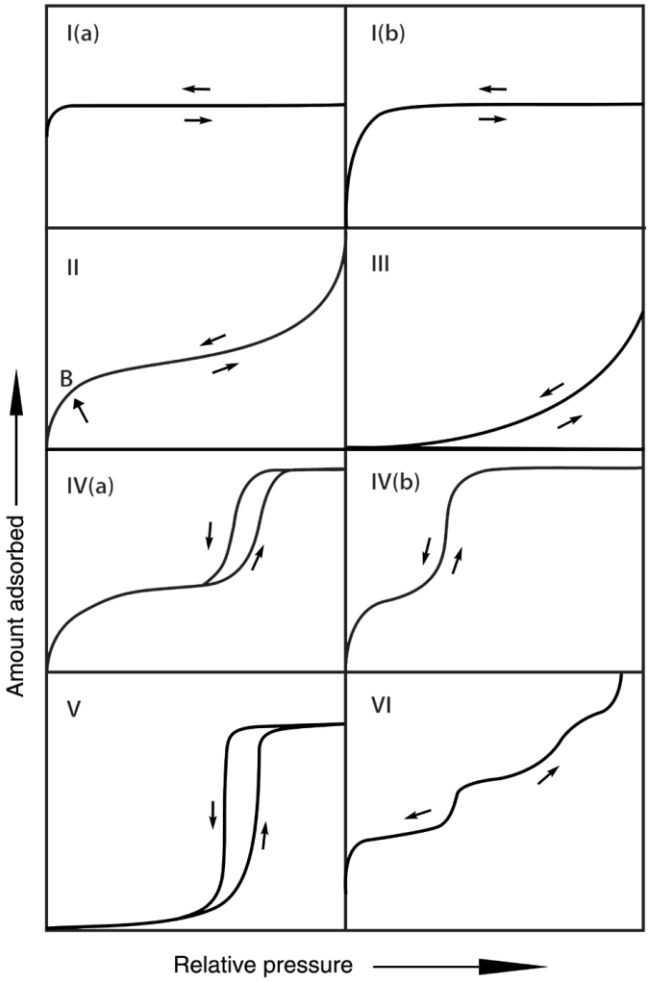

Figure 2.7 The IUPAC classification of physisorption isotherms. Re-printed with copyright © permission by IUPAC and De Gruyter from ref. 18

The type II isotherm is associated to non-porous materials or materials whose internal surface area is negligible. This isotherm is generated by the formation of more than one layer: once the gas molecules are adsorbed on the surface of the solid, further adsorption is possible due to condensation of more gas on top of the first layer. We note that in this case, the concavity of the curve is different and the system does not reach saturation. Point B refers to the completion of monolayer coverage.

The type III isotherm is generated by systems where there are weak solid-gas interactions. Solids that generate this isotherm are generally non-porous or macroporous.

Type IV isotherms are generated by mesoporous adsorbents and consequent formation of multi-layers. Capillary condensation occurs at relatively low pressure, followed by a saturation plateau. In type IV(a) the capillary condensation is accompanied by hysteresis; this generally occurs with pores wider than 4 nm. For adsorbents with smaller mesopores, hysteresis is not noted, leading to a type IV(b) isotherm.

Type V isotherms are generated by solids where the interactions solid-gas are weak. They differ from type III isotherm for the presence of the hysteresis loop and pore filling at high pressure values

Finally, type VI isotherms are typical of solids with a very uniform and non-porous surface, where the formation of a multi-layer adsorption gives rise to the steps-shaped isotherm.

2.2.4.2. The hysteresis

The hysteresis phenomenon is present in isotherms of type IV and V and reflects the evidence that the evaporation in mesopores takes place at lower relative pressure than the condensation. Many theories have been developed for the explanation of this phenomenon. Without going into deep details, we can explain the hysteresis considering that, once a pore has been completely filled by a condensed phase, a meniscus is formed at the liquid-vapour interphase. In this condition, condensation can occur at lower pressure than the saturation value and this is described by the Kelvin equation[19]:

$$ln\frac{P}{P_0} = -\frac{2\gamma_l V_l cos\theta}{RTr_M} \qquad \text{eq. 2.6}$$

where γ_l and V_l are the surface tension and the molar volume of the liquid, r_M is the curvature radius of the meniscus and θ is the contact angle between the liquid and the wall of the pore.

When taking into account the description of the adsorption and desorption of a gas on the surface of a pore, the Kelvin equation is only valid once the meniscus is formed, therefore for the desorption branch. Conversely, in the case of the adsorption branch, when the pore is partially filled, the meniscus is still not formed. A variation of the Kelvin equation describes this system, differing just for the factor 2 and known as the Cohan equation[20]:

$$ln\frac{P}{P_0} = -\frac{\gamma_l V_l cos\theta}{RTr_M} \qquad \text{eq. 2.7}$$

Although these equations are not directly used for the calculation of the pore size, they provide a qualitative thermodynamic explanation of the hysteresis phenomenon.

Six different types of hysteresis have been classified by IUPAC[18], Figure 2.8. Their shape can give information about the features of the porous structure of a material.

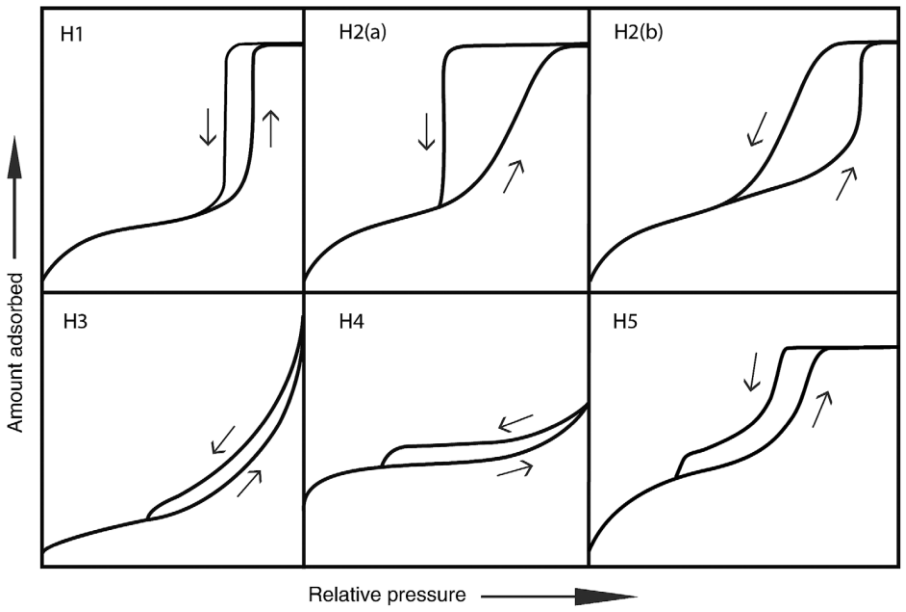

Figure 2.8 Classification of hysteresis loops. Re-printed with copyright © permission by IUPAC and De Gruyter from ref. [18]

Type H1 is found in materials with narrow and uniform mesopores. Type H2 hysteresis are given by more complex porous structure with pore-blocking effects due to neck-bottle shaped pores. The difference in the shape between the H2(a) and H2(b) is related with the size of the neck of the pores. Type H3 hysteresis loops are given by materials with plate-like particles or with macropores that are not completely filled. Type H4 is given by aggregated crystals of zeolites or carbons, with presence of micropores. Type H5 is quite unusual, but it has been attributed to materials with both open and partially blocked mesopores.

2.2.4.3. The determination of the surface area

One of the most important applications of the N_2-physisorption is the determination of the specific surface area of the adsorbent. This is achieved by using the Brunauer-Emmet-Teller (BET) method[21], which is particularly effective in the determination of the specific surface area of non-porous materials or macro- and mesoporous materials that exhibit type II or IV(a) adsorption isotherms. The BET method is based on simple assumptions:

- The adsorption heat of the first mono-layer is constant
- The adsorption heat of other layers is lower than the first
- An infinite number of adsorbed layers are allowed
- The rates of adsorption and desorption are the same

With these assumptions, the isotherms can be described with the following BET equation:

$$\frac{V}{V_m} = -\frac{c \cdot {}^{P}/_{P_0}}{\left(1 - {}^{P}/_{P_0}\right) \cdot \left[1 - (1-c) \cdot \left({}^{P}/_{P_0}\right)\right]} \qquad \text{eq. 2.8}$$

with

$$c \approx e^{-{}^{(\Delta H_d - \Delta H_{vap})}/_{RT}} \qquad \text{eq. 2.9}$$

where V and V_m are the volume of gas adsorbed and the volume of the mono-layer respectively and c is exponentially related to the energy associated with the formation of the mono-layer, eq. 2.9.

Eq. 2.8 is usually employed in its linearized form:

$$\frac{P/P_0}{V\,(1 - P/P_0)} = \frac{c - 1}{V_m\,C}\left(P/P_0\right) + \frac{1}{V_m\,C} \qquad \text{eq. 2.10}$$

The points of the isotherm acquired in the range of P/P_0 between 0.05 and 0.3 are employed in the linear plot and the volume of the mono-layer, V_m is calculated. The BET specific area is calculated from it, knowing the molecular cross-sectional area of the adsorbate, σ_m:

$$S_{BET} = \frac{V_m\,N\,\sigma_m}{v_m\,M} \qquad \text{eq. 2.11}$$

with N the Avogadro number, M the mass of the adsorbent and v_m the molar volume of the adsorbate.

2.2.4.4. Pore size analysis

One of the classic and most used methods to determine the pore size of porous materials was proposed by Barret, Joyner and Halenda, BJH,[22] which combines the Kelvin equation, eq. 2.6, with a standard isotherm, the *t-curve*, determined on well-defined mesoporous solids. However, it was demonstrated that the BJH method underestimates the pore size for pore diameters < 10 nm. To overcome this problem, new models have been recently developed, based on microscopic methods, such as DFT simulations, called NLDFT[23]. They allow obtaining more accurate pore diameter estimations over a wide range of sizes.

2.2.4.5. Equipment

The N_2-physisorption measurements presented in Chapter 3 have been acquired using a Micromeritics ASAP 2020 porosimeter, in collaboration with the Functional Materials Group in Cagliari, (Italy).

The N_2-physisorption measurements shown in Chapters 4 and 5 have been acquired using a Thermo Scientific gas adsorption porosimeter, Surfer model.

The samples were degassed under vacuum while thermally treated with a heating rate of 1 ºC/min up to 200 ºC for 10 h.

2.2.5. X-ray absorption spectroscopy

X-ray absorption spectroscopy (XAS) refers to the analysis of the absorption spectra of an atom (in a material) near and after the energy required for the ionization of a core electron[6,7,24,25]. The X-ray beam required for these measurements must be very intense over a wide range of energies and it is produced in large facilities called *synchrotrons*. In synchrotrons, electrons are injected and accelerated inside an electron storage ring to kinetic energies above the mega electron volt. In these conditions, electrons reach velocities near the speed of light and their direction is changed by special designed magnets. The change in direction causes the emission of a very intense X-ray radiation. The UK facility, DIAMOND, has a ring with a circumference of 561 m; electrons are accelerated at energy of 3 GeV emitting X-ray radiation with wavelength between 40 and 0.04 Å. Experiments are carried out in special work stations called *beamlines*.

The absorption of X-rays follows the Beer's law[26]:

$$I(x) = I_0 \cdot e^{-\mu x} \qquad \text{eq. 2.12}$$

which can be written as:

$$\mu(E)x = \ln\left({}^{I_0}/_{I}\right) \qquad \text{eq. 2.13}$$

where μ is the absorption coefficient and x the thickness of the sample.

During the experiment, the wavelength of the X-rays is progressively decreased and the result is plotted as the variation of the adsorption coefficient against the energy of the X-ray beam. As the energy increases the adsorption coefficient decreases until a certain critical wavelength is reached, where the adsorption coefficient suddenly increases, Figure 2.9(a), Point A. At this point, called the *absorption edge*, the energy of the X-rays was sufficient to cause the ionisation of the atom by the ejection of a core electron. In particular, in Figure 2.9(a), the K-absorption edge of a sample containing Cu^{2+} ions is shown. This adsorption edge corresponds to the ejection of an electron from the 1s orbital, Figure 2.9(b). Much less energetic X-rays would have been needed to eject electrons from the 2s or 2p orbitals (L-level) and therefore to record the L-edge of Cu^{2+}. The wavelength at which an absorption edge occurs is therefore characteristic of each element.

Two main regions are identified in the X-ray absorption spectra of an element, Figure 2.9(a), which in turns gives the name to the two main techniques that can be ascribed to X-ray absorption spectroscopy: *X-ray absorption near edge structure* (XANES) and *Extended X-ray absorption fine structure* (EXAFS). These two techniques are dominated by different physical processes, containing different information about the sample, which are used complementarily during its characterisation.

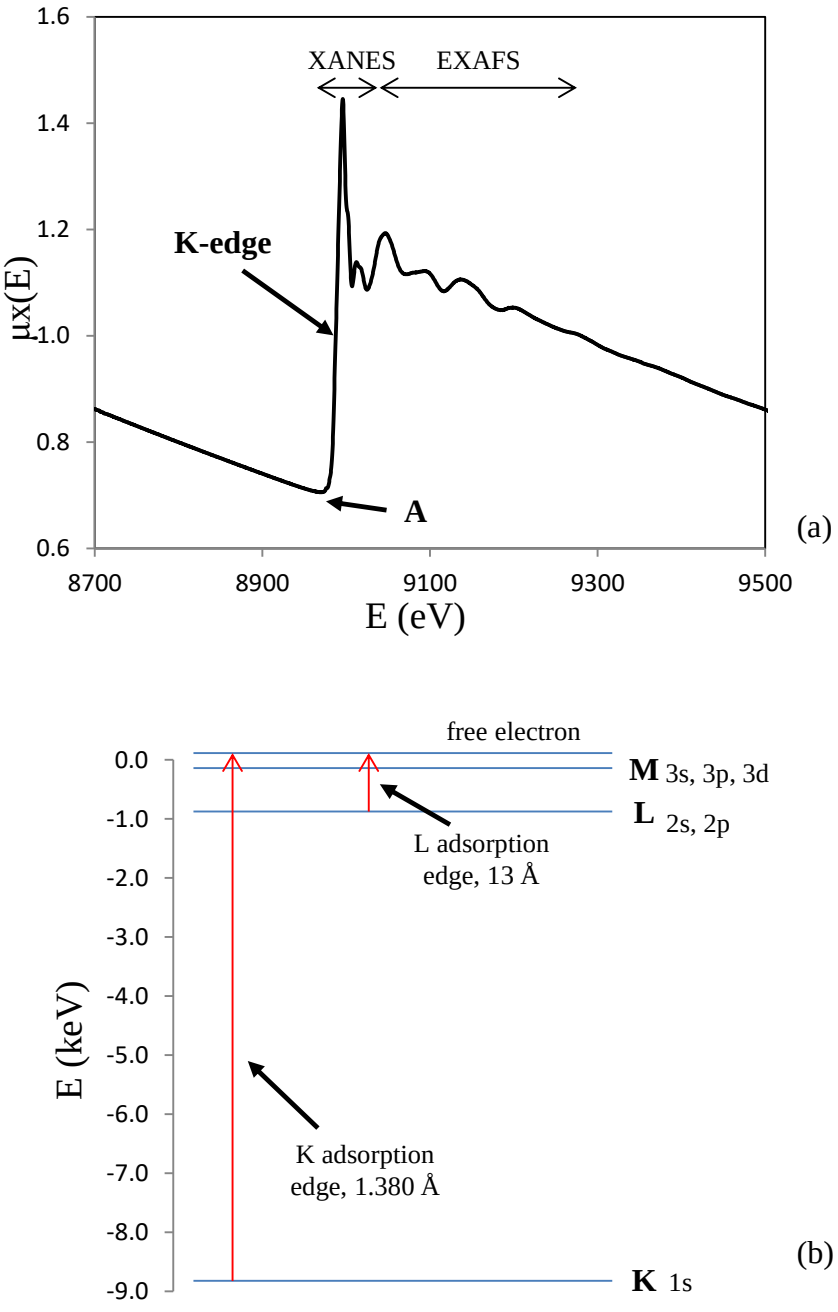

Figure 2.9 (a) XAS absorption spectrum of a copper ferrite nanocrystalline sample, showing the Cu K-edge; (b) electronic transition responsible for the absorption X-ray spectra, with wavelength values for Cu. Figure (b) is reproduced with permission from ref. [6]; [Copyright © John Wiley and Sons]

2.2.5.1. XANES

With XANES we can refer to the region of the X-ray absorption spectrum that is approximately 80 eV before and after the absorption edge. The acronym NEXAFS, which stays for *Near-edge X-ray absorption fine structure*, is also used as synonym of XANES, especially in the case of light elements such as C, N or O.

This part of the absorption spectrum is mainly influenced by the coordination geometry of the absorbing atom and by its oxidation state. The oxidation state has consequence on the position of the absorption edge; in particular, an edge may be shifted by 5 eV for an increment of +1 in the oxidation state. By a simple finger print method, measuring the spectra of a known standard, one can easily determine the oxidation state of an element in a sample, or the ratio of different oxidation states within a mixed sample.

A small peak may appear few tens of electron-volts before the main absorption edge. This so-called *pre-edge peak* can give information about the oxidation state of the element but also about its coordination geometry. This pre-peak is due to excitation of electrons into a vacant energy level. From the ligand-field theory we know that the number of electrons in the highest occupied molecular orbital varies depending on the oxidation state of the element and on the coordination geometry of the corresponding atom. As general rule, the presence of a pre-peak is more pronounced when the atom stays in a non-centrosymmetric site, e.g. tetrahedral.

The oscillations of the signal immediately after the absorption edge are due to the low kinetic energy photoelectrons that interact with the surrounding atoms by mulple-scattering events. This part of the absorption spectrum carries information about the coordination around the surrounding atoms, although its interpretation is not straightforward.

2.2.5.2. EXAFS

With EXAFS we refer to the region of the absorption spectrum that extends from ≈ 40 eV up to several hundreds of eV after the absorption edge, Figure 2.9(a). In this region, the oscillations of the spectrum are originated by scattering effects between the ejected photoelectrons and the surrounding of the absorber atom.

In particular, after absorption of X-rays, the ejected photoelectron can be thought as a spherical wave that propagates from the absorbing atom. This wave is then partially scattered by the surrounding atoms and this scattered wave can interact constructively or destructively with the outgoing spherical wave produced by the absorbing atom itself, Figure 2.10. Due to this effect, the absorption of the absorbing atom is modified, and sinusoidal oscillations appear for several hundreds of electron-volts after the absorption edge.

The EXAFS signal, $\chi(k)$, is obtained by subtracting the absorption of the isolated atom (μ_0, eq. 2.14) and changing the domain of the function from energies to wave vector (eq. 2.15):

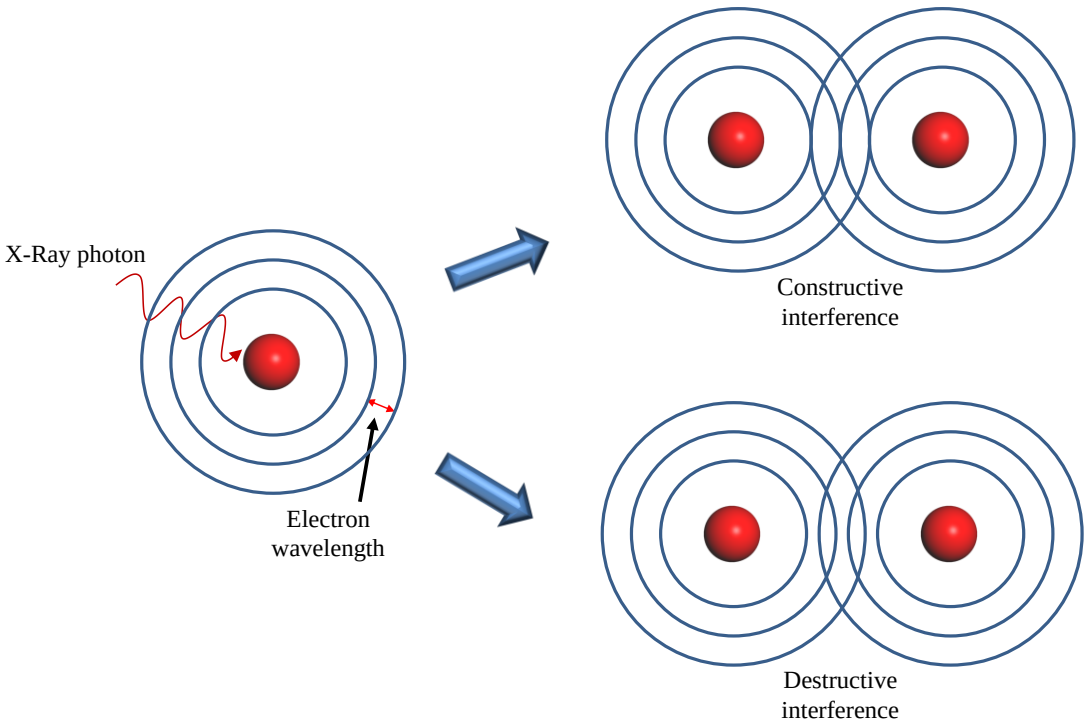

Figure 2.10 The origin of the EXAFS signal.

$$\chi(k) = \frac{\mu\,(E) - \,\mu_0(E)}{\mu_0(E)} \qquad \text{eq. 2.14}$$

$$k = \sqrt{\frac{2\,m_e}{\hbar^2} \cdot (E - \,E_0)} \qquad \text{eq. 2.15}$$

where m_e is the mass of the electron and $\hbar$ the reduced Planck constant.

The EXAFS signal, χ(k), is then fitted using the following equation:

$$\chi(k) = \,S_0^2 \sum_{i=1}^{J} \frac{F_i^{eff}(k) N_i}{k\,R_i^2} \sin(2kR_i + \,\Phi_i(k))\, e^{-2k^2\sigma_i^2} e^{-2\frac{R_i}{\lambda_i(k)}} \qquad \text{eq. 2.16}$$

The following factors in eq. 2.16 are determined during the fit:

- S_0^2: average amplitude factor. It depends on the relaxation of the electrons of the atoms after the photoemission of the core electron. It is usually a value between 0.7 and 1.0
- R_i is the distance with the neighbouring atom *i*
- N_i is the number of atoms at distance R_i
- σ_i^2 is the Debye-Waller factor[27,28]

The first exponential term, containing the Debye Waller factor, takes into account displacements of the interatomic distances due to structural and/or thermal disorder. The second exponential term takes into account the mean free path of the photoelectron, $\lambda_i(k)$. The other terms of the equation are:

- $F_i^{eff}(k)$: the scattering amplitude, which depends on the scatterer atoms;
- $\Phi_i\,(k)$: phase function, which is the sum of two potential function, one given by the absorber, one given by the scatterer
- *k*: the wave vector modulus of the photoelectron

The EXAFS signal, χ(k), usually decays very quick with increasing k; it is therefore customary to weight the function multiplying by k^2 or k^3. Furthermore, χ(k) is a

function in the space of the wave vector; the Fourier transform gives the same function in the space of the distances, R_i. Each peak that appears in the Fourier transform is related with the distances with the i^{th} coordination shell. However, it must be taken into account that this is a *pseudo*-radial distribution function: peaks are not centred at the real interatomic distances due to a phase shift and multiple scattering also gives its contribution to the total function.

2.2.5.3. Data collection and data analysis

The X-ray absorption spectra were recorded on the beamline B18 at the synchrotron DIAMOND (Oxfordshire, UK) under rapid access, proposal SP-11086. The samples, in form of powder, were diluted with polivinylpirrolidine (PVP) in an appropriate concentration and pressed to form a pellet. The data analysis has been performed using the software ATHENA and ARTEMIS[29]. With ATHENA, the absorption edge, E_0, is determined, and the absorption due to the isolated atom is subtracted, eq. 2.14, by fitting the pre-edge and post-edge regions. The software ARTEMIS is then used to perform the fit of the EXAFS region, eq. 2.16.

2.3. Molecular dynamics simulation

2.3.1. The basic idea

With molecular dynamics (MD) we identify a computer simulation technique that allows predicting the evolution of a system of N particles (atoms or molecules) on time, within the framework of classic mechanics[30]. In order to run a molecular dynamics simulation, given a system of N atoms, a set of initial conditions must be firstly specified. This includes:

- Initial positions ($\mathbf{r}_{i1}$; $\mathbf{r}_{i2}$; …; $\mathbf{r}_{iN}$) and velocities ($\mathbf{v}_{i1}$; $\mathbf{v}_{i2}$; …; $\mathbf{v}_{iN}$) of all the N atoms of the system;
- An interatomic potential which describes the interaction between the atoms as function of their position, U($\mathbf{r}_{i1}$; $\mathbf{r}_{i2}$; …; $\mathbf{r}_{iN}$).

The interatomic potential is chosen depending on the system that is to be simulated. In the case of ionic solids, such as metal oxides, the Coulomb-Buckingham potential[31] has been proven to be particularly effective. Its expression is:

$$U_{ij}(r) = \frac{Q_i Q_j}{4\pi\varepsilon_0 r} + A\exp\left(\frac{-r}{\rho}\right) - \frac{C}{r^6} \qquad \text{eq. 2.17}$$

The first term on the right hand side of the equation represent the coulombic interaction, while the second and the third terms represent the repulsive and attractive contribution of the Buckingham potential respectively. A, ρ and C are constant and are determined by fitting experimental data for each material. The Buckingham potential is a simplification of the Lennard-Jones potential[17], eq. 2.4, where an exponential function is used to describe the repulsive short range interaction, in place of the r^{-12} term.

In Figure 2.11 a representation of the Coulombic-Buckingham potential is given. Depending on the interatomic distance r, the two atoms try to minimize their potential energy by repulsion or attraction. The force acting on the atoms, due to this *pair-interaction*, can be then calculated by its definition:

$$\boldsymbol{F}_{ij} = -\boldsymbol{\nabla}_{ij} U(\boldsymbol{r}_{ij}) \qquad \text{eq. 2.18}$$

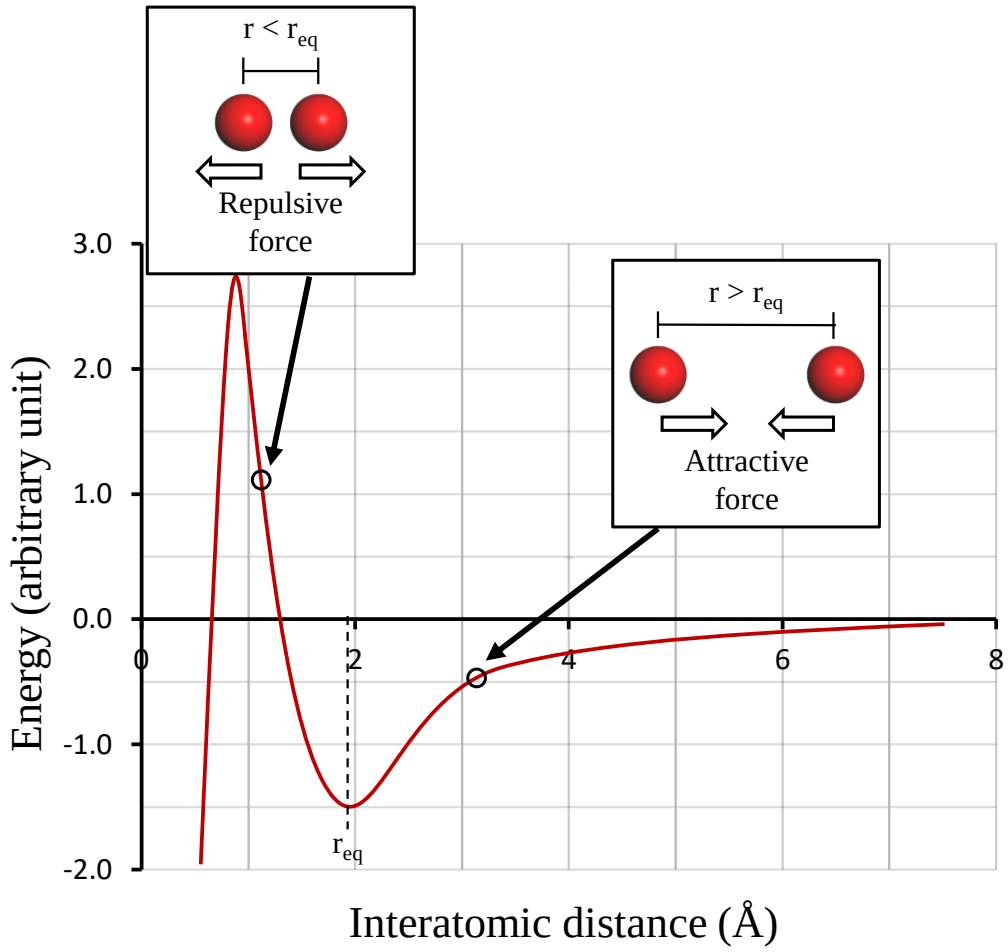

Figure 2.11 Coulombic-Buckingham interatomic potential; insets indicate regions of attraction and repulsion.

In a more complex system, where more than 2 atoms are present, the net force acting on the atom '*i*' due to N surrounding atoms, can be calculated as the vector sum of each pair-contribution:

$$\boldsymbol{F}_i = \sum_{j=1}^{N} \boldsymbol{F}_{ij} \qquad \text{eq. 2.19}$$

The acceleration can be calculated using the Newton's second law, given 'm' the mass of the specific atom:

$$\boldsymbol{F}_i = m \cdot \boldsymbol{a}_i \qquad \text{eq. 2.20}$$

A new set of coordinates and velocities ($\mathbf{r}_f$ and $\mathbf{v}_f$) can be predicted using a set of classical equations of motions and setting a time-step (t):

$$\boldsymbol{v}_f(t) = \int \boldsymbol{a}\, dt = \boldsymbol{a}t + \boldsymbol{v}_i \qquad \text{eq. 2.21}$$

$$\boldsymbol{r}_f(t) = \int (\boldsymbol{a}t + \boldsymbol{v_i})\, dt = \frac{1}{2}\,\boldsymbol{a}t^2 + \boldsymbol{v}_i t + \boldsymbol{r}_i \qquad \text{eq. 2.22}$$

The new set of coordinates and velocities associated to each atom becomes in turn the initial conditions for a new set of calculations. The dynamic evolution of the atoms can be then monitored and specific properties calculated.

2.3.2. Amorphisation and re-crystallisation

Using MD simulations to calculate specific properties of a material involves the need to obtain a suitable atomistic model of such material. In the case of metal-oxide nanoparticles, properties such as reactivity, mechanical strength, ionic conductivity, electrochemical activity, etc. are strongly dependent on the microstructural features that the material incorporates. This includes surfaces exposed, point defects, grain boundaries and dislocations. The simulator is therefore asked to incorporate all these microstructural features within its atomistic model.

The amorphisation and re-crystallisation technique[32,33] has been extensively and successfully used to accomplish this purpose. During this process, a cluster of a specific material in its pristine form, containing a sufficient amount of atoms, is simulated using a temperature value and a simulation time high enough to reach its complete amorphisation. Once the amorphous precursor it obtained, its crystallisation is simulated by careful choice of the temperature at which the simulation is performed. This simulation must be performed under the so-called *NVT ensemble* which keeps the temperature constant during the simulation by the use of specific algorithms that simulate a thermostat.

Equally to what occurs experimentally, the crystallisation is promoted by the formation of a crystalline seed, which evolves naturally from the random movement of the atoms. Once the crystalline seed is formed, the crystallisation propagates until the entire cluster becomes crystalline. Figure 2.12A represents the simulated crystallisation of a core-shell TiO_2-CeO_2 nanoparticle[34]; the temperature has been carefully chosen to promote the crystallisation of CeO_2 while TiO_2 stays molten on the surface of the

nanoparticle. The sequence of images provides the evidence of the formation of a crystalline seed, which evolves on time, promoting the crystallisation of the CeO_2 core of the nanoparticle. With this simulation technique, a large number of models of metal oxide nanomaterials in quantitative accord with experiment have been obtained, including thin films,[35] nanoparticles of various shapes,[36] nanorods[37] and nanomaterials with a 3d-mesoporous architecture[38,39].

2.3.3. The code and graphical software

All the simulations presented in this thesis have been run using the DL_POLY code[40] and are presented in Chapter 6 and Chapter 7. Molecular graphics were performed using VMD[41] and Materials Studio.

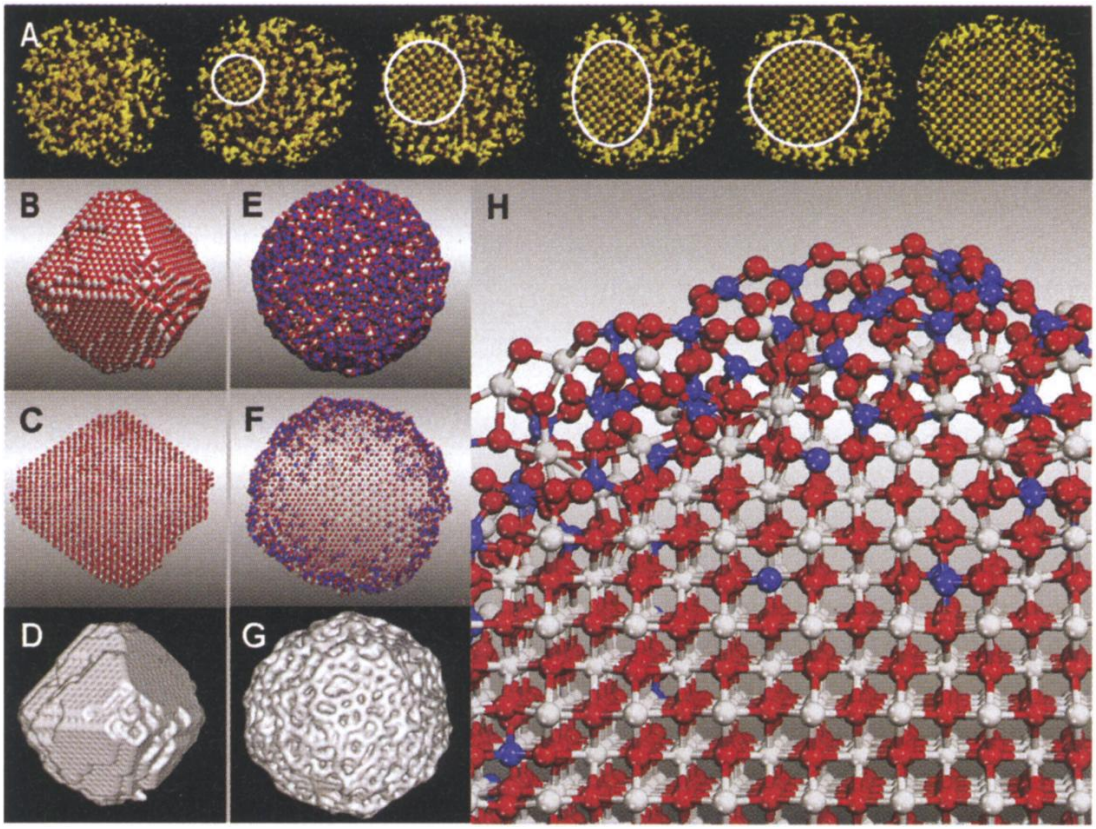

Figure 2.12 (A) Simulated crystallisation of a CeO_2-TiO_2 core-shell nanoparticle showing snapshots of the simulation with the growth of a crystalline seed; (B to D) non doped CeO_2 nanoparticles; (E to G) Ti-doped nanoparticles; (H) enlarged segment of the core-shell nanoparticle. Reprinted with permission from ref. [34] ; [Copyright © the American Association for the Advancement of Science]

2.4. References

[1] Casula, M.F., Loche, D., Marras, S., Paschina, G. and Corrias, A., 2007. Role of urea in the preparation of highly porous nanocomposite aerogels. *Langmuir*, 23(7), pp.3509-3512.

[2] Loche, D., Casula, M.F., Falqui, A., Marras, S. and Corrias, A., 2010. Preparation of Mn, Ni, Co ferrite highly porous silica nanocomposite aerogels by an urea-assisted sol–gel procedure. *Journal of Nanoscience and Nanotechnology*, 10(2), pp.1008-1016.

[3] Carta, D., Mountjoy, G., Gass, M., Navarra, G., Casula, M.F. and Corrias, A., 2007. Structural characterisation study of FeCo alloy nanoparticles in a highly porous aerogel silica matrix. *The Journal of Chemical Physics*, 127(20), pp.204705-204705.

[4] Coats, A.W. and Redfern, J.P., 1963. Thermogravimetric analysis. A review. *Analyst*, 88(1053), pp.906-924.

[5] O'neill, M.J., 1964. The analysis of a temperature-controlled scanning salorimeter. *Analytical Chemistry*, 36(7), pp.1238-1245.

[6] West, A.R., 2007. Solid state chemistry and its applications, 2nd edition, John Wiley & Sons, Chichester, West Sussex, UK.

[7] Smart, L.E. and Moore, E.A., 2012. Solid state chemistry: an introduction. CRC press, New York, USA.

[8] Bragg, W.H. and Bragg, W.L., 1913. The reflection of X-rays by crystals. *Proceedings of the Royal Society of London. Series A, Containing Papers of a Mathematical and Physical Character*, 88(605), pp.428-438.

[9] Patterson, A.L., 1939. The Scherrer formula for X-ray particle size determination. *Physical Review*, 56(10), p.978.

[10] Vernon-Parry, K.D., 2000. Scanning electron microscopy: an introduction. *III-Vs Review*, 13(4), pp.40-44.

[11] Winey, M., Meehl, J.B., O'Toole, E.T. and Giddings, T.H., 2014. Conventional transmission electron microscopy. *Molecular Biology of the Cell*, 25(3), pp.319-323.

[12] Buseck, P., Cowley, J. and Eyring, L. eds., 1989. High-resolution transmission electron microscopy and associated techniques. Oxford University Press.

[13] Titchmarsh, J.M., 1993. Energy dispersive X-ray analysis. *Quantitative Microbeam Analysis*, 40, p.275.

[14] Crewe, A.V., 1974. Scanning transmission electron microscopy. *Journal of Microscopy*, 100(3), pp.247-259.

[15] Otten, M.T., 1991. High-Angle annular dark-field imaging on a tem/stem system. *Journal of Electron Microscopy Technique*, 17(2), pp.221-230.

[16] Sing, K.S., 1995. Physisorption of nitrogen by porous materials. *Journal of Porous Materials*, 2(1), pp.5-8.

[17] Jones, J.E., 1924, October. On the determination of molecular fields. II. From the equation of state of a gas. *Proceedings of the Royal Society of London A: Mathematical, Physical and Engineering Sciences* 106, 738, pp. 463-477

[18] Thommes, M., Kaneko, K., Neimark, A.V., Olivier, J.P., Rodriguez-Reinoso, F., Rouquerol, J. and Sing, K.S., 2015. Physisorption of gases, with special reference to the evaluation of surface area and pore size distribution (IUPAC Technical Report). *Pure and Applied Chemistry*, 87(9-10), pp.1051-1069.

[19] von Helmholtz, R., 1886. Untersuchungen über Dämpfe und Nebel, besonders über solche von Lösungen. *Annalen der Physik*, 263(4), pp.508-543.

[20] Zhang, Y., Lam, F.L.Y., Yan, Z.F. and Hu, X., 2006. Review of Kelvin's equation and its modification in characterisation of mesoporous materials. *Chinese Journal of Chemical Physics*, 19(2), pp.102-108.

[21] Brunauer, S., Emmett, P.H. and Teller, E., 1938. Adsorption of gases in multimolecular layers. *Journal of the American Chemical Society*, 60(2), pp.309-319.

[22] Barrett, E.P., Joyner, L.G. and Halenda, P.P., 1951. The determination of pore volume and area distributions in porous substances. I. Computations from nitrogen isotherms. *Journal of the American Chemical Ssociety*, 73(1), pp.373-380.

[23] Monson, P.A., 2012. Understanding adsorption/desorption hysteresis for fluids in mesoporous materials using simple molecular models and classical density functional theory. *Microporous and Mesoporous Materials*, 160, pp.47-66.

[24] Yano, J. and Yachandra, V.K., 2009. X-ray absorption spectroscopy. *Photosynthesis Research*, 102(2-3), pp.241-254.

[25] Gaur, A., Shrivastava, B.D. and Nigam, H.L., 2013. X-ray absorption fine structure (XAFS) spectroscopy – a review. *Proceedings of the Indian National Science Academy*, 79(B), pp.921-966.

[26] Swinehart, D.F., 1962. The Beer-Lambert law. *Journal of Chemical Education*, 39(7), p.333.

[27] Debye, P., 1913. Interferenz von röntgenstrahlen und wärmebewegung. *Annalen der Physik*, 348(1), pp.49-92.

[28] Waller, I., 1923. Zur frage der einwirkung der wärmebewegung auf die interferenz von röntgenstrahlen. *Zeitschrift für Physik A Hadrons and Nuclei*, 17(1), pp.398-408.

[29] Ravel, B. and Newville, M., 2005. ATHENA, ARTEMIS, HEPHAESTUS: data analysis for X-ray absorption spectroscopy using IFEFFIT. *Journal of Synchrotron Rradiation*, 12(4), pp.537-541.

[30] Rapaport, D. C., 2004. The art of molecular dynamics simulations. *Cambridge University Press*. Cambridge, UK

[31] Buckingham, R.A., 1938. The classical equation of state of gaseous helium, neon and argon. *Proceedings of the Royal Society of London A: Mathematical, Physical and Engineering Sciences*, 168, 933, pp. 264-283.

[32] Sayle, D.C., Maicaneanu, S.A. and Watson, G.W., 2002. Atomistic models for CeO_2 (111),(110), and (100) nanoparticles, supported on yttrium-stabilized zirconia. *Journal of the American Chemical Society*, 124(38), pp.11429-11439.

[33] Sayle, T.X., Catlow, C.R.A., Maphanga, R.R., Ngoepe, P.E. and Sayle, D.C., 2005. Generating MnO_2 nanoparticles using simulated amorphization and recrystallisation. *Journal of the American Chemical Society*, 127(37), pp.12828-12837.

[34] Feng, X., Sayle, D.C., Wang, Z.L., Paras, M.S., Santora, B., Sutorik, A.C., Sayle, T.X., Yang, Y., Ding, Y., Wang, X. and Her, Y.S., 2006. Converting ceria polyhedral nanoparticles into single-crystal nanospheres. *Science*, 312(5779), pp.1504-1508.

[35] Sayle, D.C. and Watson, G.W., 2001. Structural exploration of thin-film oxide interfaces via 'simulated amorphisation and recrystallisation'. *Surface science*, 473(1), pp.97-107.

[36] Sayle, T.X., Parker, S.C. and Sayle, D.C., 2004. Shape of CeO_2 nanoparticles using simulated amorphisation and recrystallisation. *Chemical Communications*, (21), pp.2438-2439.

[37] Sayle, D.C., Feng, X., Ding, Y., Wang, Z.L. and Sayle, T.X., 2007. "Simulating Synthesis": ceria nanosphere self-assembly into nanorods and framework architectures. *Journal of the American Chemical Society*, 129(25), pp.7924-7935.

[38] Sayle, D.C., Seal, S., Wang, Z., Mangili, B.C., Price, D.W., Karakoti, A.S., Kuchibhatla, S.V., Hao, Q., Mobus, G., Xu, X. and Sayle, T.X., 2008. Mapping nanostructure: a systematic enumeration of nanomaterials by assembling nanobuilding blocks at crystallographic positions. *ACS Nano*, 2(6), pp.1237-1251.

[39] Sayle, D.C., Mangili, B.C., Klinowski, J. and Sayle, T.X., 2006. Simulating self-assembly of ZnS nanoparticles into mesoporous materials. *Journal of the American Chemical Society*, 128(47), pp.15283-15291.

[40] Smith, W. and Forester, T.R., 1996. DL_POLY_2. 0: A general-purpose parallel molecular dynamics simulation package. *Journal of Molecular Graphics*, 14(3), pp.136-141.

[41] Humphrey, W., Dalke, A. and Schulten, K., 1996. VMD: visual molecular dynamics. *Journal of Molecular Graphics*, 14(1), pp.33-38.

CHAPTER 3.

$CuFe_2O_4$ – SiO_2 aerogel and xerogel nanocomposites: synthesis and characterisation

The synthesis of $CuFe_2O_4$-SiO_2 nanocomposites in form of aerogel and xerogel has been successfully achieved with high homogeneity. The sol-gel procedure, involving the use of urea as a co-gelation agent, has been used, ensuring a good control of the composition of the nanocomposites. The structural and morphological characterisation of the samples has been carried out with a multi-technique approach involving the use of X-ray diffraction (XRD), Transmission Electron Microscopy (TEM), Thermo-gravimetric Analysis with simultaneous Differential Scanning Calorimetry (TGA\DSC), N_2-Physisorption at 77 K and X-ray absorption spectroscopy (XAS). The analysis of both the X-ray absorption near edge structure (XANES) and the extended X-ray absorption fine structure (EXAFS) indicates that the Cu^{2+} ions occupy octahedral sites within the crystal structure of the copper ferrite and have a Jahn-Teller distorted coordination geometry, forming a tetragonal lattice. However, the Fe^{3+} ions do not show Jahn-Teller distortion and form a cubic sub-lattice within the structure.

3.1. Introduction

Spinel ferrites are a class of ceramic materials with generic formula MFe_2O_4, where M is a divalent transition metal ion (Mn^{2+}, Co^{2+}, Ni^{2+}, etc.). Generally, the spinel crystal structure is defined by the space group *Fd3m* with a cubic unit cell, although a tetragonal distortion is also possible. Within the unit cell, 32 oxygen ions are distributed with a cubic closed packed structure, Figure 3.1(a); 24 cations are distributed within the unit cell, occupying 16 of the 32 available octahedral sites, Figure 3.1(b), and 8 of the 64 available tetrahedral sites, Figure 3.1(c).

In a 'normal' spinel, the bi-valent cation occupies all the tetrahedral sites with the octahedral sites all occupied by the Fe^{3+}. However, the Fe^{3+} can equally accommodate both the tetrahedral and the octahedral coordination, not having any crystal field stabilization energy (CFSE) under the weak field of the oxide ions. If the bi-valent cation is present just in the octahedral sites, the Fe^{3+} occupies 8 octahedral and 8 tetrahedral sites and the spinel is called 'inverse'. Identifying the tetrahedral sites with the letter A and the octahedral ones with the letter B, we can write the generic formula for a spinel ferrite as follows:

$$[M^{2+}_{1-i}\,Fe^{3+}_{i}]^{A}[M^{2+}_{i}\,Fe^{3+}_{(2-i)}]^{B}O_4 \qquad \text{eq. 3.1}$$

with *i* the inversion degree of the spinel. Partial inversion is also possible if the bi-valent cation occupies both octahedral and tetrahedral sites; in that case $0 < i < 1$.

Spinel ferrites nanoparticles have recently received increasing attention due to their magnetic and catalytic properties that differ from the corresponding bulk[1]. In particular, their magnetic properties make these materials suitable for important applications such as magnetic storage systems[2], site-specific drug delivery[3] and sensors[4]. These properties are strongly dependent on the cation distribution within the structure and therefore on the inversion degree of the spinel.

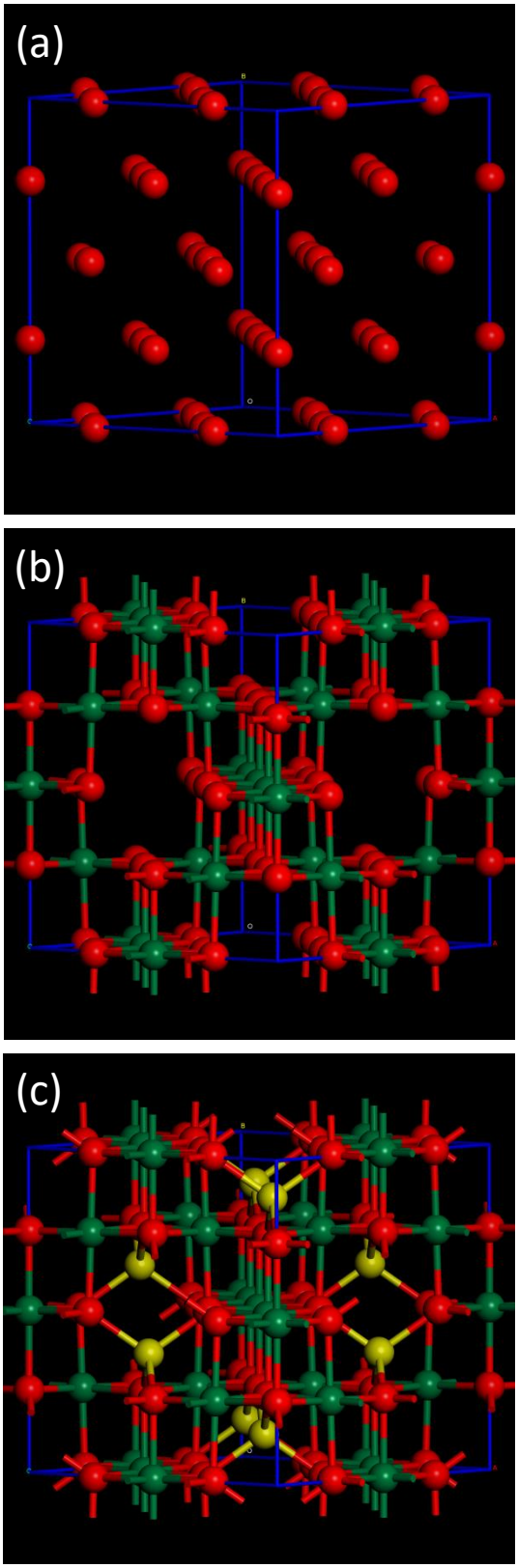

Figure 3.1 Representation of the cubic spinel crystal structure of a ferrite: (a) only O^{-2} ions present; (b) octahedral sites represented with green balls; (c) tetrahedral sites added using yellow balls. Images are created using the software Materials Studio.

Furthermore, in the field of catalysis, particular attention is recently given to the development of catalysts that can be easily separated, for example by means of a magnetic field[5], and ferrite nanoparticles are particularly suitable for this application.

Copper ferrite nanoparticles have been synthesised by the use of different synthetic approaches like combustion route,[6] aerosol method,[7] thermal decomposition of nitrates[8] and co – precipitation[9]. However, with these methods it was not possible to achieve highly monodispersed nanoparticles. Furthermore, the problem of aggregation is very common for unsupported nanoparticles, especially in the field of catalysis: nanoparticles submitted to high temperature thermal treatments tend to aggregate leading to a decrease of the exposed surface area and therefore of their reactivity. The magnetic properties of the material are also influenced: the cation distribution in the spinel structure is highly correlated with the size of the particles[10]. In this sense, it is clear the importance to develop synthetic routes that lead to the formation of nanoparticles that are highly monodispersed in size.

The dispersion of nanoparticles in an amorphous matrix such as silica aerogel and xerogel can overcome these problems. In particular, aerogel and xerogel nanocomposites can be synthesised using the two steps acid-base catalysed sol-gel technique described in section 2.1.1 (Chapter 2). During this synthesis, a solution containing an appropriate amount of metal salts is added to the sol and gelation is promoted by the use of urea as a base catalysts. Urea ensures a smooth increase of the pH avoiding the precipitation of metal hydroxides. Once the gel is formed and submitted to the appropriate drying process, the resulting nanocomposite is subjected to thermal treatments. During the thermal treatments the metals salts decompose to facilitate the growth of the metal oxide crystalline nanoparticles, confined within the amorphous silica porous structure. The result is a nanocomposite with metal oxide nanoparticles that are homogeneously dispersed and with a narrow distribution of sizes.

Mn, Ni and Co ferrite nanoparticles within silica aerogel matrix have been previously synthesised with this method.[11,12] The growth of the nanoparticles within the silica matrix was limited to 4 nm in diameter and the nanoparticles were highly dispersed and well-spaced, with no aggregation phenomena. Extended X-ray absorption fine structure (EXAFS) and X-ray absorption near edge structure (XANES) were used to

elucidate important information concerning the crystal structure of the dispersed nanophase of such synthesised nanocomposites. These techniques are element-specific and sensitive to the local structure at the short range, giving information that is not detectable with conventional techniques like X-ray diffraction (XRD).

XANES in particular gives information on the oxidation state of the absorbing atom and on its symmetry. EXAFS gives information regarding the surrounding of the absorbing atom, including bond distances, Debye-Waller factors, coordination numbers and cation distribution. Previously, our group determined the inversion degree of Mn, Co and Ni ferrite nanoparticles dispersed in silica aerogel matrix: it was found that the inversion degree increases in the series, being 0.2, 0.7 and 1.0 respectively.[11]

Copper ferrite has been found to be a complete inverse spinel[13] with a crystalline structure that can possess a *cubic* or *tetragonal* unit cell symmetry. Results in ref.[14] demonstrated that the *tetragonal* copper ferrite is stable at room temperature up to 340 ºC where the transition to the *cubic* phase begins. The tetragonal phase is associated with the Cu^{2+} ions occupying the octahedral sites that possess a Jahn-Teller distorted symmetry, which is very common for d^9 transition metal ions. In the range of temperatures between 360 – 420 ºC the crystal structure undergoes a transition from a *tetrahedral* to *cubic* phase: this transition is regarded as an 'order-disorder' transformation, with the Cu^{2+} ions migrating from octahedral sites to tetrahedral interstitial sites, losing their Jahn-Teller distortion. It was also found that the copper ions that migrates from octahedral to tetrahedral sites are reduced from Cu^{2+} to Cu^{1+} forming an oxygen deficient copper ferrite with *cubic* phase.[14]

These findings are also confirmed by the work performed by Xing et al.[15] that selectively synthesised *cubic* and *tetragonal* copper ferrite nanoparticles by changing the reaction environment: *cubic* copper ferrite was formed submitting the starting materials at 800 ºC under N_2 flow. In order to preserve the *cubic* crystal structure, once the oxygen deficient copper ferrite was formed, the temperature was cooled down under N_2 atmosphere, not giving the opportunity to the material to restore the oxygen content. If the cooling process was performed in air, the *tetragonal* phase was obtained.

Although a consistent amount of work concerning the crystal structure of copper ferrite is already present in the literature, all these studies use techniques such as XRD and Mössbauer spectroscopy. These techniques have strong limitations regarding the local structure surrounding the metal ions: XRD cannot distinguish Fe from Cu due to their similar scattering factors; Mossbauer spectroscopy does not provide information on the Cu^{2+} ion.

In this chapter, we compare silica aerogel and xerogel as a matrix for copper ferrite nanoparticles and we use XANES and EXAFS spectroscopy in order to elucidate the local structure of Cu^{2+} and Fe^{3+} within the spinel structure of the nanoparticles.

3.2. Sample preparation

The aerogel and xerogel nanocomposites were synthesised following the two-step catalysed sol-gel procedure illustrated in section 2.1.1 (Chapter 2). This procedure has been successfully used in previous work in order to prepare aerogel nanocomposites with other metal ferrites nanoparticles with a precise loading of the nanophase[12]. $Fe(NO_3)_3 \cdot 9H_2O$ (0.7985 g; 0.002 mol) and $Cu(NO_3)_2 \cdot 2.5H_2O$ (0.2299 g; 0.001 mol) are used during the sol-gel procedure in order to produce the copper ferrite nanophase. The quantities have been chosen in order to produce nanocomposites with a 10 wt % loading of the copper ferrite nanophase. After gelation starts at 85 ºC the sols were poured in a cylindrical vial which was sealed and kept at 40 ºC for 20 h: this time was sufficient in order to complete the gelation.

The gels obtained were then subjected to different drying conditions:

- The xerogel nanocomposite was obtained by slow evaporation of the wet gel, which was achieved by heating at 40 ºC for 72 h in an open container.
- The aerogel was prepared by subjecting the wet gel to supercritical extraction of the solvent, as illustrated in section 2.1.2 (Chapter 2). The wet gel was inserted in an autoclave with a volume of 300 cm^3 which was filled with 70 ml of absolute ethanol and flushed with N_2. The autoclave was then heated until a temperature of 330 ºC and a pressure of 70 atm were reached. The autoclave was then vented to atmospheric pressure to enable the extraction of the ethanol from the porous silica matrix of the nanocomposite.

After drying, both aerogel and xerogel nanocomposites were submitted to calcination treatments in static air at 450 ºC for 1 h. According with section 2.1.1 (Chapter 2), these nanocomposites will be called hereafter as 'ACuFe450_1h' and 'XCuFe450_1h' in the case of the aerogel and xerogel respectively. These already treated nanocomposites were subsequently thermally treated at 750 ºC for 1 h and 6 h and at 900 ºC for 1 h. In the same way, 'ACuFe750_1h' and 'XCuFe750_1h'will be used for the aerogel and xerogel respectively, treated at 750 ºC for 1 h. The same criteria will be chosen for the other nanocomposites. A bulk sample was also prepared following the procedure in reference[16].

3.3. Characterisation

3.3.1. TGA\DSC

Both aerogel and xerogel were analysed by means of TGA\DSC after the drying process and before any thermal treatment. The results are reported in Figure 3.2 and Table 3.1. The TGA curve of the aerogel is very similar to other aerogel nanocomposites previously studied.[12] A weight loss of about 3% occurs at temperatures below 120 ºC and another 9% weight loss occurs between 120-500 ºC. The first event is due to the loss in water that is adsorbed on the surface of the aerogel, even if the DSC curve does not give a clear endothermic peak. From the DSC curve, in the second range of temperatures, 120-500 °C, we note the presence of two exothermic events: this is probably due to the decomposition of organics present at the surface of the aerogel due to its partial esterification, which occurs during the drying process. Part of the weight loss in this region might be also due to urea residues that have not completely decomposed during the supercritical extraction. TGA/DSC curves of urea are reported in Appendix A1, Figure A1.1, together with the curves of the metal salts used during the synthesis, Figure A1.2 and Figure A1.3.

The weight loss of the xerogel sample is larger due to the fact that the drying process is done at low temperature (40 ºC) and all the organic components of the synthesis are still present, except the ethanol. A first weight loss of 24 % occurs in the range of temperature between 25-220 ºC. At this stage, after the loss of the water that is absorbed at the surface, the thermal decomposition of the metal salts occurs, together with the decomposition of urea, which begins around 200 ºC (see Figure A1.1, Appendix A1). In this region, the DSC curve shows an endothermic peak centred at 190 ºC. Other two exothermic events occur at higher temperatures, with two correspondent DSC peaks centred at 241 and 394 ºC. In this region, the TGA curve shows a further weight loss of 43 %, which is attributed to the complete decomposition of the urea.

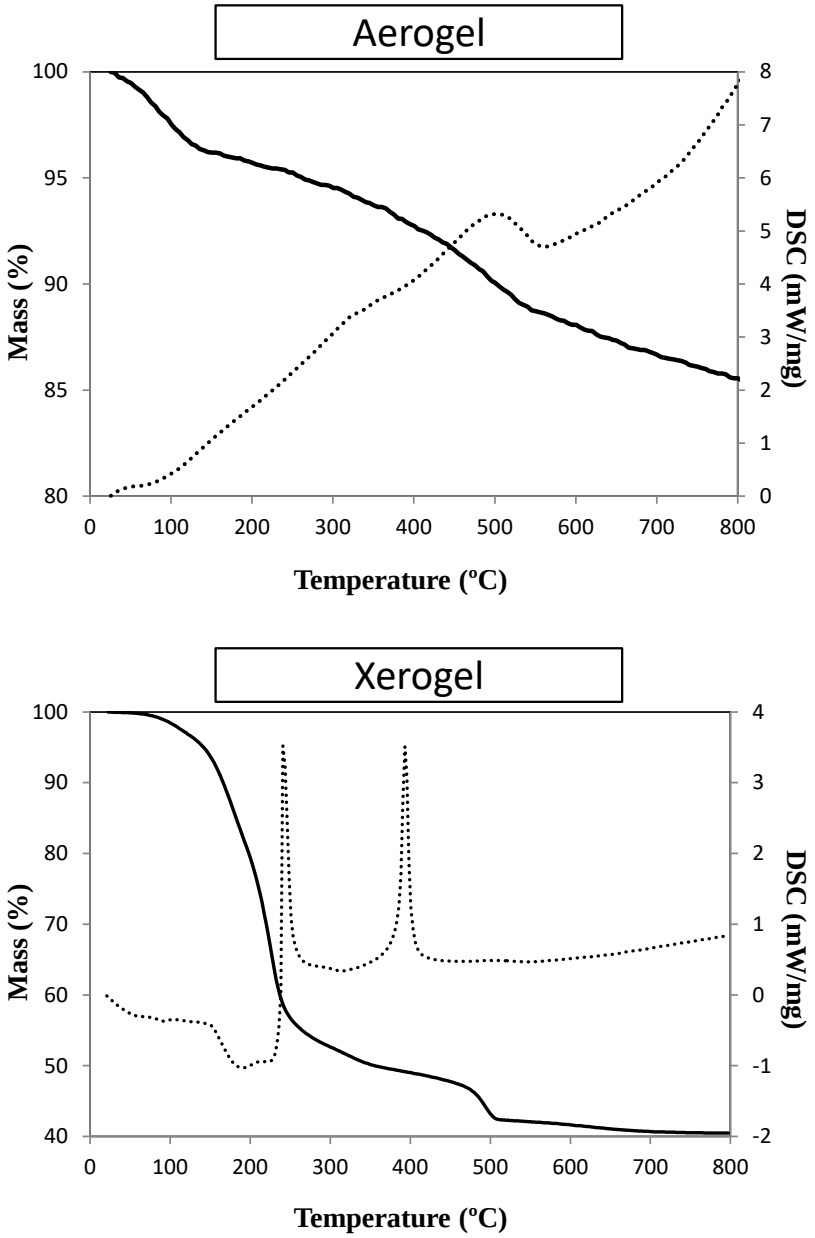

Figure 3.2 TGA/DSC curves of the aerogel (top) and xerogel (bottom) samples; bold line: TGA; dots: DSC.

Table 3.1 TGA/DSC results for the aerogel and xerogel samples.

	Peak	Mass change (%)	Temperature (°C)	Enthalpy (kJ · g^{-1})	Residual mass (%)
ACuFe	1 (endo)	2.89	25 – 120	/	81.38
	2 (exo)	4.34	120 – 400	/	
	3 (exo)	4.56	400 – 500	/	
XCuFe	1 (endo)	24.56	190.6	+ 0.07	28.10
	2 (exo)	38.50	241.3	- 0.17	
	3 (exo)	4.66	393.8	- 0.21	

3.3.2. XRD

In Figure 3.3, the XRD pattern of the bulk sample is reported, which allows the identification of the copper ferrite tetragonal phase by comparison with the corresponding reference pattern[17], reported as t-$CuFe_2O_4$. The additional peak, indicated with an asterisk, corresponds to a small impurity of CuO[18]. The XRD pattern of the cubic phase[19], c-$CuFe_2O_4$, is also reported for comparison.

The XRD patterns of all the nanocomposites obtained after each thermal treatment are reported in Figure 3.4 in the case of the aerogel and in Figure 3.5 in the case of the xerogel respectively. Every pattern presents the typical amorphous halo of the silica matrix. The peaks due to the formation of the copper ferrite nanocrystalline phase appear after the treatment at 750 ºC in both aerogel and xerogel nanocomposites. No substantial differences are noted between the treatments at 750 ºC for 1 h or 6 h. However, the formation of the copper ferrite nanophase is completed at 900 ºC where much more intense peaks appear in the diffraction patterns.

In the case of the aerogel and xerogel nanocomposites it was more difficult to determine unambiguously the phase of the copper ferrite, due to the superimposed contribution of the amorphous silica, which is the largest component. Furthermore, the peaks generated by the nanocrystalline phase appear broad. However, the best match was obtained with the reference pattern of the tetragonal phase that is the one stable at room temperature.

The average crystal size of the nanophase has been calculated for each sample using the Scherrer equation (eq. 2.2, section 2.2.2.3). The values obtained have to be

considered as the average size of the crystalline domains of the nanophase and not the actual size of the nanoparticles. Table 3.2 summarised the results obtained considering the most intense peak of the diffraction patterns. As expected, in both cases the average crystal size increases as function of the calcination temperature, up to 7 nm in the case of the xerogel and up to 6 nm in case of the aerogel. The typical error on average crystal size determination is ± 1nm.

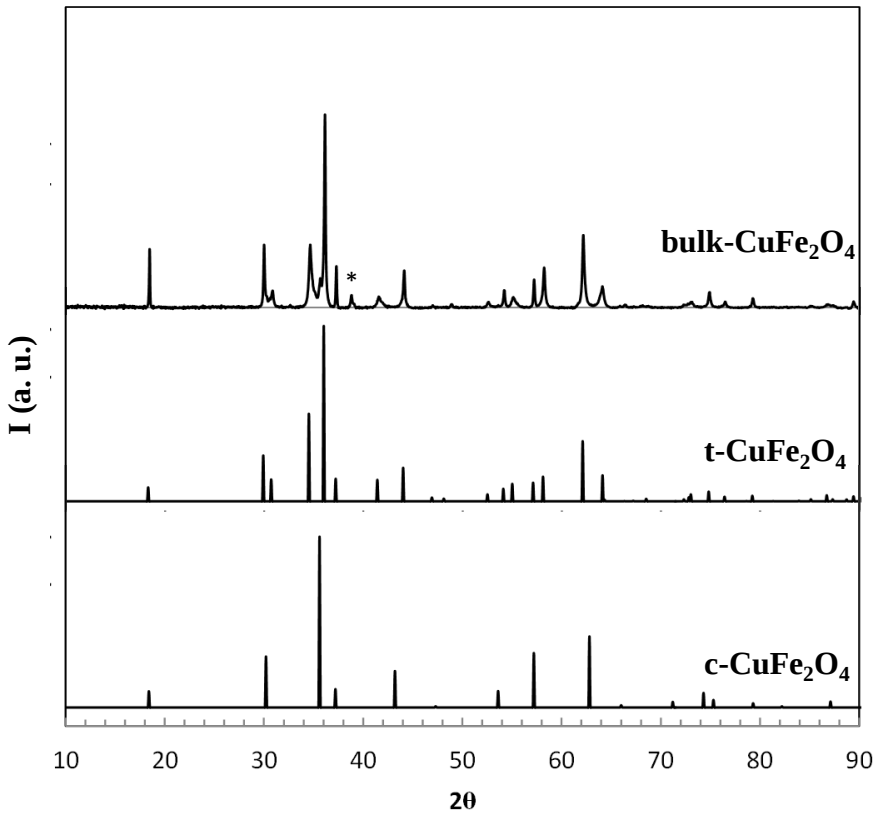

Figure 3.3 XRD pattern of the bulk $CuFe_2O_4$ sample with the pattern of the tetragonal and cubic phase, t-$CuFe_2O_4$ and c-$CuFe_2O_4$ respectively. * indicates a peak identified as CuO impurity.

Table 3.2 Crystallite average size calculated with the Scherrer equation for all the nanocomposites.

	Sample	Peak pos. [º2θ]	Crystallite size [nm]
Aerogel	ACuFe450_1h	34,16	3
	ACuFe750_1h	35.52	4
	ACuFe750_6h	35.56	5
	ACuFe900_1h	35.59	6
Xerogel	XCuFe450_1h	35.48	5
	XCuFe750_1h	35.46	5
	XCuFe750_6h	35.49	5
	XCuFe900_1h	35.53	7

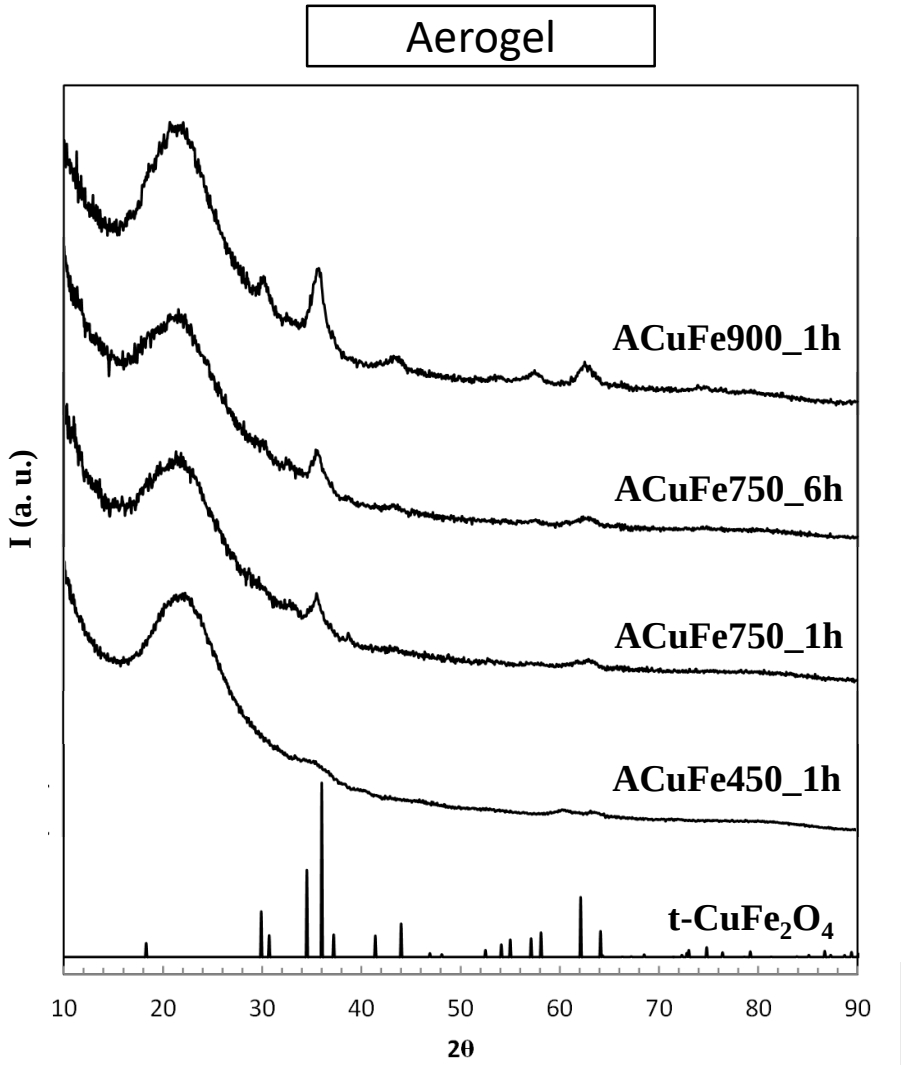

Figure 3.4 XRD patterns of the aerogel samples after all the thermal treatments. The reference pattern of the tetragonal $CuFe_2O_4$ crystalline phase is reported at the bottom of the figure.

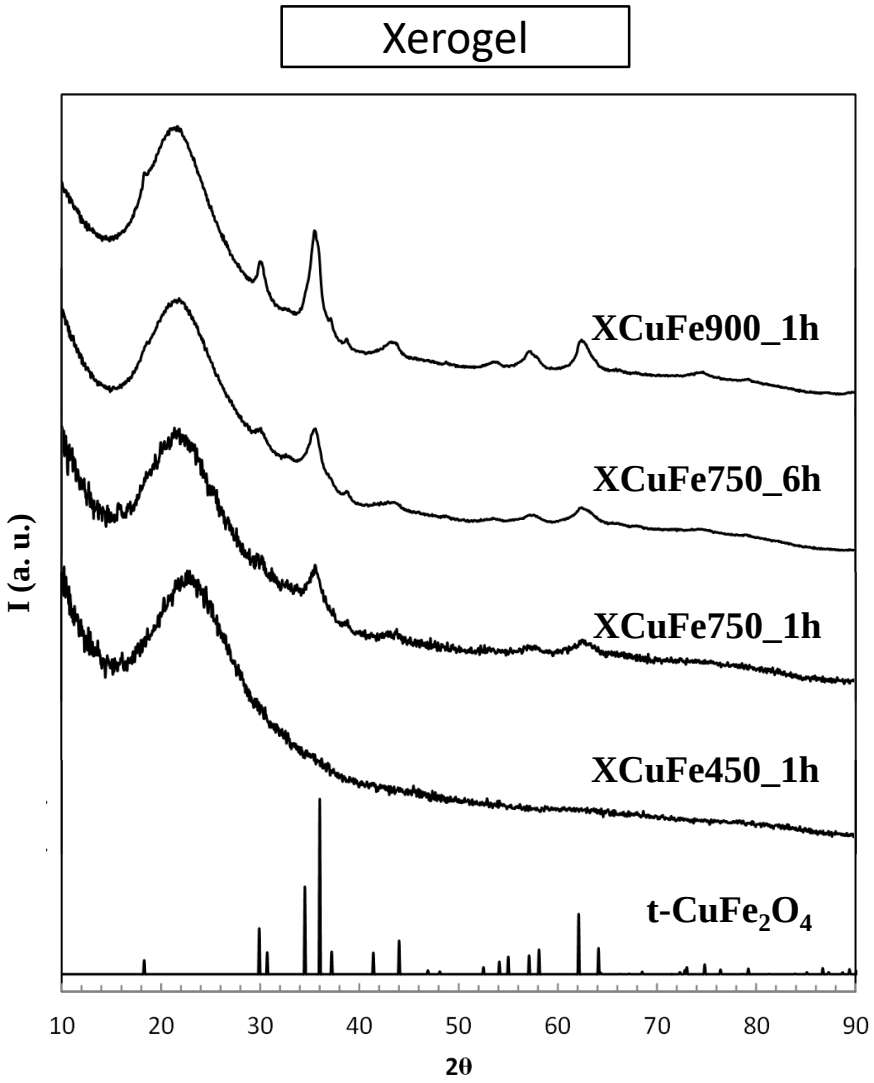

Figure 3.5 XRD patterns of the xerogel samples after all the thermal treatments. The reference pattern of the tetragonal $CuFe_2O_4$ crystalline phase is reported at the bottom of the figure.

3.3.3. TEM

The evolution of the nanophase within the amorphous silica matrix of the aerogel and xerogel was also monitored by TEM. In Figure 3.6 bright field (left) and dark field (right) images of all the aerogel samples are reported; corresponding images of the xerogel sample are reported in Figure 3.7. From the bright field images we note the difference of the matrix texture between the aerogel and xerogel samples. The aerogel matrix appears as highly porous and much less dense compared with the xerogel. We also note that the aerogel and xerogel matrix stay unchanged after the thermal treatments; this is very important considering applications such as catalysis. However, from the bright field images is difficult to obtain information concerning the crystalline nanophase embedded within the amorphous silica matrix.

The crystalline nanophase can be instead monitored looking at the dark field images, where the nano-crystallites that are in diffraction conditions appear as bright spots on top of the darker background of the amorphous silica phase. Increasing the calcination temperature the number and size of the nanocrystals increases in both aerogel and xerogel samples. The sizes of the nanoparticles have been graphically measured from the dark field images, although the small number of nanoparticles does not allow to have good statistics; however, the average diameter of the nanoparticles correspond to 7 nm and 6 nm in the aerogel and xerogel samples respectively with the typical error for the size determination being ± 1 nm. These results are in agreement with the XRD.

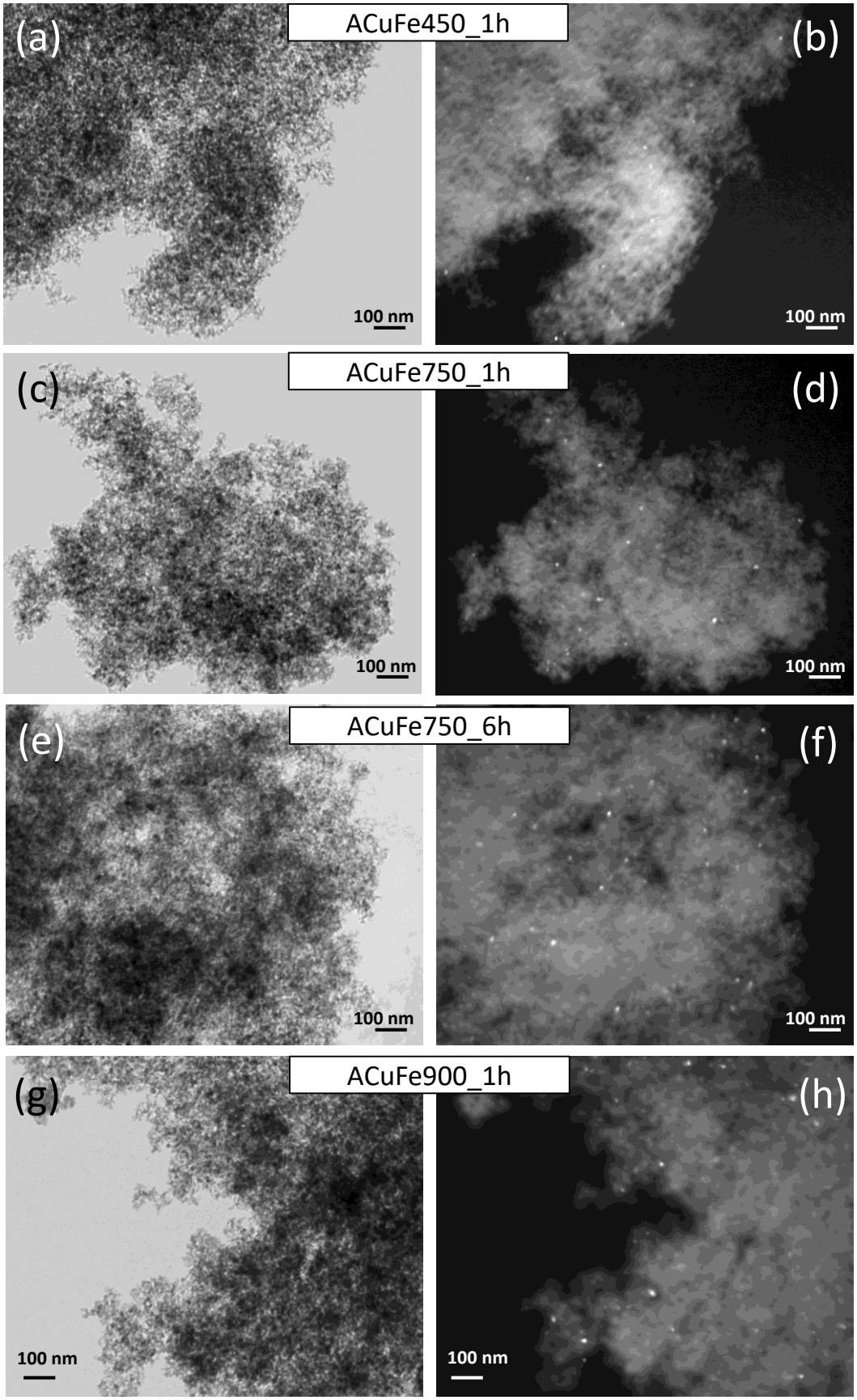

Figure 3.6 TEM images of the aerogel samples as function of the calcination temperature. Bright field images are in the left, dark field in the right.

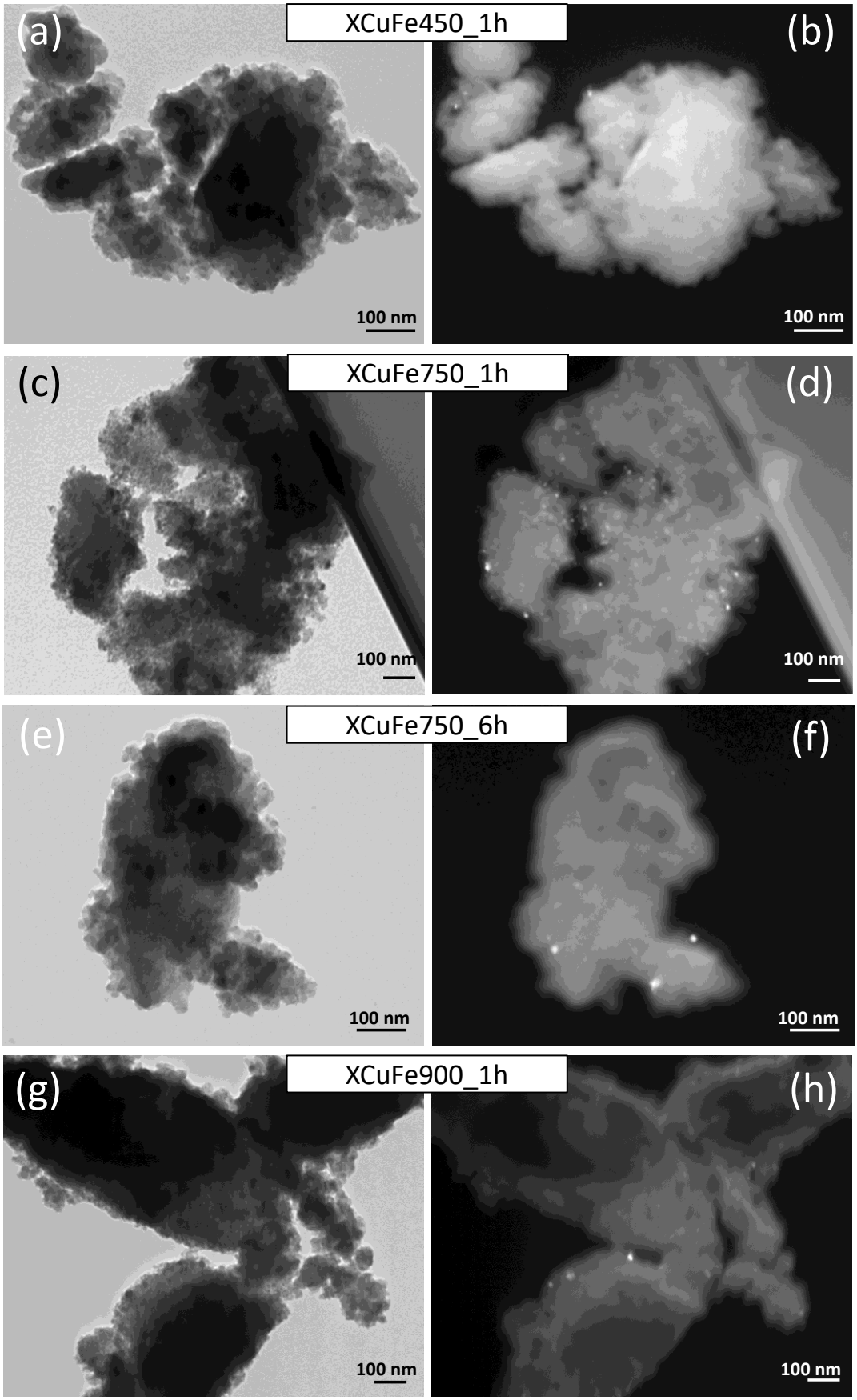

Figure 3.7 TEM images of the xerogel samples as function of the calcination temperature. Bright field images are in the left, dark field in the right.

3.3.4. N_2 - Physisorption

The porosity of the samples thermally treated at 900 ºC, ACuFe900_1h and XCuFe900_1h, has been analysed by means of N_2-physisorption measurements. The differences in the textural features of the silica matrixes are confirmed by looking at the absorption and desorption isotherms, shown in Figure 3.8. Both aerogel and xerogel samples exhibit a type IV isotherm; the shape of the aerogel isotherm is very similar to those obtained in previous studies[12] and is indicative of the presence of a highly interconnected inner surface and extended mesoporosity, being the increasing of the absorption curve at relative high partial pressure values. The isotherm generated by the xerogel sample is different: the more pronounced adsorption at relative low partial pressure values is indicative of microporosity; this was expected for this sample. Both isotherms present a hysteresis loop that can be classified as H3-type in the case of the aerogel and H2(b)-type in the case of the xerogel. The H3-type hysteresis loop located at high values of partial pressure indicates that the pore size is in the upper range of mesoporosity, typical feature for aerogel samples. The hysteresis loop of the isotherm generated by the xerogel sample closes at lower values of partial pressure, indicating the presence of a narrower distribution of smaller pores. This is confirmed by the pore size distribution obtained by the analysis of the desorption part of the isotherm, assessed by the BJH method.[20] Table 3.3 provides the values of surface area S, calculated by BET method, the total pore volume V_P together with the average pore diameter.

Table 3.3 N_2-physisorption results for the aerogel and xerogel nanocomposites after calcination at 900 ºC. Surface area, S, pore volume, V_P, and pore diameter are reported.

Sample	S ($m^2 \cdot g^{-1}$)	V_P ($cm^3 \cdot g^{-1}$)	Pore diameter (nm)
ACuFe900_1h	325	2.53	30
XCuFe900_1h	224	0.47	6 - 7

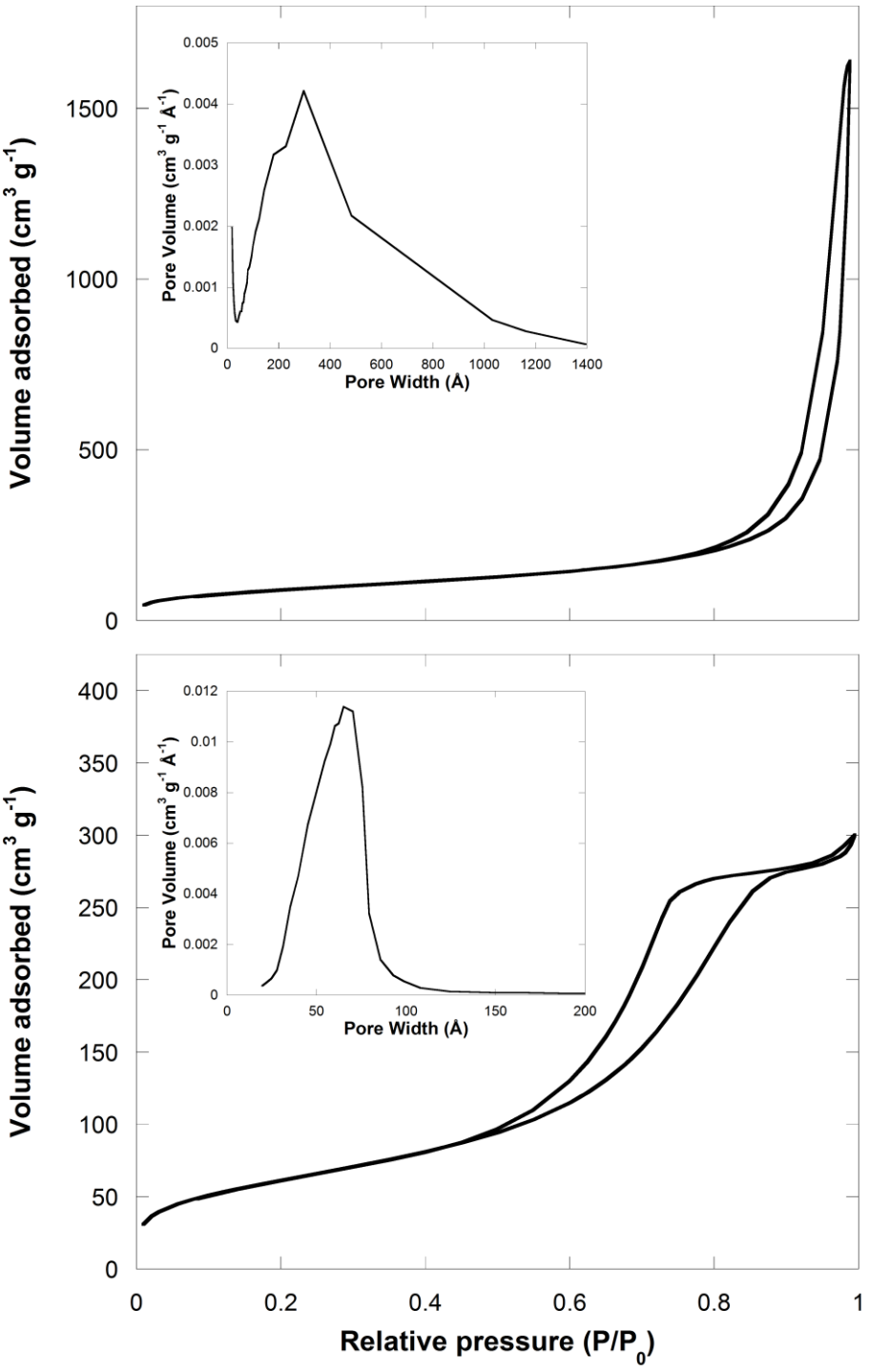

Figure 3.8 N_2 physisorption isotherms of the ACuFe900_1h (top) and XCuFe900_1h (bottom) sample and pore size distribution calculated using the desorption branch (inset)

3.3.5. X-ray absorption Spectroscopy (XAS)

The analysis of the absorption spectra in the XANES region gives information on the oxidation state and local environment of the absorbing atoms. In Figure 3.9 the XANES spectra of ACuFe900_1h and XCuFe900_1h are reported, together with the bulk sample. At the Fe K-edge, the spectra of the α-Fe_2O_3 (hematite) and γ-Fe_2O_3 (maghemite) are reported superimposed on those of the samples while, at the Cu K-edge, the absorption spectra of CuO (tenorite) is also reported. The position of both Fe

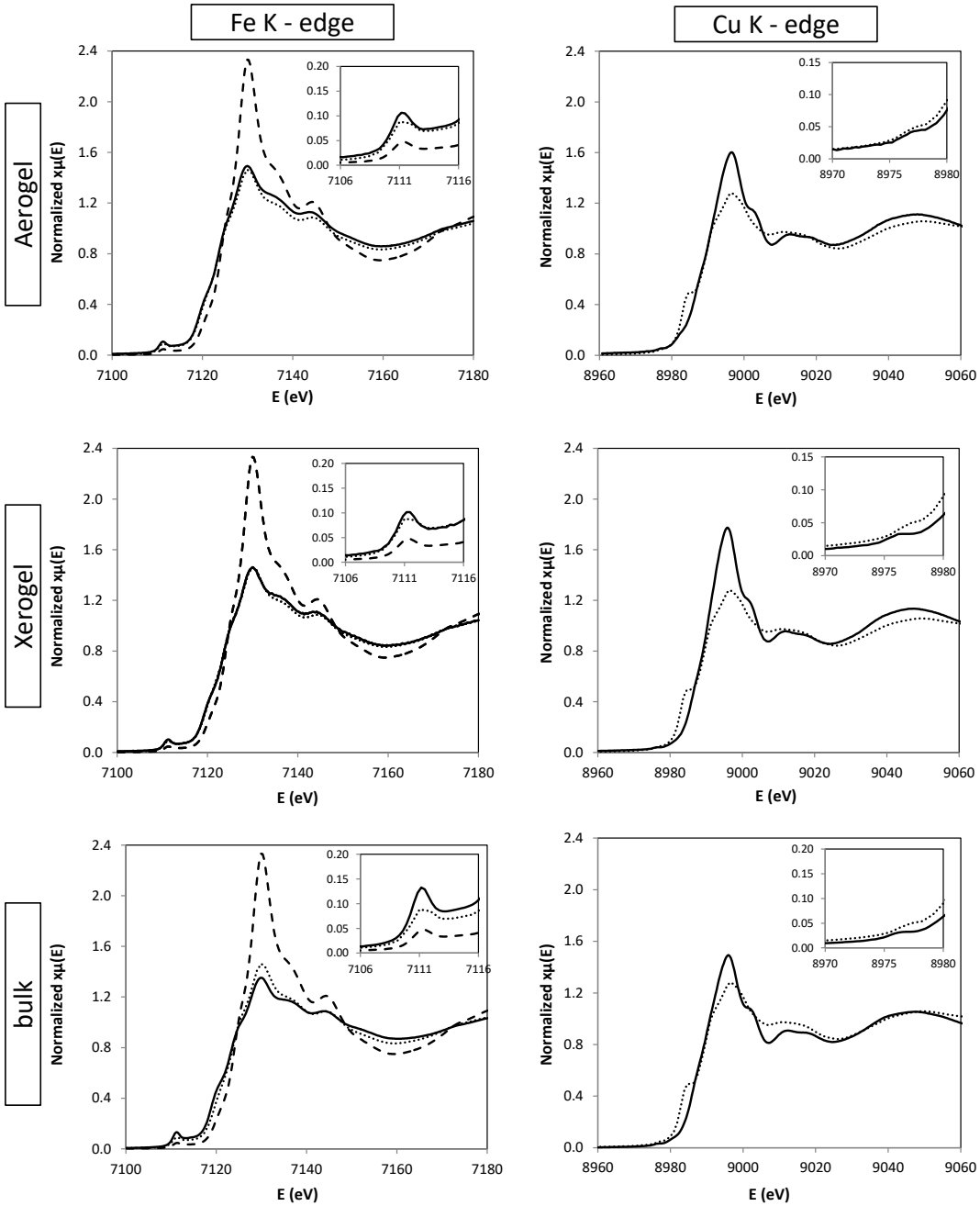

Figure 3.9 XANES spectra of ACuFe900_1h and XCuFe900_1h, together with the bulk sample, at the Fe and Cu K – edge. Bold line: samples; dots: α-Fe_2O_3 in the case of Fe K-edge, CuO in the case of Cu K-edge; dashed line: γ-Fe_2O_3. The pre-peak region is enlarged in the inset.

and Cu edges are typical of Fe^{3+} and Cu^{2+} [11,21]; values of the absorption edges (E^0) and oxidation states are reported in Table 3.4. A close inspection of the pre-peak region, enlarged in the insets in Figure 3.9, can give qualitative information about the coordination geometry of the absorbing atoms. This region of the spectra is mainly due to transitions involving 3d orbitals[22] and the intensity of the pre-edge peak is sensitive to the local coordination geometry of the metal ion, being more intense in the case of non-centrosymmetric sites, like the tetrahedral ones. We note that a defined pre-peak is present at the Fe K-edge indicating the presence of Fe atoms in the tetrahedral positions. The pre-peak in the case of the Cu K-edge is much less intense, indicating that the majority of Cu^{2+} ions are present in octahedral positions. This is an indication that the spinel is likely to be completely (or highly) inverted.

From a qualitative point of view, we also note that the XANES spectra of both aerogel and xerogel samples are very similar to the bulk, showing the same features at both Fe and Cu K-edge. This can be an indication that the samples possess the same crystalline phase as the bulk.

To obtain more information on the local environment of the metal ions within the crystal structure, the analysis of the EXAFS region has been performed. Figure 3.10 shows the $k^3\chi(k)$ and the corresponding Fourier transforms (FTs) of the Cu K-edge; Figure 3.11 shows the $k^3\chi(k)$ and the corresponding FTs of the Fe K-edge. FTs are corrected for phase shift.

The FTs, of both Cu and Fe K-edge, show two main peaks. The first peak is generated by the distances between the absorber (i.e. Fe or Cu) and its first coordination shell with oxygens, while in the second region the most important contributions are given by distances between Fe and Cu cations.

Table 3.4 Absorption energies and oxidation states for the samples and references for both Cu and Fe K-edges

Sample	Element	Oxidation state	E^0 (eV)
ACuFe900_1h	Cu	2+	8990.0
	Fe	3+	7126.8
XCuFe900_1h	Cu	2+	8990.0
	Fe	3+	7126.8
α – Fe_2O_3	Fe	3+	7126.5
γ – Fe_2O_3	Fe	3+	7126.6
CuO	Cu	2+	8990.1

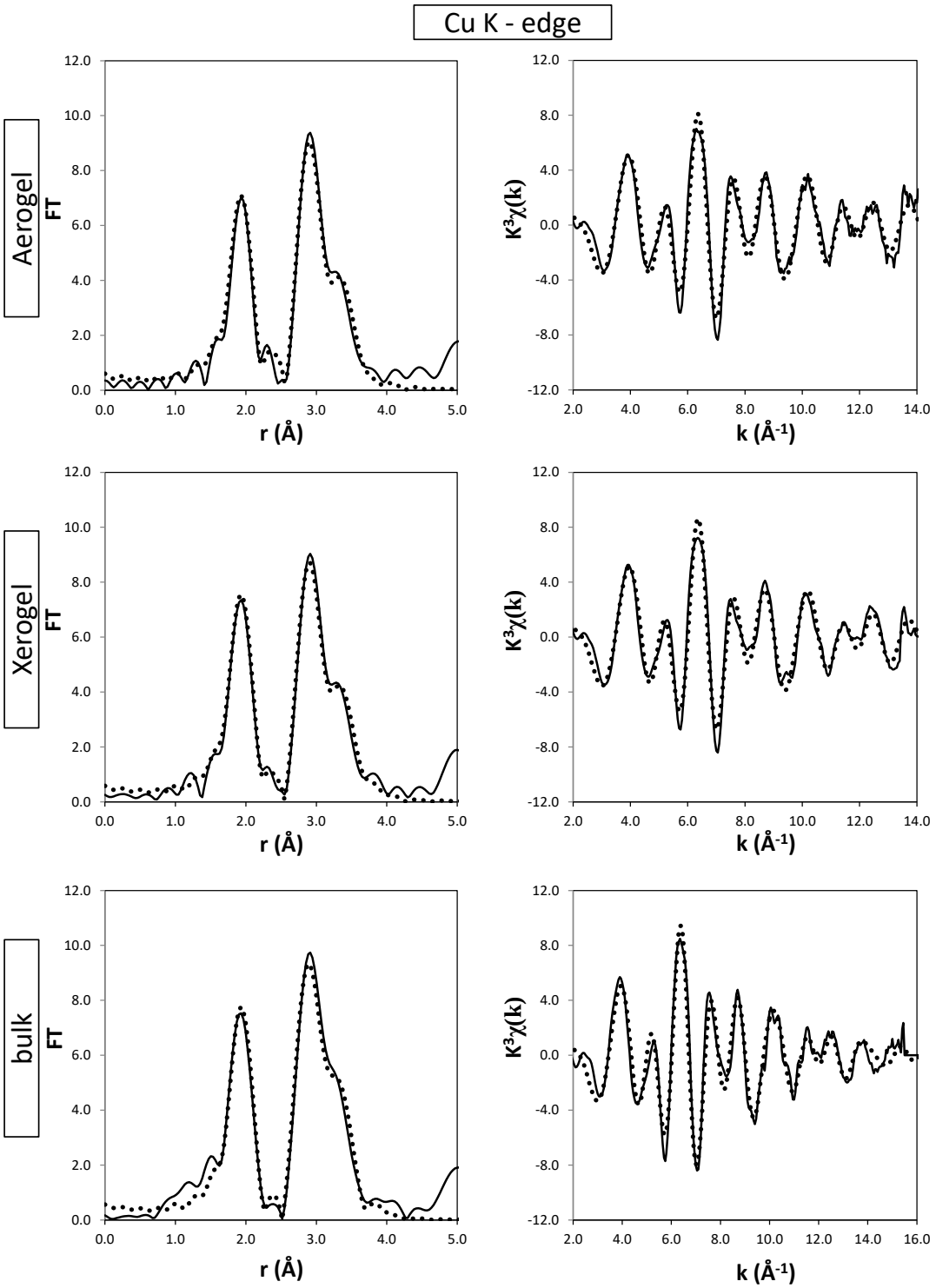

Figure 3.10 $k^3\chi(k)$ (right) and corresponding FTs (left) of the EXAFS region at the Cu K-edge for the bulk, aerogel and xerogel samples. Full line: experiment; dots: fit.

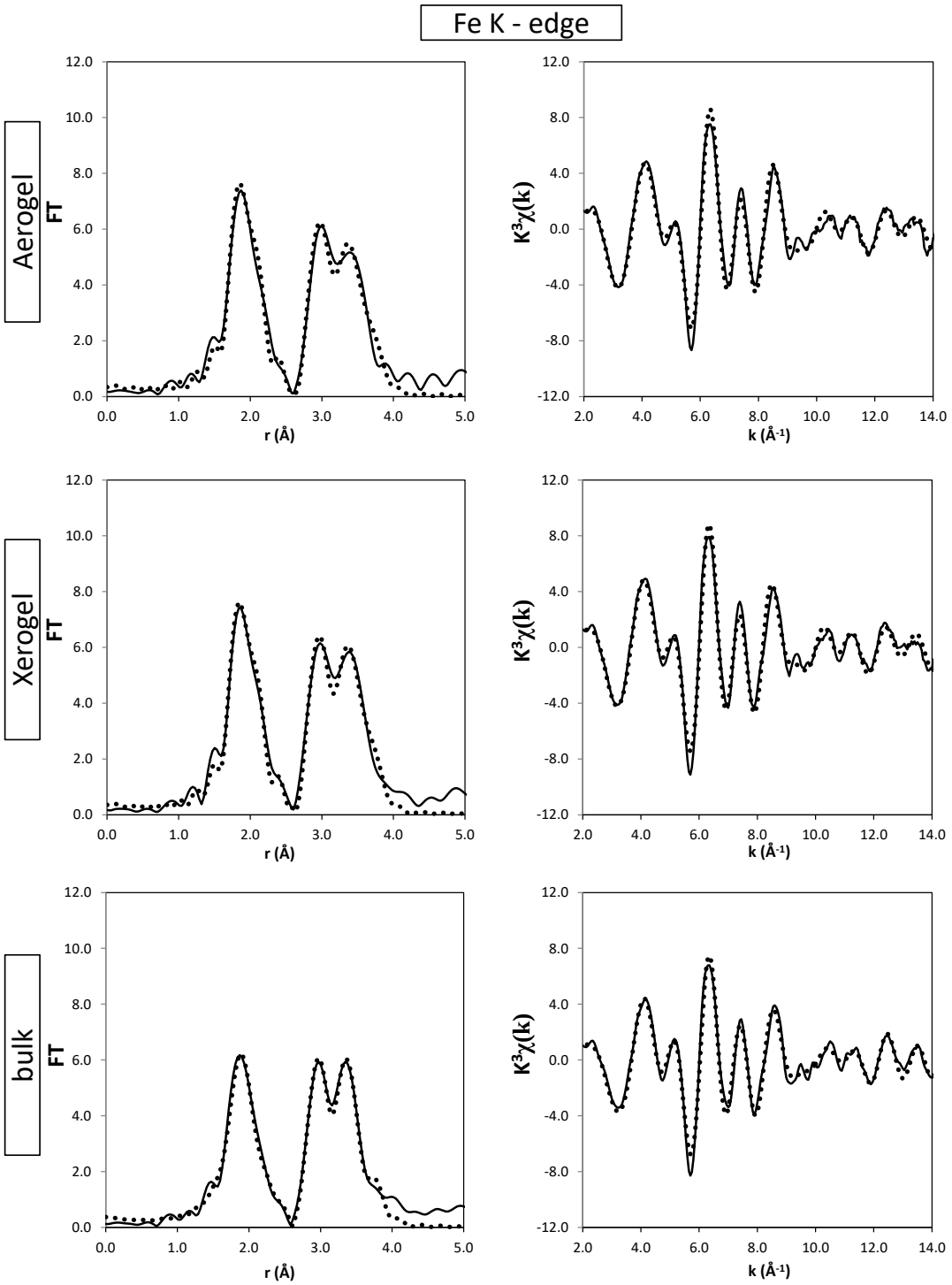

Figure 3.11 $k^3\chi(k)$ (right) and corresponding FTs (left) of the EXAFS region at the Fe K-edge for the bulk, aerogel and xerogel samples. Full line: experiment; dots: fit.

Considering that the distance between two octahedral sites in the spinel crystal structure is centered approximately around 2.9 Å and the distances involving the tetrahedral sites are all centered around 3.5 Å, the qualitative analysis of the FTs can give information on the inversion degree of the spinel. In particular, looking at the FTs at the Cu K-edge, Figure 3.10, we note that, in the region between 2.5 and 4.0 Å, the most intense peak is centered around 2.9-3.0 Å; this peak is due to distances involving two octahedral sites (M_B-M_B, see eq. 3.1); considering that this peak is the most intense in the FT at the Cu K-edge, this can be an indication of the presence of all Cu^{2+} ions at the octahedral positions with the the backscatter being either a Cu^{2+} or a Fe^{3+} ion. The peak around 3.5 Å is much less intense; this is another indication that Cu^{2+} ions are mostly located at tetrahedral sites, and this peak is generated by M_B-M_A distances with Fe^{3+} as the backscatter in tetrahedral sites. The same features were previously found for nickel ferrite nanoparticles.[11] In the case of the Fe K-edge, the iron ions seem to be equally distributed between octahedral and tetrahedral sites, since the contribution at 2.9 Å due to M_B-M_B distances and the one at 3.5 Å due to M_A-M_B/ M_B-M_A and M_A-M_A distances have comparable heights.

In order to perform the fit of the EXAFS region, a careful choice of the theoretical model is to be made. The first attempt of fitting the data at the Cu K-edge done using a model of the *cubic* copper ferrite crystalline phase did not give a satisfactory result. However, it is known from the XRD analysis performed on the bulk sample that the copper ferrite has a *tetragonal* crystalline phase. Although the XRD analysis on the aerogel and xerogel samples does not determine unambiguously the crystalline phase, due to the broadening of the peaks, we note that the XANES spectra, at both Fe and Cu K-edge, show the same feature shown by the bulk sample. With this qualitative indication, we have chosen a model of a *tetragonal* copper ferrite crystalline phase comprising 9 coordination shells, up to a distance of 4 Å in order to fit the EXAFS spectra at the Cu K-edge. This model takes into account the Jahn-Teller distortion that is particularly strong for the first peak of the FT.

During the fit, coordination numbers were kept fixed, given by the crystal structure, and the distances (ΔR_i), the Debye-Waller factors (σ^2) and ΔE^0 left free to vary. S_0^2 has been determined by fitting data of the bulk sample, and then kept fixed for the

fitting of the aerogel and xerogel samples. We also note that, in the case of the Cu K-edge, the M_B-M_B contribution, which is the distance between two octahedral sites, is given by two different components: the octahedral sites are occupied by both Cu and Fe atoms. This contribution has been fitted considering that the backscatter is either Fe or Cu, with occupancy of 0.5. The best fit parameters are reported in Table 3.5, Table 3.6 and Table 3.7 for the bulk sample, aerogel sample and xerogel sample respectively.

By looking at the values of the distances, we can appreciate the the Jahn Teller distortion; the very different Debye-Waller factors indicates that the apical positions at the first coordination shell of the Cu^{2+} have a higher degree of disorder.

Table 3.5 Best fit parameters obtained by fitting the experimental EXAFS spectra of the bulk sample at the Cu K-edge with a 9 shell model of a tetragonal copper ferrite. Coordination numbers (N), interatomic distances (R), Debye-Waller factors, S_0^2, ΔE_0 and R-factor are shown.

Bulk $CuFe_2O_4$		**Cu K-edge**		
Abs. – Backscatter	**N**	**σ^2(Å^2)**	**R(Å)**	**Occupancy**
Cu-O	4.0	0.006 ± 0.001	1.97 ± 0.01	1.0
Cu-O	2.0	0.011 ± 0.004	2.24 ± 0.03	1.0
Cu-Cu_B	2.0	0.004 ± 0.002	2.86 ± 0.02	0.5
Cu-Cu_B	4.0	0.007 ± 0.003	2.98 ± 0.01	0.5
Cu-Fe_B	2.0	0.004 ± 0.002	2.86 ± 0.02	0.5
Cu-Fe_B	4.0	0.007 ± 0.003	2.98 ± 0.01	0.5
Cu-Fe_A	4.0	0.008 ± 0.002	3.42 ± 0.02	1.0
Cu-Fe_A	2.0	0.009 ± 0.003	3.62 ± 0.03	1.0
Cu-O	2.0	0.040	3.557	1.0
Cu-O	4.0	0.040	3.633	1.0
Cu-O	2.0	0.040	3.705	1.0
S_0^2 = 0.9 ± 0.1			**ΔE_0** = -1 ± 1	
R-factor = 0.014				

Table 3.6 Best fit parameters obtained by fitting the experimental EXAFS spectra of the aerogel sample at the Cu K-edge with a 9 shell model of a tetragonal copper ferrite. Coordination numbers (N), interatomic distances (R), Debye-Waller factors, S_0^2, ΔE_0 and R-factor are shown.

ACuFe900_1h			**Cu K-edge**	
Abs.-Backscatter	**N**	**σ^2(Å^2)**	**R(Å)**	**Occupancy**
Cu-O	4.0	0.007 ± 0.001	1.97 ± 0.01	1.0
Cu-O	2.0	0.009 ± 0.003	2.22 ± 0.02	1.0
Cu-Cu_B	2.0	0.005 ± 0.001	2.90 ± 0.01	0.5
Cu-Cu_B	4.0	0.010 ± 0.003	3.00 ± 0.02	0.5
Cu-Fe_B	2.0	0.005 ± 0.001	2.90 ± 0.01	0.5
Cu-Fe_B	4.0	0.010 ± 0.003	3.00 ± 0.02	0.5
Cu-Fe_A	4.0	0.010 ± 0.002	3.44 ± 0.03	1.0
Cu-Fe_A	2.0	0.012 ± 0.006	3.65 ± 0.06	1.0
Cu-O	2.0	0.040	3.557	1.0
Cu-O	4.0	0.040	3.633	1.0
Cu-O	2.0	0.040	3.705	1.0
S_0^2 = 0.9			**ΔE_0** = 0 ± 1	
R-factor = 0.021				

Table 3.7 Best fit parameters obtained by fitting the experimental EXAFS spectra of the xerogel sample at the Cu K-edge with a 9 shell model of a tetragonal copper ferrite. Coordination numbers (N), interatomic distances (R), Debye-Waller factors, S_0^2, ΔE_0 and R-factor are shown.

XCuFe900_1h			**Cu K-edge**	
Abs.-Backscatter	**N**	**σ^2(Å^2)**	**R(Å)**	**Occupancy**
Cu-O	4.0	0.006 ± 0.001	1.96 ± 0.01	1.0
Cu-O	2.0	0.011 ± 0.003	2.22 ± 0.02	1.0
Cu-Cu_B	2.0	0.006 ± 0.001	2.90 ± 0.02	0.5
Cu-Cu_B	4.0	0.011 ± 0.003	2.98 ± 0.02	0.5
Cu-Fe_B	2.0	0.006 ± 0.001	2.90 ± 0.02	0.5
Cu-Fe_B	4.0	0.011 ± 0.003	2.98 ± 0.02	0.5
Cu-Fe_A	4.0	0.010 ± 0.001	3.43 ± 0.02	1.0
Cu-Fe_A	2.0	0.011 ± 0.004	3.62 ± 0.04	1.0
Cu-O	2.0	0.040	3.557	1.0
Cu-O	4.0	0.040	3.633	1.0
Cu-O	2.0	0.040	3.705	1.0
S_0^2 = 0.9			**ΔE_0** = 0 ± 1	
R-factor = 0.014				

Although the *tetragonal* phase was used to fit the EXAFS of the Cu K-edge, the best fit of the EXAFS of the Fe K-edge, Figure 3.11, was obtained considering a *cubic* phase. Fe^{3+} ions have been considered to be in octahedral and tetrahedral sites with an occupancy of 0.5. Taking into account distances up to 4.0 Å, a 4 shell model have been used for the contribution of the Fe atoms in tetrahedral sites and a 5 shell model for the Fe atoms in octahedral sites. In the case of the Fe ions in tetrahedral sites, the distances with the atoms in octahedral sites (M_A-M_B) are due to either Fe^{3+} or Cu^{2+}: the two contributions have been considered separately, scaling the occupancy by 50%, therefore to 0.25. The same thing has been done for the distances considering the absorber in the octahedral sites. As it has been done for the Cu K-edge, also during this fit the coordination numbers have been kept fixed to the values given by the crystal structure while distances (ΔR_i) and the Debye-Waller factors (σ^2) left free to vary. The best fit parameters are reported in Table 3.8, Table 3.9 and Table 3.10 for the bulk sample, aerogel sample and xerogel sample respectively.

Table 3.8 Best fit parameters obtained by fitting the experimental EXAFS spectra of the bulk sample at the Fe K-edge with a 4 shell model in the case of the tetrahedral site and a 5 shell model in the case of the octahedral site using a cubic copper ferrite model. Coordination numbers (N), interatomic distances (R), Debye-Waller factors, S_0^2, ΔE_0 and R-factor are shown.

Bulk $CuFe_2O_4$			**Fe K-edge**	
Abs. – Backscatter	**N**	**σ^2(Å^2)**	**R(Å)**	**Occupancy**
Fe_A-O	4.0	0.005 ± 0.003	1.90 ± 0.05	0.50
Fe_A-Fe_B	12.0	0.009 ± 0.002	3.45 ± 0.02	0.25
Fe_A-Cu_B	12.0	0.009 ± 0.002	3.45 ± 0.02	0.25
Fe_A-O	12.0	0.02 ± 0.1	3.5 ± 0.4	0.50
Fe_A- Fe_A	4.0	0.005 ± 0.002	3.63 ± 0.03	0.50
Fe_B-O	6.0	0.011 ± 0.009	1.98 ± 0.04	0.50
Fe_B-Fe_B	6.0	0.007 ± 0.001	2.97 ± 0.01	0.25
Fe_B-Cu_B	6.0	0.007 ± 0.001	2.973 ± 0.01	0.25
Fe_B-Fe_A	6.0	0.009 ± 0.001	3.455 ± 0.02	0.50
Fe_B-O	2.0	0.04 ± 2	3.552	0.50
Fe_B-O	6.0	0.03 ± 1	3.649	0.50
S_0^2 = 0.7 ± 0.1			**ΔE_0** = -3 ± 2	
		R-factor = 0.011		

Table 3.9 Best fit parameters obtained by fitting the experimental EXAFS spectra of the aerogel sample at the Fe K-edge with a 4 shell model in the case of the tetrahedral sites and a 5 shell model in the case of the octahedral sites using a cubic copper ferrite model. Coordination numbers (N), interatomic distances (R), Debye-Waller factors, S_0^2, ΔE_0 and R-factor are shown.

ACuFe900_1h			**Fe K-edge**	
Abs. – Backscatter	**N**	**σ^2(Å^2)**	**R(Å)**	**Occupancy**
Fe_A-O	4.0	0.001 ± 0.001	1.87 ± 0.01	0.50
Fe_A-Fe_B	12.0	0.009 ± 0.003	3.450 ± 0.04	0.25
Fe_A-Cu_B	12.0	0.009 ± 0.003	3.450 ± 0.04	0.25
Fe_A-O	12.0	0.01 ± 0.2	3.5 ± 0.1	0.50
Fe_A- Fe_A	4.0	0.006 ± 0.005	3.6 ± 0.2	0.50
Fe_B-O	6.0	0.003 ± 0.001	2.00 ± 0.01	0.50
Fe_B-Fe_B	6.0	0.007 ± 0.001	2.98 ± 0.01	0.25
Fe_B-Cu_B	6.0	0.007 ± 0.001	2.98 ± 0.01	0.25
Fe_B-Fe_A	6.0	0.009 ± 0.003	3.45 ± 0.04	0.50
Fe_B-O	2.0	0.01 ± 0.8	3.55	0.50
Fe_B-O	6.0	0.03 ± 0.4	3.65	0.50
S_0^2 = 0.7			**ΔE_0** = -2.6 ± 0.7	
R-factor = 0.013				

Table 3.10 Best fit parameters obtained by fitting the experimental EXAFS spectra of the aerogel sample at the Fe K-edge with a 4 shell model in the case of the tetrahedral sites and a 5 shell model in the case of the octahedral sites using a cubic copper ferrite model. Coordination numbers (N), interatomic distances (R), Debye-Waller factors, S_0^2, ΔE_0 and R-factor are shown.

XCuFe900_1h			**Fe K-edge**	
Abs. – Backscatter	**N**	**σ^2(Å^2)**	**R(Å)**	**Occupancy**
Fe_A-O	4.0	0.001 ± 0.001	1.87 ± 0.01	0.50
Fe_A-Fe_B	12.0	0.008 ± 0.003	3.45 ± 0.04	0.25
Fe_A-Cu_B	12.0	0.008 ± 0.003	3.45 ± 0.04	0.25
Fe_A-O	12.0	0.01 ± 0.5	3.5 ± 0.2	0.50
Fe_A- Fe_A	4.0	0.005 ± 0.004	3.59 ± 0.08	0.50
Fe_B-O	6.0	0.003 ± 0.001	1.99 ± 0.01	0.50
Fe_B-Fe_B	6.0	0.007 ± 0.001	2.97 ± 0.01	0.25
Fe_B-Cu_B	6.0	0.007 ± 0.001	2.97 ± 0.01	0.25
Fe_B-Fe_A	6.0	0.008 ± 0.003	3.45 ± 0.04	0.50
Fe_B-O	2.0	0.01 ± 3	3.55	0.50
Fe_B-O	6.0	0.03 ± 0.3	3.65	0.50
S_0^2 = 0.7			**ΔE_0** = -3.0 ± 0.8	
R-factor = 0.011				

3.3.6. Discussion

The tetragonal phase, well documented in the literature for the copper ferrite structure, is caused by the Jahn Teller distortion on the Cu^{2+} ions that are located at octahedral sites. The six Cu-O distances should be considered as two different coordination shells, with 4 short Cu-O distances and with two longer ones. This distortion at the octahedral sites occupied by the Cu^{2+} ions causes a distortion along one direction of the unit cell, forming the tetragonal system. However, the octahedral sites within the unit cell are not entirely occupied by Cu^{2+} ions, but Fe^{3+} ions occupy half of these sites. XRD does not distinguish the contributions of Cu and Fe atoms separately and the consequence of this is that all the published crystal structures for copper ferrite consider also Fe^{3+} to have a distorted octahedral geometry.[23]

The use of the EXAFS spectroscopy allowed us instead to find that the Fe^{3+} ions do not show any Jahn Teller distortion, being all the six Fe-O distances identical on the first coordination shell: we were able to fit the EXAFS region at the Fe K-edge only by using a cubic crystal system, while the fit using a tetragonal system did not give a satisfactory result.

In this context we can affirm that the Fe^{3+} ions form a *cubic* sub-lattice within the *tetragonal* lattice defined by the Cu^{2+} ions. This is probably possible because the spinel structure have a number of sites within the crystal structure that are not occupied. The Cu atoms are located entirely at the octahedral sites and their Jahn Teller distortion involving mainly the first coordination shell have consequences on the entire structure, forming a tetragonal lattice. However, Fe atoms probably chose to occupy specific sites within the structure that avoid the Jahn Teller distortion, forming a *cubic* sub-lattice within the *tetragonal* lattice defined by the Cu ions.

3.4. Conclusions

In this work, nanoparticles of $CuFe_2O_4$ dispersed in highly porous silica matrixes have been prepared reaching a good dispersion of the crystalline nanophase. The nanoparticles have been found to have average crystal sizes between 6 and 7 nm. X-ray absorption spectroscopy was found to be extremely useful in order to elucidate upon features like the cation distribution within the copper ferrite crystal structure. No substantial differences have been found between the bulk sample and the nanoparticles. However, the possibility to study separately the local structure of Cu and Fe atoms allowed us to conclude that the Cu ions are located at octahedral sites, with a geometry that is distorted due to the Jahn Teller effect. This has been identified as the reason why the stable phase of copper ferrite at room temperature is tetragonal. Conversely, Fe atoms are located in both octahedral and tetrahedral sites, but do not experience any Jahn Teller distortion. The fit of the EXAFS region show that the Fe atoms define a cubic sub-lattice within the tetragonal lattice defined by the Cu atoms.

3.5. References

[1] Qu, Y., Yang, H., Yang, N., Fan, Y., Zhu, H. and Zou, G., 2006. The effect of reaction temperature on the particle size, structure and magnetic properties of coprecipitated $CoFe_2O_4$ nanoparticles. *Materials Letters*, 60(29), pp.3548-3552.

[2] Han, D.H., Luo, H.L. and Yang, Z., 1996. Remanent and anisotropic switching field distribution of platelike Ba-ferrite and acicular particulate recording media. *Journal of Magnetism and Magnetic Materials*, 161, pp.376-378.

[3] Yoon, T.J., Kim, J.S., Kim, B.G., Yu, K.N., Cho, M.H. and Lee, J.K., 2005. Multifunctional nanoparticles possessing a "magnetic motor effect" for drug or gene delivery. *Angewandte Chemie*, 117(7), pp.1092-1095.

[4] Jeseentharani, V., George, M., Jeyaraj, B., Dayalan, A. and Nagaraja, K.S., 2013. Synthesis of metal ferrite (MFe_2O_4, M= Co, Cu, Mg, Ni, Zn) nanoparticles as humidity sensor materials. *Journal of Experimental Nanoscience*, 8(3), pp.358-370.

[5] Bazgir, A., Hosseini, G. and Ghahremanzadeh, R., 2013. Copper ferrite nanoparticles: an efficient and reusable nanocatalyst for a green one-pot, three-component synthesis of spirooxindoles in water. *ACS Combinatorial Science*, 15(10), pp.530-534.

[6] Deraz, N.M., 2010. Size and crystallinity-dependent magnetic properties of copper ferrite nano-particles. *Journal of Alloys and Compounds*, 501(2), pp.317-325.

[7] Kuznetsov, M.V., Morozov, Y.G. and Belousova, O.V., 2013. Synthesis of copper ferrite nanoparticles. *Inorganic Materials*, 49(6), pp.606-615.

[8] Stoia, M., Barvinschi, P. and Barbu-Tudoran, L., 2013. Thermal decomposition of metal nitrates. *Journal of Thermal Aanalysis and Calorimetry*, 113(1), pp.21-30.

[9] Salavati-Niasari, M., Mahmoudi, T., Sabet, M., Hosseinpour-Mashkani, S.M., Soofivand, F. and Tavakoli, F., 2012. Synthesis and characterisation of copper ferrite nanocrystals via coprecipitation. *Journal of Cluster Science*, 23(4), pp.1003-1010.

[10] Tang, Z.X., Sorensen, C.M., Klabunde, K.J. and Hadjipanayis, G.C., 1991. Size-dependent Curie temperature in nanoscale $MnFe_2O_4$ particles. *Physical Review Letters*, 67(25), p.3602.

[11] Carta, D., Casula, M.F., Falqui, A., Loche, D., Mountjoy, G., Sangregorio, C. and Corrias, A., 2009. A structural and magnetic investigation of the inversion degree in ferrite nanocrystals MFe_2O_4 (M= Mn, Co, Ni). *The Journal of Physical Chemistry C*, 113(20), pp.8606-8615.

[12] Loche, D., Casula, M.F., Falqui, A., Marras, S. and Corrias, A., 2010. Preparation of Mn, Ni, Co ferrite highly porous silica nanocomposite aerogels by an urea-assisted sol–gel procedure. *Journal of Nanoscience and Nanotechnology*, 10(2), pp.1008-1016.

[13] Gomes, J.A., Sousa, M.H., Tourinho, F.A., Mestnik-Filho, J., Itri, R. and Depeyrot, J., 2005. Rietveld structure refinement of the cation distribution in ferrite fine particles studied by X-ray powder diffraction. *Journal of Magnetism and Magnetic Materials*, 289, pp.184-187.

[14] Darul, J., 2009. Thermal instability of the tetragonally distorted structure of copper-iron materials. *Zeitschrift für Kristallographie*, 30, pp.335-340.

[15] Xing, Z., Ju, Z., Yang, J., Xu, H. and Qian, Y., 2013. One-step solid state reaction to selectively fabricate cubic and tetragonal $CuFe_2O_4$ anode material for high power lithium ion batteries. *Electrochimica Acta*, 102, pp.51-57.

[16] Tasca, J.E., Quincoces, C.E., Lavat, A., Alvarez, A.M. and González, M.G., 2011. Preparation and characterisation of $CuFe_2O_4$ bulk catalysts. *Ceramics International*, 37(3), pp.803-812.

[17] PDF card, reference code: 00-034-0425; Prince, E., Treuting, R.G., 1956, *Acta Crystallographica*, 9(12), pp.1025-1028

[18] PDF card, reference code: 00-005-0661; Asbrink, S., Norrby, L., 1970, *Acta Crystallographica*, B(26), pp.8-15

[19] PDF card, reference code: 01-077-0010; Verwey, E. J. W., Heilmann, E. L., 1947, *Journal of Chemical Physics*, 15(4), pp.174-180

[20] Barrett, E.P., Joyner, L.G. and Halenda, P.P., 1951. The determination of pore volume and area distributions in porous substances. I. Computations from nitrogen isotherms. *Journal of the American Chemical Society*, 73(1), pp.373-380.

[21] Krishnan, V., Selvan, R.K., Augustin, C.O., Gedanken, A. and Bertagnolli, H., 2007. EXAFS and XANES investigations of $CuFe_2O_4$ nanoparticles and $CuFe_2O_4$-MO_2 (M= Sn, Ce) nanocomposites. *The Journal of Physical Chemistry C*, 111(45), pp.16724-16733.

[22] Grunes, L.A., 1983. Study of the K edges of 3d transition metals in pure and oxide form by x-ray-absorption spectroscopy. *Physical Review B*, 27(4), pp.2111-2131.

[23] Balagurov, A.M., Bobrikov, I.A., Maschenko, M.S., Sangaa, D. and Simkin, V.G., 2013. Structural phase transition in $CuFe_2O_4$ spinel. *Crystallography reports*, 58(5), pp.710-717.

CHAPTER 4.

Growth of CeO_2 nanocrystals within silica aerogel and xerogel matrix: synthesis and characterisation

In this chapter, the synthesis and characterisation of new CeO_2-SiO_2 nanocomposites in form of aerogel and xerogel will be discussed. CeO_2 (ceria) nanocrystals are grown within the amorphous silica matrix by using cerium (III) nitrate as a precursor of the ceria nanophase during the sol-gel process. Capping agents are used during this synthesis in order to facilitate the formation of ceria nanoparticles with dimension < 10 nm. Sets of aerogel and xerogel samples have been prepared, changing the capping agent and its concentration. In the case of the aerogel, the ceria nanophase starts to crystallise during the supercritical drying. Aerogel and xerogel samples are treated at 450 ºC and 900 ºC for 1h. The characterisation of the samples has been done by the use of thermogravimetric analysis coupled with differential scanning calorimetry (TGA/DSC), X-ray diffraction (XRD), transmission electron microscopy (TEM) and N_2 physisorption. The results show how the different nature of the amorphous silica texture and the presence of the capping agent influence and drive the growth of the ceria nanoparticles. Results also show that the presence of the amorphous silica matrix prevents the aggregation of the nanoparticles under thermal treatment, a common problem in the case of unsupported nanoparticles.

4.1. Introduction

In the last years, increasing attention has been given to the development of new synthetic routes for ceria nanomaterials[1]. This interest comes from the extraordinary properties exhibited by ceria-based nanomaterials in terms of reactivity[2]. Ceria acts in fact as an oxygen buffer, releasing and storing oxygen ions depending on the oxygen partial pressure of the environment, retaining the fluorite structure[3], Figure 4.1. This unique property originates from the labile and reversible redox cycle between Ce^{4+} and Ce^{3+}, generating the following equilibrium:

$$CeO_2 \rightleftharpoons (Ce^{3+}_{2x})(Ce^{4+}_{1-2x})O_{2-x} + x/2\ O_2 + xV_O^{\circ\circ}$$

Oxygen ions are released and stored through a vacancy driven mechanism[3]. This property is particularly enhanced at the nanoscale, and it is a function of size and shape, leading to the need of a careful rationalization of the synthetic methods. Hydrothermal[4] and solvothermal[5] crystallisation, thermal decomposition[6], precipitation[7] and spray pyrolysis[8] have been successfully used to synthesise ceria nanoparticles with polyhedral[9], cuboidal[10] and spherical shapes[8], nanorods[11], nanotubes[12] and nanoceria with 3-dimensional mesoporous architecture[13].

From a catalytic point of view, ceria nanostructured materials are promising catalysts for important industrial processes like the preferential oxidation of CO[14], elimination of auto-exhaust gases[15] and low temperature water gas shift[16].

It has been demonstrated that the catalytic activity of ceria nanomaterials is strongly dependent on the number of oxygen vacancies that is formed and this is function of the shape of the nanoparticles[17]. Zhang et al.[18] demonstrated that cubic ceria

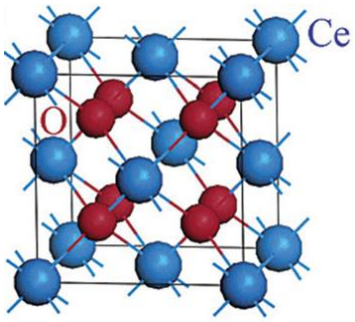

Figure 4.1 Fluorite crystal structure of CeO_2. Ce atoms: blue spheres; Oxygen atoms: red spheres. Reproduced with permission from reference [19]; [copyright © Royal Society of Chemistry]

nanoparticles show a potential enhanced catalytic activity in comparison with their polyhedral counterparts. However, one of the main problems of these materials is their thermal stability. In that work the authors show that ceria cubic nanoparticles suffer aggregation phenomena after thermal treatment at 400 ºC, leading to a decrease in the surface area and therefore in their reactivity. In this sense, if these nanoparticles have to be used in heterogeneous catalysis, new methods to obtain ceria based nanomaterials stable under thermal treatments must be found.

Silica aerogel and xerogel have been extensively studied in the past because of their extraordinary properties; these materials find application in sensors[20], thermal insulation[21], drug delivery[22], adsorption of organic pollutants[23] and heterogeneous catalysis[24].

In terms of heterogeneous catalysis, part of the research on silica aerogels and xerogels has been focused on the synthesis of nanocomposites where a reactive nanocrystalline phase, often in form of nanoparticles, is dispersed within the silica matrix. Its open and highly porous texture makes this material suitable for this application. Once the nanoparticles are dispersed within the porous matrix, they are held apart, limiting the aggregation phenomena under high temperature treatments.

Our group developed a synthetic procedure to synthesise these kinds of nanocomposites by co-gelation of both the precursor of the silica matrix and the dispersed nanophase[25]. This sol-gel procedure, detailed in Chapter 2 (section 2.1.1), is a two-step acid-base catalysed reaction, with the use of urea as a co-gelation agent; the use of urea avoids the precipitation of the metal hydroxides from the precursor of the dispersed nanophase, ensuring a good control of its homogeneity within the silica porous matrix. With this method, nanocomposites containing either metal alloy[26] or and metal oxide[27] nanoparticles within the aerogel porous matrix have been successfully synthesised reaching a high homogeneity and narrow size distribution of the dispersed nanophase.

Nanocomposites containing CeO_2 nanoparticles dispersed within the aerogel and xerogel matrix have not been yet reported in the literature. In this chapter, we show the synthesis and the characterisation of this kind of nanocomposites. In order to achieve the formation of the nanoparticles, we have used capping agents during the synthetic procedure.

4.2. Sample preparation

The samples discussed in this chapter were prepared following the synthetic method described in section 2.1.1. Briefly, an ethanolic solution (7.5 ml) of cerium nitrate pentahydrate ($Ce(NO_3)_3 \cdot 5H_2O$) and the appropriate capping agent was added to the prehydrolysed TEOS (7.9 ml) under acidic conditions. A solution containing urea (3.513 g, 9 ml of ethanol, 4.92 ml of distilled water) was then added and the resulting solution stirred under reflux (85 ºC) until it became more viscous. Gelation was then completed in a sealed cylindrical vial at 40 ºC for 24 h. Xerogel samples were then obtained by simply drying the gel in open air at 40 ºC for 72 h. Aerogels were instead obtained submitting the gel to supercritical extraction of the ethanol, as described in section 2.1.2.

A first series of samples was synthesised by using dodecanoic acid as a capping agent; the amount of ceria precursor was calculated in order to obtain a loading in CeO_2 phase of 5 wt. %, 10 wt. % and 15 wt. %, Table 2.3 (Chapter 2); the dodecanoic acid was used in 1:4 Ce^{3+}/dodecanoic acid molar ratio. A second series of samples was synthesised by using two additional Ce^{3+}/dodecanoic acid molar ratios, 1:1 and 1:8, while keeping a 5 wt. % CeO_2 loading. Lastly, a third series of sample was synthesised by changing the nature of the capping agent, using hexanoic acid. In Table 2.3 (chapter 2) the details of all the syntheses are outlined.

After the synthesis, samples were subjected to thermal treatments at 450 ºC and 900 ºC for 1 h. Samples will be named hereafter depending on the thermal treatment: as an example A15CeO_2_dod1:4_450 is used for the aerogel samples with 15 wt. % CeO_2 loading, with dodecanoic acid as capping agent in molar ratio 1:4, treated at 450 ºC for one hour. Xerogel samples are named using the letter ‘X’ in place of ‘A’ in their name.

4.3. Characterisation

4.3.1. CeO_2-SiO_2 nanocomposite without capping agent

A first attempt was made to synthesise a CeO_2-SiO_2 aerogel nanocomposite without the use of a capping agent. The two-step acid-base catalysed sol-gel synthesis was applied by using cerium nitrate as precursor for the ceria phase. In Figure 4.2, two TEM images of the nanocomposite obtained after supercritical extraction are shown, together with the corresponding XRD pattern. The TEM images show the presence of spheroidal particles with dimensions spanning from 150 nm to 500 nm on top of the highly porous silica aerogel matrix. The XRD pattern allowed us to identify the presence of cerium carbonate hydroxide[28], whose reference pattern is shown by the dashed line. The peaks appear intense and narrow on top of the superimposed contribution due to the amorphous silica. The XRD pattern also shows the presence of an additional broad and weak peak, indicated by the asterisk, due to the presence of a small amount of nanocrystalline ceria[29].

Similar ceria particles, with average diameter of 320 nm and spherical shape, synthesised in presence of urea, were already reported in the literature[30]. In that work, the authors prepared ceria nanospheres using a hydrothermal route involving urea. The authors show that the decomposition of urea, which forms CO_3^{2-} ions, play a crucial role in determining the size and shape of the ceria nanoparticles, forming a crystalline cerium (III) carbonate phase that then evolves to CeO_2 under thermal treatment. It was also shown that the decrease of the amount of urea used during the synthesis caused an increase in the particles size, up to 1 μm. The authors suggested that the ceria particles crystallise around the ammonia bubbles (due to the urea decomposition) that act as a 'structure directing agent'. By using less urea the pressure on the reaction environment is lower and ammonia forms bigger bubbles, leading to bigger particles.

In our case, the sol-gel synthesis and the supercritical extraction form a different reaction environment, but a consistent amount of urea is used. Urea decomposes during the supercritical extraction of the ethanol and a similar crystallisation mechanism can be supposed. However, no further investigation has been done on this sample since the main aim in this thesis was to obtain small particles capable of storing large amount of oxygen vacancies.

For this reason, the following attempts in synthesising CeO_2-SiO_2 aerogel or xerogel nanocomposites were done using capping agents. Surfactants are used as capping agents during the synthesis of nanoparticles either to inhibit their growth or to inhibit the growth of specific facets where they preferentially bind.

Among several classes of surfactants, fatty acids with long carbon chains, such as oleic acid[10] and hexanoic acid,[18] have shown to work well to control the growth of CeO_2 nanoparticles with controlled shape. The carboxylic acid group binds selectively the {100} surface of the crystal, stopping the crystallisation growth in that direction

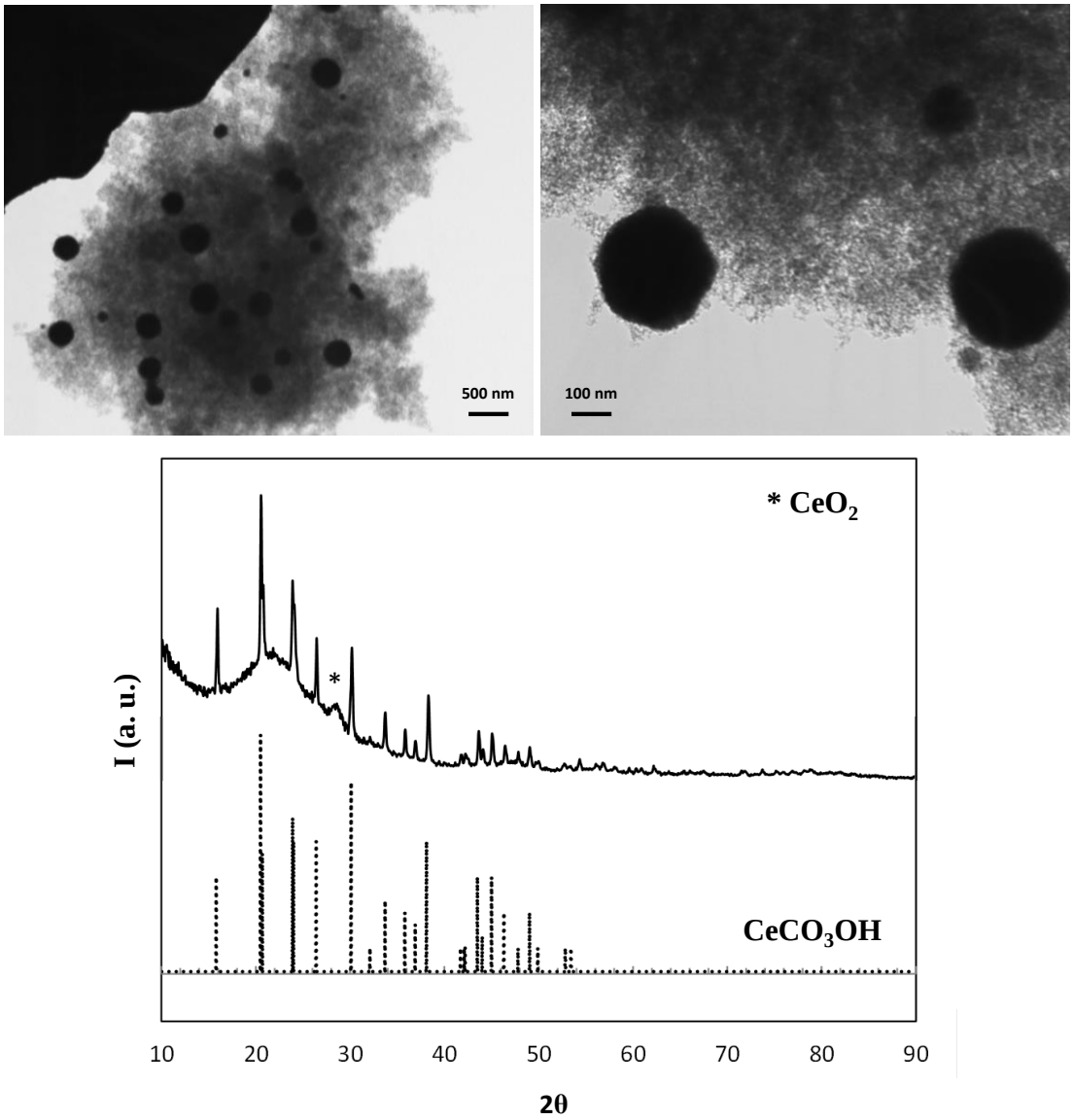

Figure 4.2 Top: two TEM images of the sample obtained by performing the sol-gel synthesis without the use of a capping agent. Bottom: XRD pattern of the sample (full line) and reference XRD pattern of $CeCO_3OH$ phase (dashed line).

In this work, the purpose of using a carboxylic acid is to limit the growth of the particles. Supposedly, the capping agent that binds to the surface of a small just formed nanoparticle avoids the particle growth by oriented attachment[31] or Ostwald ripening[32]. Results are discussed in the next sections.

4.3.2. CeO_2-SiO_2 nanocomposites with Ce^{3+}/dodecanoic acid 1:4

In this section, the characterisation of the CeO_2-SiO_2 nanocomposites synthesised by the use of dodecanoic acid as a capping agent in 1:4 Ce^{3+}/dodecanoic acid molar ratio will be discussed.

4.3.2.1. TGA\DSC

Figure 4.3 shows the TGA/DSC curves of the samples A15CeO_2_dod1:4 and X15CeO_2_dod1:4 The temperature range investigated was 25-800 °C with a ramp of 10 °C\min. The TGA curve in the case of the aerogel is similar to those obtained in previous studies on aerogel nanocomposites synthesised with a similar sol-gel procedure[27]. After a loss in weight of about 3% around 100 ºC due to the water absorbed on the surface, the aerogel undergo a further weight loss of about 13%. The DSC curve shows two main exothermic peaks, centred at 227 ºC and 416 °C, which are likely due to the combustion of organics. The silica matrix is partially esterified after the supercritical drying, as already mentioned in (section 1.1.3). Organic residuals from the incomplete decomposition of the dodecanoic acid might be also present; for a comparison, TGA/DSC curves of starting materials are also reported in Appendix A1. The residual mass of all aerogel samples is found to be always above 80% (Table 4.1).

The residual mass in the case of the xerogel samples has been found instead to be around 30% for all samples. This is mostly due to the presence of a consistent amount of urea, which is still present in the sample, because the gel in this case was dried at 40 °C. The DSC curve shows the presence of 4 peaks. The endothermic peak associated with the largest weight loss is centred between 220 and 230 ºC and this is due to the decomposition of urea. This can be verified by comparison with the TGA\DSC curves of pure urea, Appendix A1, Figure A1.1. TGA/DSC curves for the other nanocomposites are very similar to those shown in Figure 4.3 and are reported in Appendix A2, Figure A2.1-2.

Table 4.1 summarises the results for all the nanocomposites analysed including the mass change, temperature and heat exchange associated with each DSC peak. The same parameters are shown in Table A1.1 and A1.4-5 (Appendix A1) for the starting materials.

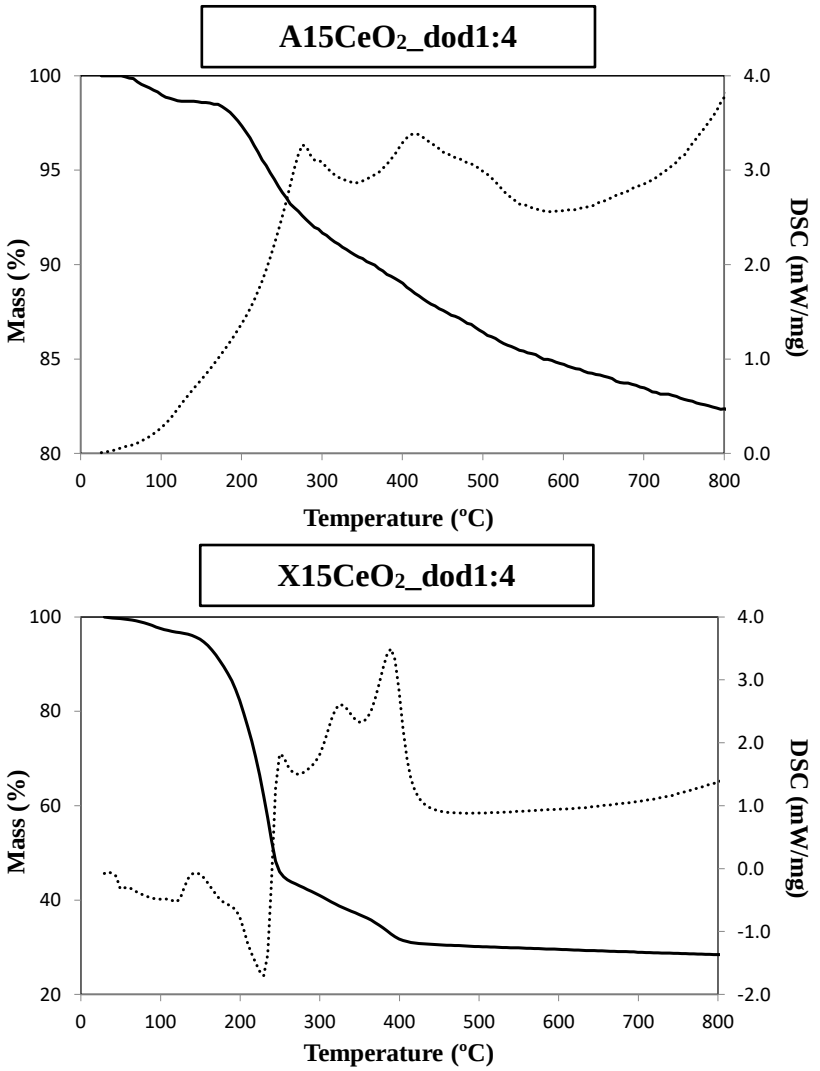

Figure 4.3 TGA\DSC curves of the 15 wt. % CeO_2-SiO_2 aerogel (top) and xerogel (bottom) nanocomposites. TGA: bold line; DSC: dots.

Table 4.1 TGA\DSC results for the aerogel and xerogel samples discussed in this section. 'exo' and 'endo' are used to indicate an exothermic or endothermic event respectively.

Sample	Peak	Mass change (%)	Temperature (°C)	Enthalpy (kJ · g^{-1})	Residual mass (%)
A15CeO_2_dod1:4	1 (exo)	8.00	227.1	- 0.42	81.38
	2 (exo)	4.65	416.0	- 0.29	
A10CeO_2_dod1:4	1 (exo)	7.33	298.5	- 0.37	81.81
	2 (exo)	6.63	420.2	- 0.57	
A5CeO_2_dod1:4	1 (exo)	5.00	289.3	- 0.24	84.07
	2 (exo)	6.14	523.8	- 0.17	
X15CeO_2_dod1:4	1 (exo)	8.00	144.0	- 0.09	28.10
	2 (endo)	41.63	229.1	+ 0.52	
	3 (exo)	5.45	326.3	- 0.11	
	4 (exo)	5.84	389.0	- 0.25	

4.3.2.2. XRD

After thermal treatments at 450 ºC and 900 ºC, all samples have been analysed by means of XRD; patterns are shown in Figure 4.4 for the A15CeO_2_dod1:4 and X15CeO_2_dod1:4 samples. The reference pattern for the ceria crystal structure is superimposed with dashed lines.[29] All patterns show the typical halo due to the amorphous silica matrix; in the case of the aerogel, the peaks due to the ceria nanocrystalline phase are already present after the supercritical extraction. The XRD peaks of the sample thermally treated at 900 ºC appear more intense and narrower, which is an indication that the mean size of the nanoparticles increases. In the case of the xerogel, the peaks due to the formation of the ceria crystalline phase appeared just after calcination at 900 ºC.

By comparing the XRD peaks of the aerogel and xerogel samples treated at 900 ºC it can be seen that the peaks of the xerogel appear much broader; this is an indication of the presence of smaller crystallites. The average dimensions of the crystallites have been then calculated using the Scherrer equation (section 2.2.2.3, eq. 2.2) and are reported in Table 4.2. In the case of the aerogel, the average dimension of the crystallites increases with the calcination temperature up to 6 nm. In the case of the xerogel, an average size of 2 nm has been determined for the sample treated at 900 ºC.

We also note a decrease of the average crystal size of the dispersed nanophase with the decrease of the ceria loading in the aerogel, down to 5 nm in the case of the 5 wt. % CeO_2-SiO_2 nanocomposite. Typical errors on the determination of the average crystal size are ± 1 nm. XRD patterns of the aerogel samples with 10 wt. % and 5 wt. % ceria loading are reported in Appendix A2, Figure A2.3-4.

Table 4.2 Average crystallite size calculated using the Scherrer equation for all samples analysed in this section.

Sample	Peak pos. [º2θ]	Crystallite size [nm]
A15CeO_2_dod1:4_NT	47.26	3
A15CeO_2_dod1:4_450	47.47	4
A15CeO_2_dod1:4_900	47.45	6
X15CeO_2_dod1:4_450	no peaks	/
X15CeO_2_dod1:4_900	47.26	2
A10CeO_2_dod1:4_NT	47.26	3
A10CeO_2_dod1:4_450	47.43	4
A10CeO_2_dod1:4_900	47.47	5
A5CeO_2_dod1:4_NT	47.18	3
A5CeO_2_dod1:4_450	47.49	4
A5CeO_2_dod1:4_900	47.47	5

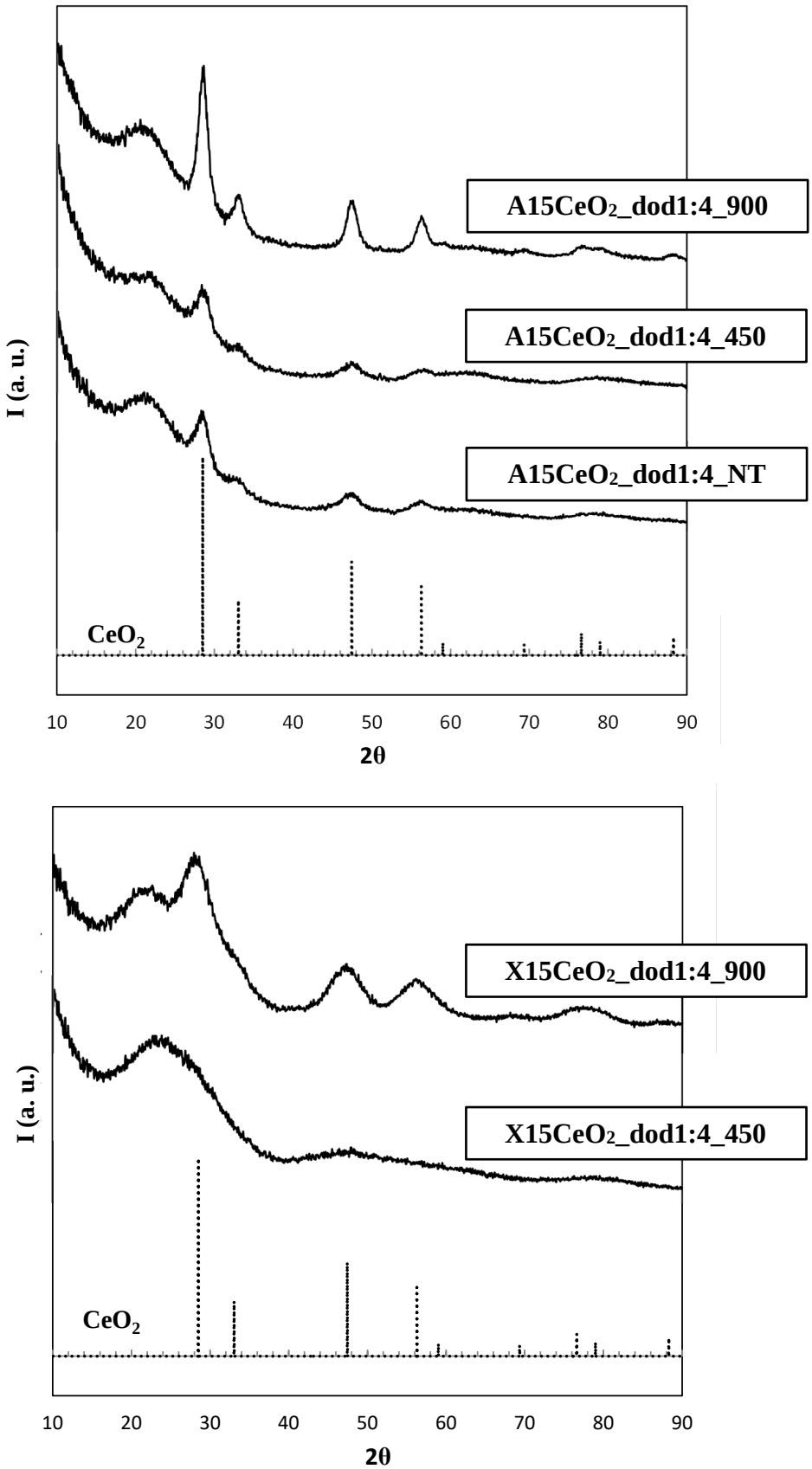

Figure 4.4 XRD patterns of the 15 wt. % CeO_2-SiO_2 aerogel (top) and xerogel (bottom) nanocomposites synthesised using dodecanoic acid in 1:4 Ce^{3+}/acid molar ratio after thermal treatments at 450 ºC and 900 ºC. The XRD pattern of the CeO_2 cubic crystal structure is reported with dashed lines.

4.3.2.3. TEM

In Figure 4.5, TEM images of the A10CeO_2_dod1:4 sample, after the supercritical extraction of the ethanol, are reported. As pointed out by the XRD patterns, the nanocrystalline ceria phase has already formed after the supercritical extraction and it can be seen as darker regions on top of the silica aerogel, in the bright field image shown in Figure 4.5(a). The aerogel appears as less dark and highly porous. The nanocrystalline ceria phase can be seen also in the dark field TEM image, Figure 4.5(b), where it appears as white spots on top of the darker amorphous silica phase. By close inspection of the TEM images, we note that the nanoparticles are organised in specific regions within the silica matrix, forming 'aggregates', rather than being homogeneously dispersed. One of these aggregates is highlighted by a black square in Figure 4.5(c) and enlarged in Figure 4.5(d). Although the nanoparticles seem to be organised in aggregates, they appear separate within each aggregate and not form a single large particle. This is probably due to the effect of the capping agent, which avoided the formation of big particles.

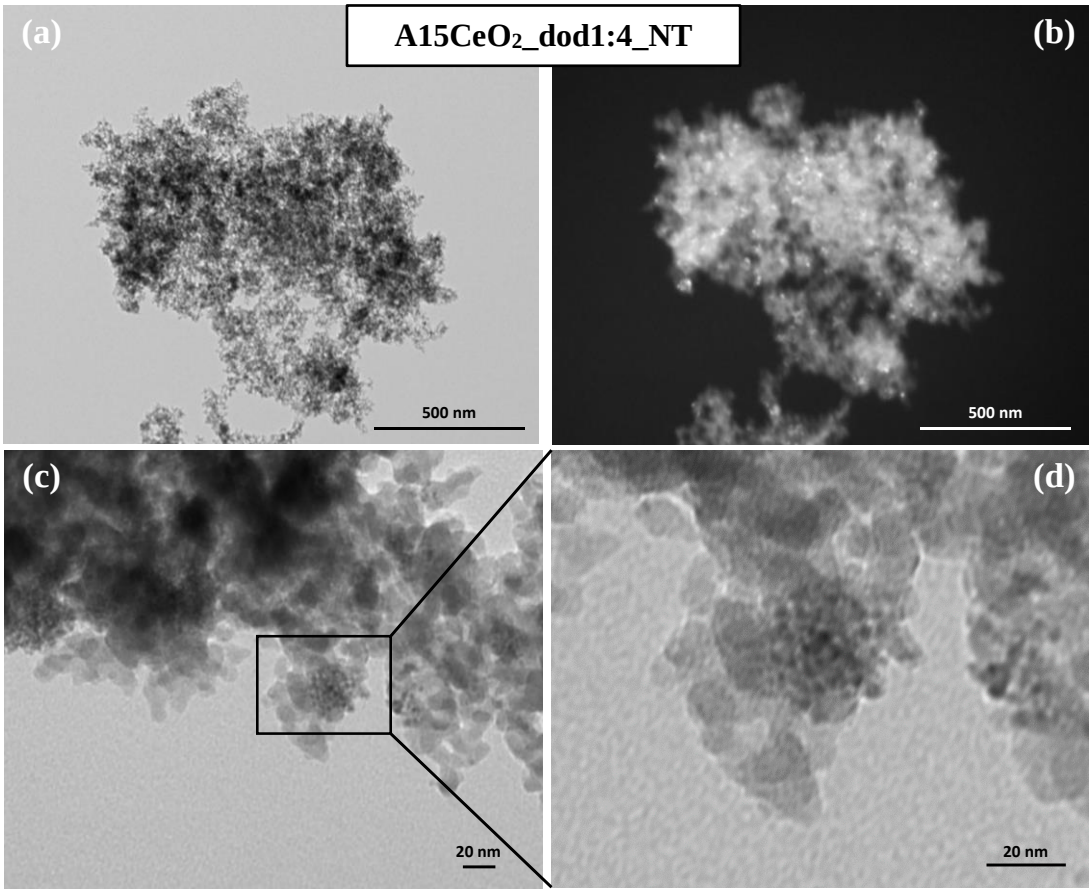

Figure 4.5 TEM images of the 15 wt. % CeO_2-SiO_2 aerogel; (a) bright field and (b) dark field images at low magnification showing the distribution of the CeO_2 nanocrystalline phase within the silica matrix; (c) and (d) high magnification TEM images of the same sample.

The same microstructural features have been observed after thermal treatment at 450 °C for 1 h. In the TEM images reported in Figure 4.6, we still note the presence of aggregates of ceria nanoparticles on top of the highly porous silica aerogel matrix. The nanoparticles present in the aggregates appear as white spots in the dark field image, Figure 4.6(b). Figure 4.6(c) and Figure 4.6(d) report two images at higher magnification corresponding to the two regions highlighted by the two squares in Figure 4.6(a).

TEM images of the sample treated at 900 °C are also reported in Figure 4.7. In this case, from the bright field and dark field images it can be seen that the nanoparticles appear much better distributed within the matrix, with absence of the aggregates previously seen. In this case, the high temperature of the thermal treatment might promote the migration through diffusion of the nanoparticles within the silica matrix.

TEM images of the corresponding xerogel samples are reported in Figure 4.8 and Figure 4.9. The slow evaporation of the solvent causes the collapse of the fine porous

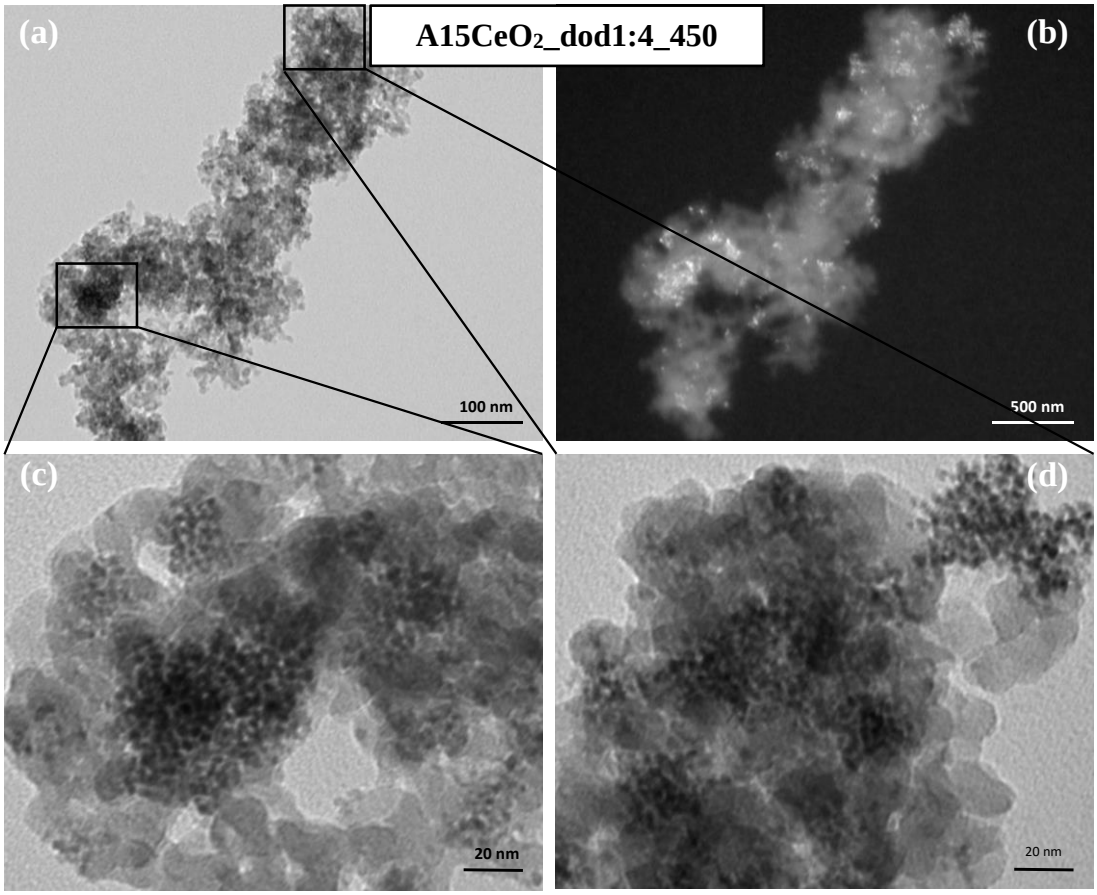

Figure 4.6 TEM images of the 15 wt. % CeO_2-SiO_2 aerogel after thermal treatment at 450 ºC; (a): low magnification bright field image and (b) dark field image showing the distribution of the ceria nanocrystalline phase within the silica matrix; (c) and (d) high magnification bright field images showing the ceria aggregates.

structure of the gel and the resulting material appears much denser; this can be clearly appreciated in the TEM bright field images. Figure 4.8 show the sample after thermal treatment at 450 ºC. By looking at the images, it is not possible to distinguish the nanocrystalline ceria phase from the amorphous silica matrix. Nanoparticles, that are possibly present, are likely to be very small and therefore difficult to visualise due to the presence of the silica xerogel matrix that causes a poor contrast.

However, after thermal treatment at 900 ºC the formation of the ceria crystalline phase can be appreciated in the TEM images in Figure 4.9. Figure 4.9(b) represent a dark field image of the sample and the presence of bright spots corresponds to the ceria nanophase, which is visible in the thinner regions on the edges of the particles. By looking at higher magnifications in Figure 4.9(c-f), focusing on the regions were the sample is thinner, it can be clearly appreciated, in bright field mode, the presence of the ceria nanoparticles, as darker regions on top of the silica amorphous matrix. In this

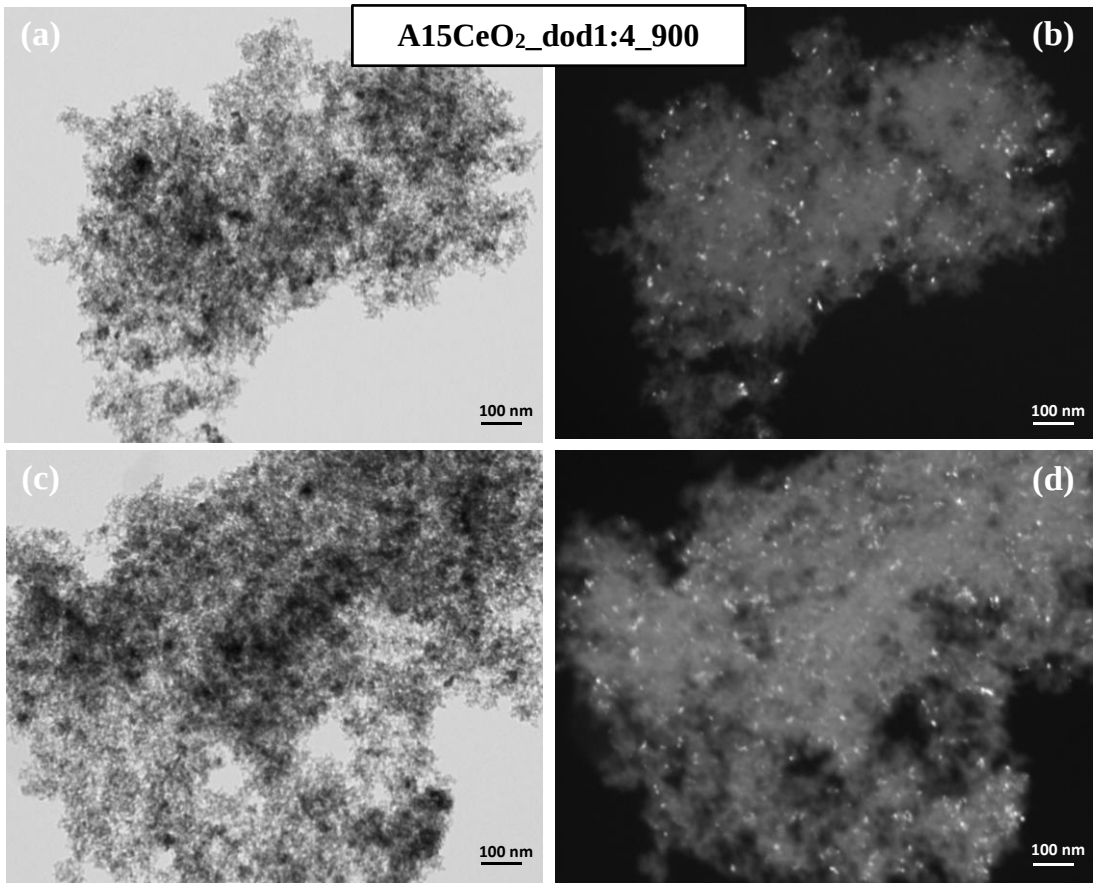

Figure 4.7 TEM images of the 15 wt. % CeO_2-SiO_2 aerogel after thermal treatment at 900 ºC. (a) and (c): bright field images; (b) and (d) dark field images showing the distribution of the ceria nanocrystalline phase within the silica matrix.

case, the nanoparticles are not organised in aggregates, such as in the aerogel, instead they are rather homogeneously dispersed within the silica matrix.

From the dark field images, it was possible to determine the average size of the nanoparticles. In the case of the aerogel samples, the nanoparticles grow up to 7 nm after thermal treatment at 900 ºC while for the xerogel samples the growth of the nanoparticles was limited to 5 nm; results are summarised in Table 4.3. Due to the poor contrast caused by the presence of the silica matrix in the background, the error affecting these measurements is at least ± 1 nm.

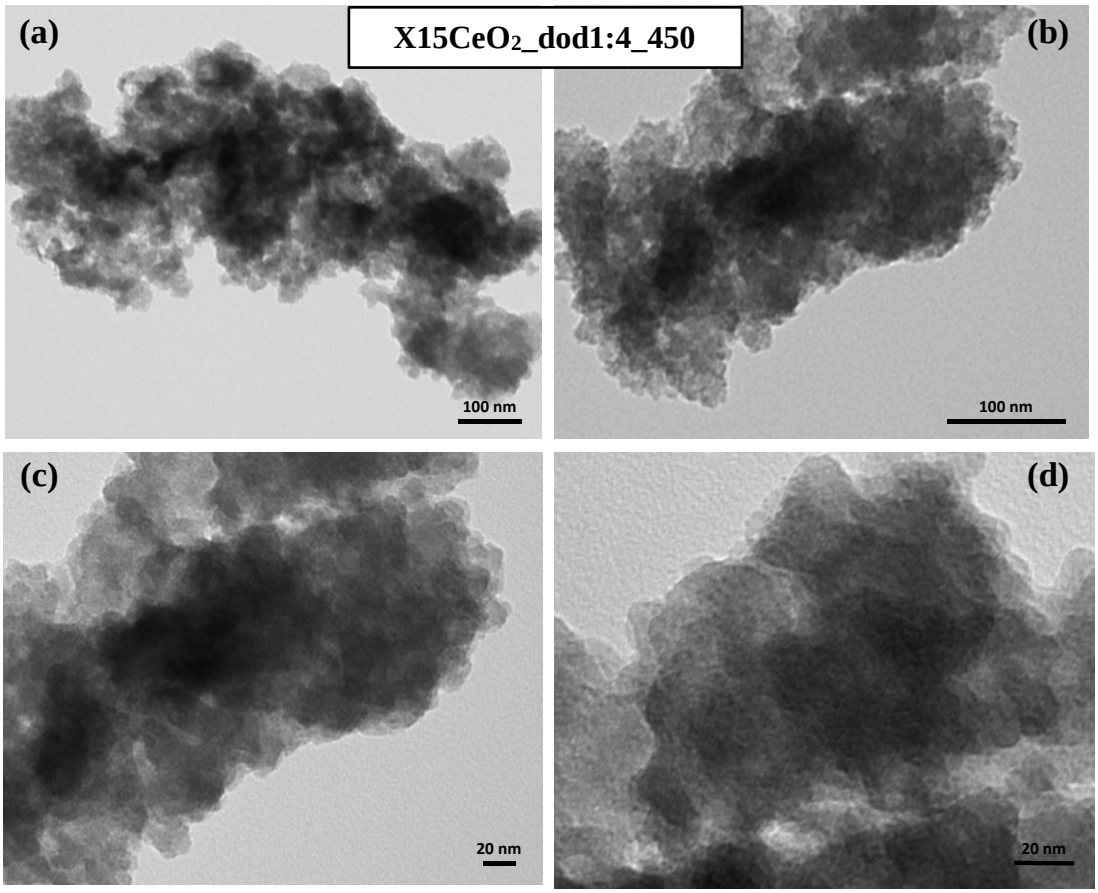

Figure 4.8 TEM images of the 15 wt. % CeO_2-SiO_2 xerogel after thermal treatment at 450 ºC; (a) and (b): low magnification; (c) and (d) high magnification; all images are in bright field mode.

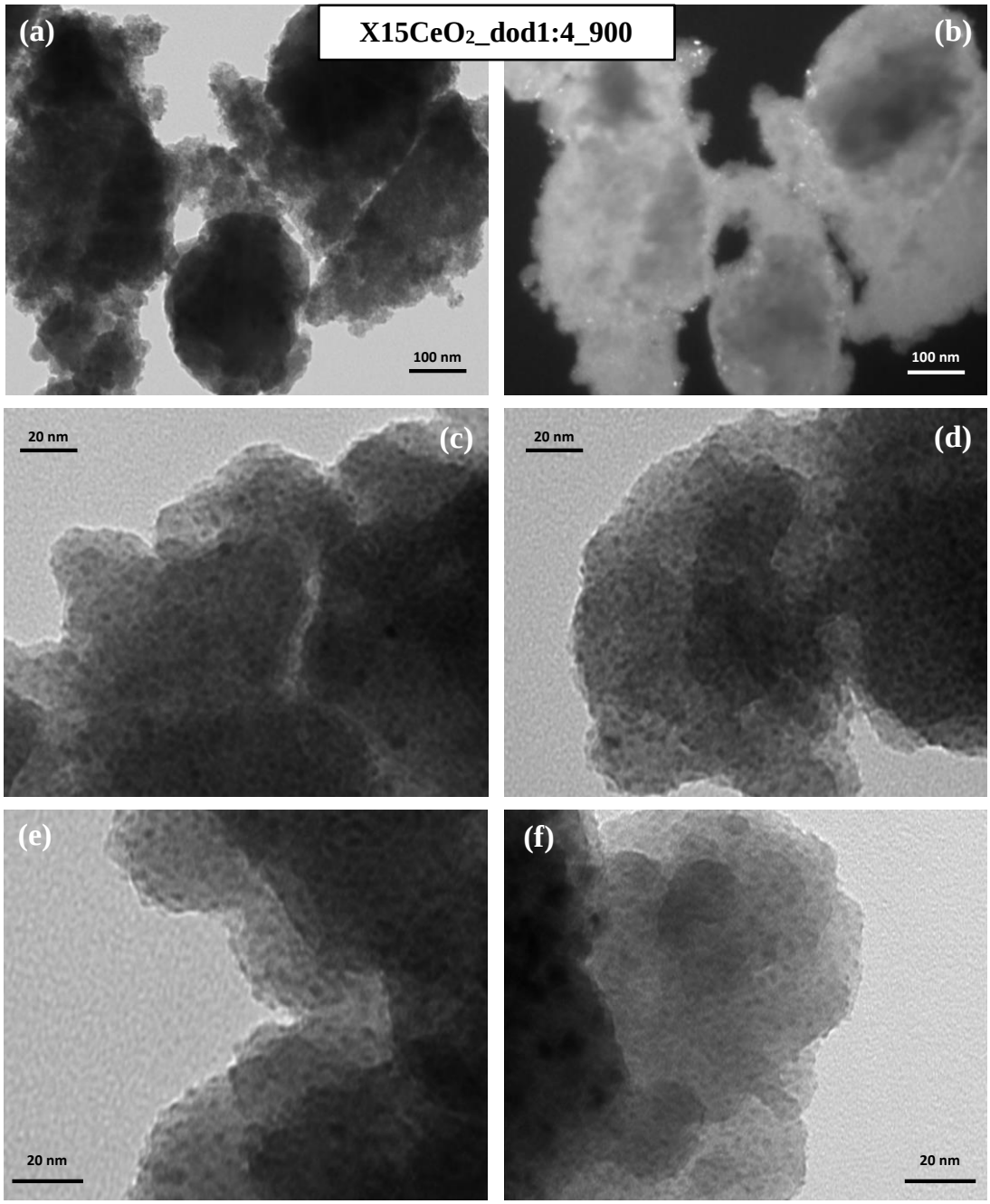

Figure 4.9 TEM images of the 15 wt. % CeO_2-SiO_2 xerogel after thermal treatment at 900 ºC; (a): low magnification bright field image and (b): low magnification dark field image. (c) – (f): high magnification bright field images showing the distribution of the ceria nanocrystalline phase within the silica xerogel matrix.

In the case of the aerogel samples, the average sizes of the nanoparticles determined by TEM are in line with the values found from the XRD patterns. In the case of the xerogel, an average size of 5 nm has been found using the TEM images, which is quite larger than the value of 2 nm determined from the XRD patterns. This discrepancy might be due to the presence of a large amount of small particles that are not visible in the dark field TEM images.

Samples with 10 wt. % and 5 wt. % ceria loading have been also analysed by TEM (see Figure 4.10) after the supercritical extraction of the solvent. The TEM analysis shows the same features observed on the aerogel samples shown above. Nanoparticles crystallise in specific regions within the silica aerogel matrix after the supercritical extraction of the ethanol.

Table 4.3 Average size of the nanoparticles obtained by analysing the dark field TEM images.

Sample	Size nanoparticles (nm)
A15CeO_2_dod1:4_NT	5
A15CeO_2_dod1:4_450	5
A15CeO_2_dod1:4_900	7
X15CeO_2_dod1:4_450	/
X15CeO_2_dod1:4_900	5

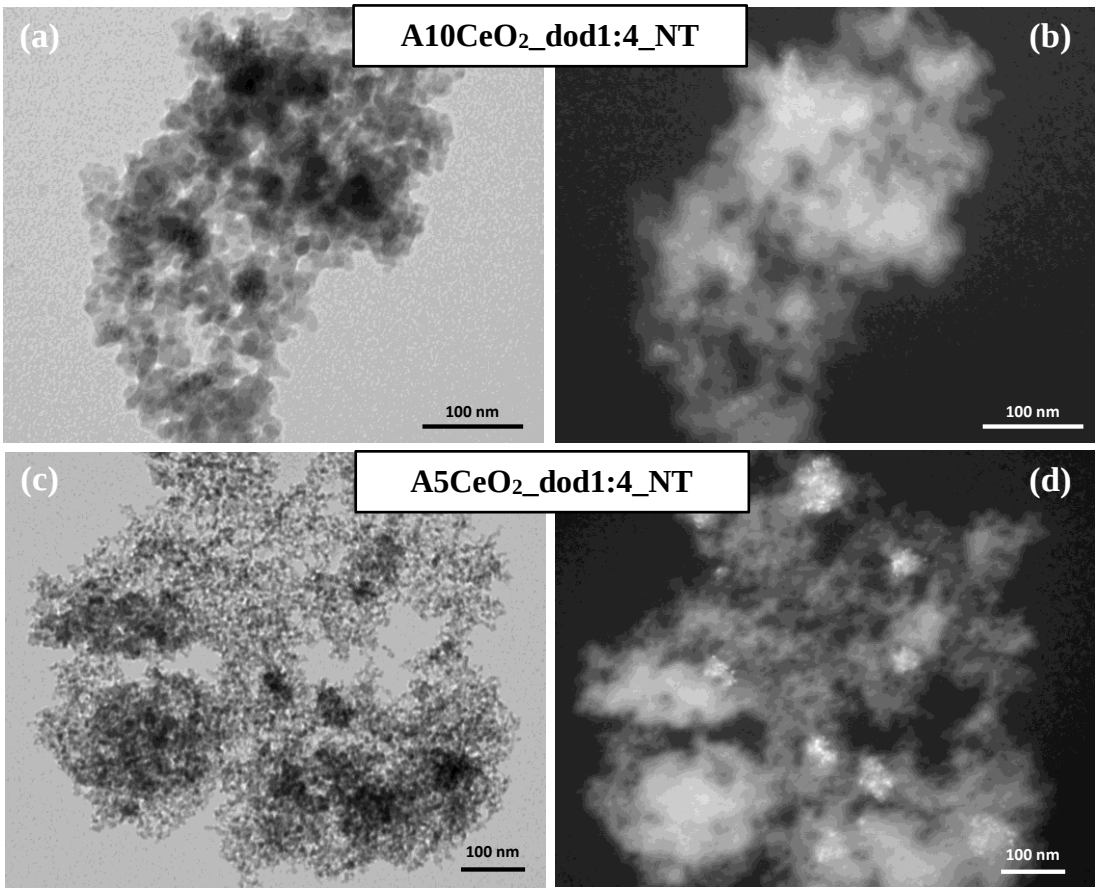

Figure 4.10 TEM images of the 10 wt. % (top) and 5 wt. % (bottom) CeO_2-SiO_2 aerogel nanocomposite after supercritical extraction; (a) and (c) bright field mode; (b) and (d) dark field mode.

4.3.2.4. N_2-physisorption

The morphological characterisation of the aerogel and xerogel samples is completed by means of N_2-physisorption measurements. The samples were analysed after the thermal treatment at 900 ºC; in Figure 4.11, the isotherms of the samples A15CeO_2_dod1:4_900 (top) and X15CeO_2_dod1:4_900 (bottom) are reported. The effect of the drying conditions on the texture of the silica matrix is highlighted by the shape of the isotherms: in particular, the pronounced adsorption at relative high partial pressures indicates, in the case of the aerogel, the presence of a highly interconnected inner surface and extended mesoporosity. In the case of the xerogel, the isotherm shows a consistent adsorption at lower partial pressures, which is indicative of microporosity. Both isotherms can be classified as type IV with a H3-type hysteresis loop in the case of the aerogel and a H2(b)-type loop in the case of the xerogel. The insets in the picture report the pore size distributions, obtained by the BJH method.[33] In Table 4.4, the values of the surface area S, calculated by the BET method, the total pore volume V_P and the average pore diameter are reported for all the samples. In the case of the aerogels, the values of surface area and pore diameter are in agreement with previous studies on similar aerogel nanocomposites synthesised with the same sol-gel procedure[26]. The value of 20 nm for the average pore size indicates that the aerogels are mainly mesoporous, as expected. In the case of the xerogel, a much lower value for the pore diameter has been found, which confirms its microporosity. The isotherms of the aerogel samples with a 10 wt. % and 5 wt. % CeO_2 loading (samples A10CeO_2_dod1:4_900 and A5CeO_2_dod1:4_900) are very similar to the one reported for the sample with a 15% CeO_2 loading and are reported in Appendix A2, Figure A2.11

Table 4.4 Surface area, S, pore volume, V_P, and pore diameter values for the aerogel and xerogel nanocomposites obtained by N_2-physisorption.

Sample	S ($m^2 \cdot g^{-1}$)	V_P ($cm^3 \cdot g^{-1}$)	Pore diameter (nm)
A15CeO_2_dod1:4_900	358.4 ± 0.7	0.86	21
X15CeO_2_dod1:4_900	394.0 ± 0.9	0.28	4
A10CeO_2_dod1:4_900	338.9 ± 0.2	0.76	21
A5CeO_2_dod1:4_900	412.5 ± 1.2	0.89	20

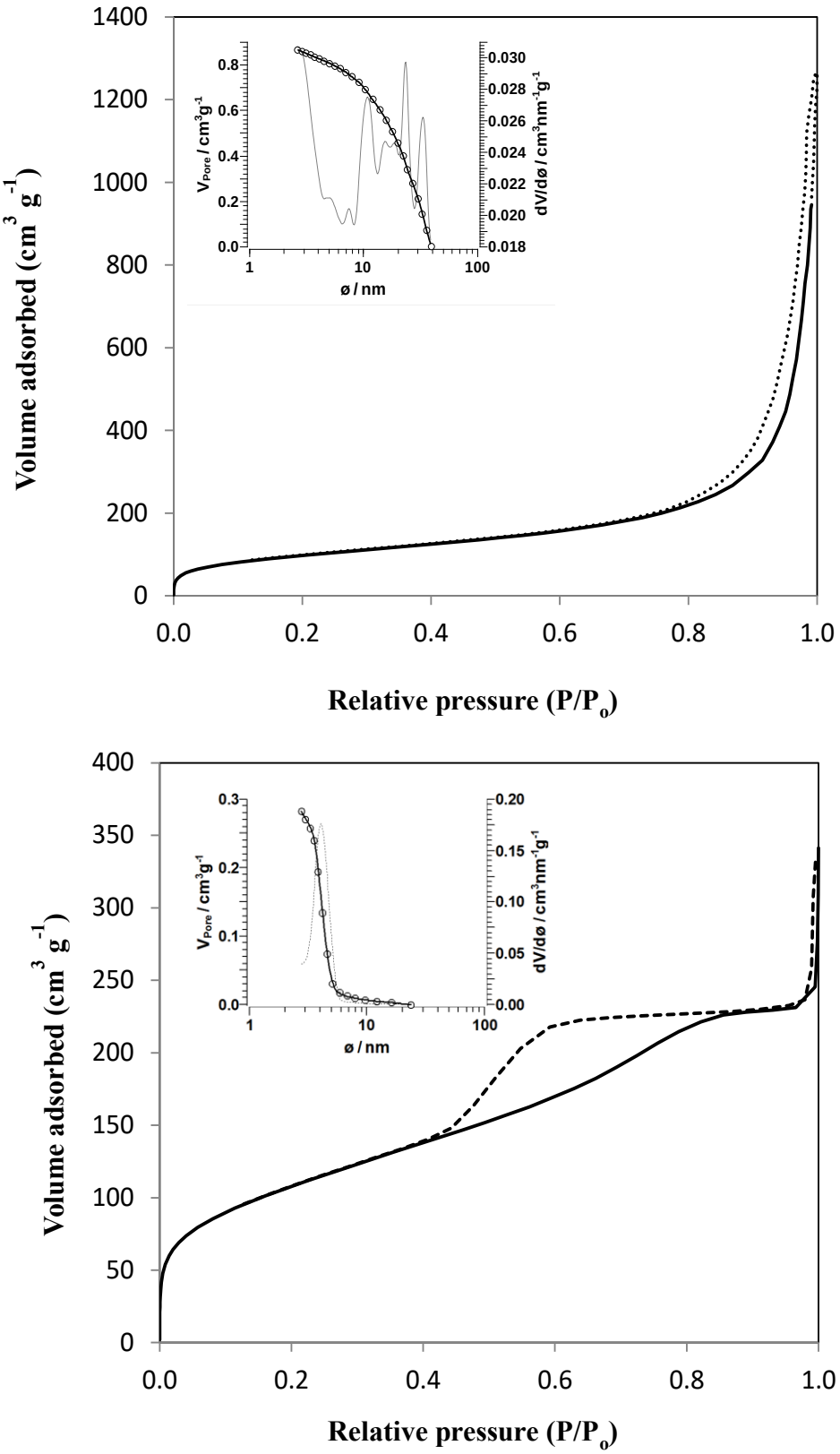

Figure 4.11 N_2-physisorption isotherms of the sample A15CeO_2_dod1:4_900 (top) and X15CeO_2_dod1:4_900 (bottom) and pore size distribution calculated using the desorption branch (inset).

4.3.3. CeO_2-SiO_2 nanocomposites with Ce^{3+}/dodecanoic acid 1:1 and 1:8

The effect of the relative amount of capping agent used has also been studied. In this section, aerogel samples using a 1:1 and 1:8 molar ratios with a 5 wt. % CeO_2 loading are discussed and compared with the samples shown above.

Figure 4.12 shows TEM images of the sample obtained using a 1:1 molar ratio, while Figure 4.13 shows the sample obtained using a 1:8 molar ratio. The samples appear to be very similar to those presented previously, showing the CeO_2 nanoparticles crystallising in specific regions of the silica aerogel matrix, forming 'aggregates'. By looking at the TEM images, it seems that the different Ce^{3+}/dodecanoic acid molar ratios used do not cause any influence in terms of growth of the crystalline ceria phase and of the silica matrix.

TGA/DSC, XRD and N_2-physisorption characterisation of these samples are similar to those already showed for the previous ones and are reported in Appendix A2.

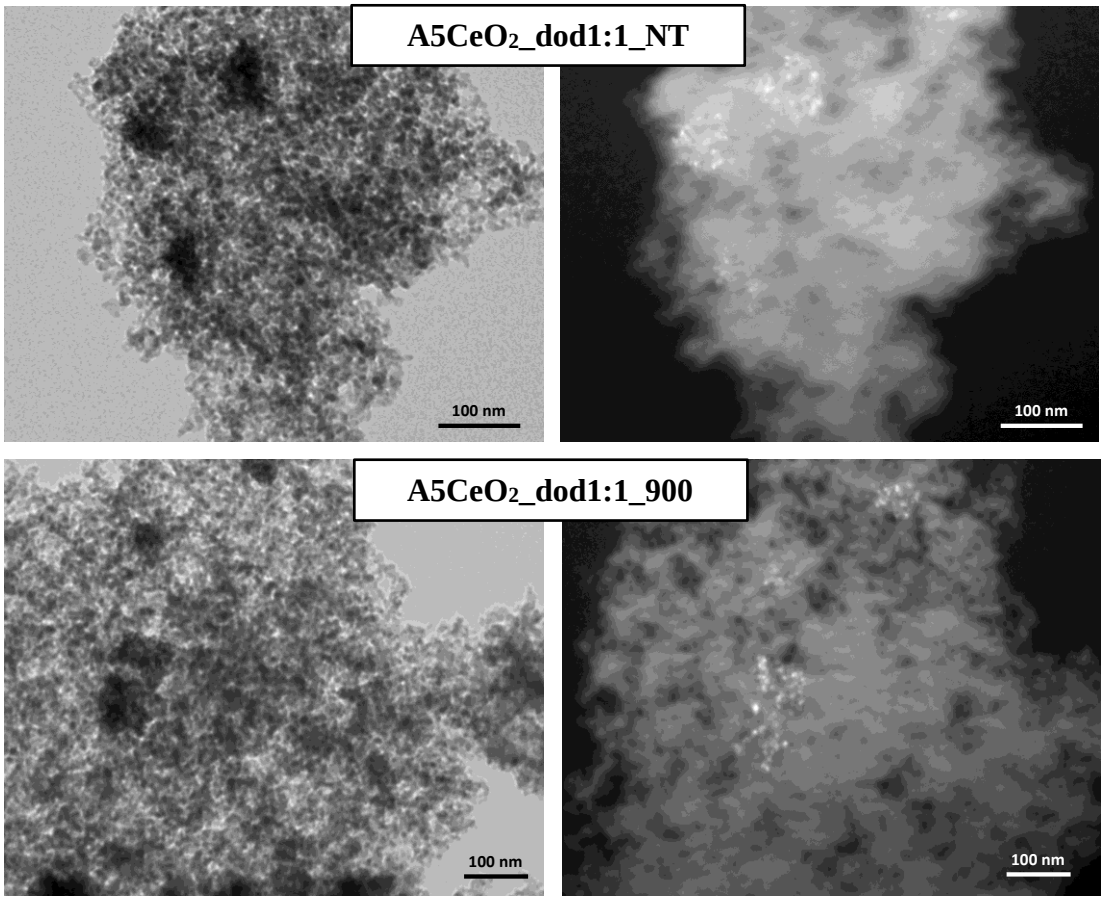

Figure 4.12 TEM images of the sample obtained using a 1:1 Ce^{3+}/dodecanoic acid molar ratio after supercritical extraction (top) and after thermal treatment at 900 ºC (bottom). Left: bright field mode; right: dark field mode.

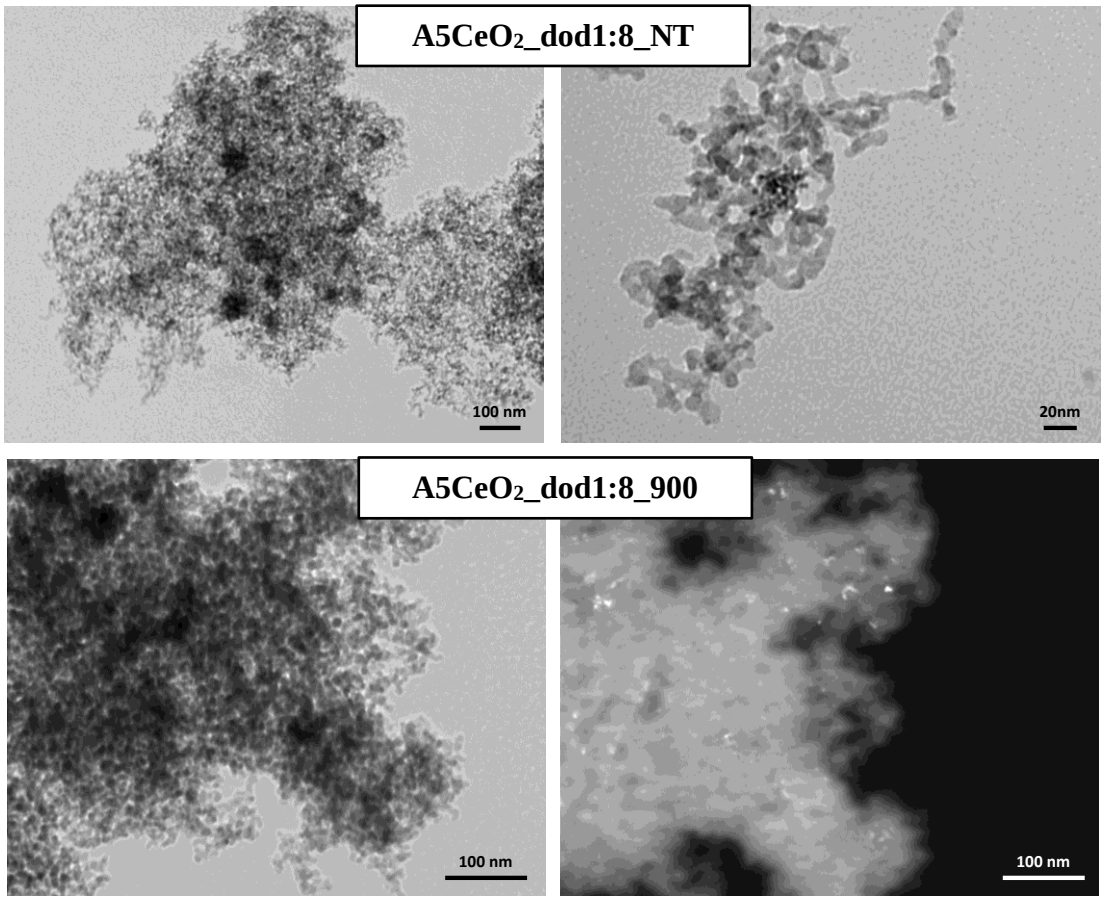

Figure 4.13 TEM images of the sample obtained using a 1:8 Ce^{3+}/dodecanoic acid molar ratio after supercritical extraction (top) and after thermal treatment at 900 ºC (bottom).

4.3.4. CeO_2-SiO_2 nanocomposites with hexanoic acid as a capping agent

Changing the capping agent did not bring any significant difference compared to what we have seen so far with previous samples. Figure 4.14 shows TEM images of the aerogel nanocomposite after supercritical extraction of the solvent (Figure 4.14(a-b)), and after thermal treatments at 450 ºC (Figure 4.14(c-d)) and 900 ºC (Figure 4.14(e-f)). The images show the same microstructural features already observed for the samples obtained using dodecanoic acid. Figure 4.14(a) shows a low magnification image of the sample obtained after supercritical extraction where we can see the distribution of the aggregates of nanoparticles within the silica aerogel matrix. Figure 4.14(b) shows an image of one of these aggregates at higher magnification where the single nanoparticles can be easily distinguished. The same is observed for the sample treated at 450 ºC, Figure 4.14(c-d). In Figure 4.14(e) and (f) two low magnification images in bright field and dark field respectively are shown, where the distribution of the ceria nanocrystalline phase within the matrix can be appreciated.

The rest of the results on these nanocomposites, which includes TGA/DSC, XRD and N_2-physisorption measurements, is reported in Appendix 2A. TGA\DSC measurements are reported in Figure A2.5 and Table A2.5 and are similar to those already shown for the other aerogel samples. The XRD patterns are reported in Figure A2.9 and the average crystalline size in Table A2.6. The nanoparticles grow up to 5 nm in size; however, it must be always taken into account that the error associated with these results is estimated to be around ± 1 nm. The N_2-physisorption measurement is shown in Figure A2.12, performed on the sample treated at 900 ºC. Values of surface area and pore diameter are reported in Table A2.7 and are in line with the values expected for these samples.

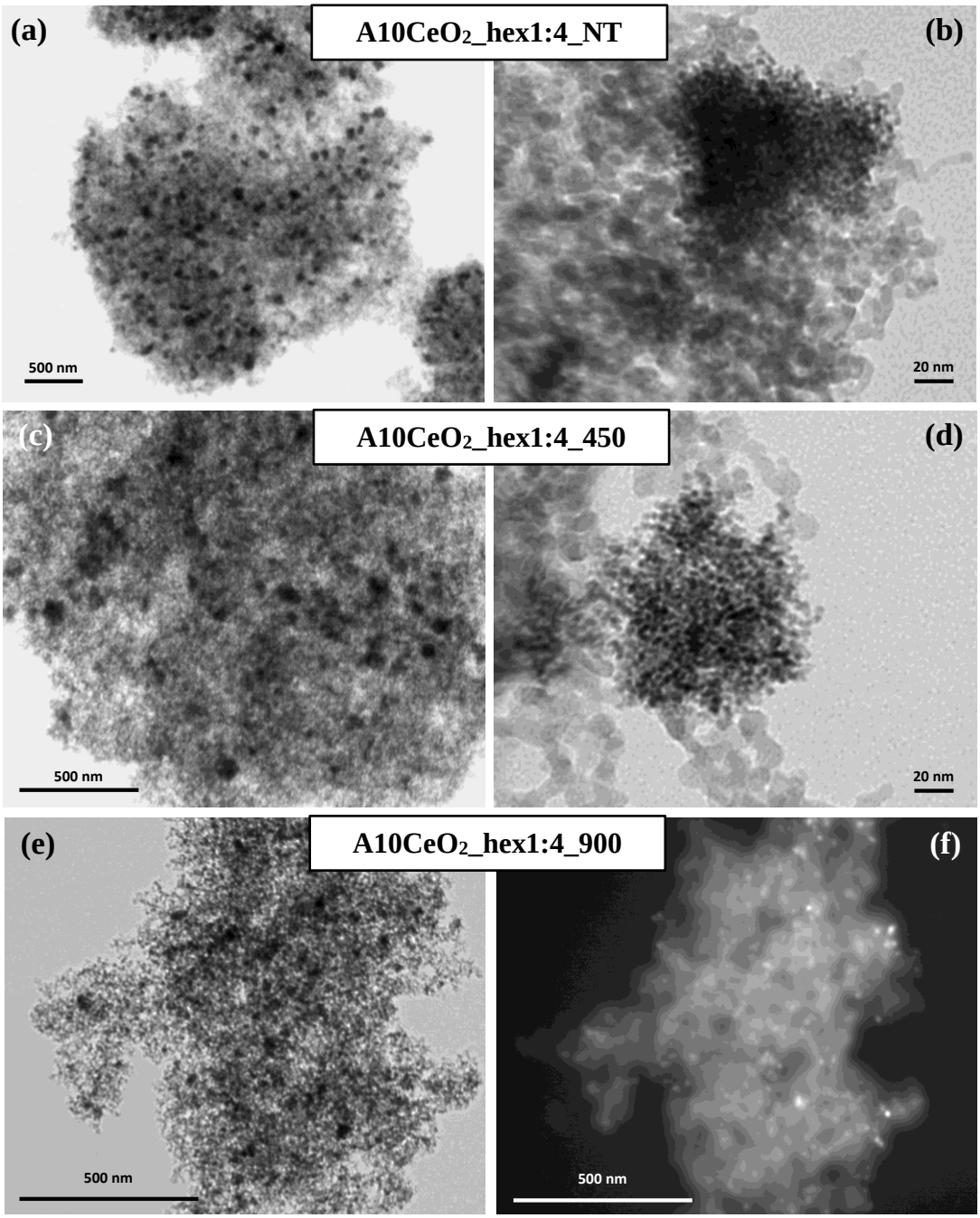

Figure 4.14 TEM images of the sampe A10CeO_2_hex1:4; (a) and (b) as synthesised; (c) and (d) after thermal treatment at 450 ºC; (e) and (f) after thermal treatment at 900 ºC; (a-e) bright field mode; (f) dark field mode.

4.4. Discussion and conclusions

The crystallisation of the ceria nanocrystalline phase is driven by the microstructural features of the silica matrix and the presence of the capping agent. N_2-physisorption measurements indicate an average pore size of 20 nm in the case of the aerogel and 4 nm in the case of the xerogel. Because the crystallisation of ceria is confined within the pores of the silica matrix, the difference in porosity between aerogel and xerogel leads to a different organisation of the ceria nanophase. It must be also taken into account that in the case of the aerogel the crystallisation of the dispersed nanophase occurs during the supercritical extraction. As it will be shown in Chapter 5, the dodecanoic acid might undergo a thermal decomposition already at 180 ºC, a much lower temperature compared with the one reached during the supercritical extraction. The thermal decomposition of the dodecanoic acid might promote the crystallisation of the nanoparticles, particularly in the regions within the largest pores. Surprisingly, the nanoparticles are found to be well distributed after thermal treatment at 900 ºC. In this case, the high temperature might promote the migration of the nanoparticles and their rearrangement within the matrix.

In the case of the xerogel, the crystallisation of ceria is confined within its mostly microporous texture. After thermal treatment at 900 ºC, the nanoparticles appear then homogeneously distributed within the matrix with no presence of regions with aggregates.

The use of the carboxylic acid as a capping agent plays an important role during the synthesis, avoiding the formation of ceria particles with diameters in the order of micrometres. We also note that the formation of the silica matrix, in both the aerogel and xerogel samples, is not affected by the presence of the carboxylic acid used during the synthesis; the values of surface area and the average pore size for all aerogel and xerogel samples are in line with previous findings[27]. However, the difference in concentration and nature of capping agent seems not to have any relevant effect on the resulting nanocomposite.

The nanocomposites are stable up to high temperature thermal treatments such as at 900 °C for one hour; this feature is very important for a possible use of these nanocomposites in heterogeneous catalysis. The nanoparticles do not show any

aggregation (sintering) to form big particles; this is instead very common in the case of unsupported nanoparticles, as it will be shown in Chapter 5.

4.5. References

[1] Sun, C., Li, H. and Chen, L., 2012. Nanostructured ceria-based materials: synthesis, properties, and applications. *Energy & Environmental Science*, 5(9), pp.8475-8505.

[2] Ta, N., Liu, J. and Shen, W., 2013. Tuning the shape of ceria nanomaterials for catalytic applications. *Chinese Journal of Catalysis*, 34(5), pp.838-850.

[3] Mamontov, E., Egami, T., Brezny, R., Koranne, M. and Tyagi, S., 2000. Lattice defects and oxygen storage capacity of nanocrystalline ceria and ceria-zirconia. *The Journal of Physical Chemistry B*, 104(47), pp.11110-11116.

[4] Taniguchi, T., Katsumata, K.I., Omata, S., Okada, K. and Matsushita, N., 2011. Tuning growth modes of ceria-based nanocubes by a hydrothermal method. *Crystal Growth & Design*, 11(9), pp.3754-3760.

[5] Qian, L., Zhu, J., Du, W. and Qian, X., 2009. Solvothermal synthesis, electrochemical and photocatalytic properties of monodispersed CeO_2 nanocubes. *Materials Chemistry and Physics*, 115(2), pp.835-840.

[6] Kamruddin, M., Ajikumar, P.K., Nithya, R., Tyagi, A.K. and Raj, B., 2004. Synthesis of nanocrystalline ceria by thermal decomposition and soft-chemistry methods. *Scripta Materialia*, 50(4), pp.417-422.

[7] Bugayeva, N. and Robinson, J., 2007. Synthesis of hydrated CeO_2 nanowires and nanoneedles. *Materials Science and Technology*, 23(2), pp.237-241.

[8] Feng, X., Sayle, D.C., Wang, Z.L., Paras, M.S., Santora, B., Sutorik, A.C., Sayle, T.X., Yang, Y., Ding, Y., Wang, X. and Her, Y.S., 2006. Converting ceria polyhedral nanoparticles into single-crystal nanospheres. *Science*, 312(5779), pp.1504-1508.

[9] Cordeiro, M.A., Weng, W., Stroppa, D.G., Kiely, C.J. and Leite, E.R., 2013. High resolution electron microscopy study of nanocubes and polyhedral nanocrystals of cerium (IV) oxide. *Chemistry of Materials*, 25(10), pp.2028-2034.

[10] Yang, S. and Gao, L., 2006. Controlled synthesis and self-assembly of CeO_2 nanocubes. *Journal of the American Chemical Society*, 128(29), pp.9330-9331.

[11] Gao, F., Lu, Q. and Komarneni, S., 2006. Fast synthesis of cerium oxide nanoparticles and nanorods. *Journal of Nanoscience and Nanotechnology*, 6(12), pp.3812-3819.

[12] Pan, C., Zhang, D., Shi, L. and Fang, J., 2008. Template-free synthesis, controlled conversion, and CO oxidation properties of CeO_2 nanorods, nanotubes, nanowires, and nanocubes. *European Journal of Inorganic Chemistry*, 2008(15), pp.2429-2436.

[13] Deori, K., Gupta, D., Saha, B. and Deka, S., 2014. Design of 3-dimensionally self-assembled CeO_2 nanocube as a breakthrough catalyst for efficient alkylarene oxidation in water. *ACS Catalysis*, 4(9), pp.3169-3179.

[14] Deng, W., De Jesus, J., Saltsburg, H. and Flytzani-Stephanopoulos, M., 2005. Low-content gold-ceria catalysts for the water–gas shift and preferential CO oxidation reactions. *Applied Catalysis A: General*, 291(1), pp.126-135.

[15] Masui, T., Ozaki, T., Machida, K.I. and Adachi, G.Y., 2000. Preparation of ceria–zirconia sub-catalysts for automotive exhaust cleaning. *Journal of Alloys and Compounds*, 303, pp.49-55.

[16] Tabakova, T., Boccuzzi, F., Manzoli, M., Sobczak, J.W., Idakiev, V. and Andreeva, D., 2004. Effect of synthesis procedure on the low-temperature WGS activity of Au/ceria catalysts. *Applied Catalysis B: Environmental*, 49(2), pp.73-81.

[17] Lawrence, N.J., Brewer, J.R., Wang, L., Wu, T.S., Wells-Kingsbury, J., Ihrig, M.M., Wang, G., Soo, Y.L., Mei, W.N. and Cheung, C.L., 2011. Defect engineering in cubic cerium oxide nanostructures for catalytic oxidation. *Nano Letters*, 11(7), pp.2666-2671.

[18] Zhang, J., Kumagai, H., Yamamura, K., Ohara, S., Takami, S., Morikawa, A., Shinjoh, H., Kaneko, K., Adschiri, T. and Suda, A., 2011. Extra-low-temperature oxygen storage capacity of CeO_2 nanocrystals with cubic facets. *Nano Letters*, 11(2), pp.361-364.

[19] Zhang, D., Du, X., Shi, L., & Gao, R., 2012. Shape-controlled synthesis and catalytic application of ceria nanomaterials. *Dalton Transactions*, 41(48), 14455-14475.

[20] Harel, E., Granwehr, J., Seeley, J.A. and Pines, A., 2006. Multiphase imaging of gas flow in a nanoporous material using remote-detection NMR. *Nature Materials*, 5(4), pp.321-327.

[21] Gao, T., Jelle, B.P., Gustavsen, A. and He, J., 2014. Lightweight and thermally insulating aerogel glass materials. *Applied Physics A*, 117(2), pp.799-808.

[22] Alnaief, M. and Smirnova, I., 2010. Effect of surface functionalization of silica aerogel on their adsorptive and release properties. *Journal of Non-Crystalline Solids*, 356(33), pp.1644-1649.

[23] Perdigoto, M.L.N., Martins, R.C., Rocha, N., Quina, M.J., Gando-Ferreira, L., Patrício, R. and Durães, L., 2012. Application of hydrophobic silica based aerogels and xerogels for removal of toxic organic compounds from aqueous solutions. *Journal of Colloid and Interface Science*, 380(1), pp.134-140.

[24] Cao, S., Yeung, K.L. and Yue, P.L., 2006. Preparation of freestanding and crack-free titania–silica aerogels and their performance for gas phase, photocatalytic oxidation of VOCs. *Applied Catalysis B: Environmental*, 68(3), pp.99-108.

[25] Casula, M.F., Loche, D., Marras, S., Paschina, G. and Corrias, A., 2007. Role of urea in the preparation of highly porous nanocomposite aerogels. *Langmuir*, 23(7), pp.3509-3512.

[26] Casu, A., Casula, M.F., Corrias, A., Falqui, A., Loche, D., Marras, S. and Sangregorio, C., 2008. The influence of composition and porosity on the magnetic properties of FeCo–SiO_2 nanocomposite aerogels. *Physical Chemistry Chemical Physics*, 10(7), pp.1043-1052.

[27] Loche, D., Casula, M.F., Falqui, A., Marras, S. and Corrias, A., 2010. Preparation of Mn, Ni, Co ferrite highly porous silica nanocomposite aerogels by an urea-assisted sol–gel procedure. *Journal of Nanoscience and Nanotechnology*, 10(2), pp.1008-1016.

[28] PDF card reference code: 00-041-0013; Akinc, M., Sordelet, D., *Advanced Ceramic Materials*, 2987, 2(3), pp.232-237

[29] PDF card reference code: 01-078-5328; Wang, G, Mu, Q., Chen, T., Wang, Y., 2010, *Journal of Alloys and Compounds*, 493(1), pp.202-207.

[30] Na, T.A., Zhang, M., Juan, L.I., Huaju, L.I., Yong, L.I. and Wenjie, S., 2008. Facile synthesis of CeO_2 nanospheres. *Chinese Journal of Catalysis*, 29(11), pp.1070-1072.

[31] Penn, R.L. and Soltis, J.A., 2014. Characterizing crystal growth by oriented aggregation. *CrystEngComm*, 16(8), pp.1409-1418.

[32] Hansen, T.W., DeLaRiva, A.T., Challa, S.R. and Datye, A.K., 2013. Sintering of catalytic nanoparticles: particle migration or Ostwald ripening? *Accounts of Chemical Research*, 46(8), pp.1720-1730.

[33] Barrett, E.P., Joyner, L.G. and Halenda, P.P., 1951. The determination of pore volume and area distributions in porous substances. I. Computations from nitrogen isotherms. *Journal of the American Chemical Society*, 73(1), pp.373-380.

CHAPTER 5.

CeO_2-SiO_2 aerogel nanocomposites: shape selective synthesis of the CeO_2 dispersed nanophase

In the previous chapter, the synthesis of CeO_2-SiO_2 aerogel and xerogel nanocomposites by co-gelation of the silica and the ceria precursors was presented. In this chapter, another approach to synthesise this kind of nanocomposites is presented, which consists in pre-synthesising the nanocrystalline ceria phase and then perform the gelation of the silica matrix in the presence of a solution of the nanoparticles. This method allows a good control of the size and shape of the ceria nanoparticles, not achievable by co-gelation. Cubic and polyhedral nanoparticles have been synthesised by a hydrothermal method and characterised by means of TGA/DSC, TEM, HRTEM and XRD. The nanoparticles have been then dispersed in the silica aerogel matrix reaching a loading of 1.5 wt. %.

5.1. Introduction

As it has been already mentioned in Chapter 4, the interest on ceria-based nanomaterials is mainly focused on the application of these materials in catalysis. Their reactivity is due to the ability of ceria to form a non-stoichiometric oxide, CeO_{2-x}, through the release or storage of oxygen ions depending on the oxygen partial pressure of the environment. This property is generated by the labile and reversible redox cycle between Ce^{4+} and Ce^{3+}, and from the possibility to form a large number of oxygen vacancies preserving the cubic fluorite crystal structure.[1] It has been demonstrated that the concentration of Ce^{3+} within the crystal structure, and therefore the number of oxygen vacancies, depends on the size of the particles, reaching its maximum in nanoparticles that are 3 nm in size.[2]

However, the reactivity of ceria nanoparticles is not only dependent on the size of the nanoparticles themselves but also on the type of the surfaces exposed. The surfaces that are usually exposed in ceria nanomaterials can be identified by three low-index Miller indices: {100}, {110} and {111}. Density functional theory[3] (DFT) and molecular dynamics[4] (MD) calculations show that the stability of the surfaces follows the sequence {111} > {110} > {100}, therefore their reactivity follows the opposite trend, Figure 5.1.

The relative low thermodynamic stability of the {100} surface is associated with its dipolar nature. Figure 5.1 shows a representation of the {100} pristine surface: Ce^{4+} ions are all located in one plane and O^{2-} ions in the plane below, generating a dipole that makes this surface inherently unstable.

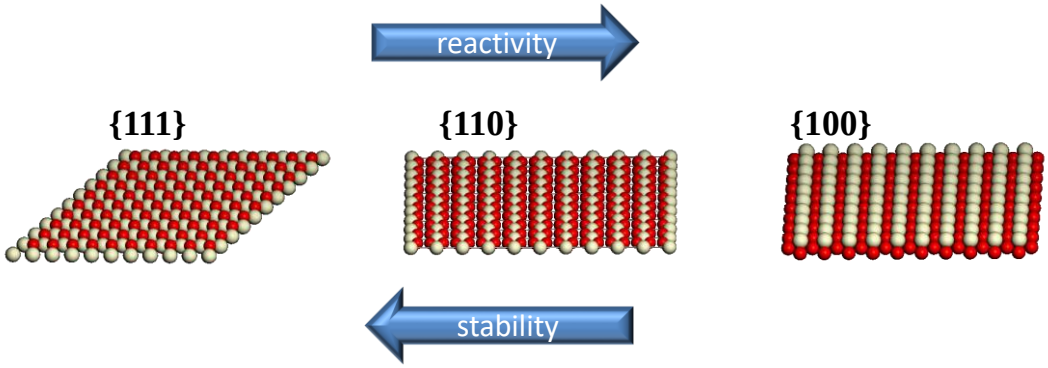

Figure 5.1 Representation of the {111}, {110} and {100} low index crystal planes of CeO_2 and its relative stability and reactivity.

However, MD simulations showed that the {100} surface of CeO_2 polyhedral nanoparticles undergoes a structural rearrangement, reducing its oxygen content by 50%, quenching the dipole[5]. This explained the reason why the unstable {100} surface was observed experimentally on polyhedral and truncated octahedral nanoparticles. The lower thermodynamical stability of the {110} surface compared with the {111} is probably attributable to the lower coordination of the surface ions, as the surface is corrugated.

In Figure 5.2 three possible shapes of ceria nanoparticles are represented, with a different {100}/{111} surface ratio. The truncated octahedron shape, Figure 5.2(a) represents the most stable form of ceria nanoparticles, as the mostly exposed surface is the {111}.[6] This type of ceria nanoparticles is usually obtained by hydrothermal methods in basic aqueous solution. The formation of a specific shape is driven by the difference in growth ratio between the [100] and [111] direction. The {111} face has a lower surface energy, thus the crystal growth is faster along the [100] direction, forming nanoparticles with truncated octahedron shape.

However, a big effort has been made in order to find synthetic routes that could yield large fractions of {100} surfaces and therefore more reactive nanoparticles. In Figure 5.2(b, c), other two possible shapes for ceria nanoparticles are represented, polyhedral and cuboidal, with increasing {100}/{111} surface ratio.

Gao et al.[7] selectively synthesised for the first time cuboidal nanoparticles exposing large portions of {100} surfaces by a hydrothermal route with the use of oleic acid (OLA) as a capping agent. The procedure involved the use of two non-miscible solvents, water and toluene. Tuning the concentration of the Ce(III) solution and the OLA/Ce(III) ratio, ceria nanocubes with sizes spanning from 4 to 16 nm have been synthesised. Dang et al.[8] selectively synthesised polyhedral and cubic nanoparticles with the same method by tuning the amount of OLA used and the reaction time. It has been showed that, using a OLA/Ce(III) 8:1 molar ratio, polyhedral nanoparticles where obtained after 24 h reaction, while cubic nanoparticles were formed after a reaction time of 48 h. The nanoparticles obtained with these methods are highly monodispersed in size.

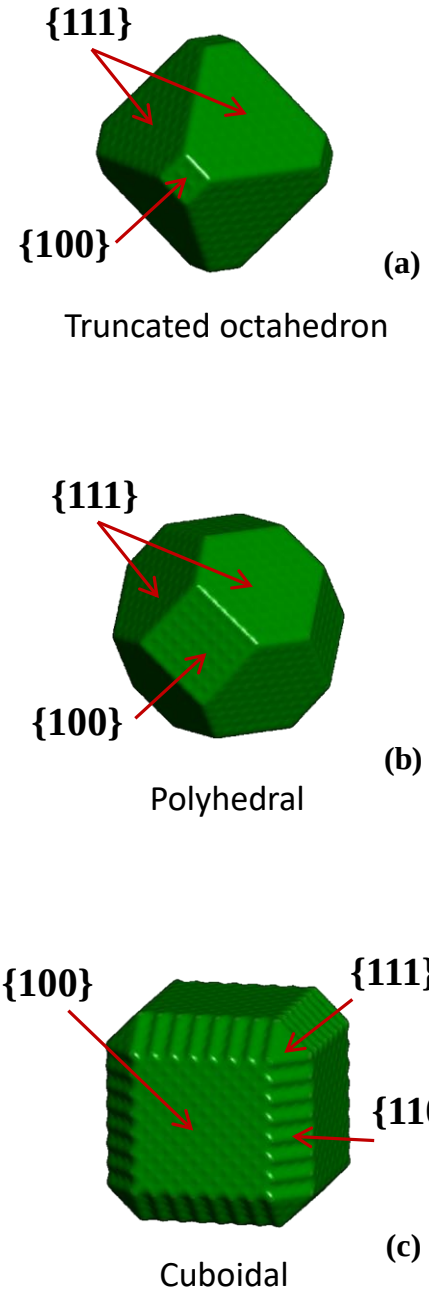

Figure 5.2 Schematic representation of the three different shapes of ceria nanoparticles with increasing {100}/{111} surface area ratio; (a) truncated octahedraon; (b) polyhedral; (c) cuboidal. Images built using the software Materials Studio

The mechanism behind the formation of polyhedral and cuboidal ceria nanoparticles is shown in Figure 5.3. Once a nanoparticle with truncated octahedron shape is formed in aqueous solution, the oleic acid at the toluene/water interphase binds the nanoparticle selectively at the {100} face, which has the highest surface energy. The oleic acid acts therefore as a shield, reducing the crystallisation rate in that direction. The crystallisation of the nanoparticle can then proceed selectively along the [111] direction until the formation of the cubic nanoparticle is reached, Figure 5.3(a). In Figure 5.3(b) the same mechanism is reported, showing the projection of the nanoparticle along the [100] direction; the black arrows show the [111] direction, where the preferred crystallisation occurs, leading to the formation of the cuboidal shape[8].

Other synthetic methods have been also investigated, with the main aim to obtain cuboidal ceria nanoparticles with a surfactant-free reaction. Yang et al.[9] synthesised cuboidal nanoparticles using a solution of NaOH; for this purpose KOH has been also used[10]. However, all these methods produced cuboidal nanoparticles with sizes > 20 nm and poor monodispersity in size.

The reactivity of these ceria nanoparticles has been measured by determining the so-called Oxygen Storage Capacity (OSC) defined as the μmol of O atoms that are

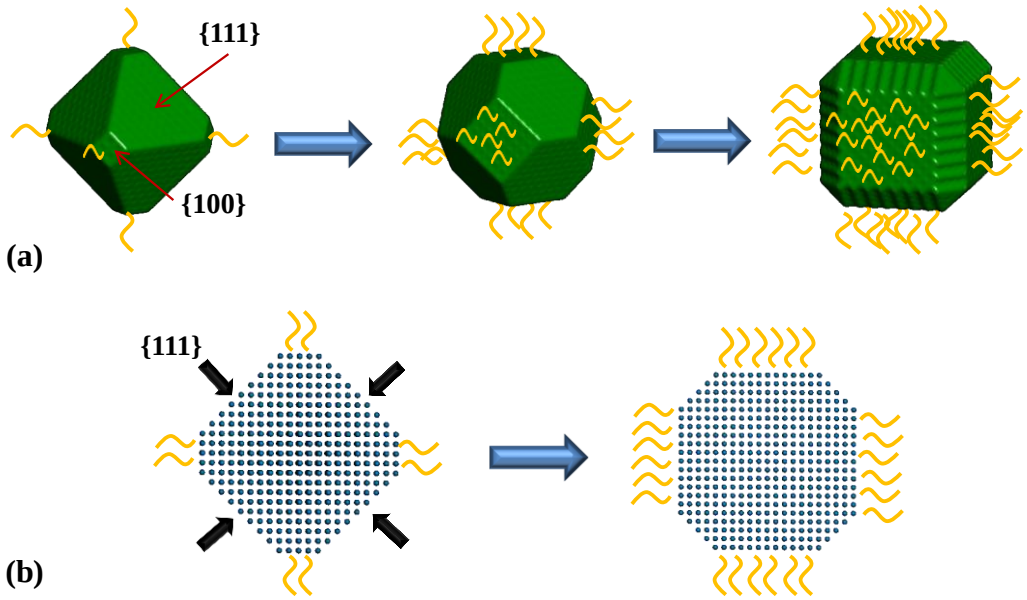

Figure 5.3 Schematic representation of the mechanism behind the formation of a ceria cuboidal nanoparticle[14]; (a) 3D reconstruction of the shape of the ceria nanoparticle with their evolution from truncated octahedron to cuboidal; (b) projection of the nanoparticles along the [100] direction: the black arrows show the [111] direction where the preferred crystallisation occurs. The blue spheres represent Ce atoms. Images built with the use of the software Materials Studio.

released and stored after a complete redox cycle, per gram of material. Suda et al.[11] found that ceria nanocubes show high values of OSC at 150 °C while ceria nanoparticles with irregular shape have the same OSC at 400 °C. Yan et al.[12] showed that ceria nanocubes have the highest OSC/S_{BET} ratio compared with polyhedral ceria nanoparticles and nanorods. Ceria nanocubes have been therefore proved a strong potential heterogeneous catalyst.

Nevertheless, a few problems must be still solved. We have already said that the only synthetic routes that were successful in yielding cuboidal ceria nanoparticles with small sizes and high monodispersion involve the use of capping agents. If a capping agent is not used, the relative big size of the obtained nanoparticles adversely affects the specific surface area of the material. Conversely, when the capping agent is used, this remains bounded at the reactive surfaces, leading to a decrease of the potential reactivity of the material[6]. It has been also shown that unsupported cuboidal ceria nanoparticles aggregate if subjected to thermal treatments[11] implying a decrease of the reactive surface area.

For these reason we have explored the possibility to embed cuboidal and polyhedral ceria nanoparticles within an amorphous silica aerogel matrix. The nanoparticles can be synthesised first by selectively tuning their shape through hydrothermal methods. A solution of the pre-synthesised nanoparticles can be then used during the sol-gel synthesis of the aerogel. Embedding the nanoparticles within the amorphous aerogel matrix could lead to some advantages: *i)* the nanoparticles are held apart by the aerogel matrix, avoiding their coalescence under thermal treatments; *ii)* thermal treatments can be used to remove the surfactant from the surface of the nanoparticles, improving their reactivity, while at the same time avoiding the coalescence and growth.

The results of this study are shown in this chapter.

5.2. Sample preparation

5.2.1. Hydrothermal synthesis of polyhedral CeO_2 nanoparticles

The ceria nanoparticles with polyhedral shape have been synthesised following a reported procedure[7] but changing the capping agent. In particular, 15 ml of 16.7 mmol/L cerium (III) nitrate solution was added into a stainless steel autoclave with a 45 ml Teflon cup; then, 15 ml solution of toluene, dodecanoic acid (0.401 g) and *tert*-butylamine (0.15 ml) were added to the autoclave without stirring. The sealed autoclave was heated at 180 ºC for 24 h (or 48 h) and then cooled at room temperature. The toluene solution was then centrifuged at 8000 rpm for 10 min. The purified solution was then precipitated by adding 30 ml of ethanol and centrifuged at 10000 rmp for 15 min to collect a pale yellow powder. The samples will be named hereafter as DOD_XX indicating the capping agent used, in this case the dodecanoic acid, followed by the number indicating the reaction time in hours.

5.2.2. Hydrothermal synthesis of cubic CeO_2 nanoparticles

The ceria nanoparticles with cubic shape have been synthesised following the same procedure used for the polyhedral ones, but using oleic acid as capping agent. 15 ml of 16.7 mmol/L cerium (III) nitrate solution was added into a stainless steel autoclave with a 45 ml Teflon cup; then, 15 ml solution of toluene, oleic acid (1.5 ml) and *tert*-butylamine (0.15 ml) were added to the autoclave without stirring. The sealed autoclave was heated at 180 ºC for 24 h (or 48 h) and then cooled at room temperature. The toluene solution was then centrifuged at 8000 rpm for 10 min. The toluene was removed from the purified solution and the nanoparticles being precipitated by adding ethanol yielding a brown solid. The samples will be named hereafter as OLA_XX indicating the capping agent used, in this case the oleic acid, followed by the number indicating the reaction time in hours.

5.2.3. Synthesis of the CeO_2-SiO_2 aerogel nanocomposites

The CeO_2-SiO_2 aerogel nanocomposites synthesised in this chapter have been prepared following the synthetic procedure detailed in Section 2.1.1. The nanoparticles are previously dissolved in toluene (3ml) and then inserted in the sol during the sol-gel process

5.3. Characterisation

In this section, the characterisation of the as synthesised polyhedral and cuboidal nanoparticles is first shown, with particular attention to the TEM and HRTEM results. The characterisation of the aerogel nanocomposites obtained by embedding the synthesised nanoparticles is also shown, as a function of the thermal treatments.

5.3.1. Characterisation of the CeO_2 nanoparticles

5.3.1.1. TGA

After the purification stages, the nanoparticles synthesised by hydrothermal synthesis have been analysed by means of TGA\DSC measurements. The temperature range investigated was 25-900 °C with a ramp of 10 °C \ min. In Figure 5.4 and Figure 5.5, the TGA/DSC curves of the nanoparticles obtained using dodecanoic acid and oleic acid are respectively shown; both figures show curves of the samples obtained after 24 and 48 hours reaction. Results are summarised in Table 5.1, which reports for each DSC peak, temperature, enthalpy and corresponding TGA mass change. The TGA/DSC curves of the pure capping agents are reported in Appendix A1, Figures A1.5 and Figure A1.6.

In the case of the nanoparticles synthesised using dodecanoic acid as a capping agent, the DSC curve shows an exothermic peak centred around 250 ºC for both samples. This exothermic peak is due to the decomposition of the dodecanoic acid that is bound to the surface of the nanoparticles. In the case of the sample obtained with a reaction time of 48 h, the mass change associated with the DSC peak is only 1.5%, while in the 24 h sample this corresponds to 21%. This indicates that the amount of capping agent that is still bound at the surface of the nanoparticles is much less after a reaction of 48 hours; dodecanoic acid thus may undergo a thermal decomposition with long reaction times.

The nanoparticles synthesised using oleic acid present a DSC curve with an exothermic peak cantered around 400-420 ºC, with an associated mass loss of ca. 60% in the case of the sample obtained after 24 h and 70% in the case of the sample obtained after 48 h. The DSC peak is due to the decomposition of the oleic acid, which is bound to the surface of the nanoparticles.

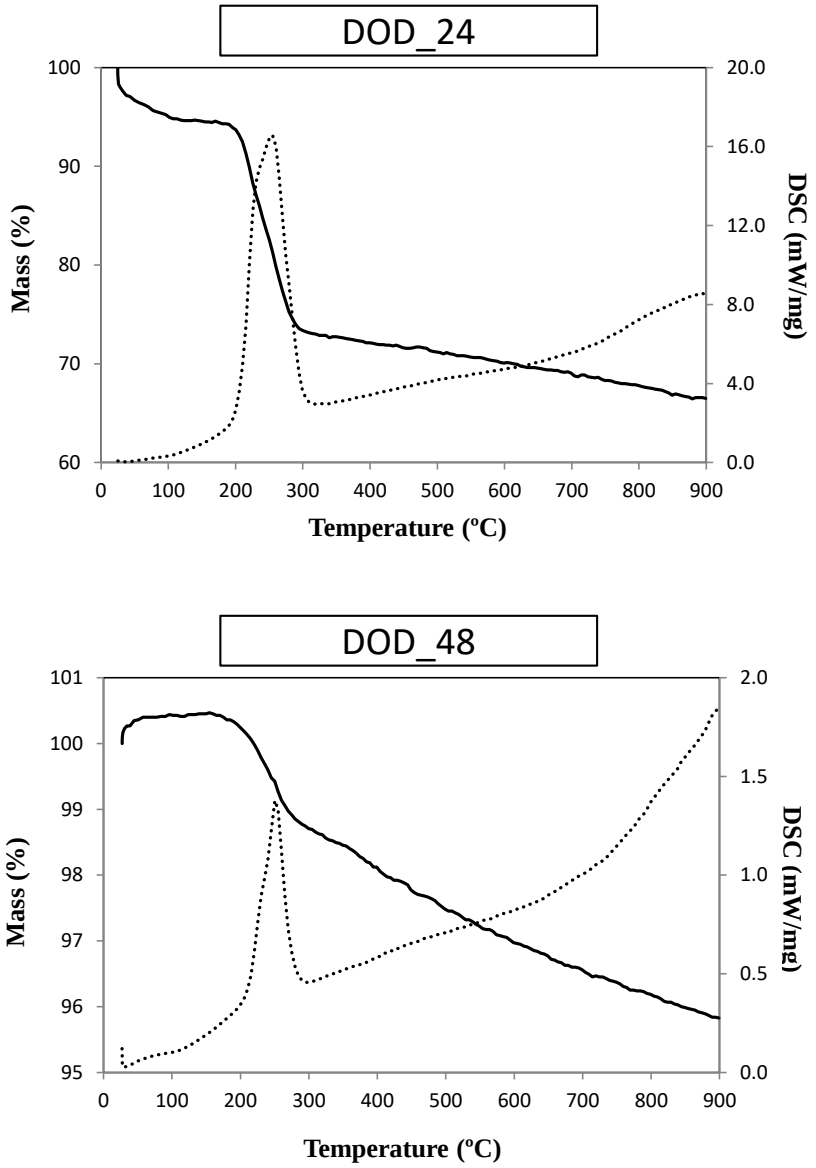

Figure 5.4 TGA\DSC measurements on the as synthesised nanoparticles using dodecanoic acid with a reaction time of 24 h (top) and 48 h (bottom). Full line: TGA; dots: DSC.

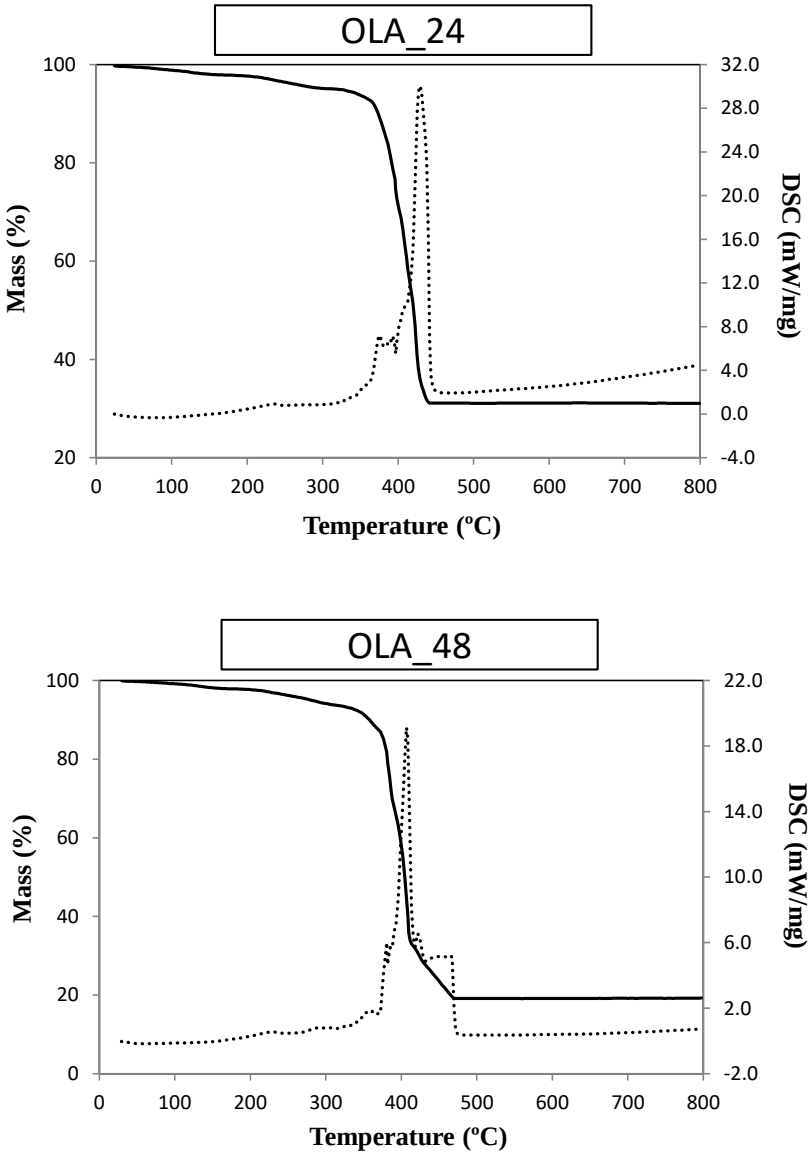

Figure 5.5 TGA\DSC measurements on the as synthesised nanoparticles using oleic acid with a reaction time of 24 h (top) and 48 h (bottom). Full line: TGA; dots: DSC.

Table 5.1 TGA\DSC results on the as synthesised nanoparticles using dodecanoic acid and oleic acid as a capping agent. TGA\DSC results on pure dodecanoic acid and oleic acid are also reported.

Sample	Peak	Mass change (%)	Temperature (°C)	Enthalpy (kJ · g^{-1})	Residual mass (%)
Dod_24h	1	21.2	254.2	- 5.13	66.50
Dod_48h	1	1.5	251.6	- 0.22	95.80
Dod. Acid	1	0.0	58.9	+ 0.28	0.00
	2	100.0	301.0	+ 0.52	
OLA_24h	1	61.6	428.3	- 5.85	31.1
OLA_48h	1	74.4	406.4	- 8.34	19.3
OLA	1	14.2	265.1	+ 0.24	0.00
	2	21.3	357.0	+ 0.24	
	3	62.3	386.0	+ 0.68	

Due to the much higher decomposition temperature, in this case, the oleic acid cannot decompose in the autoclave; therefore, the amount of oleic acid bound to the surface does not depend strongly on the reaction time. The TGA also points out that a much larger amount of surfactant is present in the case of the oleic acid. This might be due to the formation of nanoparticles with larger portions of {100} surface, which therefore bind a larger quantity of surfactant. A certain amount of oleic acid that is not bound to the surface might also be retained by the sample.

Table 5.1 shows also the decomposition temperatures of the pure carboxylic acids: the dodecanoic acid becomes less thermally stable once is bound at the surface of the nanoparticles, while the opposite happens for the oleic acid. However, the DSC curve of both dodecanoic and oleic acid, reported in Appendix A1, Figure A1.5 and Figure A1.6, show only endothermic peaks. In the case of the pure dodecanoic acid, the two endothermic peaks correspond to the temperatures at which the dodecanoic acid melts and then evaporates. Pure oleic acid might also evaporate during the thermal treatment. Conversely, the capping agents bound at the surface of the nanoparticles might decompose by combustion. This explains the different thermal stability of the carboxylic acids once bound at the surface of the nanoparticles.

5.3.1.2. TEM

TEM images of the nanoparticles are reported in Figure 5.6 and Figure 5.7 respectively. In both figures, two TEM images are reported, corresponding to the samples obtained after a reaction time of 24 and 48 h.

The nanoparticles synthesised using dodecanoic acid, appear to be highly monodisperse in size, assuming a hexagonal packing on the TEM grid; this is common for nanoparticles with a polyhedral shape.[8] The diameter of ca. 300 nanoparticles has been graphically determined using the software ImageJ[13] and the correspondent size distribution, shown as insets in Figure 5.6, has been fitted using a logNormal function. The mean size of the nanoparticles has been determined to be 5.0 ± 0.1 nm in the case of a reaction time of 24 h and 6.0 ± 0.1 nm in the case of a reaction time of 48 h.

The nanoparticles obtained using oleic acid as capping agent, shown in Figure 5.7, appear as squares on the TEM grid; this is typical for nanoparticles with a cubic/cuboidal shape.[8] In the case of the sample obtained with a reaction time of 24 h, a small amount of nanoparticles appears to be very small and yet not cubic. In both samples, the nanoparticles appear to have a wider distribution of sizes, compared with the samples obtained using dodecanoic acid. For this reason, the size of the nanoparticles has been determined by measuring the edge length of ca. 2000 nanoparticles for each sample. In particular, the length of one edge for each nanocube has been determined. The size distributions are reported for each sample as inset in Figure 5.7. The mean size of the nanoparticles has been determined to be 5.4 ± 0.2 nm in the case of a reaction time of 24 h and 6.1 ± 0.2 nm in the case of a reaction time of 48 h.

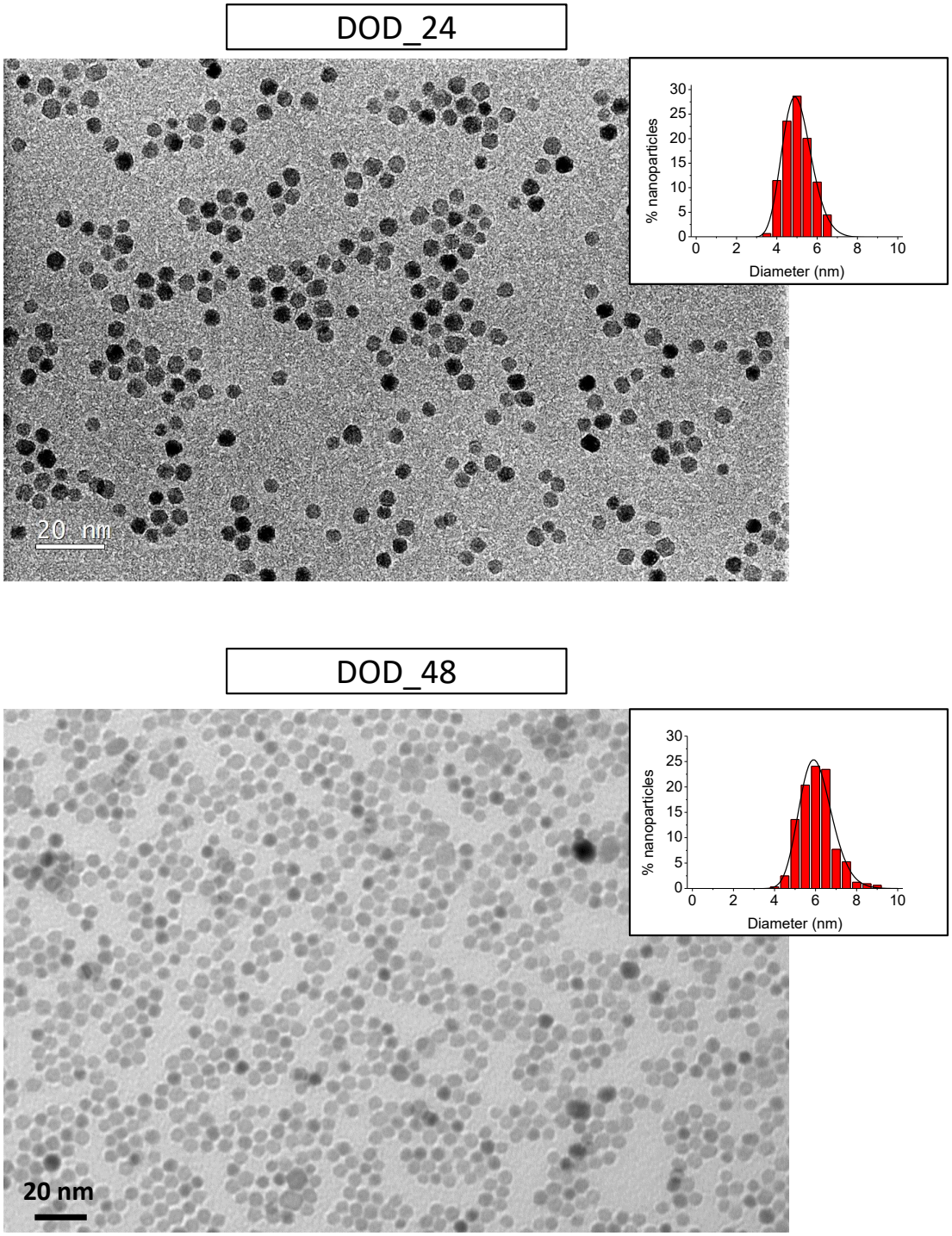

Figure 5.6 TEM images of the nanoparticles synthesised using dodecanoic acid as capping agent with a reaction time of 24 h (top) and 48 h (bottom). Insets represent the size distribution of the nanoparticles obtained by graphically measuring the diameter of ca. 300 nanoparticles.

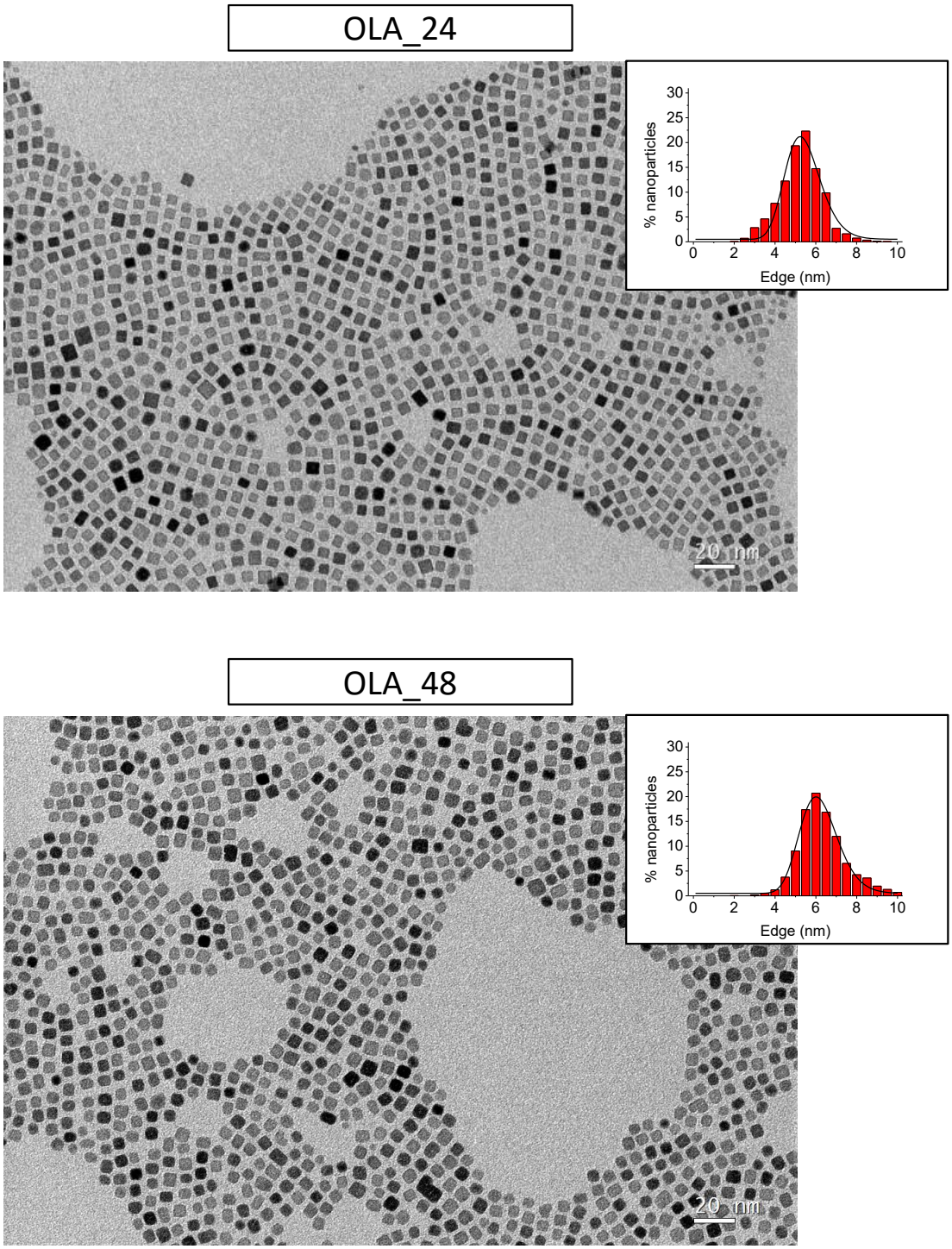

Figure 5.7 TEM images of the nanoparticles synthesised using oleic acid as capping agent with a reaction time of 24 h (top) and 48 h (bottom). Insets represent the size distribution of the nanoparticles obtained by graphically measuring the edge of ca. 2000 nanoparticles.

5.3.1.3. XRD

XRD patterns of the synthesised nanoparticles have been acquired not only to obtain information on the corresponding crystalline phase, but also on the shape of the nanoparticles. To this end, the nanoparticles have been deposited from solution on the silicon 0-background sample holder, allowing them to self-assemble on top of the holder surface.

In Figure 5.8, the XRD patterns of the nanoparticles obtained using dodecanoic acid are reported. The cubic fluorite crystalline phase of ceria can be unambiguously identified by comparison with the reference pattern,[14] reported at the bottom of the figure as dashed lines. The diffraction peaks appear to be broad due to the nanocrystalline nature of the sample.

In the case of nanoparticles with a cubic shape, the XRD patterns provide additional information upon their shape. As already seen in the TEM images, cubic nanoparticles assemble on the TEM grid by seating on one of their faces. The same preferential orientation is expected to affect the XRD patterns of the nanoparticles when deposited from solution on the 0-background XRD sample holder. Figure 5.9 reports the XRD patterns of the two samples, synthesised with different reaction times. First, it can be seen that all reflections are much less intense if compared with the samples obtained with dodecanoic acid; this is due to the presence of a large amount of oleic acid, which is amorphous, and gives its superimposed contribution, with a broad halo in the range of 2θ between 15 and 25.

Moreover, the effect of the shape is clearly noticeable since the XRD reflections appear with different relative intensity if compared with the reference pattern. In the case of the nanoparticles obtained after 24 h, the (200) and (111) reflections have the same intensity. In the case of the nanoparticles obtained after 48h, only the reflections corresponding to the (200) and (400) crystal planes are visible while the (111) reflection is still present but with a very low intensity. This is indicative that the nanoparticles assume a preferential orientation on the XRD sample holder and are overall cubic.[7] These results indicate that, although the TEM images show the formation of the cubic ceria nanoparticles already after a reaction of 24 h, the synthesis of these nanoparticles is completed after 48 h. The samples at 24 h still have a certain amount of nanoparticles that did not evolve to the cubic shape.

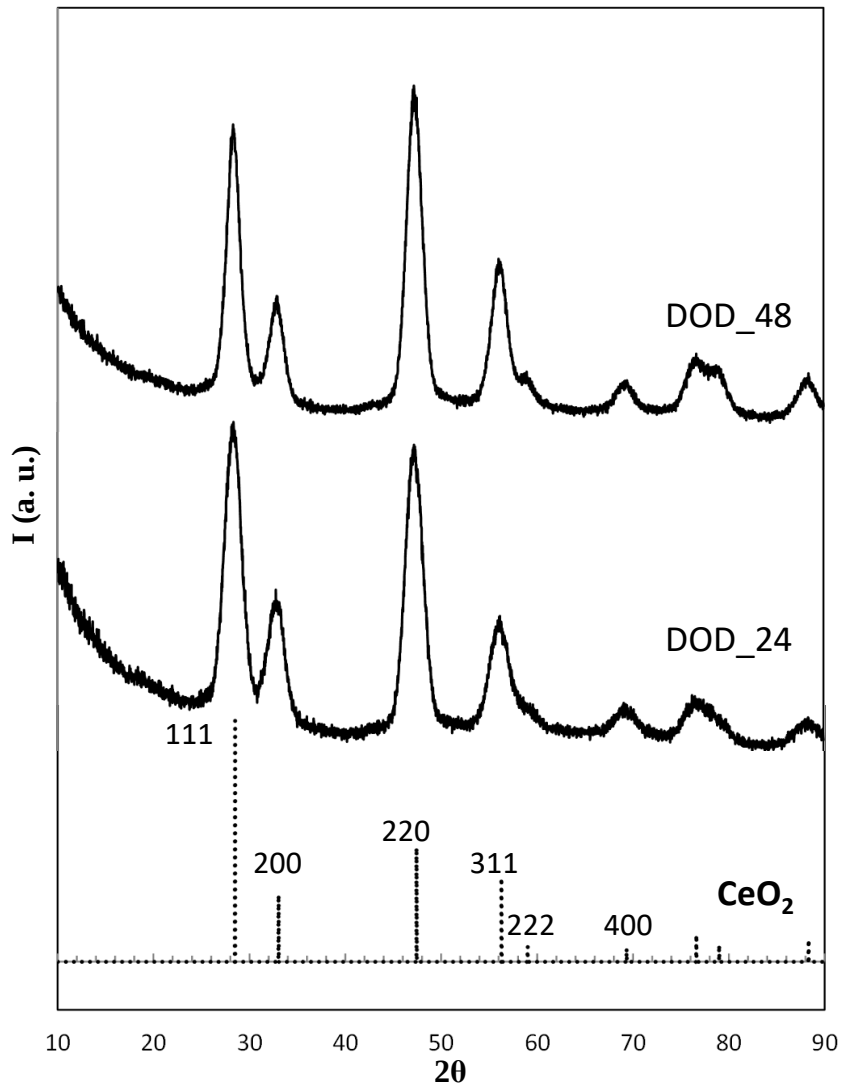

Figure 5.8 XRD patterns of the samples DOD_24 and DOD_48 corresponding to the CeO_2 nanoparticles synthesised using dodecanoic acid as capping agent with a reaction time of 24 and 48 hours respectively; dashed line: reference XRD pattern of the cubic fluorite crystalline ceria phase.

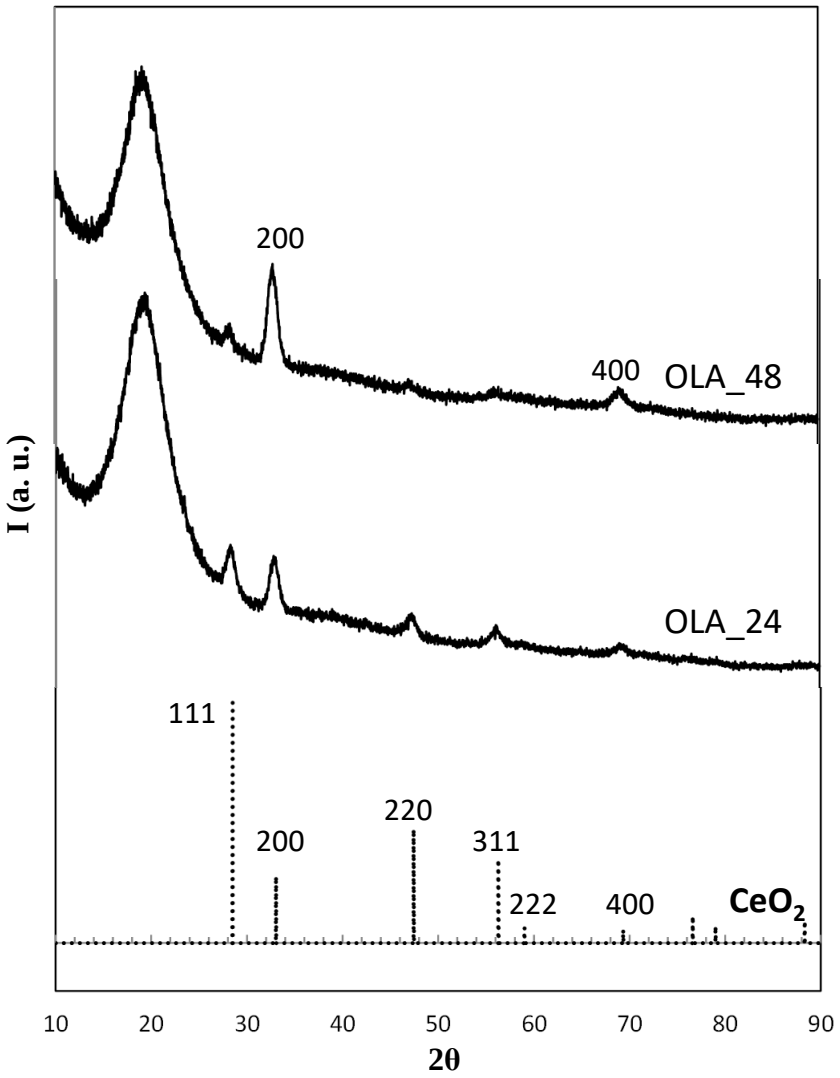

Figure 5.9 XRD patterns of the samples OLA_24 and OLA_48 corresponding to the CeO_2 nanoparticles synthesised using oleic acid as capping agent with a reaction time of 24 and 48 hours respectively; dashed line: reference XRD pattern of the cubic fluorite crystalline ceria phase.

5.3.1.4. HRTEM

The characterisation of the ceria nanoparticles is completed using high resolution TEM. In Figure 5.10(a), the HRTEM image of a nanoparticle of the sample DOD_24 is shown. The image shows the projection of the nanoparticle along the [110] direction where sets of (111) and (100) crystal planes are identified. Along this direction the nanoparticle appear to be hexagonal; this is typical for nanoparticles with a truncated octahedron shape exposing portions of both the {111} and {100} surfaces.[8] The 3D representation of the nanoparticle is inserted in the image as inset, to help the visualization of the surfaces exposed. Figure 5.10(b) shows an HRTEM image of one

of the nanoparticles of the sample OLA_48, confirming its cubic shape. The image shows the projection of the crystal along the [100] direction where the (200) and (220) crystal planes can be identified. The HRTEM image confirms that in this case the nanoparticles expose mainly the most reactive {100} surfaces.

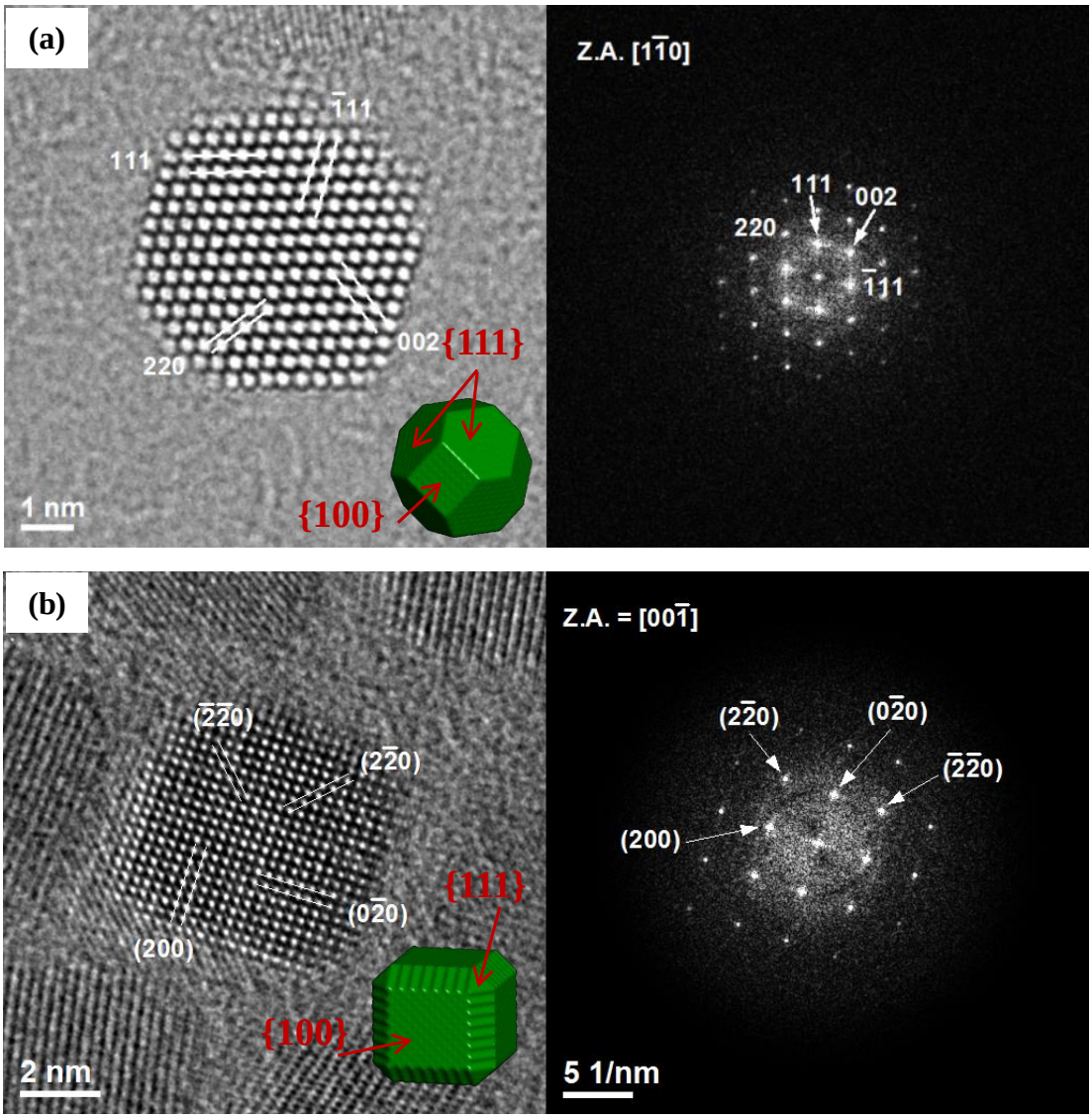

Figure 5.10 HRTEM images and FFT of the samples (a) DOD_24 and (b) OLA_48.

5.3.2. Characterisation of the CeO_2-SiO_2 aerogel nanocomposites

Two CeO_2-SiO_2 aerogel nanocomposites have been prepared: the first one using the polyhedral nanoparticles synthesised using dodecanoic acid as capping agent with a reaction time of 24 h and the second one using the cuboidal nanoparticles synthesised using oleic acid with a reaction time of 48 h. The nanocomposites have been named, following section 2.1.1, as A1.5CeO_2_poly and A1.5CeO_2_cubic respectively. In order to perform the synthesis, a solution of the nanoparticles in toluene has been used during the sol-gel process; however, only a 1.5 wt. % loading of CeO_2 has been reached, due to the low solubility of the ceria-capping agent system in ethanol, which is used in the sol-gel synthesis of the aerogel.

The XRD patterns of the CeO_2-SiO_2 aerogel nanocomposites are shown in Appendix A3, Figures A3.1 and Figure A3.2. Due to the very low loading of the dispersed ceria phase, the typical reflections of the diffraction pattern of ceria are hidden by the superimposed contribution of the amorphous silica matrix. TGA/DSC curves are reported in Appendix A3, Figure A3.3 and Figure A3.4, and are similar to the TGA/DSC curves already shown for aerogel samples. N_2-physisorption isotherms are also shown in Appendix A3, Figure A3.5 and Figure A3.6 and the values of surface area and pore diameter are reported in Table A3.3.

In Figure 5.11 TEM images of the aerogel nanocomposite synthesised using the nanoparticles with a polyhedral shape are reported, after the supercritical extraction and after thermal treatments at 450 °C and 900 °C. Bright-field images are reported on the left and dark-field images on the right. The nanoparticles are visible in both bright- and dark-field images, and are highlighted by black circles. From the dark-field images of the sample treated at 450 °C and 900 °C we can see that the nanoparticles, which appear as bright spots on top of the darker background of the amorphous silica, are well distributed within the matrix and do not show any tendency to aggregate and coalesce.

For comparison, in Figure 5.12, two TEM images of the same nanoparticles that have not been embedded within the silica aerogel matrix are show, after thermal treatment at 900 °C for 1 h. As result of the thermal treatment, the nanoparticles lose completely their shape and aggregate, reaching dimensions of more than 200 nm.

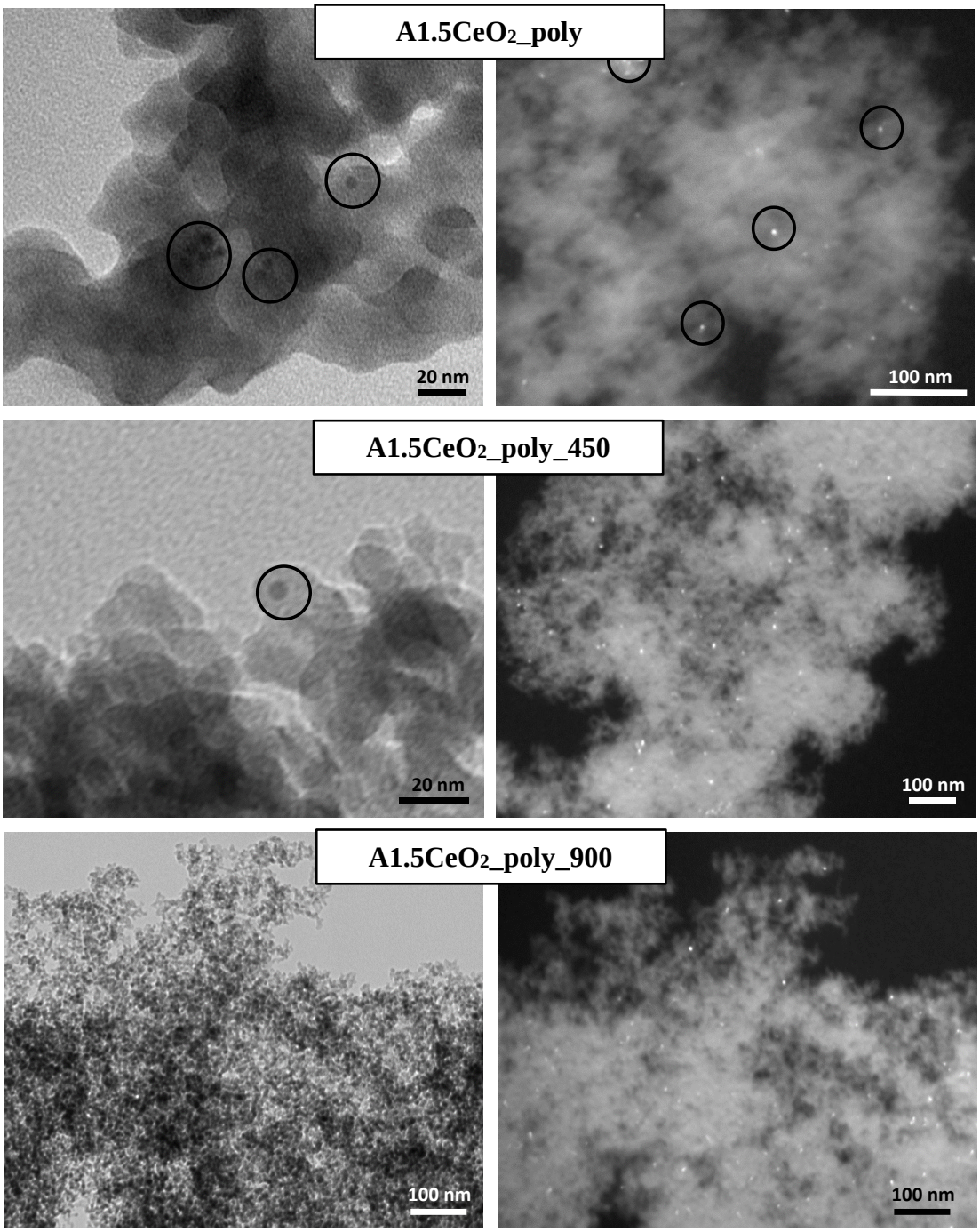

Figure 5.11 TEM images of the CeO_2-SiO_2 aerogel nanocomposite obtained using the polyhedral nanoparticles; after supercritical extraction of the solvent and after thermal treatments at 450 and 900 °C. Bright field on the left, dark field on the right.

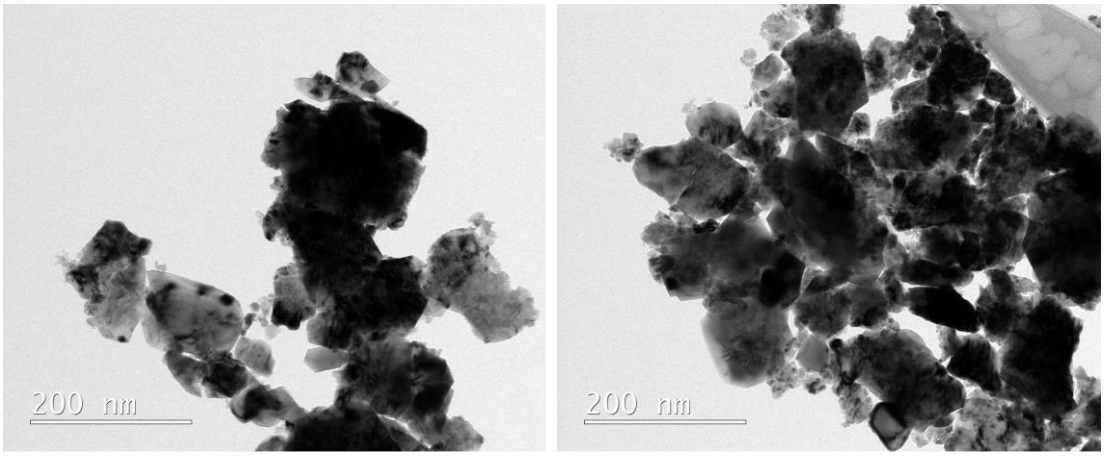

Figure 5.12 Two TEM images of non-supported polyhedral ceria nanoparticles after thermal treatment at 900 °C.

The aerogel matrix is therefore effective in holding apart the nanoparticles and preserving their size under high temperature thermal treatments.

TEM images of the CeO_2-SiO_2 nanocomposite obtained with the cuboidal nanoparticles, A1.5CeO_2_cubic, after supercritical extraction, are shown in Figure 5.13. Figure 5.13(a) shows a low magnification bright field image of the nanocomposite, where we can appreciate the typical microstructural features of the porous aerogel matrix. The nanoparticles are visible in the dark field images, as bright spots, in Figure 5.13(b-d). In particular, in the high magnification image in Figure 5.13(d) the visible nanoparticle (black circle) is suggestive of the cubic shape.

Further investigation has been attempted using HRTEM, to try answering a very important question, which is whether the nanoparticles retain their cubic shape, after the supercritical extraction and the subsequent thermal treatments.

The main problem in performing HRTEM imaging on nanoparticles embedded in a silica aerogel matrix is that the contribution of the amorphous silica adversely affects the resolution of the images. For this reason, in order to perform the HRTEM imaging, the sample was prepared using a special technique. The aerogels have been first embedded in an epoxy resin and then cut in ultra-thin sections, using a microtome, with a width of 50 nm, section 2.2.3.3, Chapter 2. The ultra-thin section is then put on an ultra-thin carbon-coated copper grid for the imaging. In this way, a consistent amount of the contribution of the silica is eliminated, allowing one to optimize the image quality.

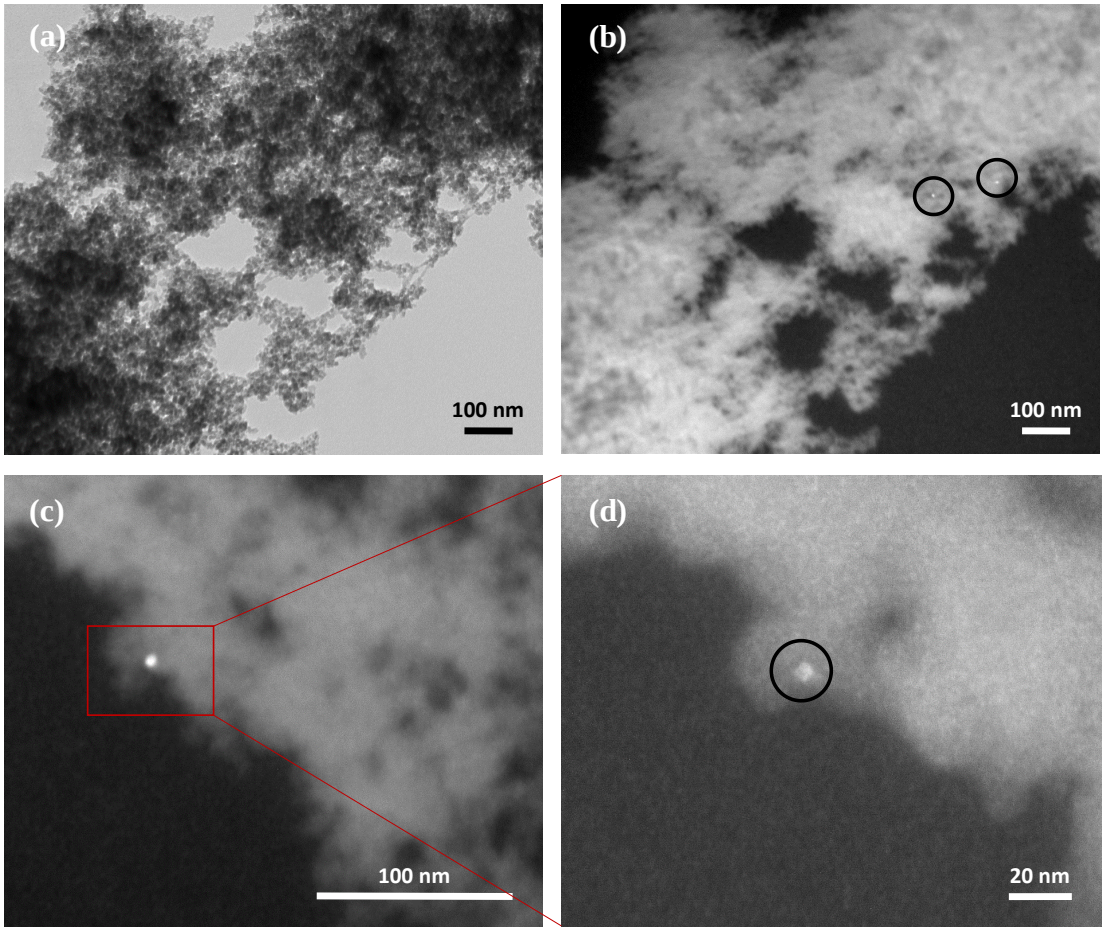

Figure 5.13 TEM images of the CeO_2-SiO_2 aerogel nanocomposite obtained using the cuboidal nanoparticles after the supercritical extraction of the solvent.

Figure 5.14 shows the HRTEM images for the aerogel samples obtained after supercritical extraction and after thermal treatments at 450 and 900 ºC. The images do not allow an unambiguous determination of the shape of the nanoparticles, due to the presence of the silica that makes the edges of the nanoparticles not clearly defined. Moreover, in the nanocomposite, the nanoparticles will assume any possible orientation and the effect of the preferential orientation on the carbon-coated grid is lost. A 2D projection that can unambiguously show the cubic shape of the nanoparticle would be produced just in the case that such nanoparticle is oriented showing the (200) crystal planes, which is an unlikely event. Instead, all the obtained images show the presence of nanoparticles oriented in such a way that only the (111) crystal planes are shown.

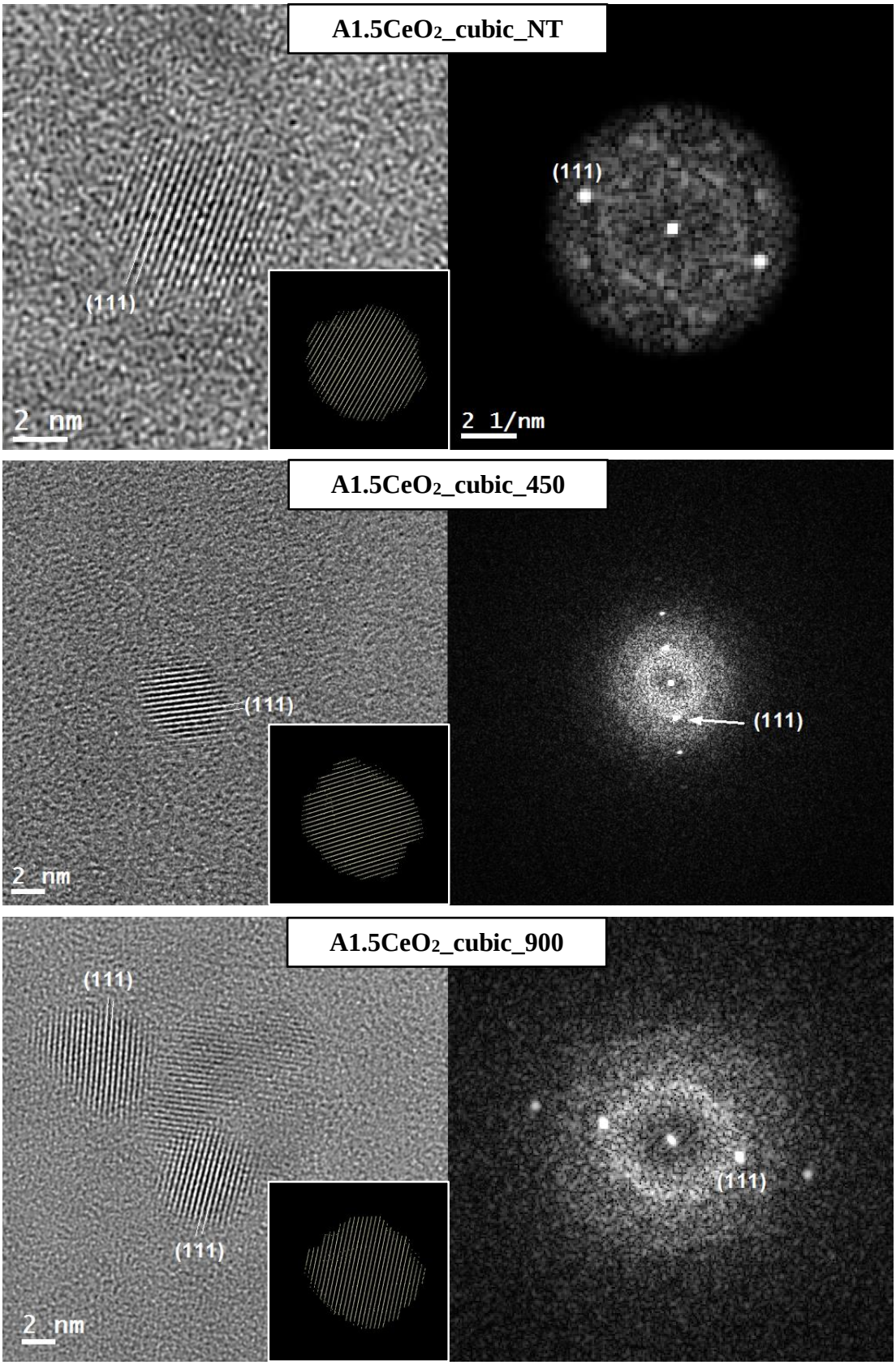

Figure 5.14 HRTEM images of the sample A1.5CeO_2_cubic after supercritical extraction and thermal treatments at 450 and 900 ºC. Insets represent projection of a simulated cuboidal ceria nanoparticle suitably oriented

To understand if nanocubes could produce the obtained 2D HRTEM images, an atomistic model of the cuboidal ceria nanoparticle, obtained using MD simulations as described in Chapter 6, has been used. The 2D projections of such a model are shown as insets in Figure 5.14, conveniently oriented to allow a comparison with the corresponding HRTEM image. These projections are consistent with the 3D atomistic model indicating that the shape has been likely maintained during the formation of the aerogel.

5.4. Conclusions

CeO_2 nanoparticles with polyhedral and cuboidal shapes have been selectively obtained by using a hydrothermal method involving the use of two different capping agents. The nanoparticles have been then embedded within a silica aerogel matrix. This strategy has been adopted in order to obtain nanocomposites where the reactivity of ceria nanoparticles is potentially enhanced. TEM characterisation showed that the nanoparticles are well distributed within the matrix and do not tend to aggregate under thermal treatment, which is a problem for un-supported nanoparticles. In this way, thermal treatments can be used to remove the capping agent that is bound to the reactive surface, clearing the active catalytic sites.

However, a complete characterisation of these nanocomposites is challenging. In particular, polyhedral and cuboidal nanoparticles might evolve to a different shape under thermal treatments, which could affect their reactivity. HRTEM imaging has been used to obtain further information on the shape of the nanoparticles embedded within the silica matrix. The nanoparticles are randomly oriented, leading to images that are difficult to be interpreted. However, results are consistent with 2D projections resulting from the atomistic model of a cubic ceria nanoparticle obtained using MD simulations.

5.5. References

[1] Chowdhury, S. and Lin, K.S., 2011. Synthesis and characterisation of 1D ceria nanomaterials for CO oxidation and steam reforming of methanol. *Journal of Nanomaterials*, 9(1), pp.1-16.

[2] Deshpande, S., Patil, S., Kuchibhatla, S.V. and Seal, S., 2005. Size dependency variation in lattice parameter and valency states in nanocrystalline cerium oxide. *Applied Physics Letters*, 87(13), pp.133113-133113.

[3] Jiang, Y., Adams, J.B. and Van Schilfgaarde, M., 2005. Density-functional calculation of CeO_2 surfaces and prediction of effects of oxygen partial pressure and temperature on stabilities. *The Journal of Chemical Physics*, 123(6), pp.064701-1-064701-9

[4] Sayle, T.X.T., Parker, S.C. and Catlow, C.R.A., 1994. The role of oxygen vacancies on ceria surfaces in the oxidation of carbon monoxide. *Surface Science*, 316(3), pp.329-336.

[5] Sayle, T.X., Parker, S.C. and Sayle, D.C., 2004. Shape of CeO_2 nanoparticles using simulated amorphisation and re-crystallisation. *Chemical Communications*, (21), pp.2438-2439.

[6] Sun, C., Li, H. and Chen, L., 2012. Nanostructured ceria-based materials: synthesis, properties, and applications. *Energy & Environmental Science*, 5(9), pp.8475-8505.

[7] Yang, S. and Gao, L., 2006. Controlled synthesis and self-assembly of CeO_2 nanocubes. *Journal of the American Chemical Society*, 128(29), pp.9330-9331.

[8] Dang, F., Kato, K., Imai, H., Wada, S., Haneda, H. and Kuwabara, M., 2010. Characteristics of CeO_2 nanocubes and related polyhedra prepared by using a liquid-liquid interface. *Crystal Growth & Design*, 10(10), pp.4537-4541.

[9] Yang, Z., Zhou, K., Liu, X., Tian, Q., Lu, D. and Yang, S., 2007. Single-crystalline ceria nanocubes: size-controlled synthesis, characterisation and redox property. *Nanotechnology*, 18(18), p.185606.

[10] Chen, Y., Lv, S., Chen, C., Qiu, C., Fan, X. and Wang, Z., 2014. Controllable synthesis of ceria nanoparticles with uniform reactive {100} exposure planes. *The Journal of Physical Chemistry C*, 118(8), pp.4437-4443.

[11] Zhang, J., Kumagai, H., Yamamura, K., Ohara, S., Takami, S., Morikawa, A., Shinjoh, H., Kaneko, K., Adschiri, T. and Suda, A., 2011. Extra-low-temperature oxygen storage capacity of CeO_2 nanocrystals with cubic facets. *Nano letters*, 11(2), pp.361-364.

[12] Mai, H.X., Sun, L.D., Zhang, Y.W., Si, R., Feng, W., Zhang, H.P., Liu, H.C. and Yan, C.H., 2005. Shape-selective synthesis and oxygen storage behaviour of ceria nanopolyhedral, nanorods, and nanocubes. *The Journal of Physical Chemistry B*, 109(51), pp.24380-24385.

[13] Schneider, C.A., Rasband, W.S. and Eliceiri, K.W., 2012. NIH Image to ImageJ: 25 years of image analysis. *Nature Methods*, 9(7), pp.671-675.

[14] PDF card reference code: 01-078-5328; Wang, G, Mu, Q., Chen, T., Wang, Y., 2010, *Journal of Alloys and Compounds*, 493(1), pp.202-207.

CHAPTER 6.

Amorphisation and re-crystallisation of a CeO_2 cuboidal nanoparticle using molecular dynamics simulations.

Molecular dynamics (MD) simulations have been used in order to obtain a suitable model of ceria nanoparticle with cuboidal shape using the amorphisation and re-crystallisation technique. This process has not been trivial as ceria, during the crystallisation, tends to expose the {111} surface that is the most thermodynamically stable, yielding a polyhedral shape. In order to form a nanocube and drive the crystallisation to the formation of the less stable {100} surfaces, an inner crystalline seed with cubic shape has been used during the simulated crystallisation. In this chapter, this process will be described, together with the morphological characterisation of the model.

6.1. Introduction

During the last few decades molecular dynamics simulation has proven to provide valuable insights to experiment in order to understand and predict the properties of materials at the nanoscale. The properties of nanomaterials are profoundly different from the parent bulk and its properties are typically a function of the microstructural features that the nanomaterial incorporates. For example it has been demonstrated that ceria nanomaterials that expose high portion of {100} surface have a higher catalytic activity[1]. The presence of grain boundaries plays also a crucial role in properties like the catalytic activity,[2] ionic conductivity[3] and mechanical strength[4] of nanomaterials. In these terms, it is very important that, if simulation is meant to provide useful insights to experiment, the atomistic models, interrogated to predict the properties, must include all the microstructural features observed experimentally. These features include surfaces exposed, vacancies, grain boundaries and dislocations.

The increasing complexity of nanomaterials makes this work very challenging. The simulator is asked indeed to embed within an atomistic model all the features that make this model realistic to predict some properties. Inserting "manually" defects such as dislocations in a pristine material is very challenging and can lead to an unrealistic model.

Considering that all the microstructural features of a material are generated during the synthesis, one can think that the best way to obtain a realistic model is to reproduce the synthetic conditions, by simulating, in the case of crystalline materials, their crystallisation from an amorphous precursor.

The so-called amorphisation and re-crystallisation technique has been used successfully in the past in order to generate atomistic models with molecular dynamics simulations in quantitative agreement with the experiment. In ref.[5] this technique has been employed in order to generate atomistic models of ceria nanoparticles. In particular, the authors show how the amorphisation and re-crystallisation technique generates atomistic models that are independent of the starting material. Starting from three pristine models with three different morphologies (cubic, polyhedral and truncated octahedral) the authors simulated the amorphisation of the nanoparticles and the subsequent crystallisation. As a result, the morphology of the three models

generated was independent of the starting materials. Three ceria nanoparticles with polyhedral shape were formed exposing mostly the {111} and the {100} surfaces. The authors also discussed that the system arranges naturally in order to quench the intrinsic dipole of the {100} surface with no need to do it "by hand". The result was in agreement with experiment.

The amorphisation and re-crystallisation technique has been then applied to generate atomistic models of many other ceria nanomaterials including core-shell nanospheres,[6] nanorods and nanochains[4] and ceria atomistic models with three-dimensional nanoporous architectures[7] in accord with experiment.

An atomistic model of ceria nanoparticle with cuboidal shape and rich microstructure, has not, thus far, been generated although ceria nanocubes have been synthesised experimentally[8]. Ceria nanocubes expose mostly the unstable {100} surface and it has been demonstrated to be a metastable form of ceria nanoparticle[9]. Experimentally, during the synthesis, surfactants that bind selectively the {100} surface are used; in this way ceria nanocubes are formed and it has been demonstrated to have an enhanced reactivity compared with the more thermodynamically stable polyhedral nanoparticles[10]. However, the instability of the {100} surface makes this kind of ceria nanoparticle difficult to obtain using MD simulations. Using the amorphisation and re-crystallisation technique the system tries to minimize the surface energy, yielding big portions of {111} surfaces, and therefore a nanoparticle with polyhedral shape[5].

In ref.[11] the authors produced an atomistic model of a ceria nanocube using MD simulations. However, that model was simply obtained by equilibrating a pristine ceria nanoparticle with cubic shape. In terms of morphology and microstructural characterisation, a poor agreement with experiment was obtained.

In this work, an atomistic model of ceria nanoparticle with cuboidal shape and rich microstructure has been obtained using MD simulation. The issue of the instability of the {100} surface has been overcome using an inner crystalline seed with cubic shape during the crystallisation process. The crystalline seed drives the crystallisation to the cubic shape. The model has been analysed using graphical techniques and has been found to be in agreement with experiment.

6.2. Methods

In this section, the potential model used to perform the simulations is reported, together with the approach followed to generate the atomistic models.

6.2.1. Potential models

All simulations presented in this study are based on the Born model of the ionic solid, where the energy of the system is given by:

$$E(r_{ij}) = \sum_{ij} \frac{Q_i Q_j}{4\pi\varepsilon_o r_{ij}} + \sum_{ij} A\exp\left(\frac{-r_{ij}}{\rho}\right) - C r_{ij}^{-6}$$

where the first term represents the Coulombic interaction of a pair of ions and the second term is in the Buckingham form (eq. 2.17, section 2.3.1). The model parameters used to describe CeO_2 nanoparticles are shown in Table 6.1.[12] This potential model has been successfully used in previous studies involving ceria based nanostructures. In particular, ceria nanoparticles have been previously amorphized and re-crystallised. The crystallisation proceeds via the formation of a fluorite structured crystalline seed that propagates and generate a crystalline nanoparticles in quantitative agreement with experiment. This encourages us to use this model in order to generate new ceria atomistic models.

Table 6.1 Potential model for the simulations done in this chapter.

Atom i	Atom j	A / eV	ρ/ Å	C / eV Å^6	Cut – off / Å
O	O	22764.30	0.149	27.96	10.00
O	Ce(IV)	1986.83	0.351	20.40	10.00
Ce(IV)	Ce(IV)	Set to zero			
Atom		**Mass / amu**		**Charge / e**	
O		16.00		-2.0	
Ce(IV)		140.12		+4.0	

6.2.2. Atomistic model generation

To generate an atomistic model of a ceria nanocube a crystal of pristine CeO_2 comprising 20736 atoms (6912 Ce atoms, 13824 O atoms) was melted while holding fixed a fluorite-structured inner core with cuboidal morphology comprising 12000 atoms (4000 Ce, 8000 O) and performing constant volume MD simulation at 8000 K for 50 ps. Crystallisation was then performed applying constant volume MD simulation at 1500 K for 300 ps. During the crystallisation, all the atoms (including the inner core) were allowed to move to prevent any bias in the structural evolution of the model. Once the nanocube had formed, constant volume MD simulation at 3750 K was performed for 27 ns; the evolution to a polyhedral shape was not observed, indicating that the cuboidal morphology is structurally stable in accord with experiment. We note that 27 ns is a very short time period – more than 12 orders of magnitude shorter than experimental annealing conditions. However, simulated annealing at elevated temperatures (3750 K) helps accelerate the dynamics and mitigate the difference in timescales. Finally, the structure was cooled by performing constant volume MD simulation at 1 K for 50 ps. Figure 6.1 summarises this process.

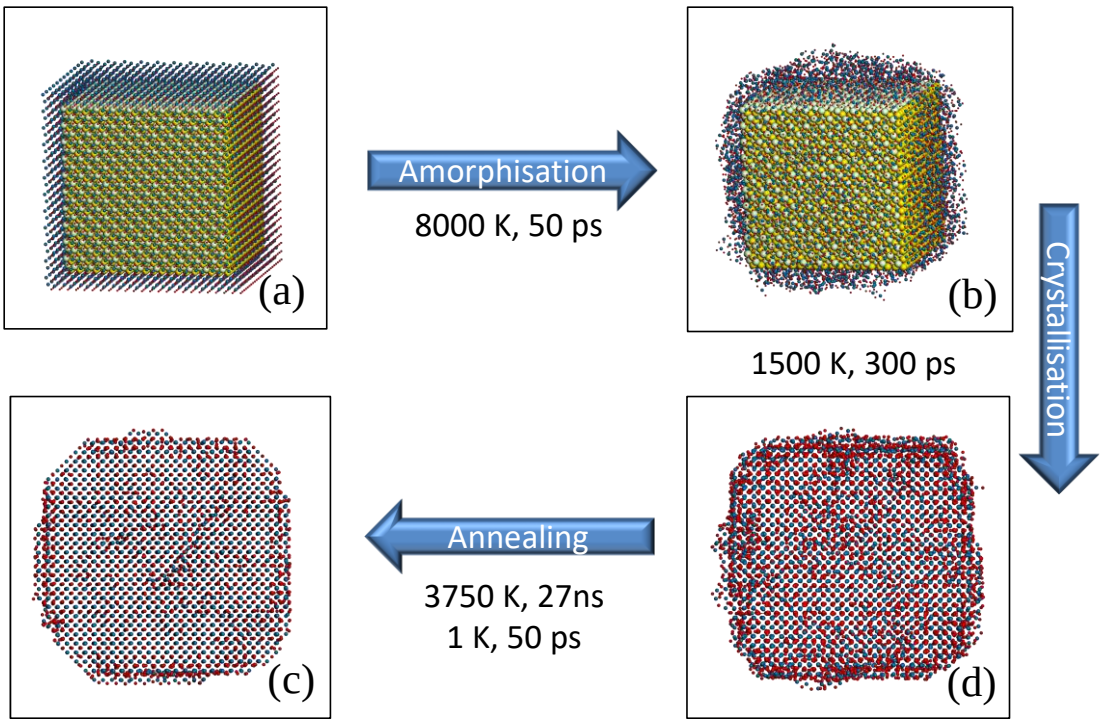

Figure 6.1 Amorphisation and re-crystallisation process of the ceria nanocube; (a) pristine cubic ceria nanoparticle; the atoms of the inner cubic core are coloured differently; (b) amorphisation of the ions surrounding the inner cubic seed; (c) crystallisation of the nanoparticle with the cubic inner seed allowed to move; (d) cubic nanoparticle after the annealing simulation. The four images showed represent actual atom positions and are not schematic.

6.3. Results

6.3.1. The crystallisation and annealing process

The cubic nanoparticle obtained after the simulated crystallisation is shown in Figure 6.2, together with the corresponding heat of crystallisation. During this simulation, the nanoparticle is cooled down from 8000 K to 1500 K allowing the atoms of the cubic crystalline seed to move. The amorphous 'sea of ions' surrounding the cubic crystalline seed immediately crystallises as result of the interaction with the seed. The result of this first simulation is the formation of a cubic nanoparticle showed in Figure 6.2(a). Figure 6.2(b) shows a surface rendered model of the nanoparticle, that improves the visualization of its cubic shape. Analysis of the surface of the nanoparticle reveals that the atoms nearby the surface occupies out of lattice positions. This evidence agrees with the instability of the {100} surface pointed out by both experiment and simulation

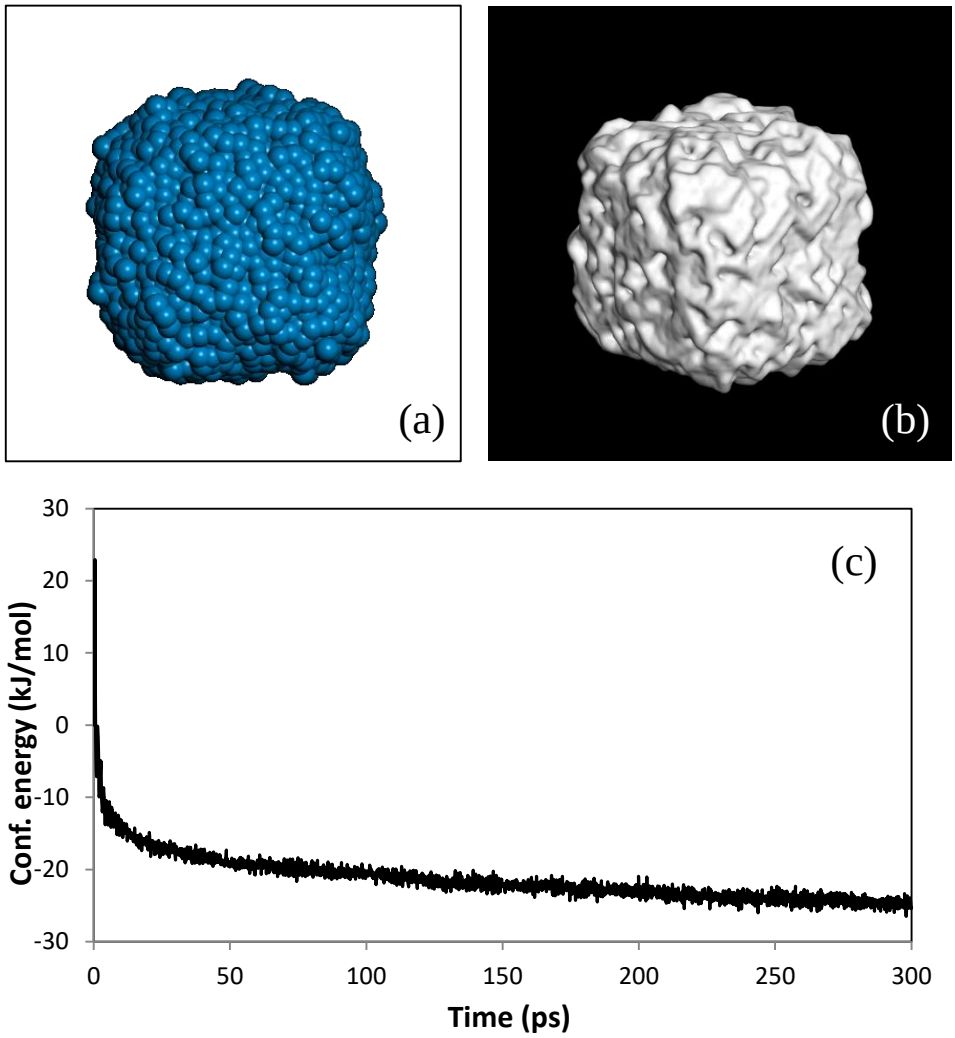

Figure 6.2 (a) Atomistic model of the ceria cubic nanoparticle after crystallisation process – only cerium ions are shown; (b) surface rendered model of the ceria cubic nanoparticle; (c) configurational energy of the system during the crystallisation process.

in previous studies.[12] Figure 6.2(c) shows the configurational energy of the system as function of time. The energy drops immediately reaching a plateau, suggesting that after this time all the nanoparticle is crystalline.

However, does this model correspond to the most thermodynamically stable form of a ceria nanocube? In order to reply to this question, an annealing process was simulated, increasing the temperature to 3750 K, just below its melting point, and monitored the structural and morphological evolution of the nanoparticle with time. In Figure 6.3 a series of snapshots of the nanoparticle are shown during the annealing simulation. Well defined {111} and {100} surfaces are formed from the most early stages of the simulation. In particular, Figure 6.3(b) corresponds to the nanoparticle after 1.2 ns of

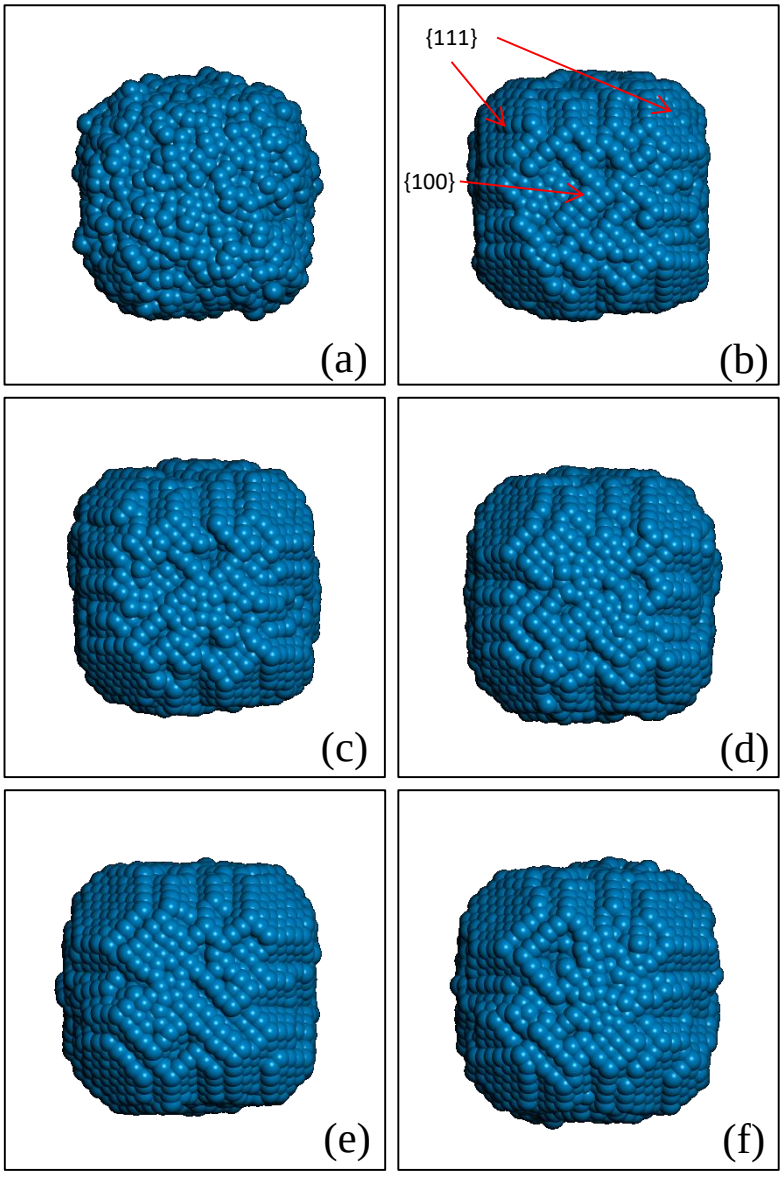

Figure 6.3 Annealing simulation at 3750 K after (a) 0 ns; (b) 1.2 ns; (c) 2.5 ns; (d) 7.5 ns; (e) 15 ns; (f) 25 ns

the annealing simulation. The corner of the nanocube become truncated, exposing the {111} surface. The most exposed surface is however the {100}, as pointed out also by experiment for ceria nanoparticles with cuboidal shape. Very important is that the size of the surfaces exposed, and therefore the shape of the nanoparticle, stays constant during all the simulation time investigated. The {111} surfaces do not tend to increase in size and a transition to a polyhedral shape has not been observed.

6.3.2. Microstructural characterisation of the cuboidal nanoparticle

In Figure 6.4(a), a surface rendered model of the cuboidal ceria nanoparticle is reported with schematic lines drawn to improve the visualization of the shape of the nanoparticle and the presence of different surfaces. The cuboidal nanoparticle is single crystalline, exposing mostly {100} surfaces; edges and corners are truncated exposing

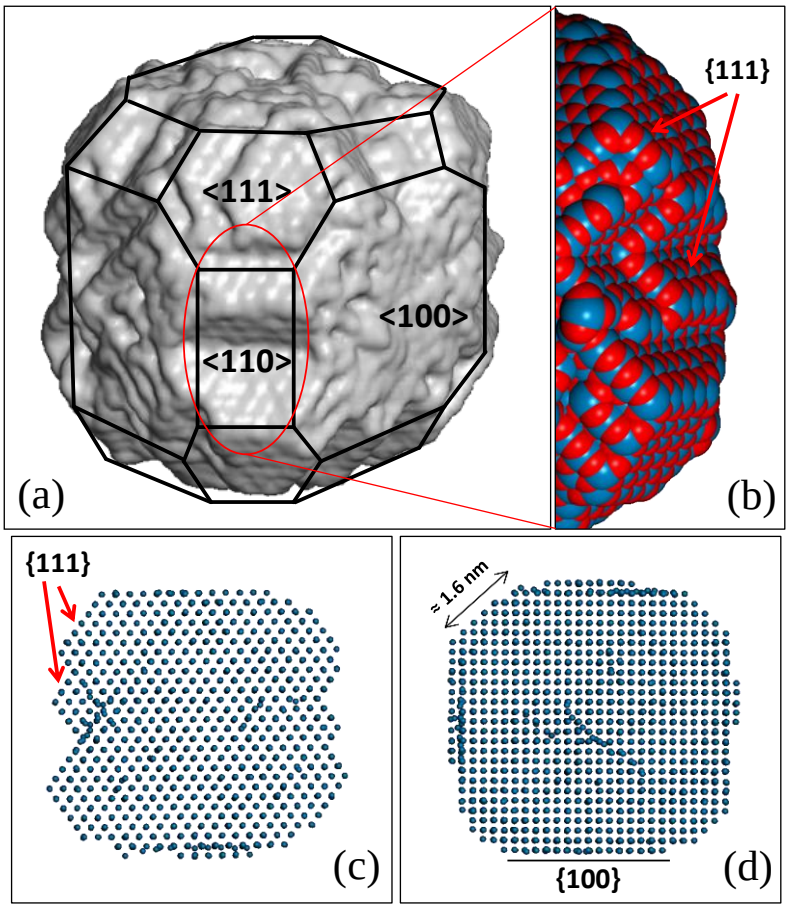

Figure 6.4 Atomistic model of the ceria cuboidal nanoparticle after the annealing simulation; (a) surface rendered model of the nanoparticle with lines drown on top of it in order to improve the visualization of its shape; (b) enlarged segment of one of the edges of the nanoparticle showing the stepped {111} surface; cerium ions are coloured by blue; oxygen ions by red; (c) view of the nanoparticle along the [110] direction; (d) view of the nanoparticle along the [100] direction. Last two figures only show the cerium ions positions.

the {110} and {111} surfaces respectively. A close inspection of the edges of the nanoparticle reveals that the {110} surface can be describes as faceted {111}, Figure 6.4(b); this tendency reflects the high thermodynamic stability of this surface. Figure 6.4(c-d) represent two projections of the nanoparticle along the [111] direction and the [100] direction. The stepped nature of the edges of the nanocube is visible only looking along the [111] direction. The lengths of all projected corners of the model have been also measured to be 1.6 nm; surprisingly, this length stays constant during the simulated annealing. We also note that the cuboidal nanoparticle is a single crystal with no presence of grain boundaries; this is in accord with experiment.

6.3.3. Dynamic mobility of ions at the surface

Using graphical techniques it is possible to monitor the behaviour of the ions at the surface. During the simulation, a dynamic exchange of ions between surfaces has been noted. In Figure 6.5, a section of the nanocube is shown along one of the edges and two cerium ions are coloured differently to improve the visualization of their mobility. Following the sequence of images, we note that the cerium ion coloured in yellow

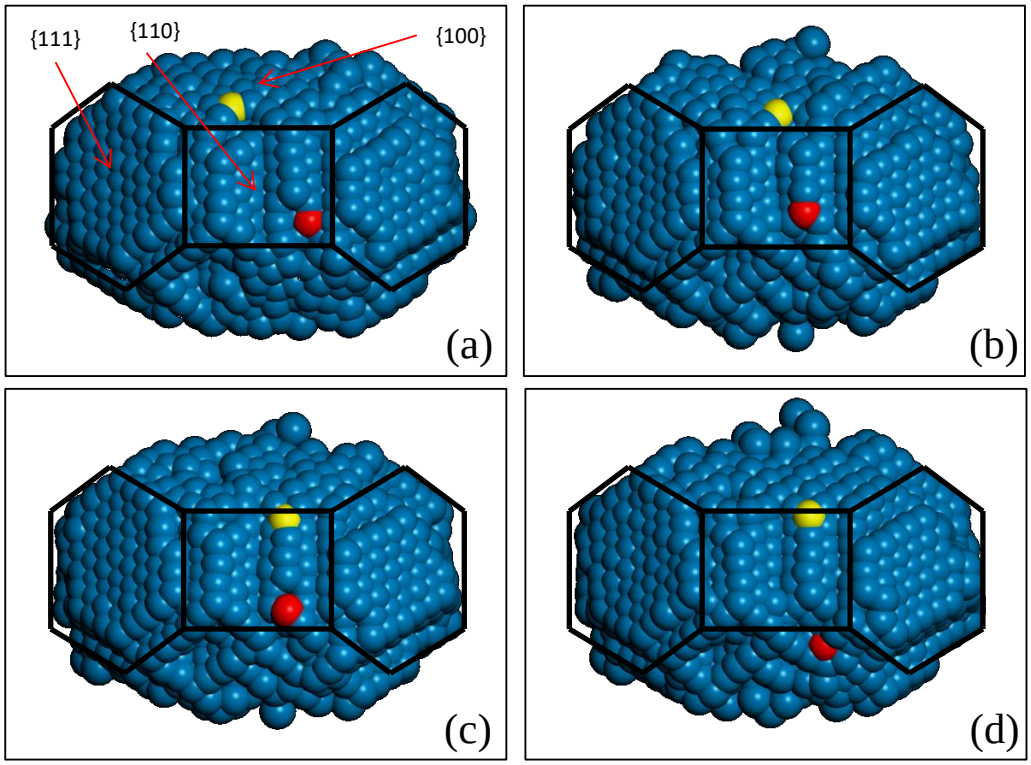

Figure 6.5 Section of the nanocube along one of the edges showing the dynamic mobility of cerium ions at (a) 25.0 ns; (b) 25.7 ns; (c) 26.0 ns; (d) 26.3 ns.

move from the {100} surface to the {110} (stepped {111}) surface and at the same time the cerium ion coloured in red move from the {110} surface to the other {111} surface. This exchange of ions at the surface keeps constant the truncation at the edges and corners, avoiding a transition to a polyhedral shape.

6.4. Discussion

The use of a simulation technique that emulates the synthetic routes allowed us to obtain atomistic models that are in agreement with experiments. Microstructural features such as the types of surfaces exposed by a nanoparticle or the formation of defects such as grain boundaries evolve naturally during the crystallisation process. In the case of the atomistic model of the ceria cuboidal nanoparticle, we found that such model, obtained by simulating the amorphisation and re-crystallisation, is in agreement with experiments. In ref.[11] the authors used experimental techniques such as Transmission Electron Microscopy (TEM) and High Resolution Transmission Electron Microscopy (HRTEM) coupled with Electron Tomography in order to study the microstructural features of ceria nanocubes obtained by using hydrothermal methods. In this study it is outlined that the nanocubes expose mostly the less stable {100} surface and edge and corners are cut into {110} and {111} surfaces. It was also

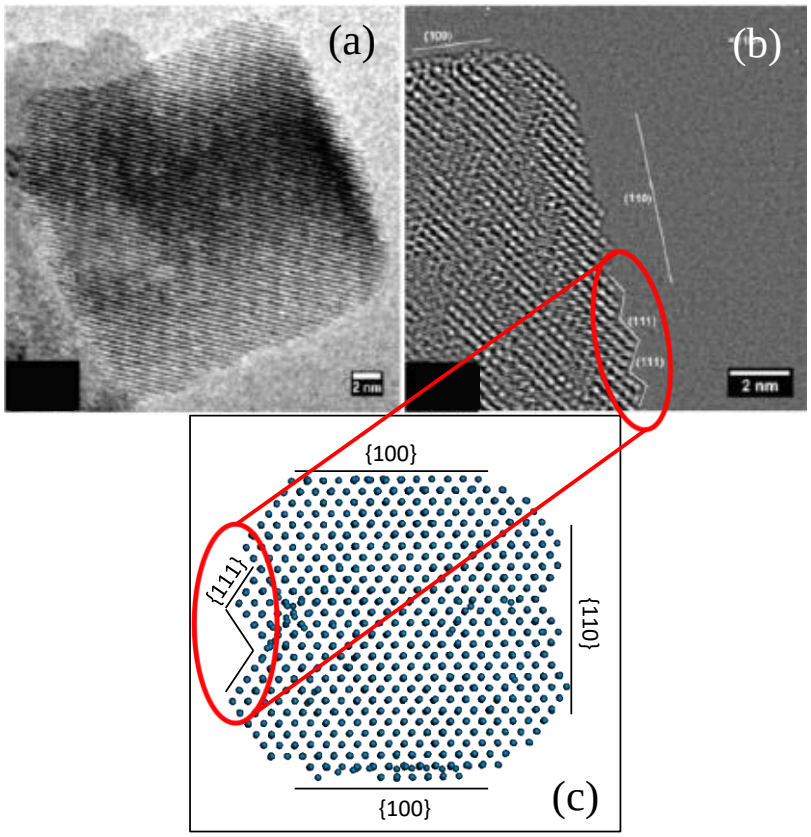

Figure 6.6 Morphological characterisation: (a) HRTEM image of ceria cubiodal nanoparticle; (b) enlarged segment of (a); (c) view along <110> direction of the obtained atomistic model of the ceria nanocube. The image show the similarities with experiments in terms of surfaces exposed. Figures (a) and (b) are re-printed with permission from reference[11] [Copyright © 2013 American Chemical Society]

found a rupture of the {110} into nanofacets of {111}, Figure 6.6(b). This has been attributed to the relative instability of the {110} surface compared to the {111}; the system arranges in more energetically stable morphologies like for example stepped surfaces. In Figure 6.6, a comparison of our atomistic model, Figure 6.6(c) with the HRTEM images of this study, Figure 6.6(a – b) is shown; our atomistic model is in quantitative accord with experiment. In particular, the similarity in terms of nanofaceting of the {110} surface into stepped {111} is highlighted with circles.

Experimentally, some of the corners and edges of the nanocubes are curved, rather than flat. However, ceria nanocubes must be thought as metastable phase of nanoceria and always in dynamic evolution. In ref.[11] authors show an experiment where a nanocube is irradiated by a focused electron beam during a HRTEM experiment. The evolution of corners and edges has been monitored during the irradiation. Figure 6.7(a-b) show the nanoparticle before irradiation and Figure 6.7(c-d) after irradiation. It was found that the curved edges and corners turn into flat surfaces and incomplete monolayers start growing due to the incident electron beam. These results can be compared with our atomistic model before and after annealing, Figure 6.7(e-f): the

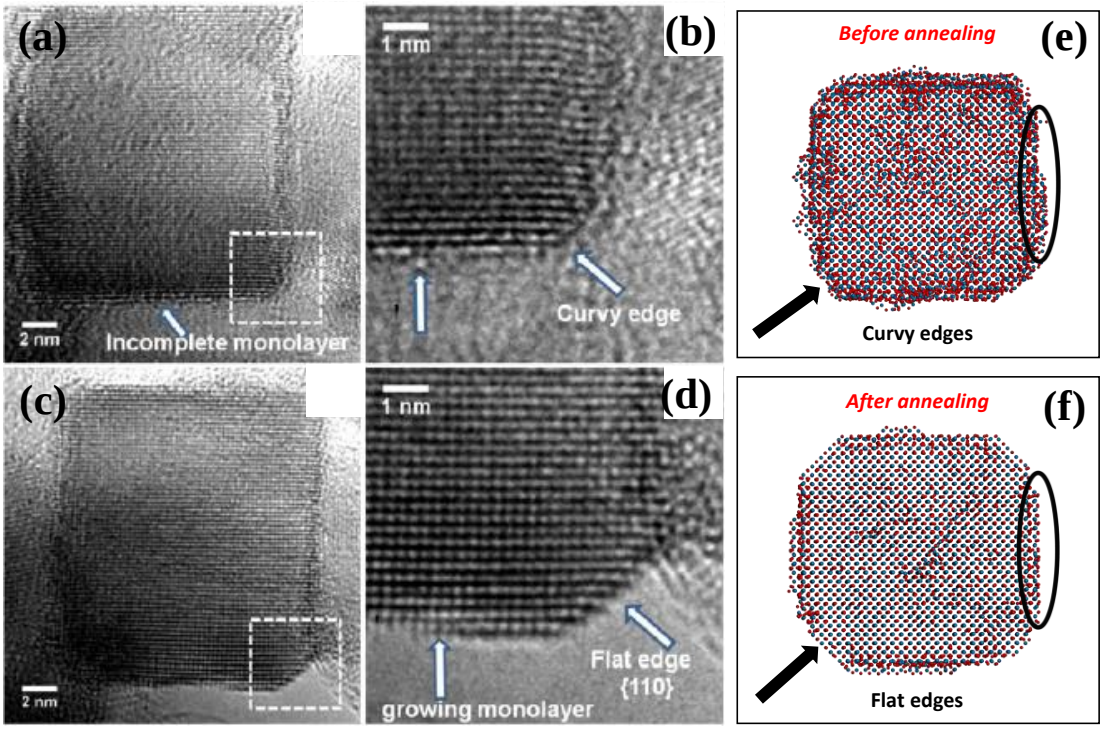

Figure 6.7 (a – d) HRTEM images of ceria nanocube before (a – b) and after (c – d) irradiation by a focused electron beam; (e) atomistic model of ceria nanoparticles before annealing and (f) after annealing process. Figures (a-d) are re-printed with permission from reference[11] [Copyright © 2013 American Chemical Society]

planarise (black arrows). Also incomplete monolayers were found in the model before annealing; after annealing the atoms from the edges and corners move to complete the last monolayer comprising the {100} surface (black circles). Experimentally, the incident beam gives the activation energy to the system to evolve to a thermodynamically more stable state; with simulation, that energy is provided by the high temperature during the annealing process.

In the same paper, ref.[11], the authors also proposed an atomistic model of a ceria nanocube, Figure 6.8(a). However, the atomistic model did not show features observed experimentally like the {111} surfaces at the corners and the stepped {111} surfaces at the edge of the nanocube. It is very important to note that the model proposed by the authors has been obtained by simply equilibrating the pristine cubic ceria crystal performing a simulation increasing the temperature from 300 K to 2500 K and back to 300 K in a 3 ns time. During this simulation the atoms simply move and relax to low energy positions in order to quench the intrinsic dipole of the {100} surface. It is also worth noting that the model of the nanocube has a length of 4 nm with only 2048 atoms. The model proposed in this chapter instead, Figure 6.8(b), has been obtained by performing amorphisation and re-crystallisation on the pristine material with 20736 atoms resulting in a cuboidal shaped nanoparticle with length of 8 nm. The model has been crystallised and then annealed at a much higher temperature (3750 K) for a much longer simulation time (27 ns). We find that in this way the model can accommodate a much richer microstructure and have a higher accord with

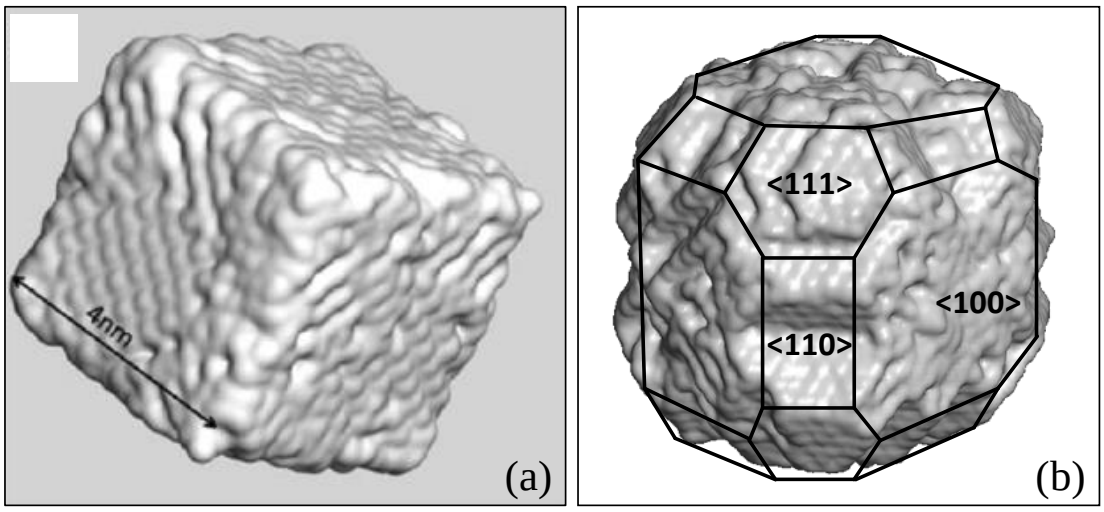

Figure 6.8 Surface rendered atomistic models of ceria nanocube obtained (a) in ref.[11] and (b) in this work. Figure (a) is re-printed with permission from reference[11] [Copyright © 2013 American Chemical Society]

experiment. The difficulty in obtaining a model of a ceria nanocube was to stabilize the cubic shape, where the instable {100} surfaces are predominantly exposed. The choice of using a cubic crystalline seed overcomes this problem, as it has been demonstrated that the cubic seed drives the crystallisation through the cubic shape, rather than the polyhedral. The resulting nanoparticle, during the annealing process, does not show any tendency to convert from the cuboidal shape to the more thermodynamically stable polyhedral. This confirms the relative stability of ceria cuboidal nanoparticles pointed out by experiment.

Finally, we propose that the technique of using an inner crystalline seed in order to drive the simulated crystallisation could be a way of more general use that can find application for the design of atomistic models of other materials with any other shapes.

6.5. Conclusions

Molecular dynamics simulations have been used in order to obtain an atomistic model of a ceria nanocube. The amorphisation and re-crystallisation technique has been coupled with the use of a crystalline seed with cubic shape in order to drive the simulated crystallisation of the nanoparticle. The atomistic model obtained has been found in good structural agreement with experiment. In particular, the nanoparticle is a single crystal with no presence of grain boundaries or dislocations. The surface mostly exposed is the {100} as expected and corners and edge are cut exposing the {111} and {110} surfaces. However, the {110} has been found to be stepped {111}, in agreement with experiment. The atomistic model has been annealed for 27 ns at 3750 K and the eventual tendency to convert its shape to the more stable polyhedral has not been noted. We can conclude that the use of a crystalline seed during the simulated amorphisation and re-crystallisation was an optimal tool in order to obtain a suitable model of a nanoparticle with a non-thermodynamically stable morphology.

6.6. References

[1] Zhang, D., Du, X., Shi, L., & Gao, R., 2012. Shape-controlled synthesis and catalytic application of ceria nanomaterials. *Dalton Transactions*, 41(48), 14455-14475

[2] Landau, M.V., Vidruk, R., Vingurt, D., Fuks, D. and Herskowitz, M., 2014. Grain boundaries in nanocrystalline catalytic materials as a source of surface chemical functionality. *Reviews in Chemical Engineering*, 30(4), pp.379-401.

[3] An, J., Bae, J., Hong, S., Koo, B., Kim, Y.B., Gür, T.M. and Prinz, F.B., 2015. Grain boundary blocking of ionic conductivity in nanocrystalline yttria-doped ceria thin films. *Scripta Materialia*, 104, pp.45-48.

[4] Sayle, T.X., Inkson, B.J., Karakoti, A., Kumar, A., Molinari, M., Möbus, G., Parker, S.C., Seal, S. and Sayle, D.C., 2011. Mechanical properties of ceria nanorods and nanochains; the effect of dislocations, grain-boundaries and oriented attachment. *Nanoscale*, 3(4), pp.1823-1837.

[5] Sayle, T.X., Parker, S.C. and Sayle, D.C., 2004. Shape of CeO_2 nanoparticles using simulated amorphisation and re-crystallisation. *Chemical Communications*, (21), pp.2438-2439.

[6] Feng, X., Sayle, D.C., Wang, Z.L., Paras, M.S., Santora, B., Sutorik, A.C., Sayle, T.X., Yang, Y., Ding, Y., Wang, X. and Her, Y.S., 2006. Converting ceria polyhedral nanoparticles into single-crystal nanospheres. *Science*, 312(5779), pp.1504-1508.

[7] Sayle, T.X., Cantoni, M., Bhatta, U.M., Parker, S.C., Hall, S.R., Möbus, G., Molinari, M., Reid, D., Seal, S. and Sayle, D.C., 2012. Strain and architecture-tuned reactivity in ceria nanostructures; enhanced catalytic oxidation of CO to CO_2. *Chemistry of Materials*, 24(10), pp.1811-1821.

[8] Yang, S. and Gao, L., 2006. Controlled synthesis and self-assembly of CeO_2 nanocubes. *Journal of the American Chemical Society*, 128(29), pp.9330-9331.

[9] Aneggi, E., Wiater, D., de Leitenburg, C., Llorca, J. and Trovarelli, A., 2013. Shape-dependent activity of ceria in soot combustion. *ACS Catalysis*, 4(1), pp.172-181.

[10] Zhang, J., Kumagai, H., Yamamura, K., Ohara, S., Takami, S., Morikawa, A., Shinjoh, H., Kaneko, K., Adschiri, T. and Suda, A., 2011. Extra-low-temperature oxygen storage capacity of CeO_2 nanocrystals with cubic facets. *Nano Letters*, 11(2), pp.361-364.

[11] Bhatta, U.M., Reid, D., Sakthivel, T., Sayle, T.X., Sayle, D., Molinari, M., Parker, S.C., Ross, I.M., Seal, S. and Möbus, G., 2013. Morphology and surface analysis of pure and doped cuboidal ceria nanoparticles. *The Journal of Physical Chemistry C*, 117(46), pp.24561-24569.

[12] Sayle, T.X.T., Parker, S.C. and Catlow, C.R.A., 1994. The role of oxygen vacancies on ceria surfaces in the oxidation of carbon monoxide. *Surface Science*, 316(3), pp.329-336.

CHAPTER 7.

Simulating the mechanical properties of CeO_2 nanoparticles: the effect of shape, size and microstructure

The atomistic model of the ceria cuboidal nanoparticle shown in the previous chapter is used, together with a set of other models of ceria nanoparticles, to calculate their mechanical properties. In particular, we have used a set of ceria nanoparticles with cuboidal, polyhedral and spherical shape, with sizes spanning from 6 to 10 nm, comprising rich microstructure including Σ3 and Σ11 grain boundaries, and {100}, {110} and {111} surfaces exposed. A model of partially reduced ceria nanoparticle with a high content of oxygen vacancies has been also considered. All the models have been obtained using the amorphisation and re-crystallisation technique, ensuring a good agreement with experiment in terms of microstructure. We found that the mechanical properties of ceria nanoparticles are dominated by the presence of grain boundaries: a Σ3 grain boundary reduces the compressive strength of polyhedral ceria nanoparticles by 33%. We also found *stress-induced Ostwald ripening* along a Σ11 grain boundary: under compression, one crystal grain grows at the expenses of another one along the grain boundary. Furthermore, the compression of a single crystalline ceria cuboidal nanoparticle leads to the evolution of dislocations and grain boundaries within the crystal. The possibility of tuning the properties of ceria nanoparticles by applying uniaxial force is therefore discussed.

7.1. Introduction

In the previous chapters, it has been shown that nanoceria plays a central role in the field of catalysis,[1] because of its ability to store and release oxygen atoms due to the labile and reversible redox cycle between Ce^{4+} and Ce^{3+}. However, nanoceria represent a key material for a more broad range of applications including solar cells,[2] solid oxide fuel cells,[3] nanomedicine[4] and chemical mechanical planarization[5]

Although ceria nanomaterials have been widely studied in terms of morphology, surfaces exposed and reactivity, the mechanical properties have received much less attention even though are different from the parent bulk material[6] and are central to applications such as chemical mechanical planarization (CMP). During this process, ceria nanoparticles are used as an abrasive material to polish and planarize surfaces for integrated circuits, which need to be ultra-smooth. It is estimated that the global production of nanoceria for CMP process is ca. 170 tons per year. Clearly, predicting the compressive strength, elastic modulus, mechanism of elastic and plastic deformation and the relationships with shape, size and microstructure, will facilitate the computational design of nanomaterials for CMP applications with optimum properties.

Experimentally, nanoindentation, in-situ Transmission Electron Microscopy (TEM) and Atomic Force Microscopy (AFM) have been used to determine the relationships between the mechanical properties and structures of nanomaterials.[7,8,9,10] However, the lack of a rich investigation reflects the difficulties to apply such techniques to some nanomaterials: the majority of the studies found in the literature regard nanoparticles with sizes around 100 nm or more and there are no studies on ceramics nanoparticles; a review is given in ref.[11] In this context, atomistic simulation can be used to provide prediction for experiments.

In Chapter 6, we also showed that the structure of a ceria nanoparticle is in dynamic evolution, and a dynamic exchange of ions between surfaces has been highlighted by the simulations. The oxygen ions that are removed from the surface during a catalytic process must be replenished, and therefore the oxygen ion conductivity of the material have an impact on its catalytic activity. Moreover, the oxygen ion conductivity of ceria is sufficiently high to enable ceria to be used as an electrolyte in solid oxide fuel cells;

therefore, it is not surprising that considerable effort has been directed at controlling the ionic conductivity of the material.[12]

The ionic conductivity of a material is vacancy driven[13] and therefore sensitive to the local environment. It has been demonstrated that the ionic conductivity of a material containing grain boundaries can be two orders of magnitude lower compared to the parent bulk with no presence of grain boundaries.[14] In this context, it is also crucial to control microstructural features, such as the grain boundary content, in order to impact upon technological important areas such as solid oxide fuel cells and catalysis.

In this work, we show that grain boundaries can be purged by applying uniaxial force, facilitating the formation of a single crystal, via a strain-induced Ostwald ripening. Our simulations thus predict the possibility to mechanically tune the grain boundary content of a material, therefore its oxygen ion conductivity and reactivity.

7.2. Method

In this section, the potential models used to describe the ceria nanoparticles are reported as well as the computer code used to perform the molecular dynamics simulations and the approach used to generate the atomistic structure of the nanoparticles. The method used to simulate uniaxial compression of the nanoparticles is also reported.

7.2.1. Potential models

All simulations presented in this study are based on the Born model of the ionic solid. The energy of the system is given by:

$$E(r_{ij}) = \sum_{ij} \frac{Q_i Q_j}{4\pi\varepsilon_o r_{ij}} + \sum_{ij} A\exp\left(\frac{-r_{ij}}{\rho}\right) - Cr_{ij}^{-6}$$

where the first term represents the Coulombic interaction of a pair or ions and the second term is in the Buckingham form (eq. 2.17, section 2.3.1). The model parameters used to describe the CeO_2 nanoparticles are shown in Table 7.1.[15,16] These potential models have been successfully used in previous studies involving ceria-based nanostructures.[17]

Table 7.1 Potential parameters used to run all the simulations described in this chapter. The cation-cation interactions are set to zero.

Atom *i*	Atom *j*	*A*/eV	*ρ*/Å	*C*/eV Å^6	Cut – off / Å
O	O	22764.30	0.149	27.89	10.0
O	Ce (IV)	1986.83	0.351	20.40	10.0
O	Ce (III)	1731.62	0.3640	14.43	10.0
O	Ti (IV)	760.47	0.388	0.00	10.0

Atom	Mass/amu	Charge/e
O	16.00	-2.0
Ce(IV)	140.12	+4.0
Ce(III)	140.12	+3.0
Ti (IV)	47.87	+4.0

7.2.2. Simulation code

The simulations were performed using the DL_POLY code;[18] the user manual provides comprehensive analytical description and discussion of the molecular dynamics simulations, force fields, boundary conditions and algorithms used in these simulations.

7.2.3. Generation of the atomistic models

In this section, the method used to generate the atomistic models of the ceria nanoparticles is outlined. The amorphisation and re-crystallisation technique[19] is employed, ensuring a high agreement with experiment in terms of microstructure. The generation of the ceria cuboidal nanoparticle has been extensively outlined in the previous chapter; a cubic crystallisation seed has been employed in order to drive the crystallisation of the nanoparticle to the cuboidal shape; in this section, the details will be summarised. Two atomistic models of polyhedral nanoparticles, generated in a previous study[20] have been also used, with different size. In this case, the use of a crystalline inner seed was not needed, as the polyhedral shape is the most thermodynamically stable form of ceria nanoparticles. Two ceria nanoparticles coated with TiO_2 have been also used and were generated in a previous study;[19] in this case, the nanoparticles crystallise with spherical shape. The difference between the two models stay in the nature of the ceria inner core: one is single crystalline and the second is polycrystalline. A model of a partially reduced ceria has been also obtained. Ceria nanoparticles in fact are never fully oxidized, rather are partially reduced. Therefore, in this chapter, the effect of the reduction of the nanoparticles on their mechanical properties has been also studied. In Figure 7.1 all the atomistic models considered in this chapter are reported.

7.2.3.1. Ceria nanocube

To generate an atomistic model of a ceria nanocube, Figure 7.1(a), a crystal of CeO_2 comprising 20736 atoms (6912 Ce atoms, 13824 O atoms) was melted, while holding fixed a fluorite-structured inner core with cuboidal morphology, comprising 12000 atoms (4000 Ce, 8000 O), and performing constant volume MD simulation at 8000 K for 50 ps. The crystallisation was then performed applying constant volume MD simulation at 1500 K for 300 ps. During the crystallisation, all the atoms (including the inner core) were allowed to move to prevent any bias in the structural evolution of the model. The strategy of using a cubic seed has been chosen in order to avoid the

natural tendency of ceria to crystallise with truncated octahedral shape, exposing the most thermodynamically stable {111} surface.[20] Once the nanocube had formed, constant volume MD simulation at 3750 K was performed for 27 ns; the evolution of an octahedral shape was not observed, indicating that the morphology is structurally stable in accord with experiment. We note that 27 ns is a very short time period – more than 12 orders of magnitude shorter than experimental annealing conditions. However, simulated annealing at elevated temperatures (3750 K) helps accelerate the dynamics and mitigate the difference in timescales. Finally, the structure was cooled by performing constant volume MD simulation at 1 K for 50 ps.

7.2.3.2. Ceria polyhedral nanoparticles

Two ceria nanoparticles with polyhedral shape were generated following methods reported in ref.[20] In particular, nanoparticles of CeO_2 comprising 7761 and 18849 atoms were amorphized and re-crystallised, resulting in two polyhedral nanoparticles with diameters of ca. 6 nm and 8 nm respectively, Figure 7.1(b).

7.2.3.3. Spherical CeO_2-TiO_2 core-shell nanoparticles

To generate spherical nanoparticles, we employed a method reported previously in ref.[19] In particular, a nanoparticle of CeO_2 comprising 15972 atoms was taken and Ce^{4+} ions within the outer region of the particle were replaced by Ti^{4+}. The particle was then amorphized and re-crystallised using MD simulation. The temperature was chosen carefully such that the inner CeO_2 core crystallises while the outer TiO_2 shell stays molten. A molten material will minimise its surface energy by adopting a spherical morphology, thus facilitating a spherical nanoparticle. The strategy exploits the fact that the melting point of CeO_2 is higher than TiO_2 and therefore at a particular temperature, the CeO_2 is able to crystallise while the TiO_2 remains molten. Two nanoparticles were generated, with single crystal and polycrystalline CeO_2 cores respectively, Figure 7.1(c, d). In particular, careful choice of the re-crystallisation temperature facilitated the evolution of either a single crystal or a polycrystalline CeO_2 core.[21]

7.2.3.4. Oxygen vacancies

Starting from the model of the polyhedral nanoparticle with a diameter of 8 nm, a nanoparticle comprising 5% oxygen vacancies ($CeO_{1.9}$) was generated by removing 628 oxygen atoms from random positions within the crystal structure. For each oxygen

atom removed, the oxidation state of two cerium atoms was changed from 4+ to 3+ to ensure charge neutrality. To facilitate a low-energy configuration, the nanoparticle was equilibrated by performing NVT (constant number of atoms, N, constant volume V and constant temperature, T) at 2000 K for 2.5 ns, enabling the oxygen vacancies to locate to low-energy positions. We note that oxygen vacancies initially generated on the surface of the nanoparticle moved to sub-surface positions in accord with previous findings.[22]

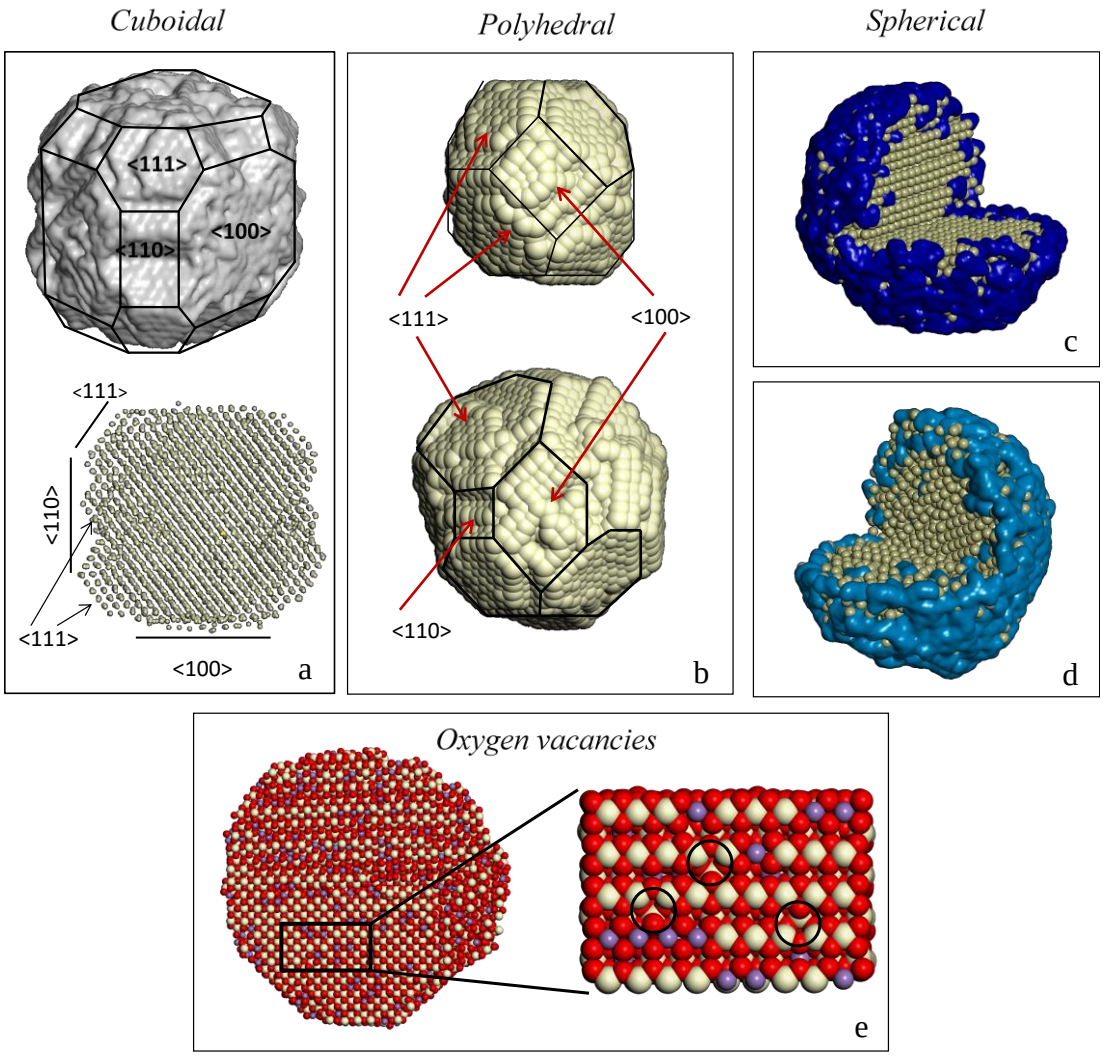

Figure 7.1 Full atomistic models of CeO_2 Nanoparticles, NP: (a) 8 nm nanocube, (b) 6 nm polyhedral NP and 8 nm polyhedral NP, (c) 8 nm core-shell (single crystal core) NP, (d) 8 nm core-shell (polycrystalline core) NP, (e) Partially reduced 8 nm polyhedral NP ($CeO_{1.9}$) showing the presence of oxygen vacancies (circled). A section has been cut from both spherical particles to reveal the inner CeO_2 core. Ce^{4+} ions are represented by white spheres, O^{-2} ions by red spheres and Ce^{3+} ions by purple spheres. Surface rendering is used to show the outer TiO_2 shell.

7.2.4. Method used to perform the uniaxial compression

The mechanical properties are calculated by simulating the nanoparticles under uniaxial compression. In particular, a nanoparticle was positioned at the centre of the simulation cell and two planes of atoms (acting as an "anvil") were inserted perpendicular to the compression direction, Figure 7.2. The nanoparticle is then equilibrated by performing constant pressure (NPT) MD simulation at 300 K for 100 ps.

Uniaxial compression is simulated by moving the planes of atoms (anvils) towards one another under NVT MD simulation at 300 K. In particular, the anvil is moved by 0.01% of the length of the simulation cell followed by MD simulation performed for 100 ps to give an average strain rate of 0.07 m/s. The strain is expressed as:

$$\text{Strain} = (L_O - L_F)/L_O$$

where L_O and L_F correspond to the original and final length of the nanoparticle along the direction of imposed stress respectively; as we only consider uniaxial compression, the strains are all reported as positive values.

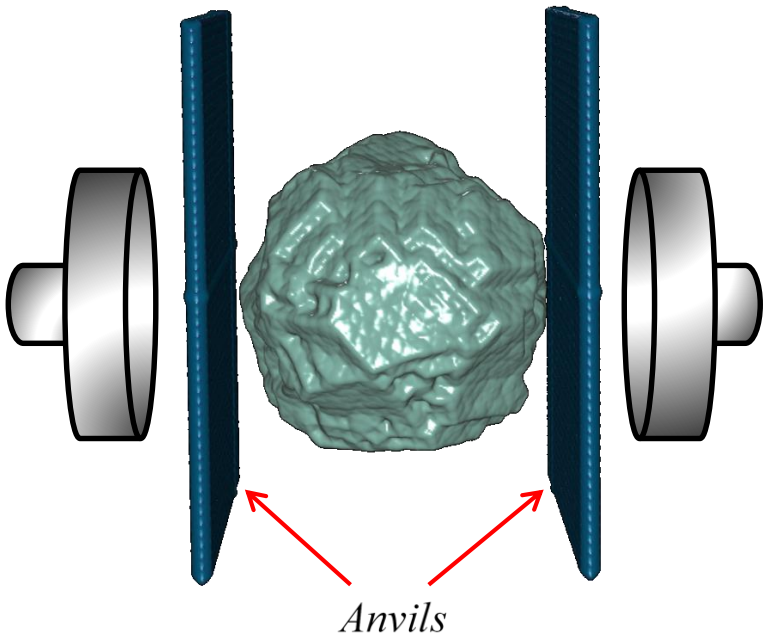

Figure 7.2 Schematic describing the method for imparting uniaxial stress upon the nanoparticles

A similar approach was used previously in order to calculate the mechanical properties of ceria nanorods;[17] however, in that work, the coordinates of all the atoms of the nanorod were scaled at the same time. Here, the nanoparticles are compressed by the repulsive interactions with the plane of atoms (anvils) between them, enabling the strain to travel from the surface to the bulk of the nanoparticles, in accord with how the real material would respond under uniaxial compression.

7.3. Results

In this section, the atomistic structure of the nanoparticles is reported, together with the calculated mechanical properties. In particular, the microstructural features of the nanoparticles have been characterised, in terms of surface exposed, point defects, grain boundaries and dislocations. The result of each simulated uniaxial compression is then reported, focusing the attention on how the microstructure governs the mechanism by which the nanoparticles deform.

7.3.1. Atomistic structure

7.3.1.1. Ceria nanocube

The atomistic structure of the model of the ceria cuboidal nanoparticle was extensively described in Chapter 6. The nanoparticle is a single crystal, exposing the predominant {100} surface with truncated edges and corners exposing the {110} and {111} surfaces respectively. Corrugation of the {110} surface - emanating from faceting into {111} - has been also found and confirmed by experiment, together with the truncation of the corners into {111} faces.[23]

7.3.1.2. Polyhedral nanoparticles

Without the "shape directing" crystalline seed, used to generate the nanocube, the (simulated) crystallisation facilitates polyhedral nanoparticles, which expose thermodynamically stable {111} surfaces truncated by {100}. The model nanoparticles are shown in Figure 7.1(b) (6 nm NP) and Figure 7.1(c) (8 nm NP) and are in structural accord with experiment.[24] Both nanoparticles are polycrystalline; the grain boundaries evolve 'naturally' during the simulated crystallisation. A Coincidence Site Lattice (CSL) theory[25] was used to characterise the grain boundaries within the nanoparticles. In particular, graphical analysis of the 6 nm NP reveals a Σ3 twin grain boundary. This special, highly symmetric grain boundary, also called a coherent twin boundary, can be described as a 60° rotation along <111> of one crystal grain with respect to the other. It has been demonstrated that this grain boundary is energetically stable[10] in ceria. Analysis of the grain boundaries structures in the 8 nm NP reveal a Σ11 grain boundary, which can be described as a rotation of one of the crystal grains by 125º along the <311> crystal plane

7.3.1.3. Spherical Core – Shell nanoparticles

Analysis of the two spherical core-shell ceria nanoparticles reveals one comprises a single crystalline inner ceria core, Figure 7.1(c), whereas the ceria core of the other is polycrystalline, Figure 7.1(d); the amorphous shell of TiO_2 prevents the formation of a faceted surface facilitating the spherical morphology.

7.3.1.4. Oxygen vacancies

Analysis of the reduced ceria nanoparticle, $CeO_{1.9}$, reveals a polyhedral morphology with {111} facets truncated by {100} which is commensurate with the fully oxidised particle. A section of the nanoparticle, viewed along <110>, is shown in Figure 7.1(e); the oxygen vacancies are highlighted by the black rings.

7.3.2. Mechanical properties

In this section, the result of each simulated uniaxial compression will be outlined. In particular, the mechanical properties, such as the compressive strength and the elastic modulus of each nanoparticle, have been calculated from the stress-strain curve, obtained for each simulated compression. The evolution of the crystal structure under the uniaxial compression has been monitored using graphical techniques. In this section, all the images of the nanoparticles represent actual atom positions and are not schematic.

The calculated mechanical properties are shown in Table 7.2, for each of the ceria nanoparticle considered, together with the literature values of the elastic moduli obtained performing experiments with different techniques.

Table 7.2 Mechanical properties calculated for each of the ceria nanoparticles and literature values of bulk moduli.

Nanoparticle	**Diameter**	**Area**	**Yield Strength**	**Yield**	**Elastic Modulus**
	nm	**nm^2**	**GPa**	**Strain**	**GPa**
Cuboidal	8	64	12	0.20	157
6 nm Polyhedral	6	28	10	0.16	84
8 nm Polyhedral	8	50	6	0.10	62
$CeO_{1.9}$ 8 nm NP	8	50	5	0.13	41
TiO_2 – CeO_2 NP	8	50	11	0.13	85
TiO_2 – CeO_2 NP (GB)	8	50	5	0.10	20
Literature	**Bulk Modulus (GPa)**		**Method**		**Reference**
CeO_2 bulk	112 - 174		Small punch (SP)		26, 27
CeO_2 bulk	190 - 264		Nano indentation (ND)		28
CeO_2 – 12 nm	282 - 289		Angular dispersive X-ray diffraction (ADXD)		29
CeO_2 – 6 nm	180		High Pressure XRD		30
CeO_2	249		DFT calculations		31

7.3.2.1. Nanocube

The stress-strain curve reported in Figure 7.3 reveals that the nanocube deforms elastically up to a strain of 0.2 before deforming plastically; plastic deformation usually causes a sudden drop of the stress in the stress-stain curve, Point A, due to the relaxation of the crystal structure. Before strain of 0.20, the nanocube deforms elastically, with a non-linear slope; the elastic modulus has been calculated to be 157 GPa, Table 7.2. After strain of 0.20, the nanocube deforms plastically via a crystalline-to-amorphous transition, nearby the surface of the nanocube, Figure 7.4(c-d). Further compression of the nanocube causes the formation of a screw dislocation that terminates at a grain boundary and provides a vehicle for further plastic deformation, corresponding at a strain value of 0.225. Images of the nanocube during this second plastic deformation are shown in Figure 7.4(e-f) and the screw dislocation is shown in the enlarged pictures in Figure 7.4(g-i). The screw dislocation does not traverse all the length of the nanocube, rather terminates at a low-angle grain boundary, induced by the compression and shown enlarged in Figure 7.4(j). The compressive strength of the nanocube has been calculated to be 12 GPa, corresponding to Point A in the stress-strain curve.

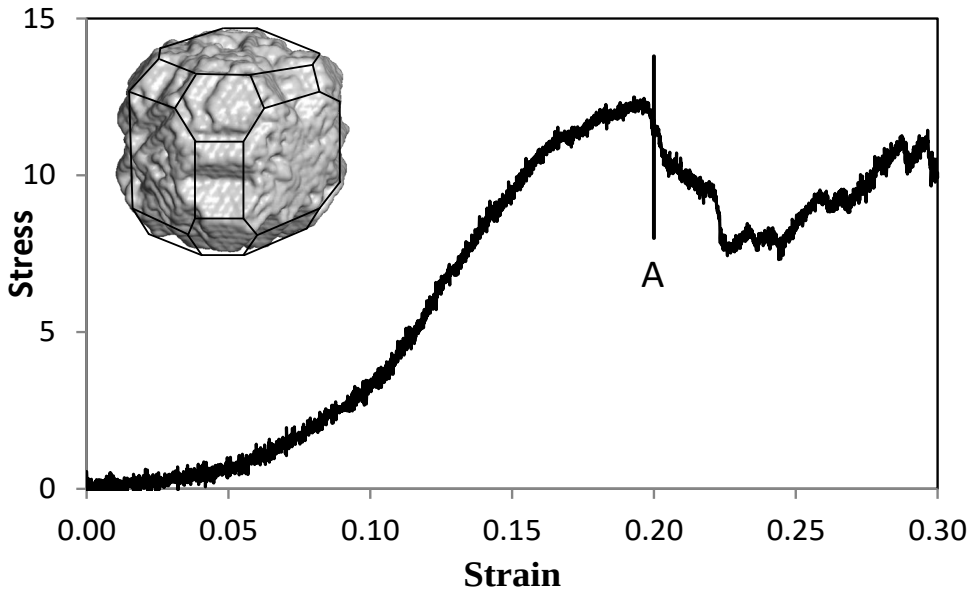

Figure 7.3 Stress-strain curve for the compression of the cuboidal ceria nanoparticle. Stress values are in GPa.

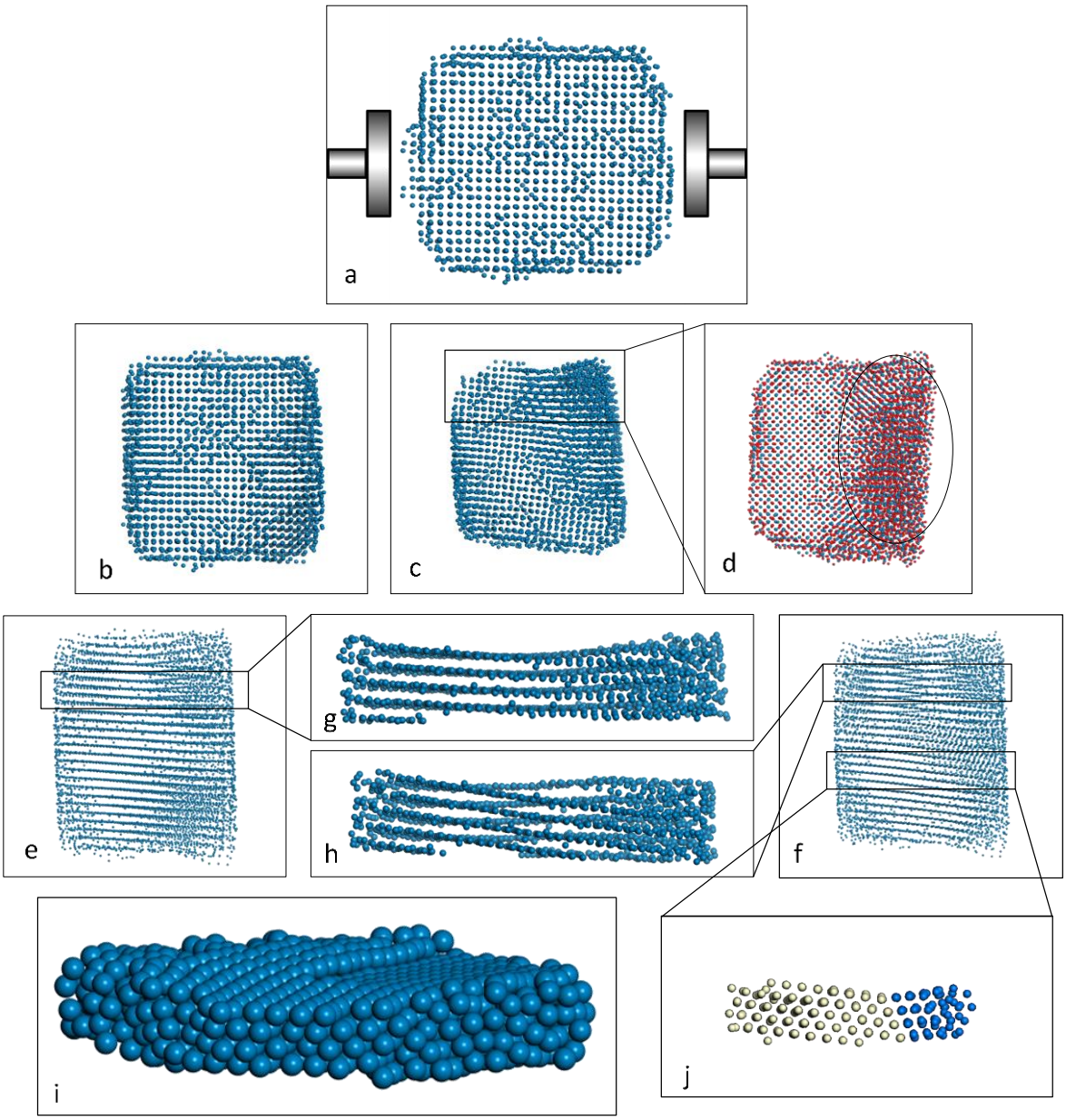

Figure 7.4 Deformation mechanism of the ceria nanocube. (a) Image showing the direction of the uniaxial compression (unstrained nanoparticle), (b) strain=0.197, (c) strain=0.213: first plastic deformation of the nanocube, (d) strain=0.213: amorphized region after the first plastic deformation; oxygen atoms are also shown, coloured red, (e) and (f) nanocube before and after the second plastic deformation corresponding strains of 0.221 and 0.225 respectively, (g) and (h) enlarged sections of (e) and (f) respectively to show more clearly the dislocation traversing the nanocube, (i) enlarged view of the screw dislocation occurring after strain of 0.225, (j) structure of a grain boundary, which forms after the second plastic deformation; cerium ions are coloured white or blue to show the structure of the grain boundary more clearly. All the images represent actual atom positions and are not schematic**.**

7.3.2.2. 6 nm polyhedral nanoparticle

The small polyhedral nanoparticle is weaker than the nanocube and exhibits a compressive strength of 10 GPa with a corresponding strain value of 0.16, Point A, Figure 7.5. The nanoparticle deforms elastically up to this strain value and then suffers plastic deformation, driven by lattice slip along the Σ3 grain boundary. This grain boundary is already present within the structure of the nanoparticle, from its crystallisation. In order to highlight the grain boundary, in Figure 7.6 the Ce atoms of different crystallites are coloured differently. In particular, two Σ3 grain boundaries are present within the structure. One of these two grain boundaries provides the vehicle for the plastic deformation, at strain value of 0.16. The mechanism of this plastic deformation is shown in the enlarged pictures in Figure 7.6(e-g), which show the lattice slip along this grain boundary. A screw dislocation evolves at higher strain values, Figure 7.5, Point B, shown in Figure 7.6(h) and enlarged in Figure 7.6(i). Similarly to the nanocube, amorphisation also occurs near the surface, Figure 7.6(j).

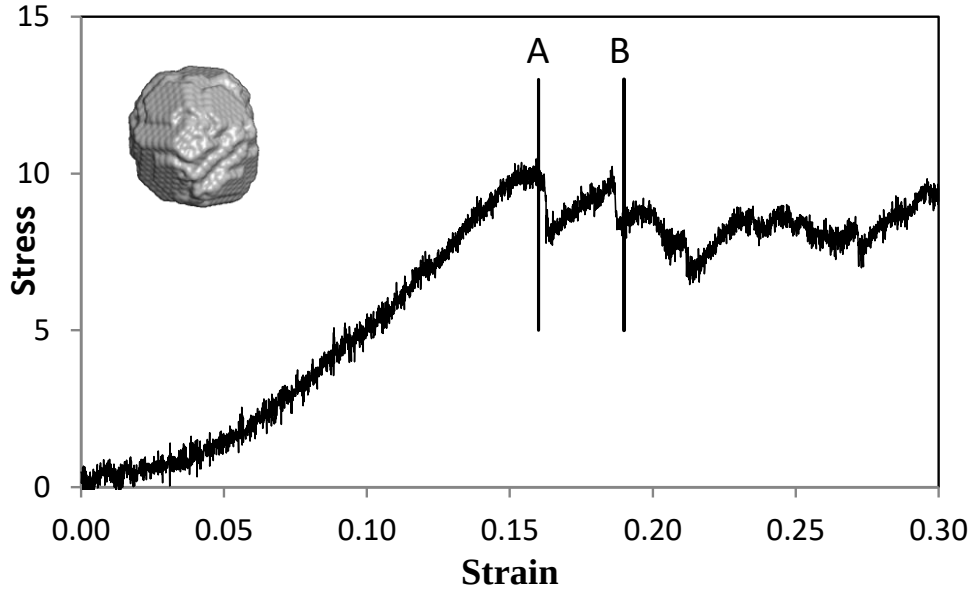

Figure 7.5 Stress-strain curve for the compression of the 6 nm polyhedral ceria nanoparticle. . Stress values are in GPa.

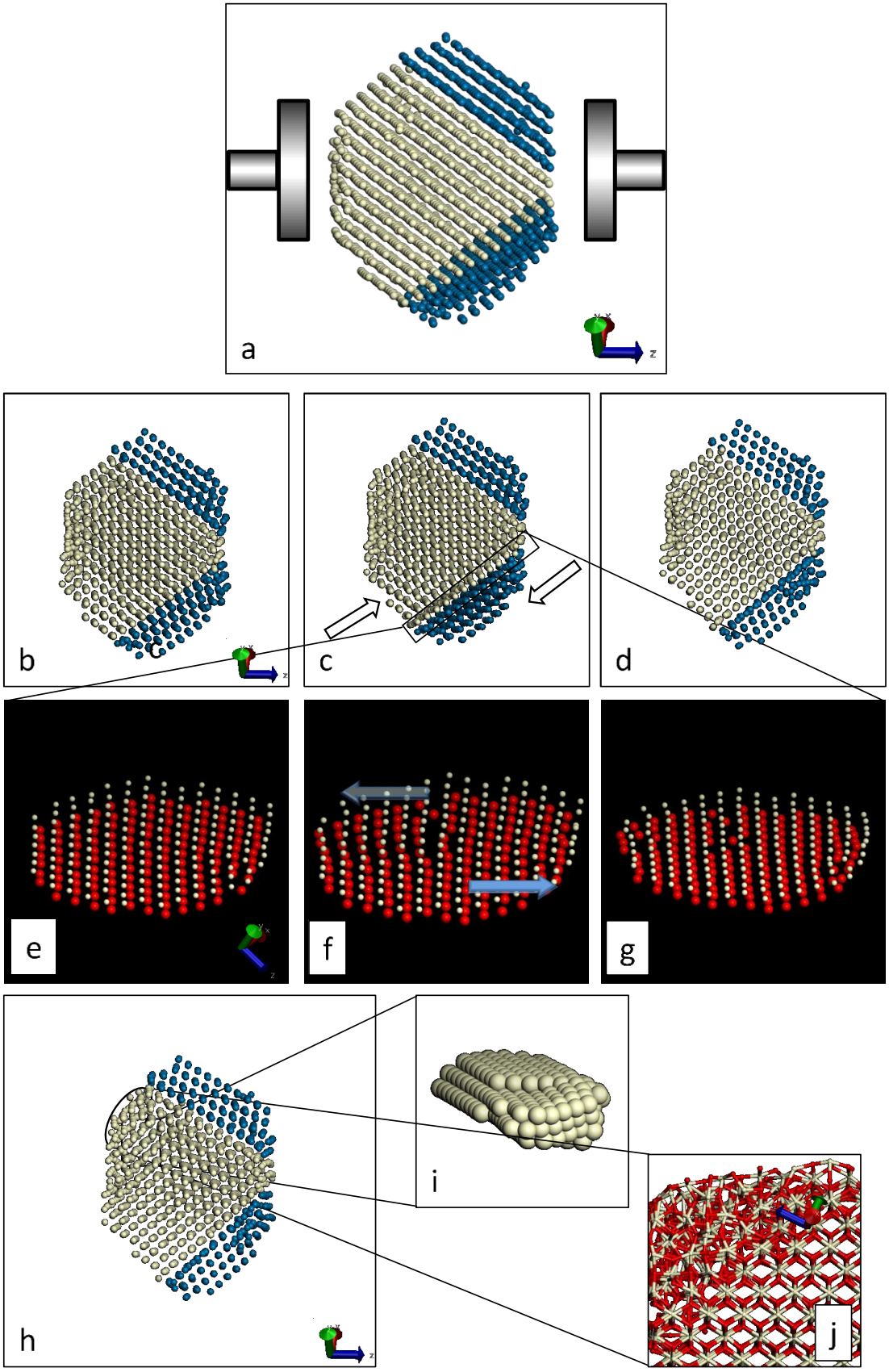

Figure 7.6 Deformation mechanism of the 6 nm NP: (a) image showing the direction of the simulated uniaxial compression. (b, e) Strain=0.160, (c, f) strain=0.163, (d, g) strain=0.165; (e-g) show more clearly the Σ3 grain boundary under compression, (h) strain=0.194, (i) enlarged segment of (h) showing the formation of a screw dislocation, (j) enlarged segment of (h) showing the amorphized region.

7.3.2.3. 8 nm polyhedral nanoparticle

In Figure 7.7, two stress-strain curve are reported: the black curve refers to the fully oxidized polyhedral nanoparticle; the red one is relative to the compression of the partially reduced ceria polyhedral nanoparticle, comprising 5% oxygen vacancies and 20% of the Ce^{4+} atoms reduced to Ce^{3+}.

The effect of the increased size of the nanoparticle is its reduced compressive strength, from 10GPa (6 nm polyhedral nanoparticle) to 6 GPa (8 nm), pressure at which the nanoparticles deforms plastically. The partially reduced nanoparticle undergoes the first plastic deformation at pressure of 5 GPa, therefore appears 16% weaker compared with the fully oxidized one. The presence of oxygen vacancies within the crystal structure besides impacts on the elastic deformation of the nanoparticle, with a calculated elastic modulus 34% lower compared with the fully oxidized nanoparticle, Table 7.2.

The evolution of the crystal structure during the simulated compression of the fully oxidized nanoparticle is shown in Figure 7.8. The close inspection of the behaviour of the two crystallites along the Σ11 grain boundary reveals that one grain grows in size at the expense of the other, which is indicative of Oswald ripening.[32] In particular, the

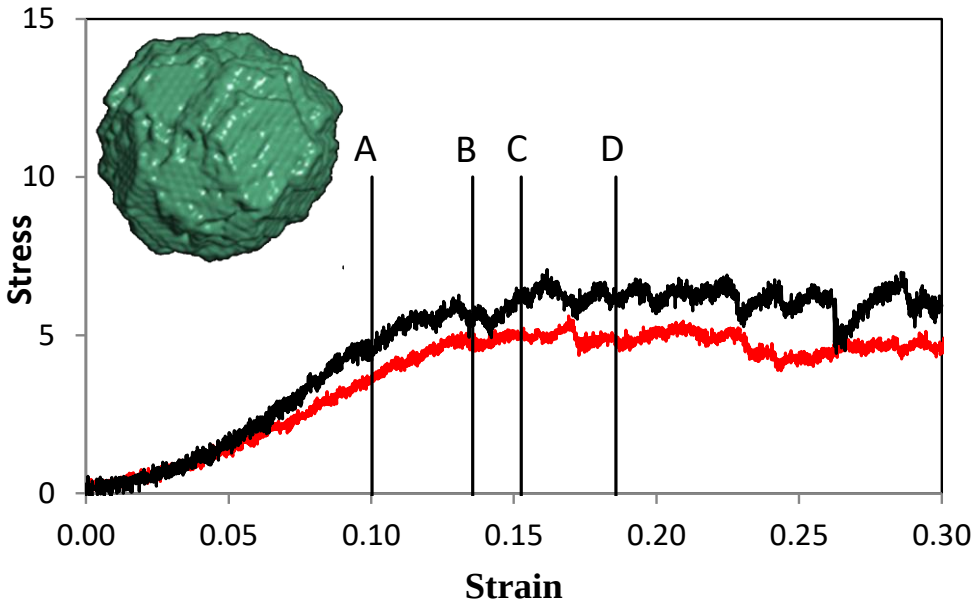

Figure 7.7 Stress-strain curves of the fully oxidized (black line) and partially reduced (red line) 8 nm polyhedral nanoparticle. Stress values are in GPa.

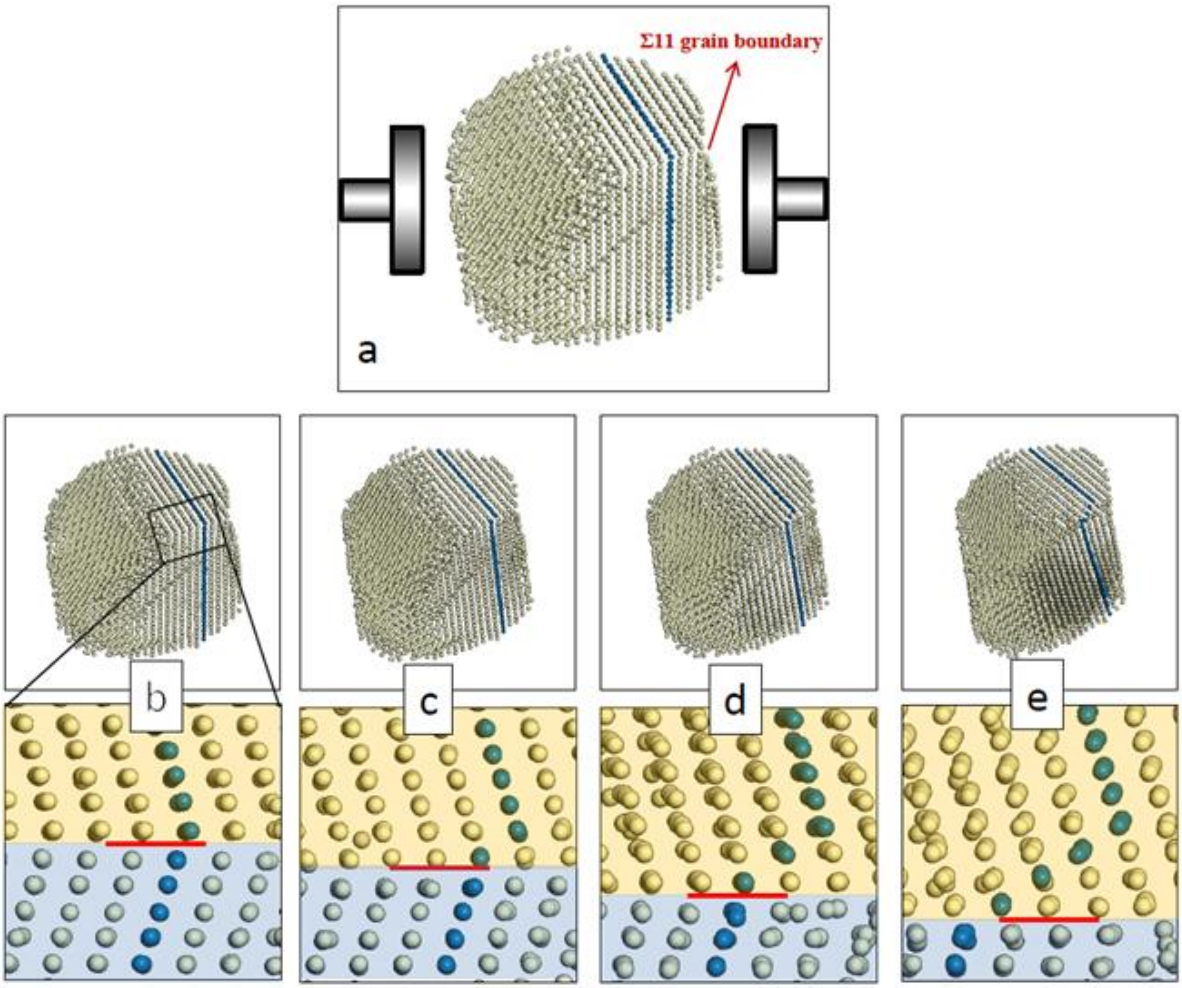

Figure 7.8 Atomistic structures of the 8nm polyhedral NP under uniaxial strain: (a) strain=0.000, (b) strain=0.100, (c) strain=0.118, (d) strain=0.153, (e) strain=0.186. A segment of the nanoparticle, viewed along <110> at each strain state, reveals more clearly the grain boundary. Indicative of Oswald ripening, the top grain (yellow) consumes the bottom grain (blue); only cerium atoms are shown for clarity.

top grain (yellow) grows by consuming the bottom grain (blue). The images, Figure 7.8(b-e) correlate with points A-D on the stress–strain curve, Figure 7.7. During the plastic deformation, the compressive strength of the nanoparticle increases from 4.7 to 7.0 GPa.

7.3.2.4. Core-Shell TiO_2-CeO_2 nanoparticles

The stress-strain curves for both the single crystalline and polycrystalline TiO_2-CeO_2 core-shell nanoparticles are reported in Figure 7.9. The nanoparticle comprising a single crystalline core deforms elastically up to a strain of 0.13, Figure 7.9, point A. At higher strain values, the nanoparticle deforms plastically with amorphisation of the ceria at the interfacial region, Figure 7.10(e-g). The ultimate yield strength of 11 GPa is reached at 0.34 strain, Figure 7.9, point B and Figure 7.10(j). The core-shell nanoparticle with a polycrystalline ceria core, perhaps unsurprisingly, is weaker compared to its single crystal counterpart; the yield strength at 0.10 strain is only 2.3 GPa, Figure 7.9, point A^I (red trace). Plastic deformation, driven by grain-boundary slip occurs at uniaxial stresses above 2.3 GPa; deformation mechanisms are presented in Figure 7.11. The plastic deformation of the nanoparticle is in this case driven by the presence of the grain boundary, Figure 7.11(e-f).

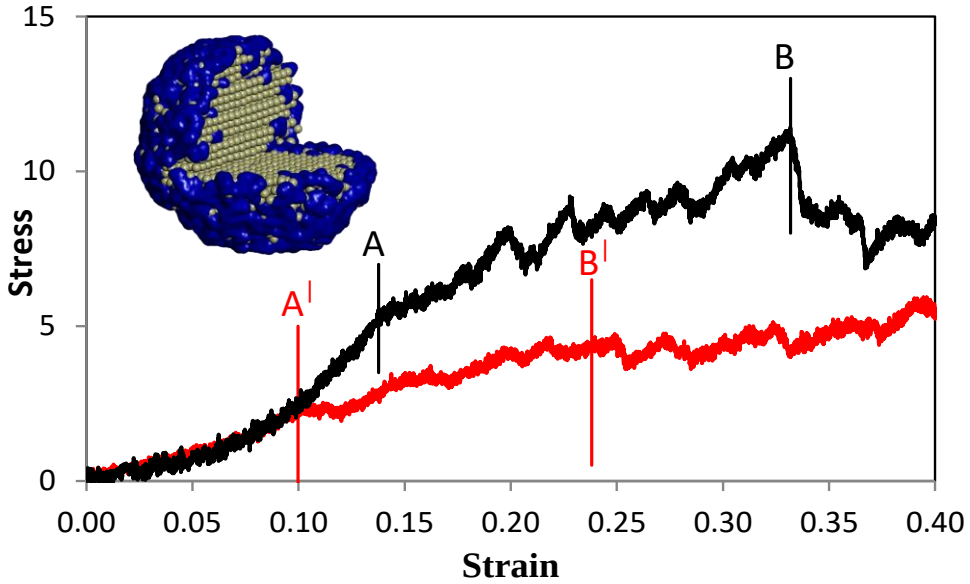

Figure 7.9 Stress-strain curves of the single crystalline (black) and polycrystalline (red) TiO_2-CeO_2 core shell nanoparticles. Stress values are in GPa.

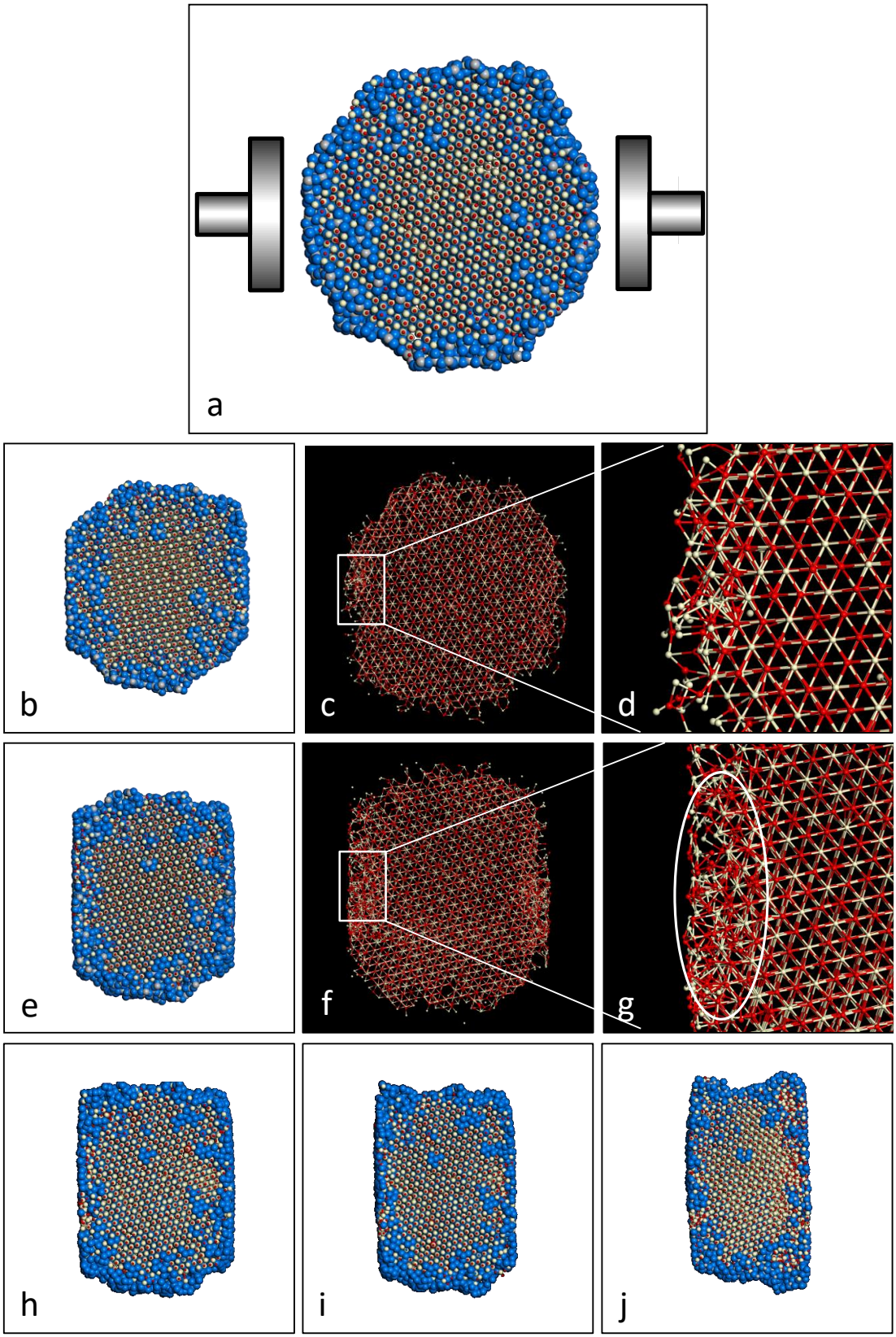

Figure 7.10 Deformation mechanism of the spherical TiO_2–CeO_2 core-shell nanoparticle comprising a single-crystal CeO_2 core. (a) Segment of the nanoparticle, viewed along <111> of the crystal core, showing the direction of the uniaxial compression, (b) strain=0.128, (c) as (b) showing only the ceria core, which is enlarged in (d), (e) strain=0.211, (f) as (e) showing only the ceria core, which is enlarged in (g) to reveal the amorphisation at the TiO_2 – CeO_2 interface, (h) strain=0.250, (i) strain=0.286, (j) strain=0.341. Cerium is coloured white, titanium is grey, oxygen (CeO_2) is red and oxygen (TiO_2) is blue.

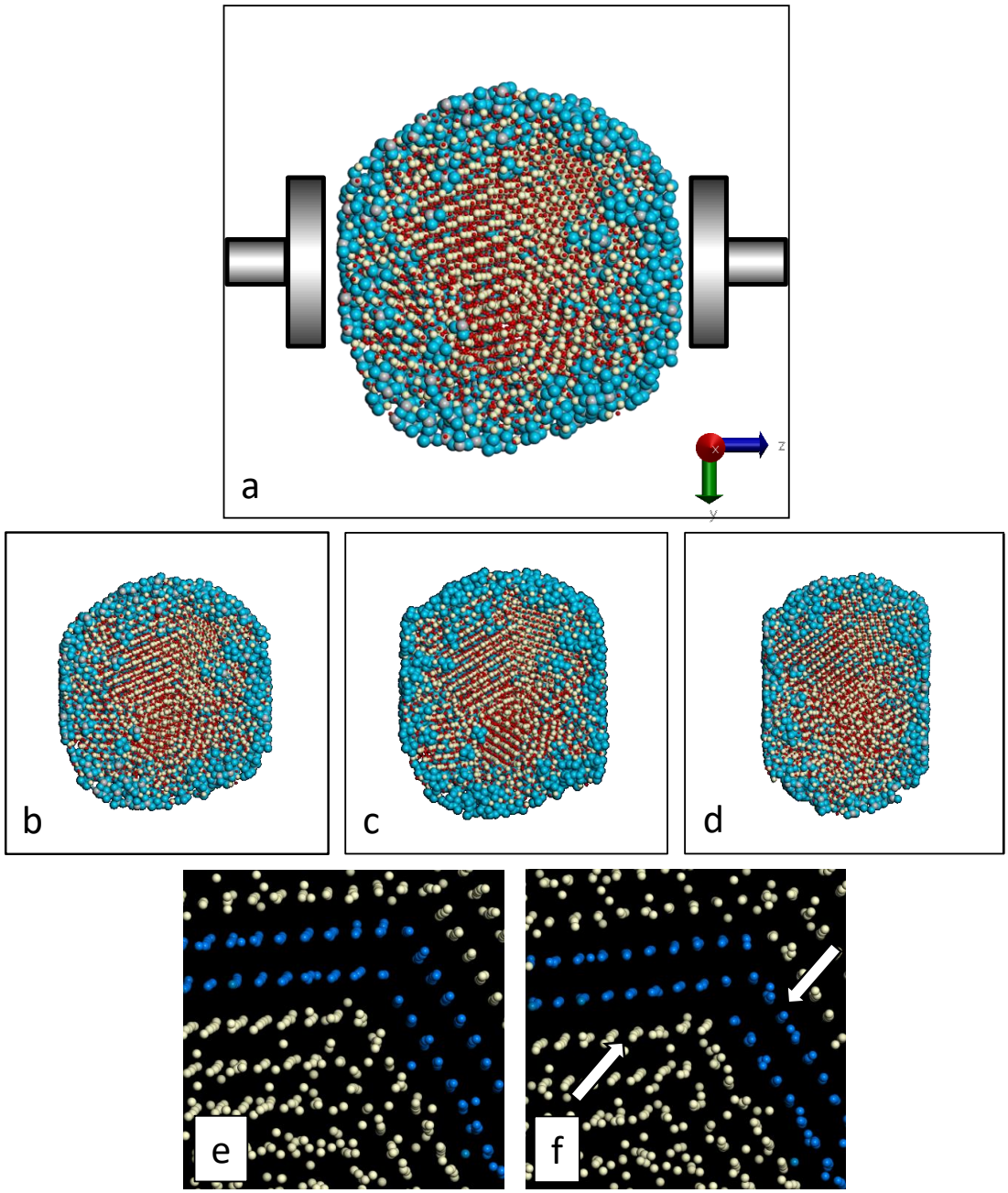

Figure 7.11 Deformation mechanism of the spherical TiO_2–CeO_2 core-shell nanoparticle comprising a polycrystalline CeO_2 core. (a) Segment of the nanoparticle showing the direction of the uniaxial compression, (b) strain=0.100, (c) strain=0.158, (d) strain=0.238. Deformation, via grain boundary slip, is shown in (e) strain=0.158 and (f) strain=0.175.

7.4. Discussion

7.4.1. Grain boundary content

The mechanical properties of ceria nanoparticles are profoundly influenced by the presence of extended defects such as grain boundaries. Figure 7.12 compares the yield strength for all the ceria nanoparticles studied: the cuboidal nanoparticle and the core-shell nanoparticles with a single crystalline ceria core present the highest yield strength, as grain boundaries are not present. The presence of grain boundaries in the other nanoparticles contribute to the decrease of their yield strength and provide the vehicle for the plastic deformation.

The nature of the grain boundary play also an important role: our simulations demonstrate that a nanoparticle comprising a Σ3 grain boundary is 66% stronger than the nanoparticle comprising a Σ11 grain boundary.

The simulated compression of the 8 nm polyhedral nanoparticle reveal that Ostwald ripening can be induced, by applying uniaxial compression, along a Σ11 grain

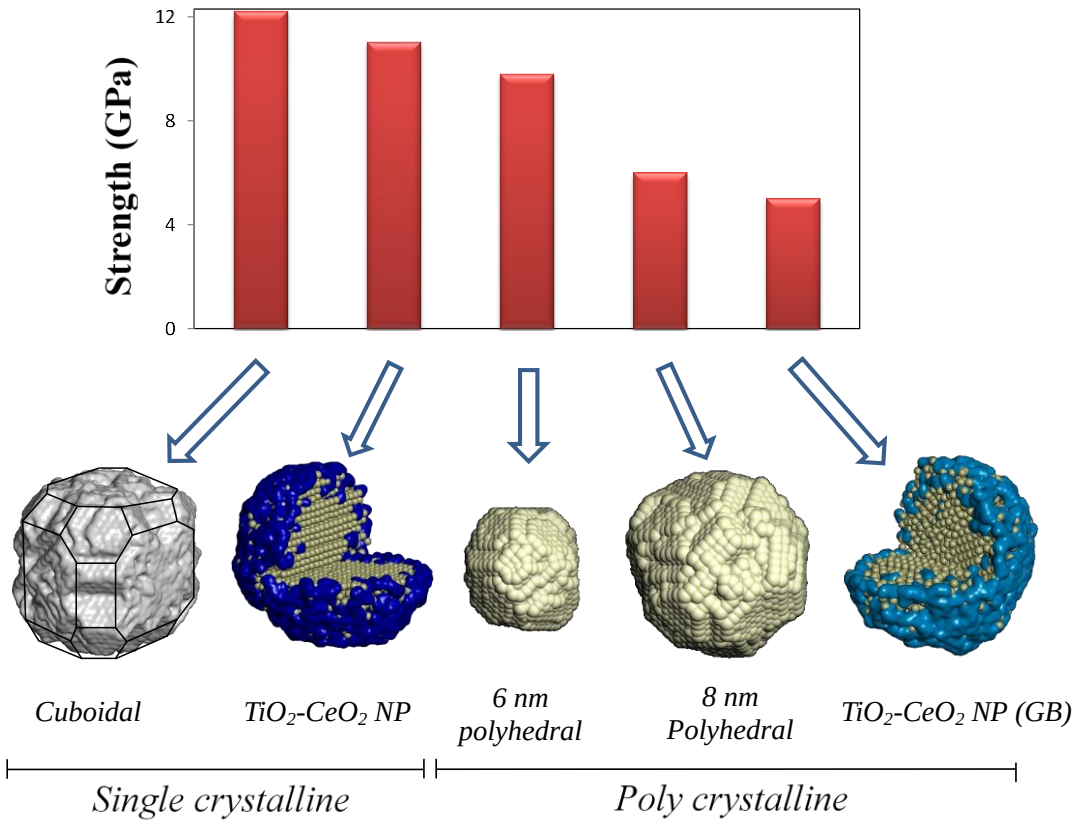

Figure 7.12 Compressive strengths of each of the ceria nanoparticles

boundary. This grain boundary is thus purged from the nanoparticle to facilitate the formation (crystal growth) of a single crystal. On the other hand, the simulations show that a single crystalline ceria nanocube form a screw dislocation and a low angle grain boundary under compression. This has important consequences on the possibility of tune the properties of a nanomaterial by applying uniaxial force.

It has been shown that grain boundaries dominate the ionic transport properties of the materials.[33] A review by Guo and Waser[34] details that 'grain-boundary conductivities of acceptor-doped zirconia and ceria are at least two orders of magnitude lower than the corresponding bulk values, depending on temperature and dopant level'.

Furthermore, a review by Landau and co-workers details the importance of engineering the content of grain boundaries in order to impact on the catalytic activity of a material. The consolidation of nanocrystals with the formation of grain boundary areas can lead to an increase of the chemical reactivity by one order of magnitude,[35] despite the decrease of the specific surface area. This is attributed to the presence of a high concentration of defects and ions with low coordination, which represent potentially active catalytic sites.

Our simulations demonstrate that grain boundaries could be induced or purged in the material via strain; the ability to mechanically engineer the grain-boundary content of a material therefore impacts upon technological important areas such as solid oxide fuel cells[36] and catalysis.[35]

7.4.2. Models with full microstructure

Atomistic models, used to calculate the mechanical properties of a material, must include all the microstructural features observed experimentally. Point defects, such as oxygen vacancies, must be present, as well as extended defects, such as grain boundaries and dislocations. In this sense, the amorphisation and re-crystallisation technique is successful in embedding all these microstructural features within the models and therefore in finding accord with experiments on the calculated properties.

Table 7.2 summarises the results obtained in this work and show a comparison with some of the results found in the literature on mechanical tests on bulk and nanoceria. Our calculated elastic moduli are lower than those determined experimentally;

however, it must be noted that experimental values change by more than 130% depending on the method used.

Wang et al.[37] used nanoindentation to determine the elastic moduli of fully oxidized and partially reduced pure and gadolinium doped ceria. The reduced ceria was prepared by thermally treating the sample at 800 ºC for 15h under oxygen partial pressure of 10^{-25} atm., promoting the formation of oxygen vacancies. They found that the elastic moduli of the reduced sample decreased by 28% when oxygen vacancies were formed. Our simulations predict that the elastic modulus of the partially reduced polyhedral nanoparticle, comprising 5% oxygen vacancies, is about 30% lower compared to the fully oxidized nanoparticle, in line with experiment.

Another group of research studied the mechanical properties of nanocrystalline ceria by performing high-pressure angular dispersive X-ray diffraction (ADXD) measurements.[29] They found that nanoceria exhibit negative volume compressibility (NVC) when isotropic pressure is applied using silicon oil as pressure transmitting medium. NVC identifies an increase of the volume of the unit cell of the crystal structure as consequence of the increase of the isotropic pressure. The authors explained this unusual phenomenon by considering the nanocrystal as a (crystalline) core – (amorphous) shell system, due to its high content of surface atoms, which are out of lattice position. The authors explain that, under isotropic pressure, the amorphous shell first undergoes a low density amorphous to high density amorphous (LDH-HDA) transition. Further increase of the isotropic pressure causes a transition of some layers of the crystalline core of the nanoparticle to the amorphous state, increasing the thickness of the amorphous shell. In this way, the crystal core can relax and an increase in its unit cell volume is observed, as X-ray diffraction can detect just the crystalline phase.

Our simulations provide evidence to this effect. In particular, we note amorphisation at the surface of the nanocrystal in the cuboidal nanoparticle, Figure 7.4(d), and at the interphase in the core-shell TiO_2-CeO_2 nanoparticle, Figure 7.10(g).

Our simulations also find accord with other simulations run by our group. In particular, in a previous work, nanorods with Σ3 grain boundaries were calculated to have a compressive strength of 10 GPa.[17] In that work, a different method was used to run the simulated compression: all atoms coordinates were progressively scaled imposing

strain within the all crystal structure at same time. Despite this difference with the method, with our simulations we found that the 6 nm polyhedral nanoparticle, which comprises a Σ3 grain boundary, has a compressive strength of 10 GPa, identical to the nanorod. This suggests that the nature of grain boundary plays a more important role than the shape of the nanoparticle. Indeed, the 8 nm NP, which includes a Σ11 grain boundary, has a compressive strength of only 6 GPa.

7.5. Conclusions

The amorphisation and re-crystallisation technique was used to generate atomistic models of ceria nanoparticles with rich microstructure (oxygen vacancies, surfaces exposed, grain boundaries and dislocations), spanning various sizes (6-8 nm) and shapes (nanocube, polyhedral, spherical), nanoform (core-shell) and oxidation state (fully oxidized CeO_2, reduced $CeO_{1.9}$). Uniaxial compression of these nanoparticles was then simulated, in order to calculate the mechanical properties and elucidate upon the mechanism behind their plastic deformation.

We found that grain boundaries play the strongest influence on the yield strength and elastic moduli of the nanoparticles. Our simulations also predict strain-induced Ostwald ripening along a Σ11 grain boundary, enabling mechanical control on the microstructure and therefore on the properties of the material.

7.6. References

[1] Na, T.A., Liu, J. and Wenjie, S.H.E.N., 2013. Tuning the shape of ceria nanomaterials for catalytic applications. *Chinese Journal of Catalysis*, 34(5), pp.838-850.

[2] Corma, A., Atienzar, P., Garcia, H. and Chane-Ching, J.Y., 2004. Hierarchically mesostructured doped CeO_2 with potential for solar-cell use. *Nature Materials*, 3(6), pp.394-397.

[3] Malavasi, L., Fisher, C.A. and Islam, M.S., 2010. Oxide-ion and proton conducting electrolyte materials for clean energy applications: structural and mechanistic features. *Chemical Society Reviews*, 39(11), pp.4370-4387.

[4] Chen, J., Patil, S., Seal, S. and McGinnis, J.F., 2006. Rare earth nanoparticles prevent retinal degeneration induced by intracellular peroxides. *Nature Nanotechnology*, 1(2), pp.142-150.

[5] Oh, M.H., Nho, J.S., Cho, S.B., Lee, J.S. and Singh, R.K., 2011. Polishing behaviour of ceria abrasives on silicon dioxide and silicon nitride CMP. *Powder Technology*, 206(3), pp.239-245.

[6] Brezesinski, T., Wang, J., Senter, R., Brezesinski, K., Dunn, B. and Tolbert, S.H., 2010. On the correlation between mechanical flexibility, nanoscale structure, and charge storage in periodic mesoporous CeO_2 thin films. *ACS Nano*, 4(2), pp.967-977.

[7] Warren, O.L., Shan, Z., Asif, S.S., Stach, E.A., Morris, J.W. and Minor, A.M., 2007. In situ nanoindentation in the TEM. *Materials Today*, 10(4), pp.59-60.

[8] Shin, C., Jeon, I., Jeon, S. and Khim, Z.G., 2009. Single nanoparticle alignment by atomic force microscopy indentation. *Applied Physics Letters*, 94(16), p.163107.

[9] Han, X., Zhang, Y., Zheng, K., Zhang, X., Zhang, Z., Hao, Y.J., Guo, X.Y., Yuan, J. and Wang, Z.L., 2007. Low-temperature in situ large strain plasticity of ceramic SiC nanowires and its atomic-scale mechanism. *Nano Letters*, 7(2), pp.452-457.

[10] Suresh, S. and Li, J., 2008. Materials science: deformation of the ultra-strong. *Nature*, 456(7223), pp.716-717.

[11] Guo, D., Xie, G. and Luo, J., 2013. Mechanical properties of nanoparticles: basics and applications. *Journal of Physics D: Applied Physics*, 47(1), p.013001.

[12] Pergolesi, D., Fabbri, E., Cook, S.N., Roddatis, V., Traversa, E. and Kilner, J.A., 2012. Tensile lattice distortion does not affect oxygen transport in yttria-stabilized zirconia–CeO_2 heterointerfaces. *ACS Nano*, 6(12), pp.10524-10534.

[13] Sayle, T.X., Sayle, L.W. and Sayle, D.C., 2015. Liquid crystal seed nucleates liquid–solid phase change in ceria nanoparticles. *Physical Chemistry Chemical Physics*, 17(6), pp.4441-4447.

[14] Guo, X. and Waser, R., 2006. Electrical properties of the grain boundaries of oxygen ion conductors: acceptor-doped zirconia and ceria. *Progress in Materials Science*, 51(2), pp.151-210.

[15] Sayle, T.X.T., Parker, S.C. and Catlow, C.R.A., 1994. The role of oxygen vacancies on ceria surfaces in the oxidation of carbon monoxide. *Surface Science*, 316(3), pp.329-336.

[16] Catlow, C.R.A., Freeman, C.M. and Royle, R.L., 1985. Recent studies using static simulation techniques. *Physica B+ C*, 131(1), pp.1-12.

[17] Sayle, T.X., Inkson, B.J., Karakoti, A., Kumar, A., Molinari, M., Möbus, G., Parker, S.C., Seal, S. and Sayle, D.C., 2011. Mechanical properties of ceria nanorods and nanochains; the effect of dislocations, grain-boundaries and oriented attachment. *Nanoscale*, 3(4), pp.1823-1837.

[18] Smith, W. and Forester, T.R., 1996. DL_POLY_2. 0: A general-purpose parallel molecular dynamics simulation package. *Journal of Molecular Graphics*, 14(3), pp.136-141.

[19] Feng, X., Sayle, D.C., Wang, Z.L., Paras, M.S., Santora, B., Sutorik, A.C., Sayle, T.X., Yang, Y., Ding, Y., Wang, X. and Her, Y.S., 2006. Converting ceria polyhedral nanoparticles into single-crystal nanospheres. *Science*, 312(5779), pp.1504-1508.

[20] Sayle, T.X., Parker, S.C. and Sayle, D.C., 2004. Shape of CeO_2 nanoparticles using simulated amorphisation and re-crystallisation. *Chemical Communications*, (21), pp.2438-2439.

[21] Sayle, D.C., Feng, X., Ding, Y., Wang, Z.L. and Sayle, T.X., 2007. "Simulating Synthesis": ceria nanosphere self-assembly into nanorods and framework architectures. *Journal of the American Chemical Society*, 129(25), pp.7924-7935.

[22] Cormack, A.N., Lamphier, S., Wang, B., Gubb, T. and Reed, K., 2015, Simulations of ceria nanoparticles. *Proceedings of the Royal Society A*, 471, 2182, 20150218.

[23] Bhatta, U.M., Reid, D., Sakthivel, T., Sayle, T.X., Sayle, D., Molinari, M., Parker, S.C., Ross, I.M., Seal, S. and Möbus, G., 2013. Morphology and surface analysis of pure and doped cuboidal ceria nanoparticles. *The Journal of Physical Chemistry C*, 117(46), pp.24561-24569.

[24] Tan, J.P.Y., Tan, H.R., Boothroyd, C., Foo, Y.L., He, C.B. and Lin, M., 2011. Three-dimensional structure of CeO_2 nanocrystals. *The Journal of Physical Chemistry C*, 115(9), pp.3544-3551.

[25] Grimmer, H., Bollmann, W.T. and Warrington, D.H., 1974. Coincidence-site lattices and complete pattern-shift in cubic crystals. *Acta Crystallographica Section A: Crystal Physics, Diffraction, Theoretical and General Crystallography*, 30(2), pp.197-207.

[26] Sato, K., Yugami, H., Hashida, T., 2004. Effect of rare-earth oxides on fracture properties of ceria ceramics. *Journal of Materials Science*, 39(18), pp.5765-5770.

[27] Sato, K., Suzuki, K., Yashiro, K., Kawada, T., Yugami, H., Hashida, T., Atkinson, A., Mizusaki, J., 2009. Effect of Y_2O_3 addition on the conductivity and elastic modulus of $(CeO_2)_{1-x}(YO_{1.5})_x$. *Solid State Ionics*, 180(20), pp.1220-1225.

[28] Wang, Y., Duncan, K., Wachsman, E. D., Ebrahimi, F. 2007. The effect of oxygen vacancy concentration on the elastic modulus of fluorite-structured oxides. *Solid State Ionics*, 178(1), pp.53-58

[29] Wang, Q., He, D., Peng, F., Lei, L., Liu, P., Shuai, Y., Wang, P., Xu, C., Liu, J., 2014. Unusual compression behaviour of nanocrystalline CeO_2. *Scientific Reports*, 4, 4441, pp. 1-8

[30] Rodenbough, P.P., Song, J., Walker, D., Clark, S.M., Kalkan, B., Chan, S.W., 2015. Size dependent compressibility of nano-ceria: Minimum near 33 nm. *Applied Physics Letters*, 106(16), 163101, pp.1-5

[31] Nakajima, A., Yoshihara, A., Ishigame, M. 1994, Defect-induced raman spectra in doped CeO_2. *Physical Review B*, 50(18), 13297

[32] Hansen, T.W., DeLaRiva, A.T., Challa, S.R. and Datye, A.K., 2013. Sintering of catalytic nanoparticles: particle migration or Ostwald ripening?. *Accounts of Chemical Research*, 46(8), pp.1720-1730.

[33] An, J., Bae, J., Hong, S., Koo, B., Kim, Y.B., Gür, T.M. and Prinz, F.B., 2015. Grain boundary blocking of ionic conductivity in nanocrystalline yttria-doped ceria thin films. *Scripta Materialia*, 104, pp.45-48.

[34] Guo, X. and Waser, R., 2006. Electrical properties of the grain boundaries of oxygen ion conductors: acceptor-doped zirconia and ceria. *Progress in Materials Science*, 51(2), pp.151-210.

[35] Landau, M.V., Vidruk, R., Vingurt, D., Fuks, D. and Herskowitz, M., 2014. Grain boundaries in nanocrystalline catalytic materials as a source of surface chemical functionality. *Reviews in Chemical Engineering*, 30(4), pp.379-401.

[36] Ye, F., Yin, C.Y., Ou, D.R. and Mori, T., 2014. Relationship between lattice mismatch and ionic conduction of grain boundary in YSZ. *Progress in Natural Science: Materials International*, 24(1), pp.83-86.

[37] Wang, Y., Duncan, K., Wachsman, E.D. and Ebrahimi, F., 2007. The effect of oxygen vacancy concentration on the elastic modulus of fluorite-structured oxides. *Solid State Ionics*, 178(1), pp.53-58.

CONCLUSIONS AND FUTURE WORK

In this thesis, experiment and atomistic simulation have been used to synthesise and study new nanostructured materials with specific properties.

Experimentally, a series of nanocomposites where metal oxide nanoparticles are dispersed within the porous architecture of silica aerogel and/or xerogel have been presented in Chapters 3, 4 and 5. All the nanocomposites synthesised present a good dispersion of the nanocrystalline phase within the silica matrix. It has been shown that the aerogel matrix plays a very important role, preventing the coalescence of the nanoparticles under high temperature thermal treatments, which is very important for the many applications suitable for these materials.

The use of capping agents during the syntheses has been explored, and has played an important role for the synthesis of the nanocomposites where ceria nanoparticles were grown within the silica matrix. It was shown that, in the case of the aerogels, ceria nanoparticles crystallise during the supercritical extraction of the solvent. In particular, when dodecanoic acid or hexanoic acid was used, the nanoparticles crystallise first within aggregates, and then are re-dispersed in the matrix by diffusion under a high temperature thermal treatment. However, the formation of the aggregates could be due to the dodecanoic acid, which probably undergoes a thermal decomposition inside the autoclave. Capping agents with a higher decomposition temperature, such as oleic acid, could be also used to synthesise this kind of nanocomposites, with the aim to obtain a better dispersion of the ceria nanophase already after the supercritical extraction.

A second approach has been also used to synthesise these nanocomposites, consisting in the pre-synthesis of the ceria nanoparticles and in their subsequent dispersion. This method allows a better control of the crystallisation of the nanoparticles, which can be finely tuned by hydrothermal method. In this case, capping agents such as dodecanoic acid and oleic acid are used to synthesise ceria nanoparticles with a specific shape, polyhedral and cuboidal respectively. The ability of tuning the shape of the nanoparticles is very important, as their reactivity is shape-dependent. Their dispersion

in an aerogel matrix has been performed in order to be able to remove the surfactant from the surface of the nanoparticles while keeping the nanoparticles apart, avoiding their coalescence, and leading to a material with a potentially enhanced reactivity. This method could also form the basis of a more general use of the technique, where nanomaterials are pre-synthesised by finely tuning their microstructural features using capping agents, and then dispersed and stabilized within and amorphous matrix, allowing the removal of the capping agent from the reactive surface.

However, in Chapter 5 it has been shown that the characterisation of these nanocomposites is still challenging. In particular, it was difficult to determine by HRTEM whether the cubic nanoparticles within the silica matrix retain their shape after the capping agent has been removed. This is because each nanoparticle is randomly oriented within the pores of the matrix. An atomistic model of a ceria nanoparticle with cubic shape, obtained using MD simulation and presented in Chapter 6, has been then used to reproduce each specific orientation, confirming that the nanoparticles likely retain their shape.

Additional information could be obtained using XANES, taking into account that different shapes of nanoparticles are expected to have a different Ce^{3+}/Ce^{4+} ratio, which influence the position of the L(III)-edge. Preliminary results confirm that the technique is able to highlight a higher amount of Ce^{3+} in the aerogel sample containing nanocubes.

The atomistic model of the cubic ceria nanoparticle has been obtained by simulating the crystallisation of the amorphous precursor, which ensures to obtain models in quantitative agreement with experiment. During this simulation, a new technique has been used, which consist in employing a crystalline seed, driving the crystallisation of the nanoparticle to a specific shape. In this way, it was possible to obtain an atomistic model of a nanoparticle that is metastable, such as a ceria nanocube. This method could therefore find a more general use, allowing the simulator to obtain suitable atomistic models of nanomaterials with specific shapes, thus tailoring the surfaces exposed.

The mechanical properties of ceria nanoparticles have been then calculated using MD simulation. Ceria nanoparticles with different shapes and size, comprising a rich microstructure, have been simulated under uniaxial compression. Also in this case, a new technique has been employed, which consist in using an atomic “anvil” to

simulate the compression. This ensures that the strain travels from the surface to the bulk of the nanoparticles, in closer agreement with how the real materials are tested. We have found that the mechanical properties of the nanoparticles are strongly dependent on the presence of grain boundaries. The simulations also predict that Ostwald ripening can be induced along a grain boundary by the applied uniaxial force. Therefore, the formation of a single crystal is induced by the strain from a polycrystalline precursor. This study therefore shows that the properties of nanomaterials could be tuned by applying force.

APPENDIX A1

TGA/DSC measurements of the precursors used during the synthesis

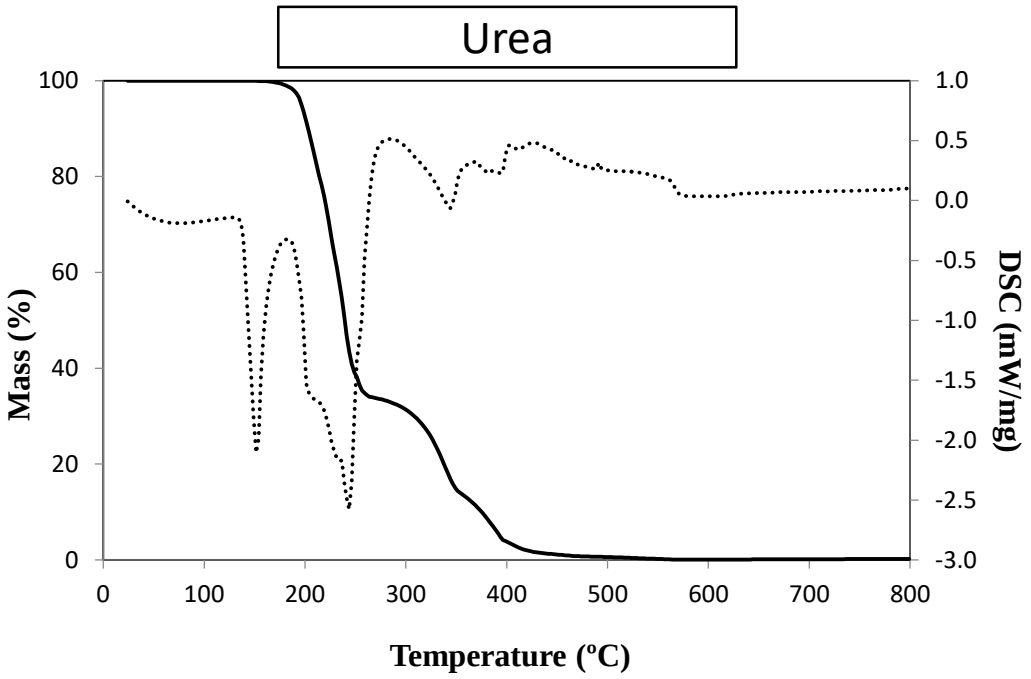

Figure A1.1 TGA/DSC curves of pure urea; full line: TGA; dots: DSC.

Table A1.1 TGA/DSC results of pure urea; 'exo' and 'endo' are used to indicate an exothermic or endothermic peak respectively.

Sample	Peak	Mass change (%)	Temperature (°C)	Enthalpy (kJ · g^{-1})	Residual mass (%)
Urea	1 (endo)	1.0	152.4	0.18	0.0
	2 (endo)	66.0	243.9	0.71	
	3 (endo)	21.0	345.1	0.08	

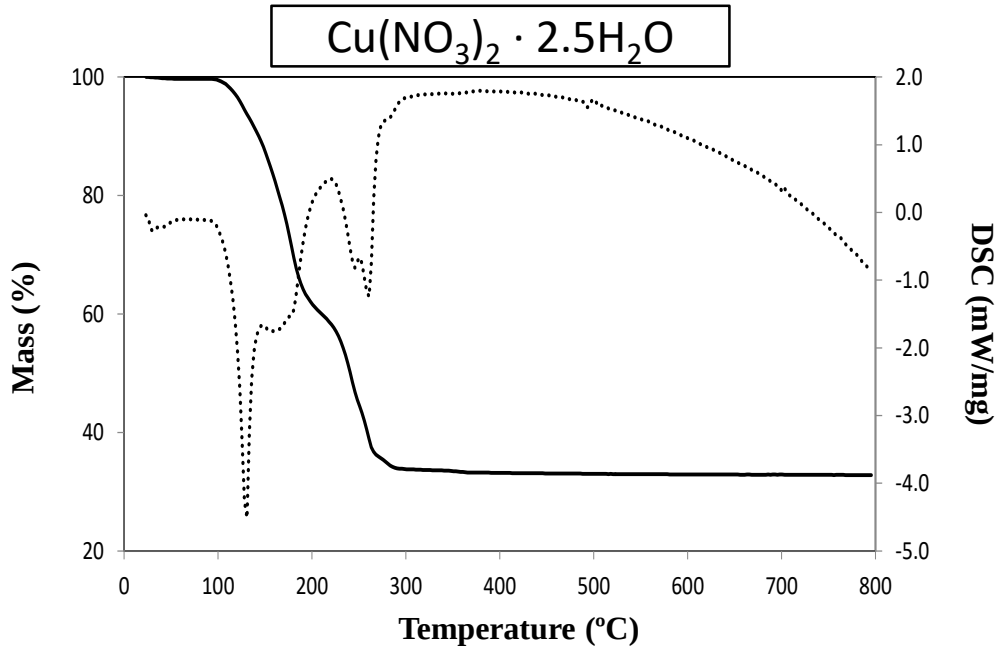

Figure A1.2 TGA/DSC curves of pure copper nitrate hemipentahydrate; full line: TGA; dots: DSC.

Table A1.2 TGA/DSC results of pure copper nitrate hemipentahydrate; 'exo' and 'endo' are used to indicate an exothermic or endothermic peak respectively.

Sample	Peak	Mass change (%)	Temperature (°C)	Enthalpy (kJ · g^{-1})	Residual mass (%)
$Cu(NO_3)_2$ ·	1 (endo)	41.6	129.9	1.04	35.9
2.5 H_2O	2 (endo)	22.5	260.2	0.35	

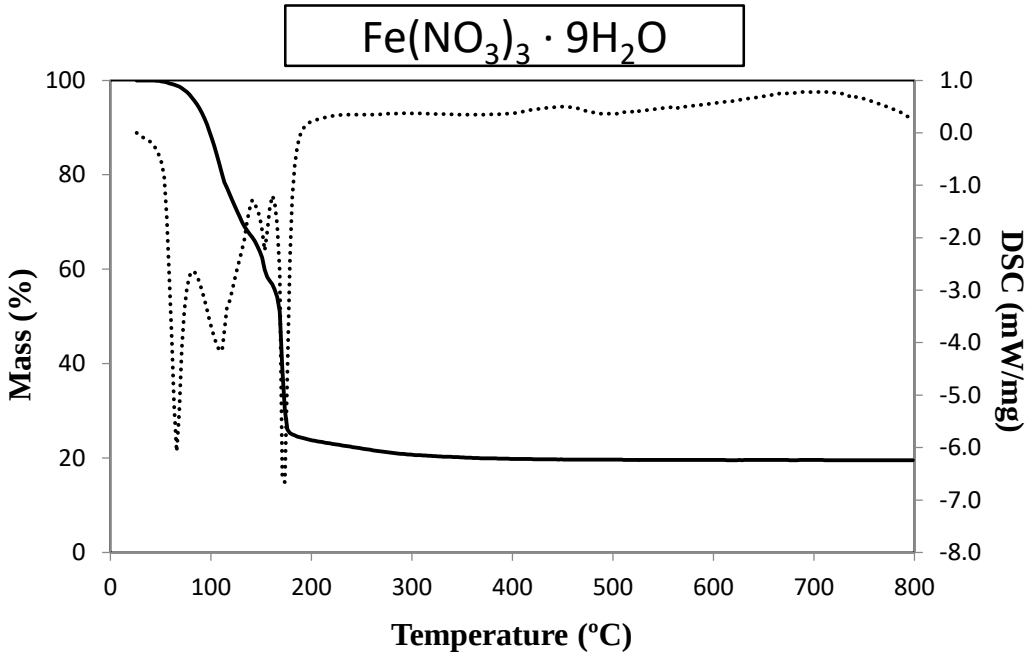

Table A1.3 TGA/DSC results of pure iron nitrate nonahydrate; full line: TGA; dots: DSC.

Figure A1.3 TGA/DSC curves of pure iron nitrate nonahydrate; 'exo' and 'endo' are used to indicate an exothermic or endothermic peak respectively.

Sample	Peak	Mass change (%)	Temperature (°C)	Enthalpy (kJ · g^{-1})	Residual mass (%)
$Fe(NO_3)_3 \cdot 9H_2O$	1 (endo)	3.9	65.5	0.23	23.9
	2 (endo)	29.7	109.5	0.32	
	3 (endo)	9.6	153.1	0.05	
	4 (endo)	32.8	171.4	0.36	

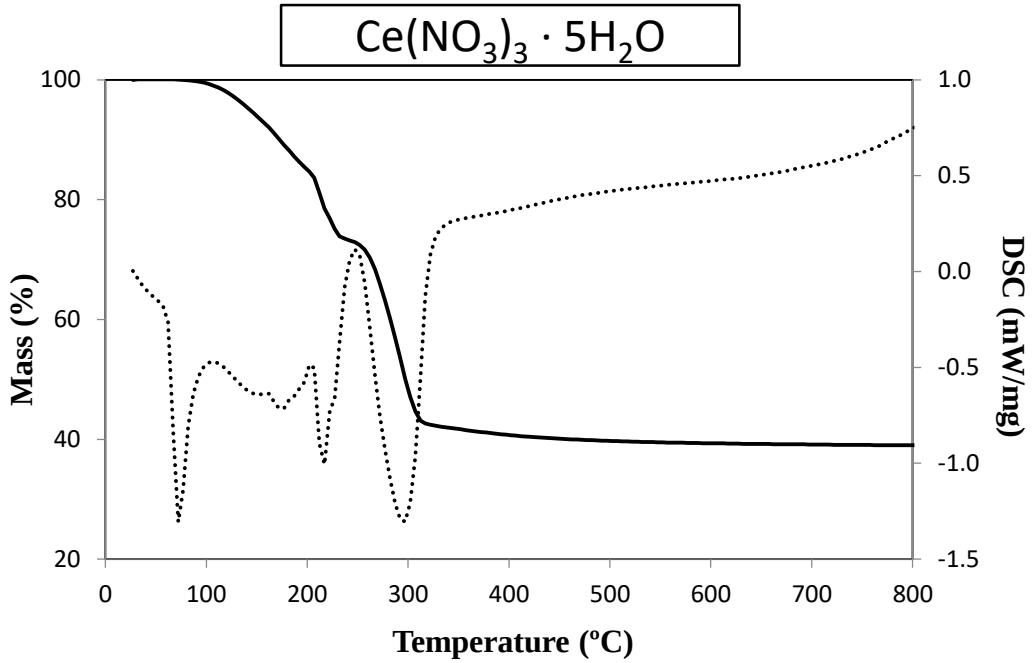

Figure A1.4 TGA/DSC curves of pure cerium nitrate pentahydrate; full line: TGA; dots: DSC.

Table A1.4 TGA/DSC results of pure cerium nitrate pentahydrate; 'exo' and 'endo' are used to indicate an exothermic or endothermic peak respectively.

Sample	Peak	Mass change (%)	Temperature (°C)	Enthalpy ($kJ \cdot g^{-1}$)	Residual mass (%)
$Ce(NO_3)_3 \cdot 5H_2O$	1 (endo)	1.0	74.0	0.09	38.9
	2 (endo)	14.5	173.8	0.08	
	3 (endo)	11.8	216.5	0.08	
	4 (endo)	30.8	295.0	0.38	

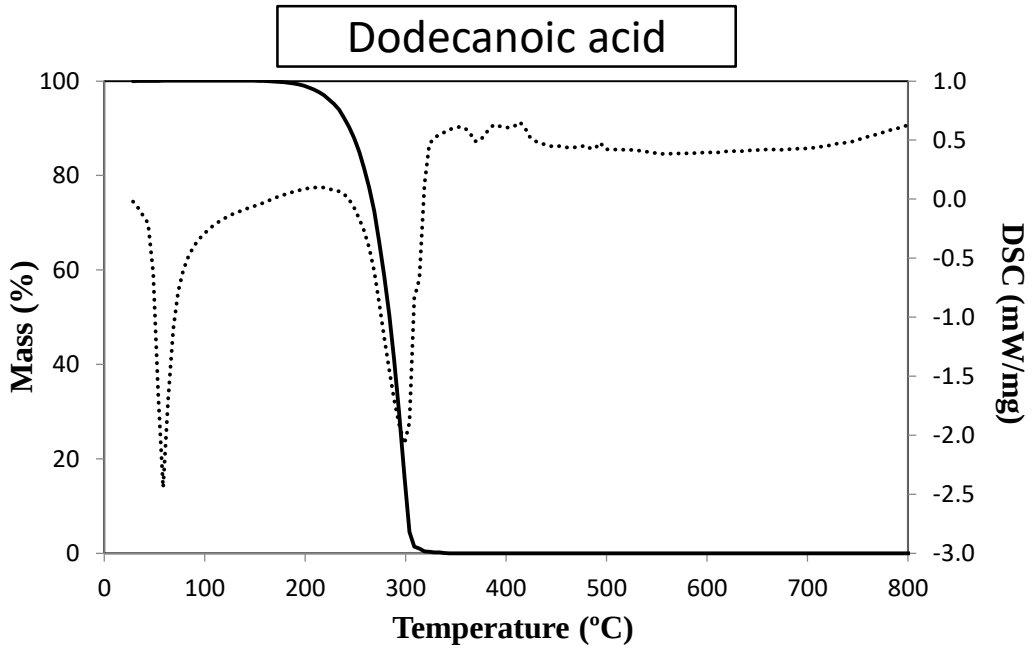

Table A1.5 TGA/DSC results of pure dodecanoic acid; full line: TGA; dots: DSC.

Figure A1.5 TGA/DSC curves of pure dodecanoic acid; 'exo' and 'endo' are used to indicate an exothermic or endothermic peak respectively.

Sample	Peak	Mass change (%)	Temperature (°C)	Enthalpy (kJ · g^{-1})	Residual mass (%)
Dodecanoic	1 (endo)	0.0	58.9	0.28	0.00
acid	2 (endo)	100.0	301.0	0.52	

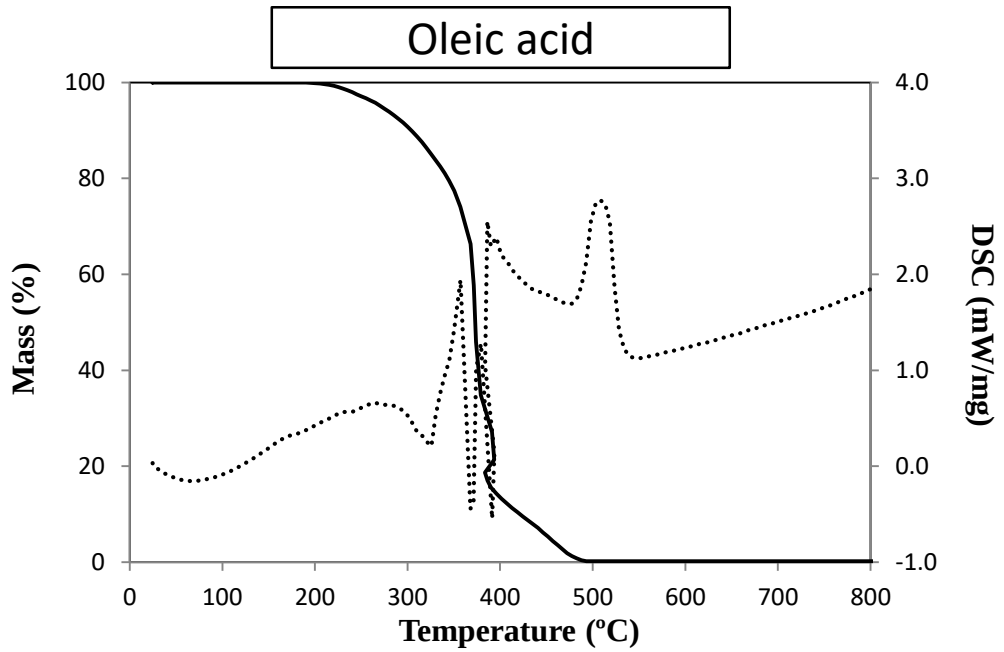

Figure A1.6 TGA/DSC curves of pure oleic acid; full line: TGA; dots: DSC.

Table A1.6 TGA/DSC results of pure oleic acid; 'exo' and 'endo' are used to indicate an exothermic or endothermic peak respectively.

Sample	Peak	Mass change (%)	Temperature (°C)	Enthalpy (kJ · g^{-1})	Residual mass (%)
OLA	1 (endo)	14.2	265.1	0.24	0.00
	2 (endo)	21.3	357.0	0.24	
	3 (endo)	62.3	386.0	0.68	

APPENDIX A2

Characterisation of CeO_2-SiO_2 nanocomposites by co-gelation

(Chapter 4)

TGA/DSC

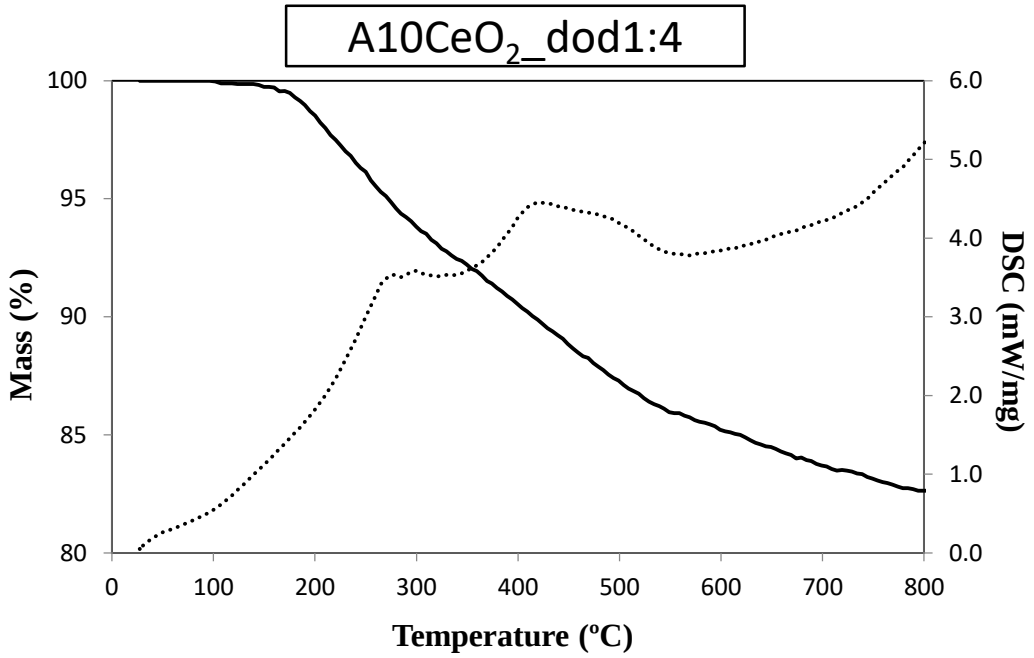

Figure A2.1 TGA\DSC curves of the A10CeO$_2$_dod1:4 aerogel nanocomposite; full line: TGA; dots: DSC.

Table A2.1 TGA\DSC results for the A10CeO$_2$_dod_1:4 aerogel nanocomposite. 'exo' and 'endo' are used to indicate an exothermic or endothermic peak respectively.

Sample	Peak	Mass change (%)	Temperature (°C)	Enthalpy (kJ · g^{-1})	Residual mass (%)
A10CeO$_2$_dod1:4	1 (exo)	7.33	298.5	- 0.37	81.81
	2 (exo)	6.63	420.2	- 0.57	

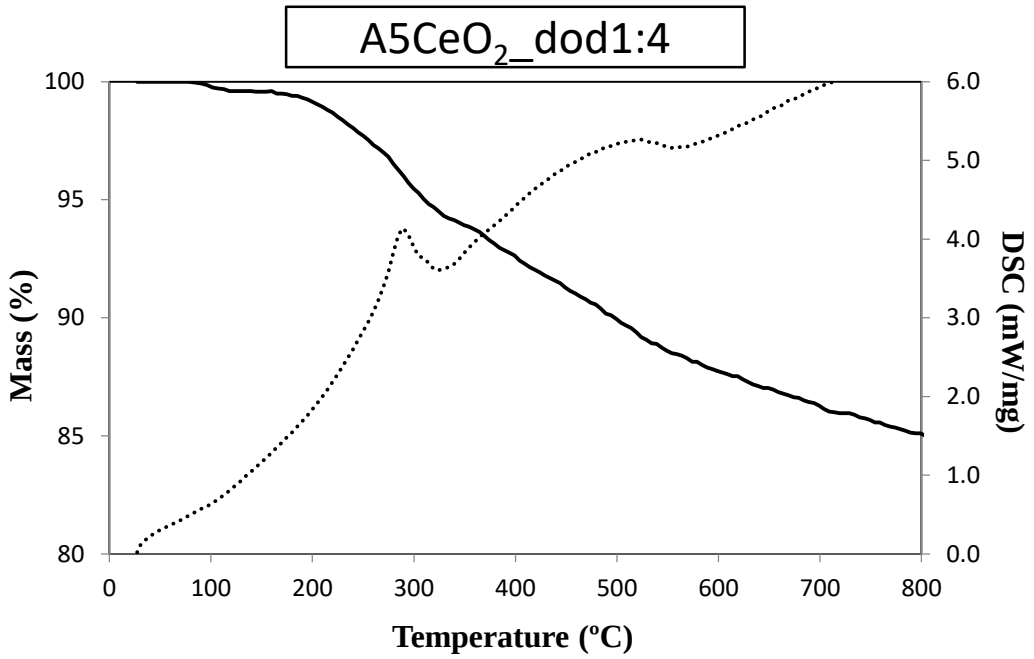

Figure A2.2 TGA\DSC curves of the A5CeO$_2$_dod1:4 aerogel nanocomposite; full line: TGA; dots: DSC.

Table A2.2 TGA\DSC results for the A5CeO$_2$_dod_1:4 aerogel nanocomposite; 'exo' and 'endo' are used to indicate an exothermic or endothermic peak respectively.

Sample	Peak	Mass change (%)	Temperature (°C)	Enthalpy (kJ · g^{-1})	Residual mass (%)
A5CeO$_2$_dod1:4	1 (exo)	5.00	289.3	- 0.24	84.07
	2 (exo)	6.14	523.3	- 0.17	

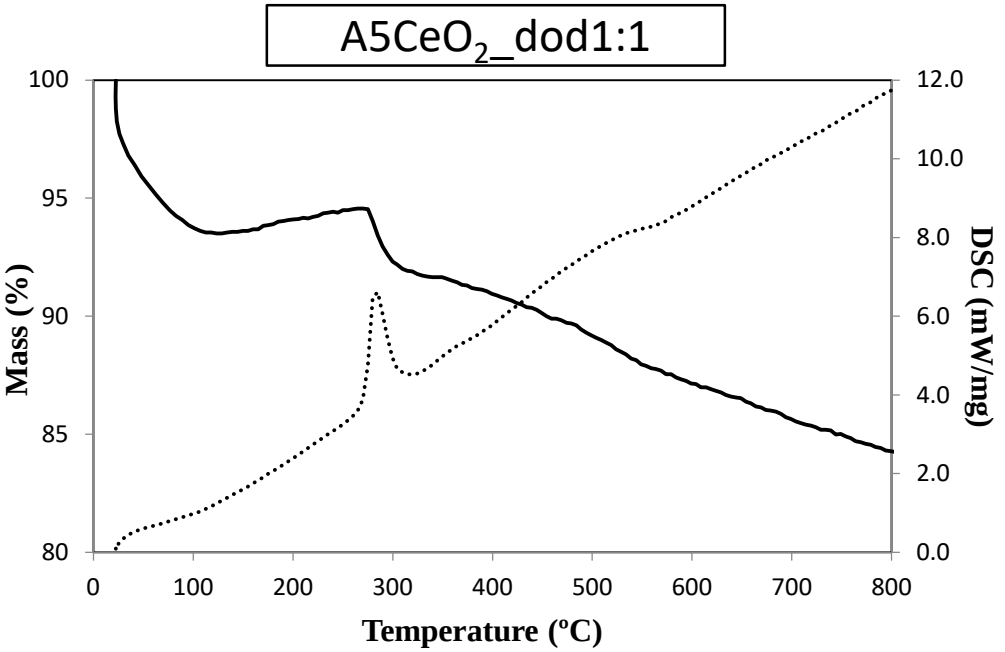

Figure A2.3 TGA\DSC curves of the A5CeO$_2$_dod1:1 aerogel nanocomposite; full line: TGA; dots: DSC.

Table A2.3 TGA\DSC results for the A5CeO$_2$_dod_1:1 aerogel nanocomposite. 'exo' and 'endo' are used to indicate an exothermic or endothermic peak respectively.

Sample	Peak	Mass change (%)	Temperature (°C)	Enthalpy (kJ · g^{-1})	Residual mass (%)
A5CeO$_2$_dod1:1	1 (exo)	2.67	282.9	- 0.36	83.26

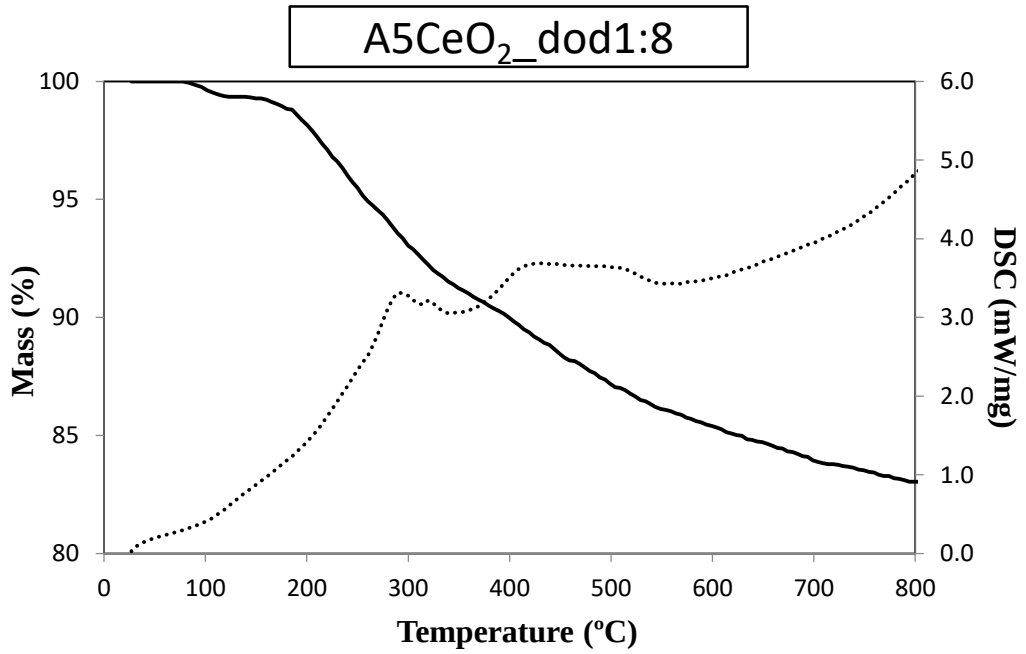

Figure A2.4 TGA\DSC curves of the A5CeO2_dod1:8 aerogel nanocomposite; full line: TGA; dots: DSC.

Table A2.4 TGA\DSC results for the A5CeO2_dod_1:8 aerogel nanocomposite. 'exo' and 'endo' are used to indicate an exothermic or endothermic peak respectively.

Sample	Peak	Mass change (%)	Temperature (°C)	Enthalpy (kJ · g^{-1})	Residual mass (%)
A5CeO$_2$_dod1:8	1 (exo)	8.13	292.3	- 0.38	81.81
	2 (exo)	4.99	433.4	- 0.32	

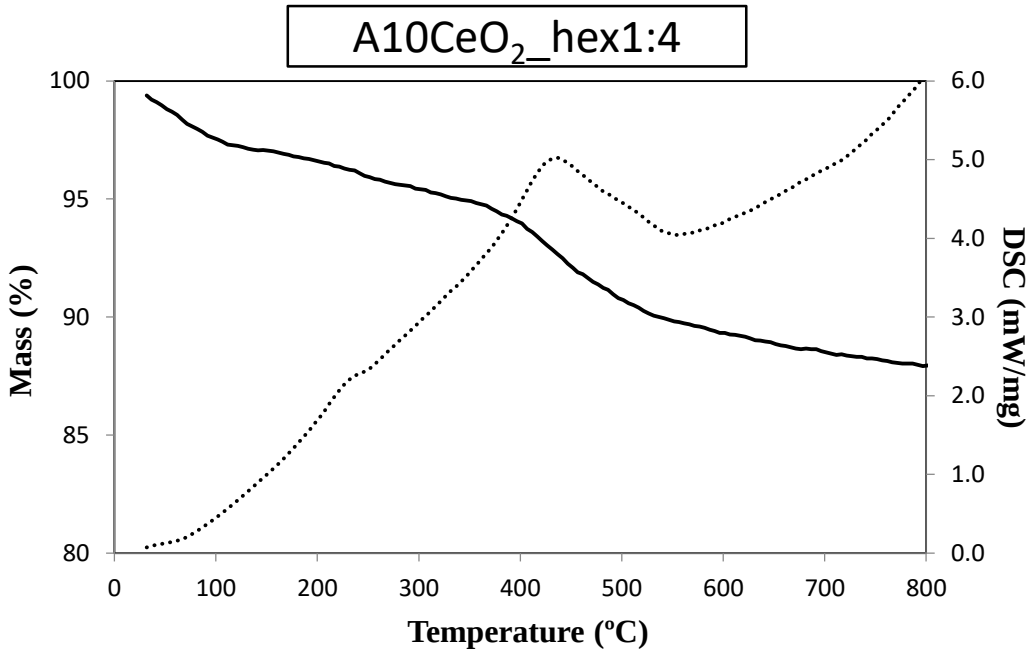

Figure A2.5 TGA\DSC curves of the A10CeO$_2$_hex1:4 aerogel nanocomposite; full line: TGA; dots: DSC.

Table A2.5 TGA\DSC results for the A10CeO$_2$_hex_1:4 aerogel nanocomposite. 'exo' and 'endo' are used to indicate an exothermic or endothermic peak respectively.

Sample	Peak	Mass change (%)	Temperature (°C)	Enthalpy (kJ · g^{-1})	Residual mass (%)
A10CeO$_2$_hex1:4	1 (exo)	5.92	437.9	- 0.82	86.26

XRD

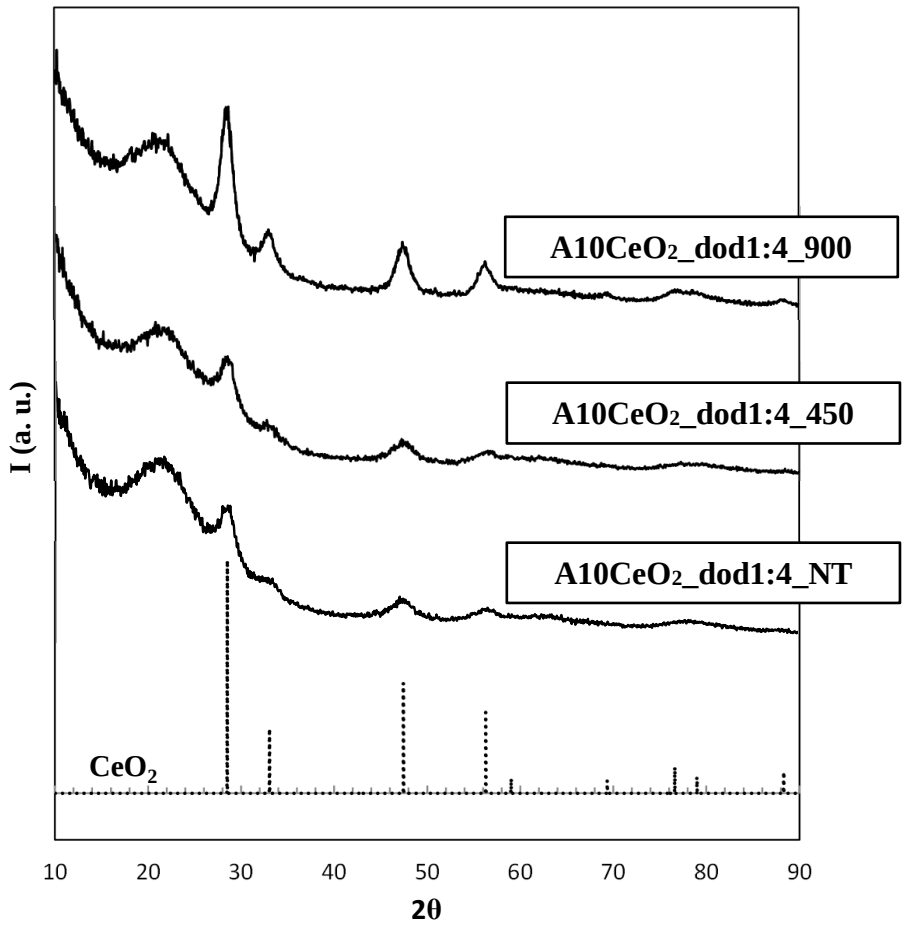

Figure A2.6 XRD patterns of the sample A10CeO_2_dod1:4 as synthesised and after thermal treatment at 450 and 900 ºC. The XRD pattern of the CeO_2 cubic crystal structure is reported at the bottom with dashed lines.

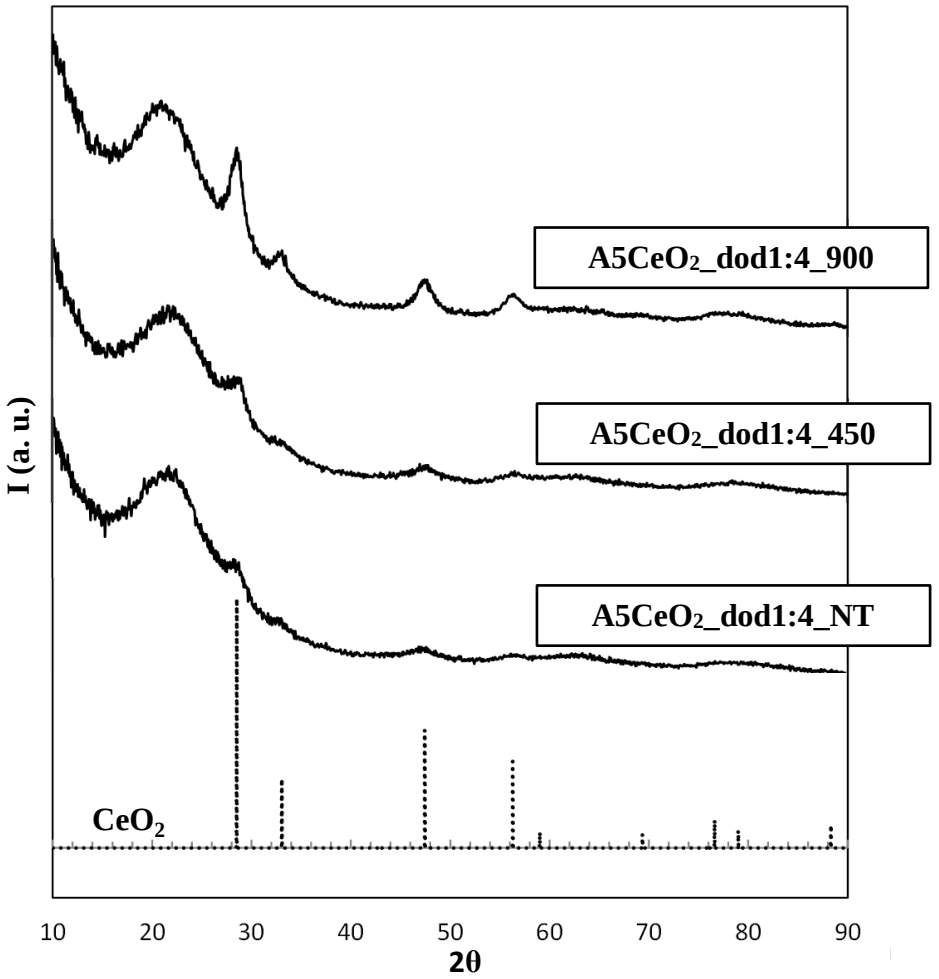

Figure A2.7 XRD patterns of the sample A5CeO_2_dod1:4 as synthesised and after thermal treatment at 450 and 900 ºC. The XRD pattern of the CeO_2 cubic crystal structure is reported at the bottom with dashed lines.

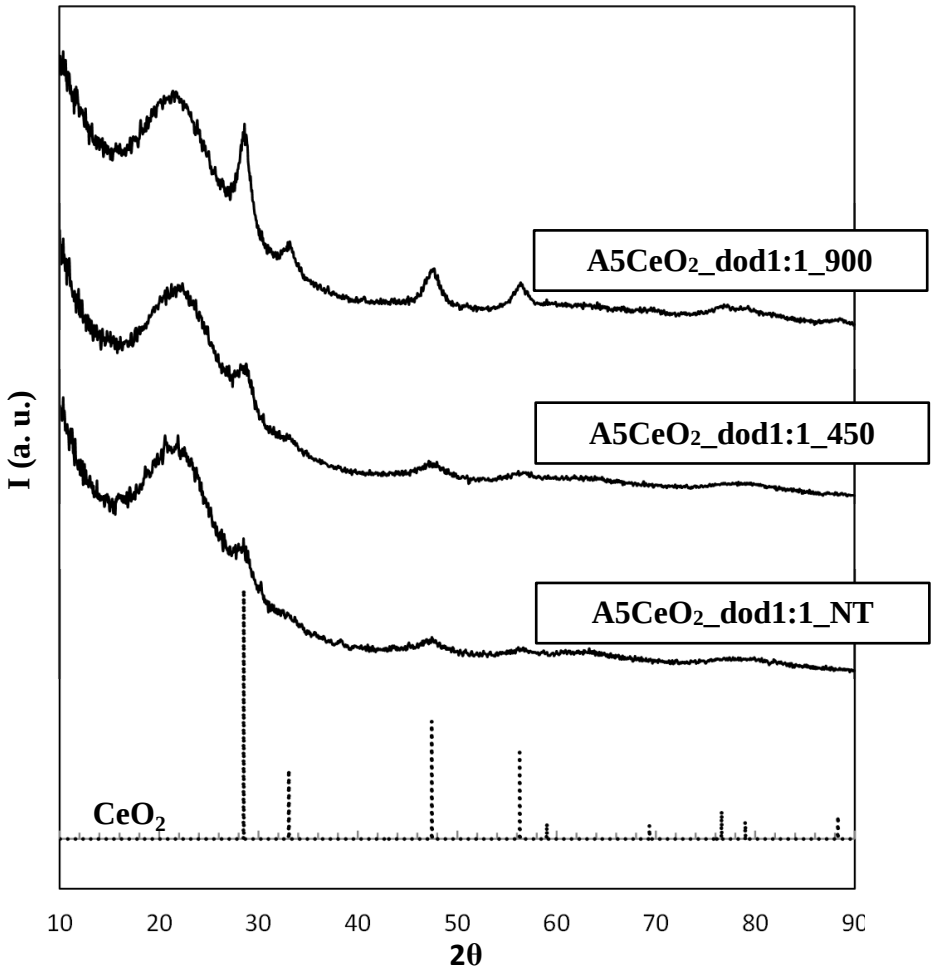

Figure A2.8 XRD patterns of the sample A5CeO_2_dod1:1 as synthesised and after thermal treatment at 450 and 900 ºC. The XRD pattern of the CeO_2 cubic crystal structure is reported at the bottom with dashed lines

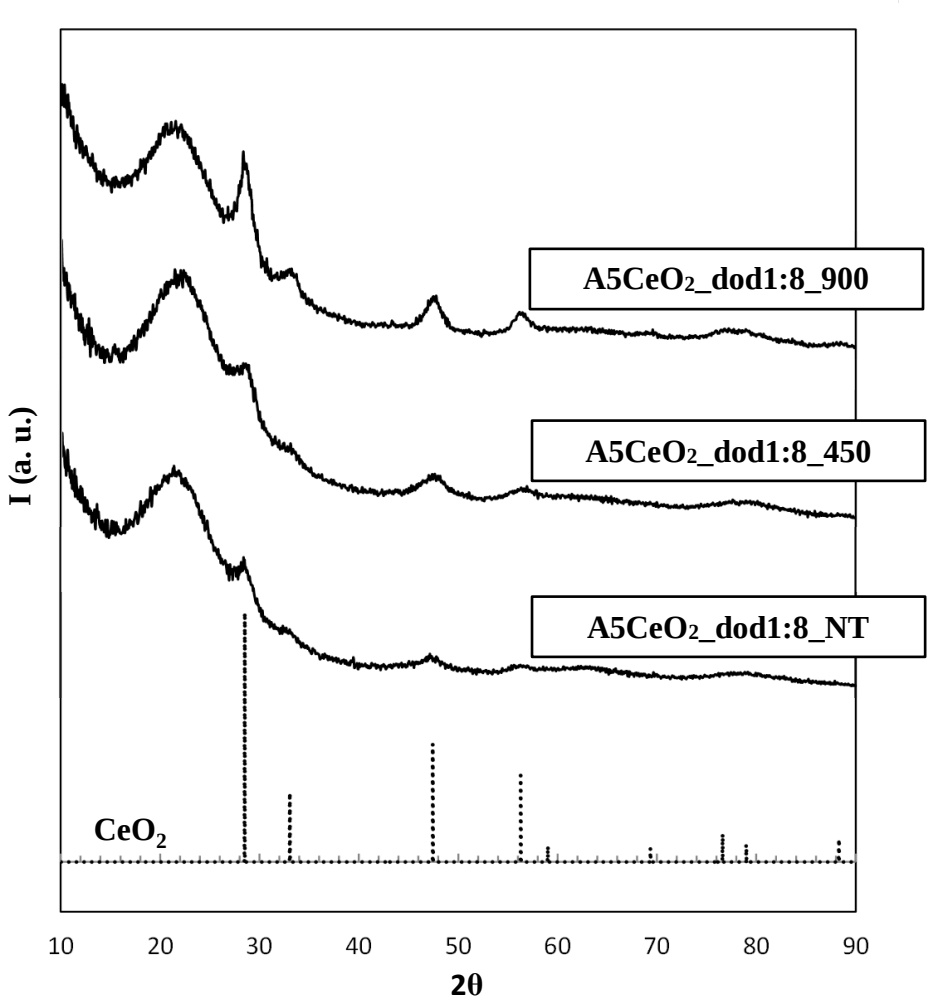

Figure A2.9 XRD patterns of the sample A5CeO_2_dod1:8 as synthesised and after thermal treatment at 450 and 900 ºC. The XRD pattern of the CeO_2 cubic crystal structure is reported at the bottom with dashed lines

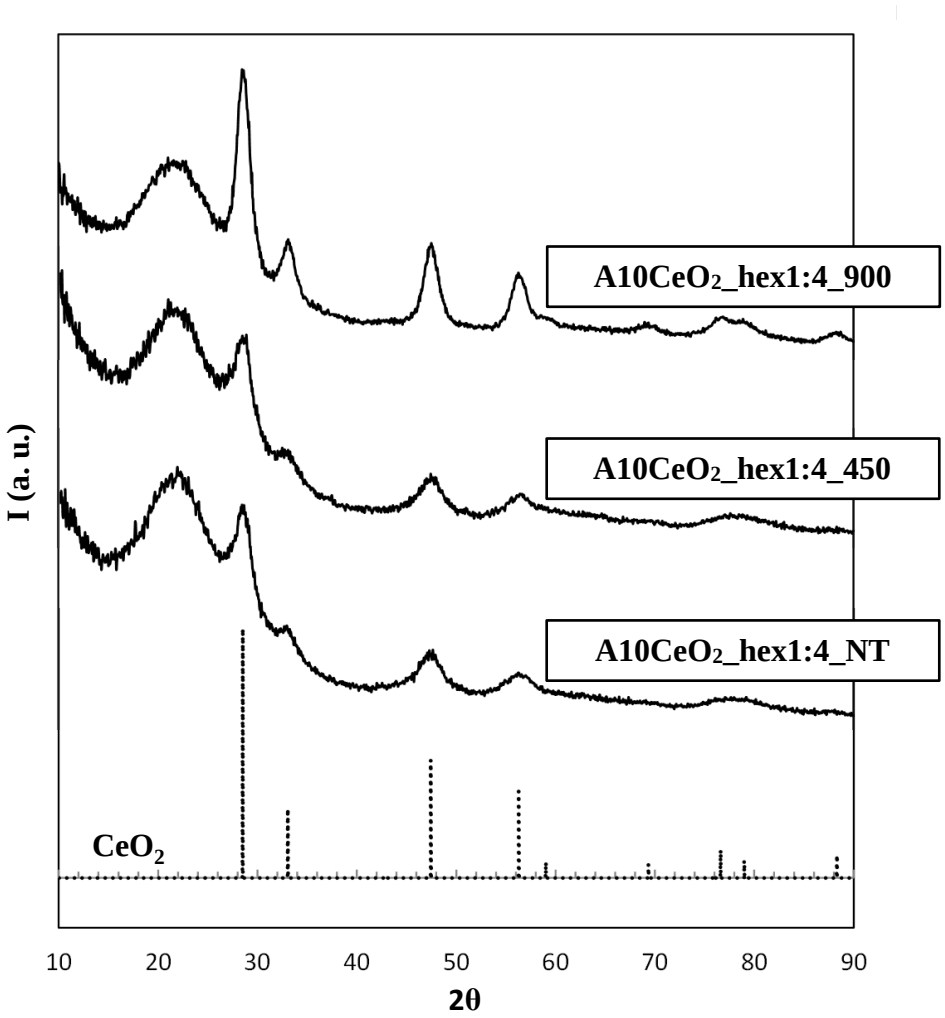

Figure A2.10 XRD patterns of the sample A10CeO_2_hex1:4 as synthesised and after thermal treatment at 450 and 900 ºC. The XRD pattern of the CeO_2 cubic crystal structure is reported at the bottom with dashed lines

Table A2.6 Average crystal sizes calculated using the Scherrer equation of all the samples shown in this section.

Sample	Peak pos. [º2θ]	Crystallite size [nm]
A5CeO_2_dod1:1_NT	47.37	4
A5CeO_2_dod1:1_450	47.47	3
A5CeO_2_dod1:1_900	47.51	6
A5CeO_2_dod1:8_NT	47.28	4
A5CeO_2_dod1:8_450	47.51	4
A5CeO_2_dod1:8_900	47.52	7
A10CeO_2_hex1:4_NT	47.38	4
A10CeO_2_hex1:4_450	47.47	4
A10CeO_2_hex1:4_900	47.51	5

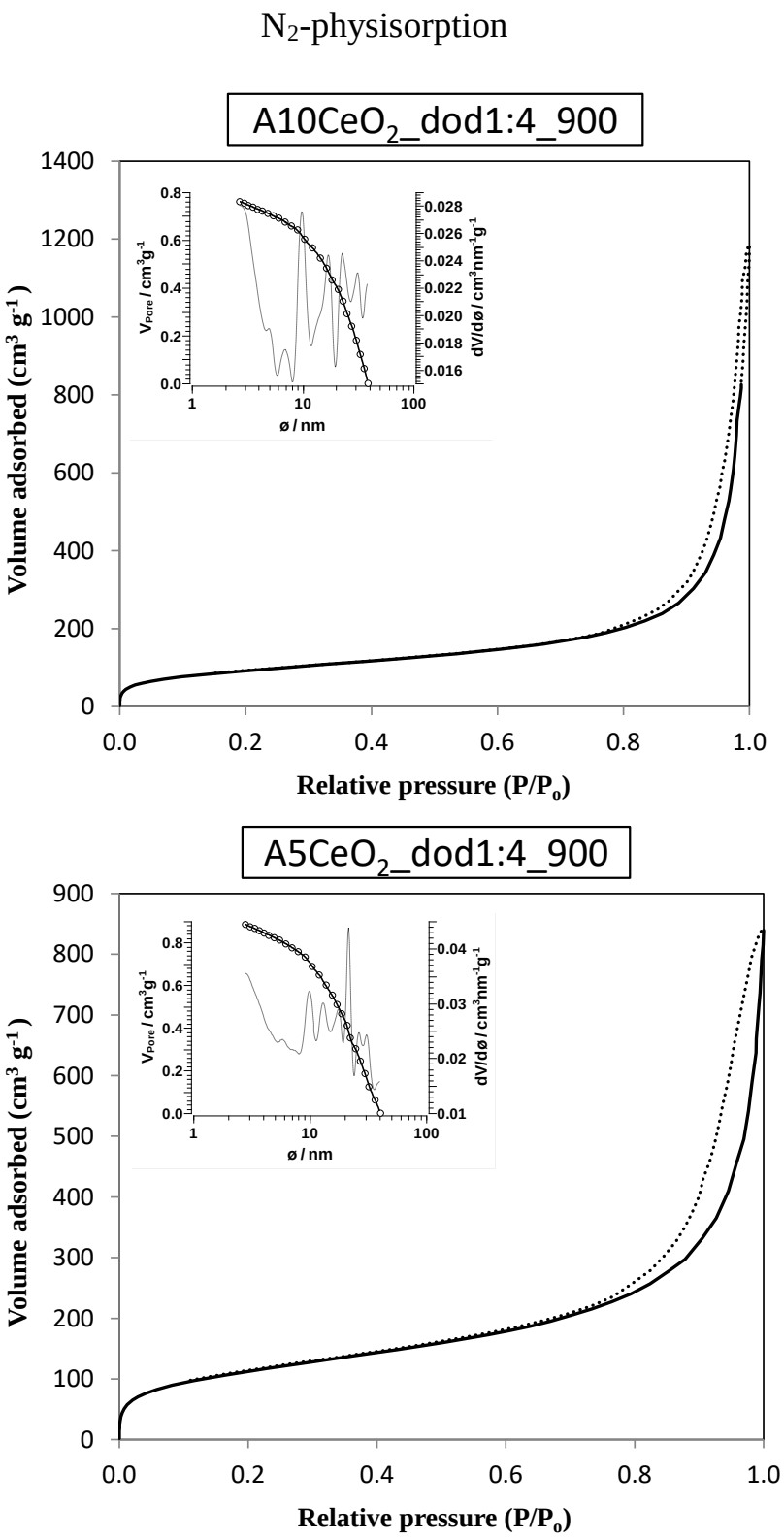

Figure A2.11 N_2 physisorption isotherms of the sample A10CeO2_dod1:4_900 (top) and A5CeO2_dod1:4_900 (bottom) and pore size distribution calculated using the desorption branch (insets).

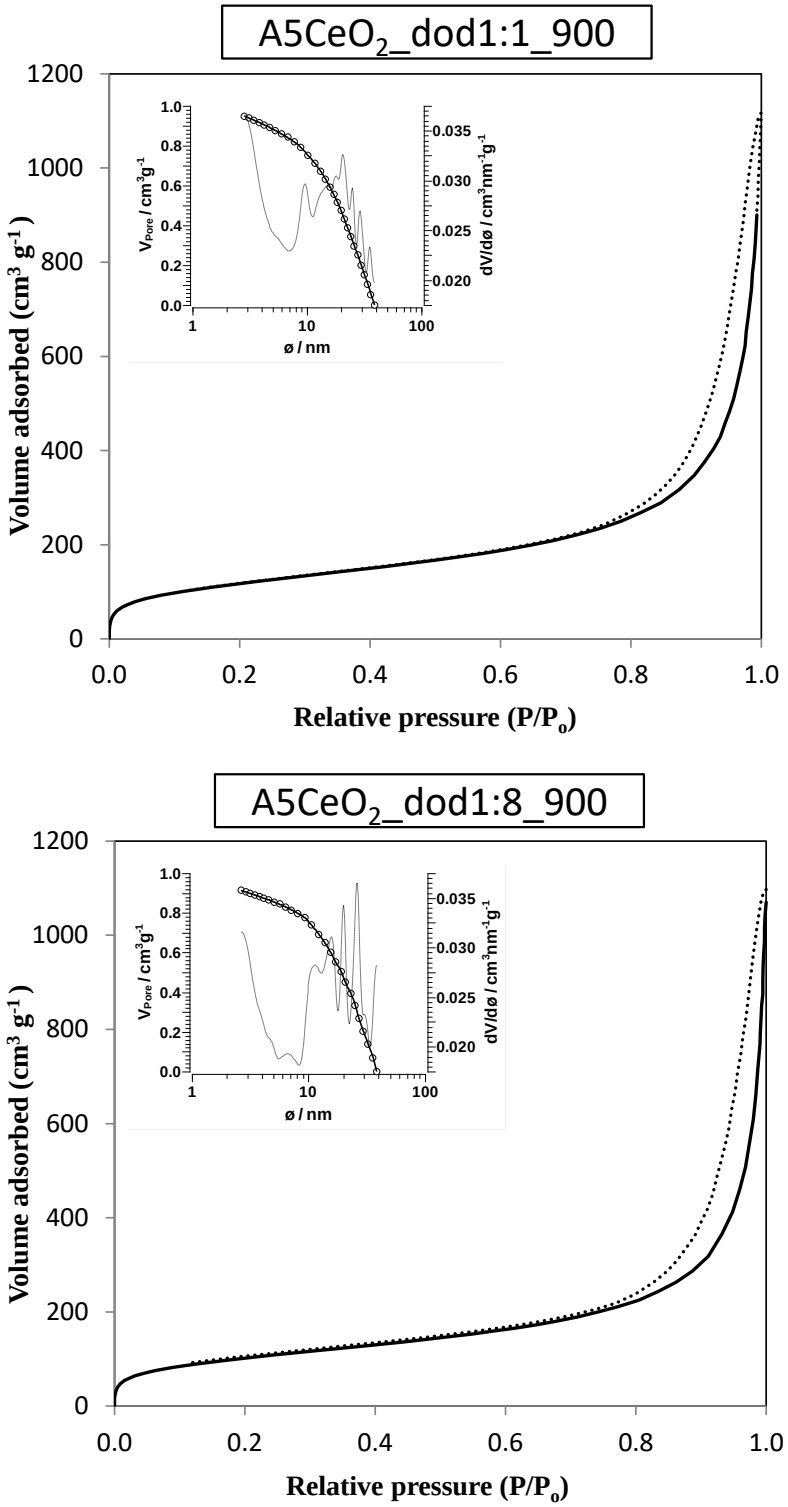

Figure A2.12 N_2 physisorption isotherms of the sample A5CeO$_2$_dod1:1_900 (top) and A5CeO$_2$_dod1:8_900 (bottom) and pore size distribution calculated using the desorption branch (insets).

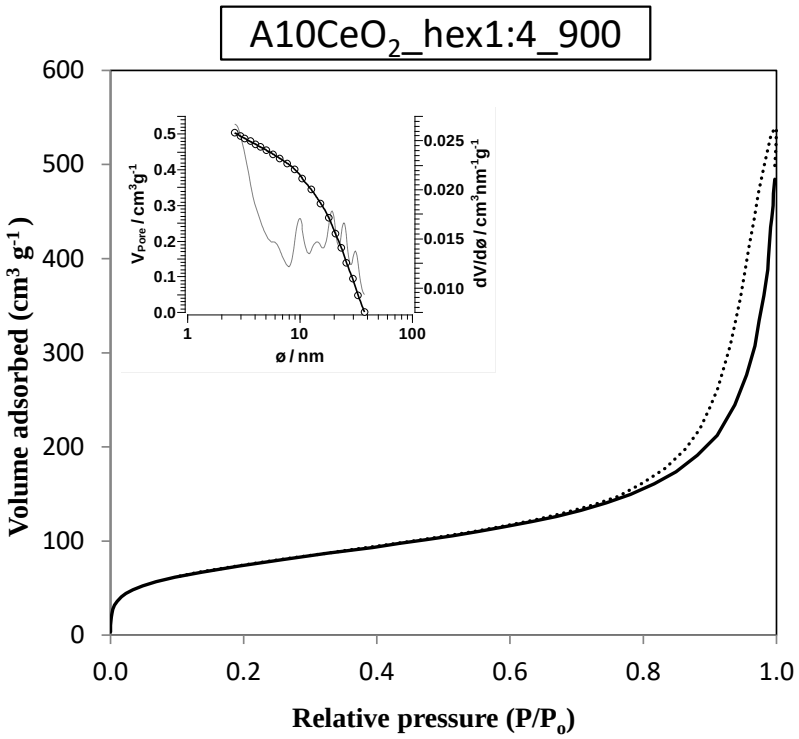

Figure A2.13 N_2 physisorption isotherms of the sample A10CeO_2_hex1:4_900 and pore size distribution calculated using the desorption branch (inset).

Table A2.7 Surface area, S, pore volume, V_P, and pore diameter values for the aerogel nanocomposites shown in this section obtained by N_2physisorption.

Sample	S ($m^2 \cdot g^{-1}$)	V_P ($cm^3 \cdot g^{-1}$)	Pore diameter (nm)
A10CeO_2_dod1:4_900	338.9 ± 0.2	0.76	21
A5CeO_2_dod1:4_900	412.5 ± 1.2	0.89	20
A5CeO_2_dod1:1_900	430.6 ± 1.2	0.95	20
A5CeO_2_dod1:8_900	373.0 ± 1.6	0.91	20
A10CeO_2_hex1:4_900	273.3 ± 0.1	0.50	19

APPENDIX A3

XRD, TGA/DSC and N_2-physisorption characterisation of CeO_2-SiO_2 nanocomposites presented in Chapter 5

XRD

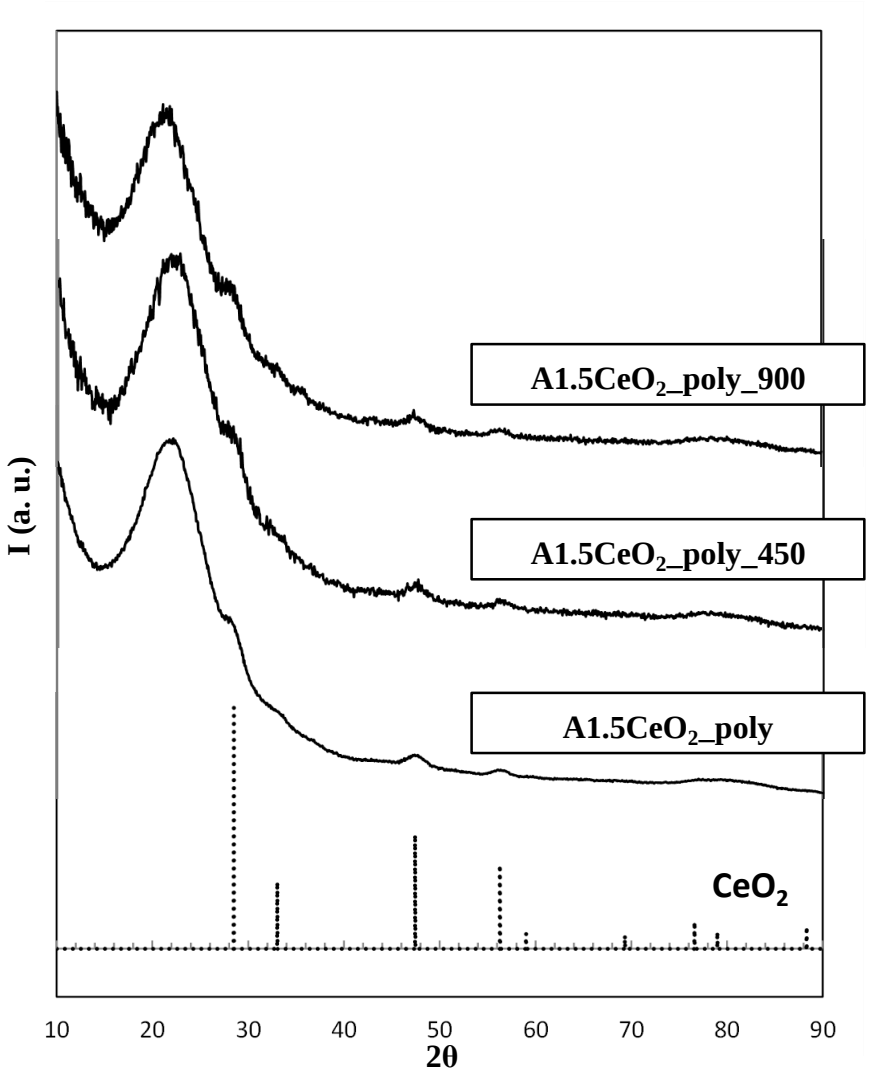

Figure A3.1 Diffraction patterns of the nanocomposite A1.5CeO_2_poly after supercritical extraction and thermal treatments at 450 and 900 ºC for 1 h.

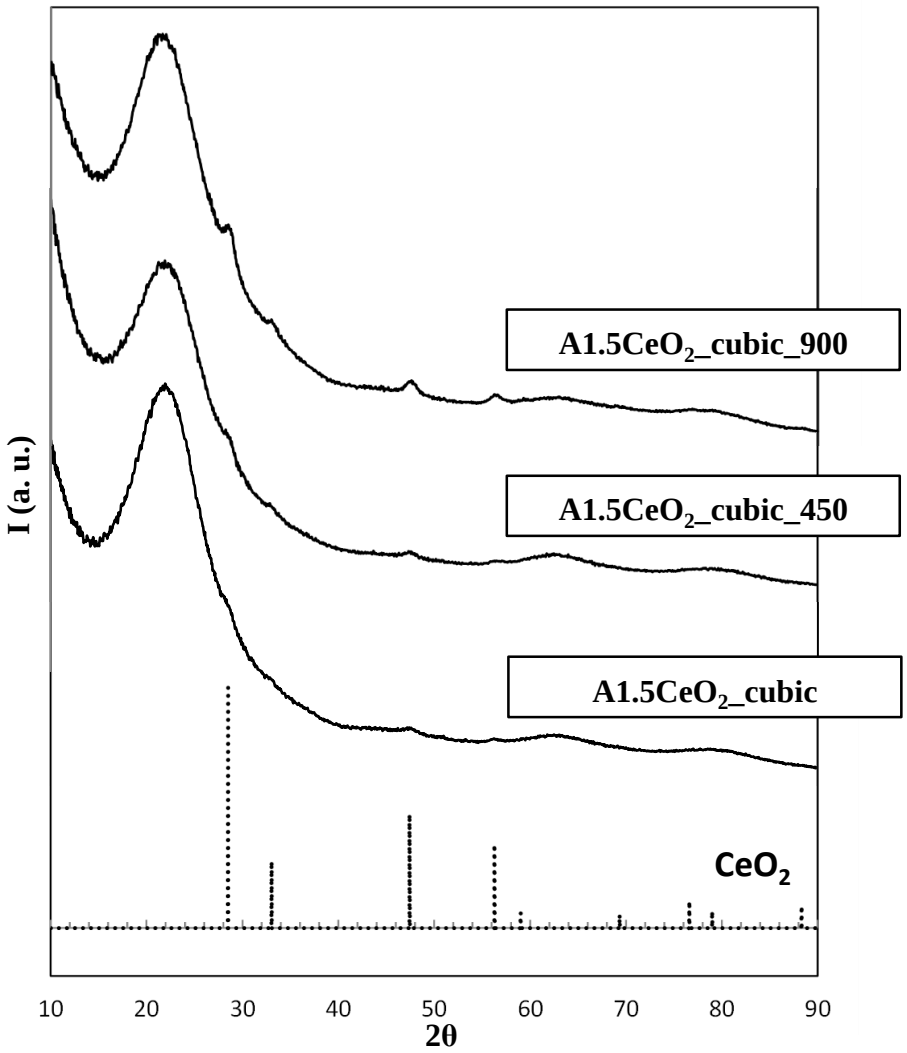

Figure A3.2 Diffraction patterns of the nanocomposite A1.5CeO_2_cubic after supercritical extraction and thermal treatments at 450 and 900 ºC for 1 h.

TGA/DSC

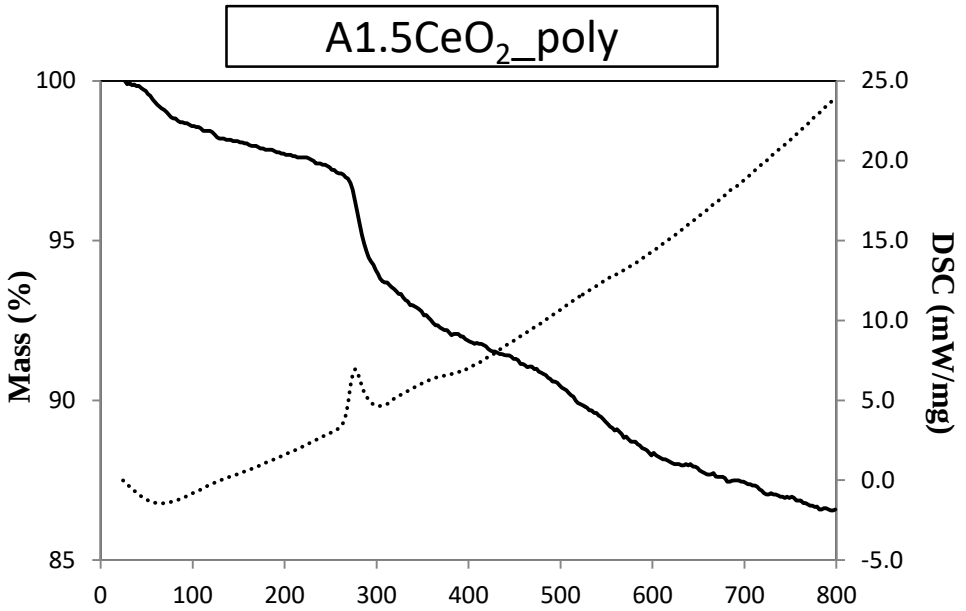

Figure A3.3 TGA\DSC curves of the A1.5CeO_2_poly aerogel nanocomposite; full line: TGA; dots: DSC.

Table A3.1 TGA\DSC results of the A1.5CeO_2_poly aerogel nanocomposite. 'exo' and 'endo' are used to indicate an exothermic or endothermic peak respectively.

Sample	Peak	Mass change (%)	Temperature (°C)	Enthalpy (kJ · g^{-1})	Residual mass (%)
A1.5CeO_2_poly	1 (exo)	3.57	276.7	- 0.33	86.63

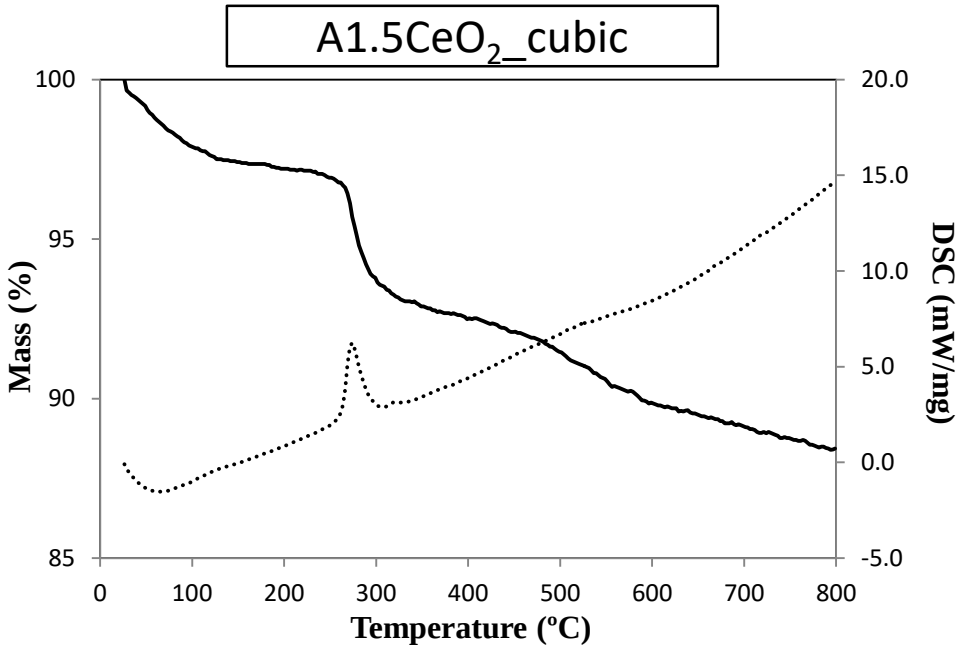

Figure A3.4 TGA\DSC curves of the A1.5CeO_2_cubic aerogel nanocomposite; full line: TGA; dots: DSC.

Table A3.2 TGA\DSC results of the A1.5CeO_2_cubic aerogel nanocomposite. 'exo' and 'endo' are used to indicate an exothermic or endothermic event respectively.

Sample	Peak	Mass change (%)	Temperature (°C)	Enthalpy (kJ · g^{-1})	Residual mass (%)
A1.5CeO_2_cubic	1 (exo)	3.85	273.4	- 0.47	88.43

N_2-physisorption

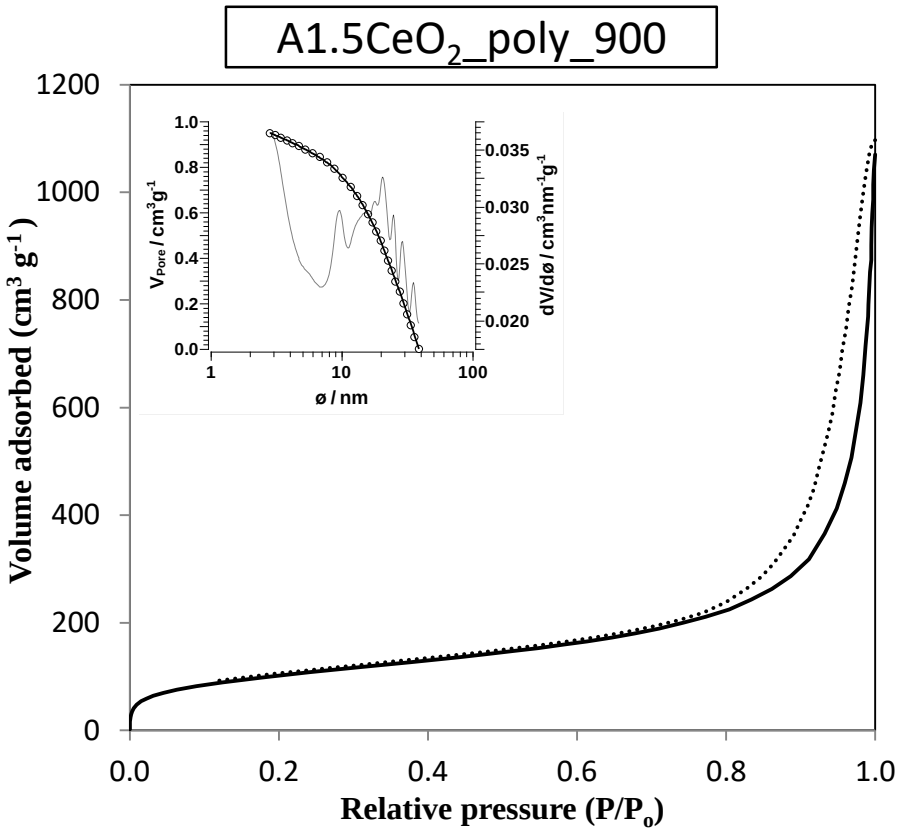

Figure A3.5 N_2-physisorption isotherms of the sample A1.5CeO_2_poly_900 and pore size distribution calculated using the desorption branch (inset)

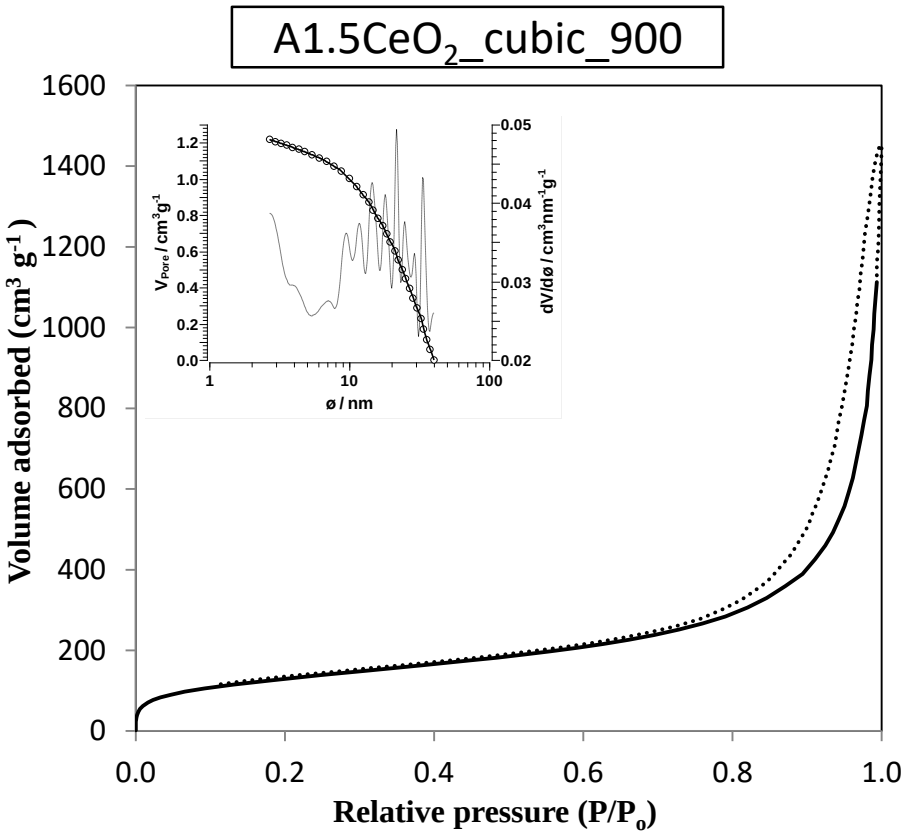

Figure A3.6 N_2-physisorption isotherm of the sample A1.5CeO_2_cubic_900 and pore size distribution calculated using the desorption branch (inset).

Table A3.3 Surface area, S, pore volume, V_P, and pore diameter values for the aerogel nanocomposites shown in this section obtained by N_2-physisorption.

Sample	S ($m^2 \cdot g^{-1}$)	V_P ($cm^3 \cdot g^{-1}$)	Pore diameter (nm)
A1.5CeO_2_poly_900	430.4 ± 1.2	0.90	20
A1.5CeO_2_cubic_900	473.2 ± 2.6	0.86	21

ACKNOWLEDGMENTS

I wish to express my sincere gratitude to my advisers, Dr. Anna Corrias and Dr. Dean Sayle, for the guidance and freedom they offered me throughout the whole project. I truly feel lucky for being one of their students.

I wish to thank the research group led by Dr. Maria Francesca Casula at University of Cagliari (Italy), for hosting me in their laboratories and for letting me using their equipment, as much as I needed. A special thank goes to Dr. Danilo Loche, who made a very strong contribution to the work presented in this thesis, in particular the TEM characterisation.

My gratitude also goes to Prof. Andrea Falqui and Efisio Zuddas from KAUST (Saudi Arabia), for the additional TEM and HRTEM characterisation.

There are also other people who played an important role for me during these three years, such as members of staff and Ph.D. fellows, as well as friends. My gratitude goes to Dr. Thi Sayle, Dr. Gavin Mountjoy, Mathew Coomber, Dr. Laura Vera Stimpson, Dr. Bruno Tomasello, Dr. Tim Kinnear, Ian Ross, Dr. Olivia Monaghan, Thomas Ashton, Yaroslav Kalinovskyy, Barbora Balonova, Nanami Yokota, Lucy Morgan, Silvia Cavuoto, Dr. Sofia Villar, Saeed Akkad and many others.

Finally, very important thanks go to my family and my girlfriend Valeria, for all their love and support.

My Ph.D. was financially supported by the School of Physical Sciences (University of Kent) and EPSRC.